

# Tidal Stream Energy Extraction in Coastal Basins

By

Scott Draper



A thesis submitted for the degree of  
Doctor of Philosophy  
at the University of Oxford

St Catherine's College  
Trinity Term 2011

# Abstract

## Tidal Stream Energy Extraction in Coastal Basins

A thesis submitted for the degree of Doctor of Philosophy

Scott Draper

St Catherine's College, Oxford

Trinity Term 2011

In recent years the extraction of energy from tidal streams has grown in popularity as a potential source of clean renewable energy. To extract this energy, tidal devices, resembling underwater turbines or hydroplanes, are deployed in a fast moving tidal stream. However, an important consequence is that the devices then act as a resistance to the tidal stream, which can influence local and far field natural tidal hydrodynamics and ultimately the power potential. This thesis is concerned with modelling idealised tidal stream devices deployed in a number of generic coastal basins, or sites, to better understand these effects on natural tidal flows and the potential to generate power.

Firstly, to describe the operation of an ideal tidal stream device Linear Momentum Actuator Disc Theory (LMADT) is applied to a porous disk placed in a steady uniform tidal stream of finite Froude number. A device efficiency is derived, which is defined as the power *available* to the device relative to the total power removed, or *extracted*, from the tidal stream including downstream mixing losses in the immediate wake of the devices.

A line sink of momentum is then proposed to represent a fence, or row, of ideal tidal devices in a 2D depth-averaged shallow water tidal flow. It is suggested that LMADT can be used to define this momentum sink in terms of the local Froude number, the spacing and size of devices, denoted by a blockage ratio, and the porosity of the devices. Implementation of the line sink of momentum into a numerical solution of the Shallow Water Equations (SWEs) using the Discontinuous Galerkin (DG) finite element method is outlined.

Extraction of energy from tidal channels, oscillating bays and an idealised coastal headland are analysed numerically and analytically using the proposed line sink of momentum. In general a maximum amount of energy extraction is calculated because the flow through the turbine fence reduces as the resistance of the fence increases. For each coastal geometry this maximum is not related in any simple way to the natural rate of energy dissipation due to bed friction or the undisturbed kinetic flux (despite the fact that both of these metrics have been used in the past to predict power extraction). The available power to devices within a tidal fence is maximised if large and closely packed turbines are adopted. Moreover, unless devices within the fence are perfectly efficient the maximum available power does not generally coincide with maximum power extraction.

For tidal channels and enclosed oscillating bays energy extraction tends to reduce tidal currents and tidal range, which may have environmental implications. In contrast energy extraction is found to increase tidal range in non-enclosed oscillating bays that are longer than a natural resonant length. Energy extraction is also found to augment tidal dispersion around coastal headlands.

A survey of real coastal sites and details of a numerical code, developed in this thesis to solve the SWEs to arbitrary spatial order of accuracy using the DG finite element method, are given in Appendices.

# Acknowledgments

I would like to thank Prof. Guy Houlby and Prof. Alistair Borthwick for their insight, encouragement and advice throughout this project. In particular Guy convinced me to undertake a DPhil in Engineering Science and introduced me to marine renewable energy, for which I am most grateful. Discussions with Prof. Richard Soulsby throughout this project have also been extremely useful. Ross McAdam, Esteban Ferrer, Claudio Consul and Richard Sandford have provided very helpful comments and advice on my work.

I am grateful to the Rhodes Trust for financial support, St Catherine's College for a science scholarship in my final year, and to Dr Byrne and Dr Gillespie for employing me as a Stipendiary Lecturer at St Catherine's for 2 years. Thank you also to Dr Willden and the Oxford Supercomputing Center, who allowed me to use their computing resources free of charge to run some of my calculations.

This thesis would not have been possible without the love and support of both my and Caitlin's family. Your timely phone calls and visits were a great treat! Finally, and most importantly, thank you to Caitlin and Holly. Your love, advice, encouragement and support have made my time in Oxford wonderful. Holly, I promise this thesis will not make it onto the bed time reading list.

# Nomenclature

## Common to Chapters 1-7

$a$	Amplitude of tidal elevation
$A_b$	Surface area of bay impounded by tidal barrage
$A_c$	Cross-sectional area of flow
$B$	Blockage ratio of actuator disc/turbine ( $=a/bh$ )
$C_d$	Depth-averaged seabed drag coefficient
$C'_d$	Effective drag coefficient
$C_{d,eff}$	Effective depth-averaged drag coefficient of an ideal device
$C_P$	Dimensionless power coefficient
$C_T$	Dimensionless thrust coefficient
$f$	Coriolis parameter
$Fr$	Froude number ( $U/\sqrt{gh}$ )
$g$	Acceleration due to gravity
$h$	Total fluid depth
$h_d$	Characteristic channel depth
$h_o$	Mean depth
$k_t$	Additional bed roughness due to tidal devices
$K_c$	Keulegan-Carpenter number ( $U/\omega L$ )
$L, L_1, L_2$	Dimensional length scales
$\mathbf{n}$	Unit normal vector
$p$	Static pressure
$P$	Instantaneous power (In Chapter 2 this is the power available to the tidal device; in all following chapters it is the total power extracted from a coastal site.)
$P_a$	Available power
$P_d$	Dissipated power
$P_f$	Kinetic flux
$P_t$	Instantaneous total power dissipated ( $P + P_d$ )
$t$	Time
$\mathbf{u} = (u, v)^T$	Depth-averaged tidal velocity vector
$U$	Characteristic velocity
$\alpha_2, \alpha_4, \beta_4$	Turbine, turbine wake and bypass velocity coefficients
$\gamma$	Power coefficient
$\eta$	Efficiency of an ideal tidal device
$\nu_T$	Depth-averaged turbulent eddy viscosity
$\xi$	Free surface elevation above mean water depth
$\rho$	Fluid density
$\tau_{x,b}, \tau_{y,b}$	Components of bed shear stress
$\omega$	Tidal frequency
$\overline{(\quad)}$	Time average (in Chapters 5-7)

## Chapter 2

$a_i$	Turbine induction factor
$A$	Cross sectional area of actuator disc/tidal device(s)

$b$	Width of open channel or center-to-center spacing between tidal devices
$P_W$	Power dissipated in the wake of an ideal tidal device
$T$	Thrust applied by an ideal tidal device on the fluid
$X$	Net thrust, above atmospheric, acting on the body of fluid contained within the streamtube
$z$	Vertical coordinate
$( )_{b,t}$	Denotes $b$ - bypass flow, $t$ -turbine flow
$( )_{1,2,3,4,5}$	Denotes location within flow field

### Chapter 3

$\mathbf{u}_*$	Velocity vector in three dimensions
$u_*, v_*, w_*$	Velocity components in three dimensions
$x, y, z$	Spatial Coordinates
$T_f$	Reynolds averaging time period
$\beta_{xx}, \beta_{xy}, \beta_{yy}$	Momentum correction factors
$\mu$	Dynamic Viscosity
$\nu_t$	Turbulent eddy viscosity

### Chapter 4

$b$	Centre to centre spacing between tidal devices
$c = \sqrt{gh}$	Celerity
$\mathbf{F}(\mathbf{U}, \mathbf{Q}), \mathbf{G}(\mathbf{U}, \mathbf{Q})$	Flux vectors
$\hat{\mathbf{F}}, \hat{\mathbf{G}}, \hat{\mathbf{R}}_x, \hat{\mathbf{R}}_y,$	Numerical flux
$i, k, p$	Integers
$h_m$	Characteristic mesh dimension
$l_v, l_h$	Vertical and horizontal mixing lengths
$M$	Degrees of freedom per element
$n$	Polynomial order of approximation
$\mathbf{Q} =$ $(\frac{\partial u}{\partial x}, \frac{\partial u}{\partial y}, \frac{\partial v}{\partial x}, \frac{\partial v}{\partial y})^T$	Vector of auxiliary variables
$\mathbf{R}_x(\mathbf{U}), \mathbf{R}_y(\mathbf{U})$	Auxiliary flux vectors
$\mathbf{S}(\mathbf{U})$	Vector of source terms
$\mathbf{U} = (u, uh, vh)^T$	Vector of dependent variables
$\mathbf{U}_h, \mathbf{Q}_h$	Polynomial approximation to the dependent and auxiliary variables
$\delta$	Smoothing variable at the edge of a turbine fence
$\Gamma_e$	Boundary of an element
$\Omega, \Omega_e$	Global and element domain
$\mathcal{B}, \mathcal{E}, \mathcal{G}, \mathcal{S}, \mathcal{A}$	Element matrices
$\mathcal{M}$	Mass matrix
$\{\phi_k\}$	Test function or auxiliary function
$\{l_k\}, \{\psi_k\}$	Nodal and modal basis function, resp.
$( )$	Normal to a computational element interface
$( )_b$	Denotes boundary value
$( )^*$	Denotes element interface values
$( )_{L,R}$	Denotes left and right of interface

## Chapter 5

$a_2$	Amplitude of elevation difference across a subchannel with tidal devices
$A$	Amplitude of linear tidal wave at boundary
$c$	Parameter describing channel geometry: equal to $\int_0^L A_c^{-1} dx$
$F_{GC}$	Force, per unit mass, due to tidal devices and bed roughness
$F_t$	Force per unit mass due to tidal devices
$P_{max}$	Maximum extracted power
$Q$	Channel flow rate (isolated channel)
$Q_{max}, Q_{X,max}$	Maximum undisturbed channel flow rate ( $X = 1, 2, 3$ )
$\delta_0, \delta_1$	Parameters related to natural bed friction and tidal devices
$\lambda_0, \lambda_1$	Non-dimensional parameters related to $\delta_0, \delta_1$
$\sigma$	Phase difference between driving tide and channel flow rate
$V, I, \mathcal{L}, \mathcal{C}, R$	Electrical voltage, current, inductance, capacitance and resistance
$( )_e$	Denotes exit of the channel
$( )_{1,2,3,4}$	Denote intermediate locations in a multiply connected channel
$( )_0$	Undisturbed conditions (i.e. without turbines)

## Chapter 6

$b$	Width of non-enclosed bay
$h_c$	Effective depth in connecting channel
$h_e$	Effective depth in enclosed bay
$j$	Complex number $j = \sqrt{-1}$
$l$	Non-dimensional length of non-enclosed bay
$L$	Length of inlet channel to enclosed bay
$m_1, m_2$	Exponents describing non-enclosed bay geometry
$S$	Surface area of bay
$x_b$	Non-dimensional position of turbine fence along non-enclosed bay
$\alpha$	Exponent describing variable surface area in an enclosed bay
$\beta$	Non-dimensional parameter describing enclosed bay geometry
$\delta_0, \delta_1$	Parameters related to natural bed friction and tidal devices, resp.
$\lambda_0, \lambda_1$	Non-dimensional parameters related to $\delta_0, \delta_1$
$\lambda'_0, \lambda'_1$	Non-dimensional parameters describing bed friction and tidal devices, resp., in a non-enclosed bay
$\lambda_0^*, \lambda_1^*$	Linearised parameters of $\lambda'_0, \lambda'_1$
$\lambda_T$	Non-dimensional parameter describing total friction in channel (= $\lambda_0 + \lambda_1$ )
$\Lambda$	Amplitude of enclosed bay elevation normalised by ocean amplitude
$\Lambda_s$	Enclosed bay intertidal area
$\xi_b$	Free surface elevation above mean water level in an enclosed bay
$\sigma$	Phase lag of bay elevation behind ocean elevation in natural state
$\phi$	Non-dimensional amplitude in an enclosed bay
$V, I, \mathcal{L}, \mathcal{C}, R$	Electrical voltage, current, inductance, capacitance and resistance
$( )_0$	Denotes undisturbed values

## Chapter 7

$K$	Diffusion coefficient
$Q_c$	Total flow rate through tidal channel
$Q_f$	Total flow rate through tidal fence
$Q_{f,0}$	Maximum undisturbed total flow rate through the location where tidal fence is to be installed
$\mathbf{u}_l$	Lagrangian velocity vector
$U_0$	Characteristic background current amplitude
$\mathbf{x}_0$	Lagrangian particle position
$\alpha$	Headland aspect ratio
$\sigma_{x,y}$	Variance of particle positions

## Appendix B

Also see Chapter 4 nomenclature.

$(a, b)$	Computational coordinates
$\hat{\mathbf{E}}(\mathbf{Y})$	One dimensional numerical flux normal to element interface
$\mathbf{H}_I, \mathbf{H}_V$	Transformed inviscid and viscous numerical flux evaluated at the element interface
$J, J_s$	Volume and surface Jacobians
$L_1, L_2$	Computational norms
$q, m$	Integers
$S$	Wave speeds in local Riemann problem
$\mathbf{T}$	Rotational transformation matrix
$\vec{x} = (x, y)$	Global coordinates
$\mathbf{Y} = (h, uh, vh)^T$	Conserved variables orientated normal to element interface
$\vec{\xi} = (\xi_1, \xi_2)$	Natural coordinates
$\vec{\xi}_q, \vec{\xi}_{q_s}$	Quadrature points within element and along element edge
$w_q, w_{q_s}$	Quadrature weights within element and along element edge

# Contents

<b>1</b>	<b>Introduction</b>	<b>11</b>
1.1	Introduction to the Tide and Tidal Energy . . . . .	11
1.1.1	Rise and Fall of the Tide . . . . .	11
1.1.2	Natural Rate of Energy Dissipation due to the Tide . . . . .	13
1.1.3	Extracting Energy from the Tide . . . . .	13
1.2	The Exploitable Tidal Stream Resource . . . . .	16
1.2.1	Tidal Stream Resource Assessments . . . . .	17
1.2.2	Theoretical Energy Potential . . . . .	18
1.3	The Need for Further Research . . . . .	20
1.4	Aims of this Thesis . . . . .	20
1.4.1	Understanding the Local Field . . . . .	21
1.4.2	Simulating Tidal Flows . . . . .	21
1.4.3	Analysis of Generic Coastal Basins . . . . .	22
1.5	Thesis Outline . . . . .	23
<b>2</b>	<b>Approximating the Local Field</b>	<b>24</b>
2.1	Introduction . . . . .	24
2.2	Linear Momentum Actuator Disc Theory . . . . .	25
2.2.1	Application of LMADT to Wind Turbines . . . . .	25
2.2.2	Application of LMADT to Tidal Devices . . . . .	27
2.3	Theoretical Extensions to LMADT . . . . .	30
2.3.1	Unbounded Flow . . . . .	30
2.3.2	Pressure Constrained Flow . . . . .	33
2.3.3	Volume Constrained Flow . . . . .	35
2.3.4	Pressure-Volume Constrained Flow . . . . .	41
2.4	Efficiency: Design Implications for Tidal Turbines . . . . .	49
2.5	Effect of Finite Froude Number on Local Field . . . . .	50
2.6	Discussion . . . . .	54
2.6.1	Limitations of LMADT . . . . .	54
2.7	Conclusions . . . . .	55
<b>3</b>	<b>Simulating Coastal Tidal Flows</b>	<b>56</b>
3.1	Introduction . . . . .	56
3.2	The Shallow Water Equations . . . . .	56
3.2.1	Bed Shear Stress . . . . .	62
3.2.2	Simplifications to the SWEs . . . . .	63
3.3	Limitations of 2D Shallow Water Models . . . . .	64
3.4	Set of Generic Coastal Basin Geometries . . . . .	65
3.4.1	Independence and Compound Sites . . . . .	68

<b>4</b>	<b>Numerical Solution of the Shallow Water Equations</b>	<b>69</b>
4.1	Introduction . . . . .	69
4.2	Characteristics of the DG Method . . . . .	70
4.2.1	Application of the DG Method to the SWEs . . . . .	71
4.3	Matrix form of the SWEs . . . . .	72
4.4	Discontinuous Galerkin Formulation of the SWEs . . . . .	73
4.5	Representing Tidal Turbines . . . . .	78
4.5.1	Additional Bed Shear Term . . . . .	78
4.5.2	Line Sink of Momentum . . . . .	79
4.5.3	Example Calculations . . . . .	86
4.6	Open Boundary Conditions . . . . .	89
4.6.1	Example Calculations . . . . .	94
4.7	Conclusions . . . . .	97
<b>5</b>	<b>Tidal Channel</b>	<b>99</b>
5.1	Introduction . . . . .	99
5.2	Tidal Channel Sites . . . . .	100
5.3	Background . . . . .	101
5.3.1	Early Analysis and Resource Assessments . . . . .	101
5.3.2	Theoretical model due to Garrett and Cummins . . . . .	103
5.3.3	Numerical Resource Assessment . . . . .	108
5.4	Numerical Simulations . . . . .	108
5.4.1	Idealised Channel . . . . .	108
5.4.2	More Complex Geometry . . . . .	122
5.4.3	Multiply Connected Channels . . . . .	127
5.5	Conclusions . . . . .	134
<b>6</b>	<b>Oscillating Bay</b>	<b>137</b>
6.1	Introduction . . . . .	137
6.2	Distinction Between Bays . . . . .	137
6.3	Enclosed Bay . . . . .	138
6.3.1	Existing Theoretical Model . . . . .	138
6.3.2	Numerical Simulations . . . . .	141
6.3.3	Enclosed Bay with Wetting and Drying . . . . .	148
6.4	Non-Enclosed Bays . . . . .	154
6.4.1	1D Model . . . . .	156
6.4.2	Maximum Power Extraction . . . . .	160
6.4.3	Maximum Available Power . . . . .	168
6.5	Conclusions . . . . .	171
<b>7</b>	<b>Coastal Headland</b>	<b>174</b>
7.1	Introduction . . . . .	174
7.2	Background . . . . .	174
7.2.1	Headland Physics and UK Sites . . . . .	175
7.3	Idealised Headland . . . . .	176
7.3.1	Undisturbed Tidal Flow . . . . .	177
7.3.2	Natural Energy Flux and Dissipation . . . . .	179
7.4	Limits to Power Extraction . . . . .	181
7.4.1	Example case: Case 7-1 . . . . .	181
7.4.2	Variation in Dynamic Balance . . . . .	184
7.4.3	Locating the Turbine Fence . . . . .	185
7.4.4	Headland Geometry . . . . .	185

7.5	Boundary Conditions . . . . .	186
7.6	Available Power . . . . .	187
7.7	Comparison to Added Bed Roughness . . . . .	190
7.8	Effect of Energy Extraction on the Flow Field . . . . .	192
	7.8.1 Steady Tidal Flow . . . . .	192
	7.8.2 Time Varying Tidal Flow . . . . .	193
	7.8.3 Mean Stress and Tidal Dispersion . . . . .	195
7.9	Discussion and Conclusions . . . . .	197
<b>8</b>	<b>Conclusions</b>	<b>200</b>
8.1	Introduction . . . . .	200
8.2	Conclusions . . . . .	200
	8.2.1 The local Field . . . . .	200
	8.2.2 Simulation of Tidal Flow . . . . .	202
	8.2.3 Analysis of Coastal Sites . . . . .	202
8.3	Future Research . . . . .	205
	8.3.1 Verification of Local Field . . . . .	205
	8.3.2 Shallow Wake of a Tidal Fence . . . . .	205
	8.3.3 Compound Sites and Fence Interaction . . . . .	206
	8.3.4 Analysis of Actual Coastal Basins . . . . .	206
<b>A</b>	<b>Survey of Tidal Stream Sites</b>	<b>208</b>
A.1	United Kingdom . . . . .	208
A.2	North America . . . . .	208
<b>B</b>	<b>DG Numerical Solver (OxTide)</b>	<b>218</b>
B.1	Numerical Solution . . . . .	218
	B.1.1 Shape Functions . . . . .	218
	B.1.2 Basis Functions . . . . .	219
	B.1.3 Forming the Spatial Operators . . . . .	222
	B.1.4 Forming the Line Integrals . . . . .	225
	B.1.5 Boundary Conditions . . . . .	229
	B.1.6 Isoparametric Elements . . . . .	230
B.2	Validation Tests . . . . .	233
	B.2.1 Linear Problems . . . . .	233
	B.2.2 Non-Linear Problems . . . . .	236
	B.2.3 Viscous Problems . . . . .	240
	B.2.4 Quiescent Initial Conditions . . . . .	245

# Chapter 1

## Introduction

The vast movement of seawater caused by the astronomical tide is a potential source of renewable energy. In addition to traditional tidal barrages, in recent years an increasing number of in-stream tidal energy devices have been proposed to exploit this resource and reduce CO<sub>2</sub> emissions. However a pressing question is how much energy can be extracted from the tide for human use? One would expect that an upper bound will exist, because tidal devices and barrages retard the movement of water. An equally important question is that of how much energy can be extracted from the tide without causing significant environmental distress?

Following a brief introduction to the tide, natural energy dissipation and the predominant methods of tidal energy extraction, comment is made in this chapter on recent studies that appear to make incorrect estimates of the energy potential of the tidal resource around the United Kingdom and North America. Consequently the need for further research into understanding the tidal resource is outlined, and the objectives of the thesis are stated.

### 1.1 Introduction to the Tide and Tidal Energy

#### 1.1.1 Rise and Fall of the Tide

The rise and fall of the ocean tide is the dynamic response of the world's oceans to the gravitational forcing of the Moon, Sun and other astronomical bodies (Pugh [1987]). It is well known that if the Earth were completely covered by very deep water, this forcing would result in an equilibrium tide that would move freely around the planet in phase with the

gravitational forcing. However, in reality, because of the variable and finite ocean depth, rough seabed and the presence of continents, the actual ocean response to the forcing is much more complicated. A consequence is that the tidal range varies significantly between different locations around the world. For example, in the deep ocean the amplitude of tidal oscillations is less than approximately 1 m (Pugh [1987]), while at certain coastal locations, such as the Bay of Fundy, Canada, and the Bristol Channel, UK, the mean tidal range is 11.7 m and 9.6 m, respectively (NOAA [2010]).

Perhaps the simplest explanation of the complicated tidal response is that the deep oceans, such as the Atlantic and the Pacific, slosh periodically, or seiche, between continents due to the direct gravitational forcing (Platzman [1991]). This seiching response is dominated by several natural modes, each having periods close to that of the gravitational forcing (Platzman [1991] and Garrett and Greenberg [1977]). In contrast to the deep oceans, the adjoining shallow continental shelves are too small in horizontal extent, despite their shallow depth, to respond significantly to direct astronomical forcing (Garrett [1975]) and are instead driven predominantly by co-oscillation with the deep ocean basins at the edge of the continental shelves (Defant [1961]). The amplified tidal range observed at various coastal locations occurs where the co-oscillation leads to resonant excitation or, more specifically, where a constituent frequency of the tidal seiching in the deep ocean at the edge of the shallow continental shelf is sufficient to establish quarter wavelength resonance of the coastal tide (Defant [1961], Garrett [1973] and Terra et al. [2004]). The proximity of a particular coastline to the resonant condition is dependent on both the depth and width of the continental shelf. In constant water depth of 75-200 m for example, simple linear shallow water theory predicts that a shelf width of approximately 300-500 km will lead to resonant excitation from the semi-diurnal M2 forcing tide. Notably, both the Bay of Fundy and the Bristol channel, which have been shown to oscillate close to resonance with the semi-diurnal tides (Garrett [1973], Heath [1981]), have depths and shelf widths within this range. As a general rule, locations with shelf width much narrower than around 300 km, assuming an average depth greater than 75 m, experience a much smaller tidal response, closer to that observed in the open ocean.

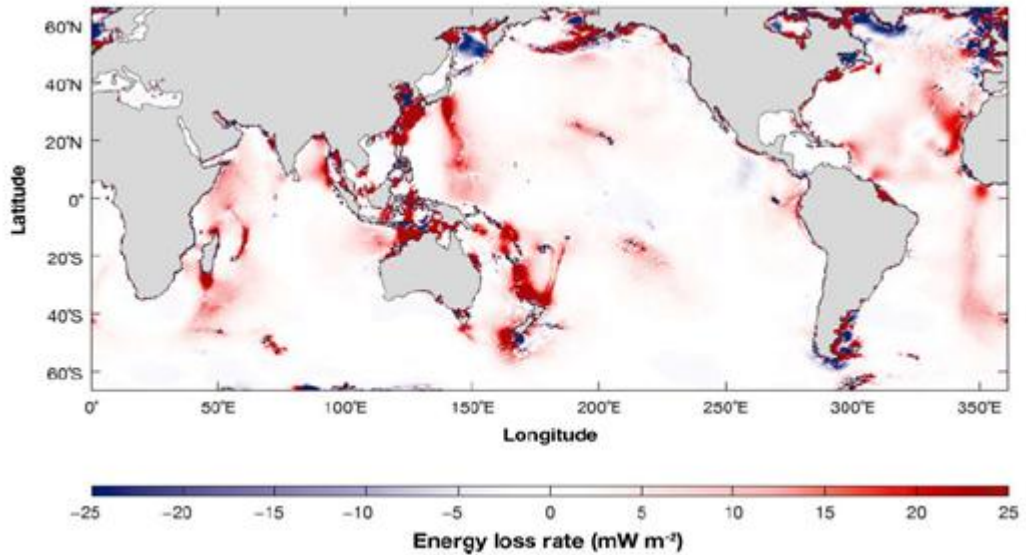


Figure 1.1: Widely accepted map of power loss due to the M2 tide. Areas of apparent negative dissipation result from empirical noise. Taken from Egbert and Ray [2001].

### 1.1.2 Natural Rate of Energy Dissipation due to the Tide

Locations with a large tidal range often generate sizeable tidal currents or *tidal streams*, which vary in direction and strength due to the presence of local bathymetric and coastal features, such as channels and headlands (Pugh [1987]). In the natural state, without artificial energy extraction, the frictional interaction of coastal tidal streams with the rough seabed leads to significant natural energy dissipation (Taylor [1920]). On a global scale this dissipation, which is mapped in Figure 1.1, is estimated at around 2-3 TW (Egbert and Ray [2001]), or two thirds of total global power dissipation due to tidal forcing; the remainder is believed to be lost in deeper water due to internal mixing processes. Compared to the current global human power consumption of 17 TW (EIA [2009]) this natural dissipation equates to roughly 10-15%.

### 1.1.3 Extracting Energy from the Tide

The extraction of energy from coastal tides can be achieved in two main ways. The first involves the construction of a barrage across an estuary (or bay) to exploit the rise and fall of the tide. The second, which is the main focus of this thesis, involves the deployment of tidal stream devices to extract energy from fast moving tidal streams.

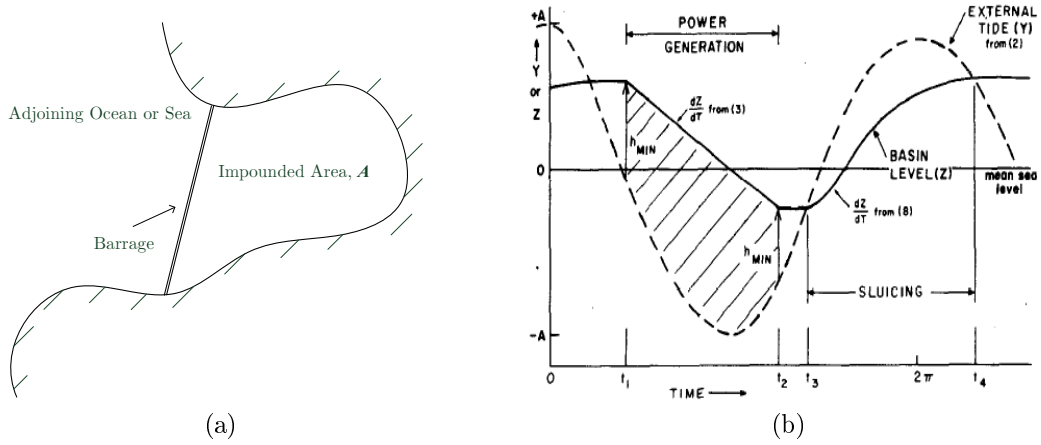


Figure 1.2: (a) Plan view of a hypothetical tidal barrage. (b) Operation of an ebb only tidal barrage over one tidal period. The dashed line is the tidal elevation seaward of the barrage and the solid line is the uniform elevation inside the barrage. Power generation occurs between  $t_1$  and  $t_2$ , and sluicing occurs between  $t_3$  and  $t_4$ . Figure taken from Prandle [1984].

### 1.1.3.1 Tidal Barrages

Figure 1.2 explains the operation of a typical tidal barrage extracting power on an ebb tide. During the flood (or rising) tide, the sluice gates of the barrage are left open and sea water is allowed to flow into the impoundment. At the point of high tide the sluices are then closed until a sufficient height difference, or head, is established between the impounded water and the falling tide. The turbines in the barrage are then used to extract energy from the water that discharges from the impoundment when the turbine gates are opened. In this way the potential energy of the impounded water, which generates the flow through the turbines, is exploited for energy extraction. It is also possible to extract energy during the flooding process, which is termed two-way operation.

If the rise and fall of the tide is uniform in the impounded area  $A_b$ , and all the water is allowed to fill and empty instantaneously at high and low tide respectively, then for a two way operation the theoretical maximum power available averaged over a tidal period is  $2\pi^{-1}\rho g A_b \omega a^2$ , for a sinusoidal tidal elevation of  $\xi = a \cos(\omega t)$ , where  $a$  is the tidal amplitude,  $\omega$  is the angular frequency,  $g$  is acceleration due to gravity,  $\rho$  is the density of seawater and  $t$  is time (Prandle [1984]). In practice a fraction of the theoretical maximum power is available because it takes time to empty and fill the impoundment. This practicality, combined with the fact that many estuaries and bays have a surface area  $A_b$  that is not constant with depth, leads to a number of interesting problems for determining the optimal time of emptying and filling of a barrage. Some of these are discussed in more detail by

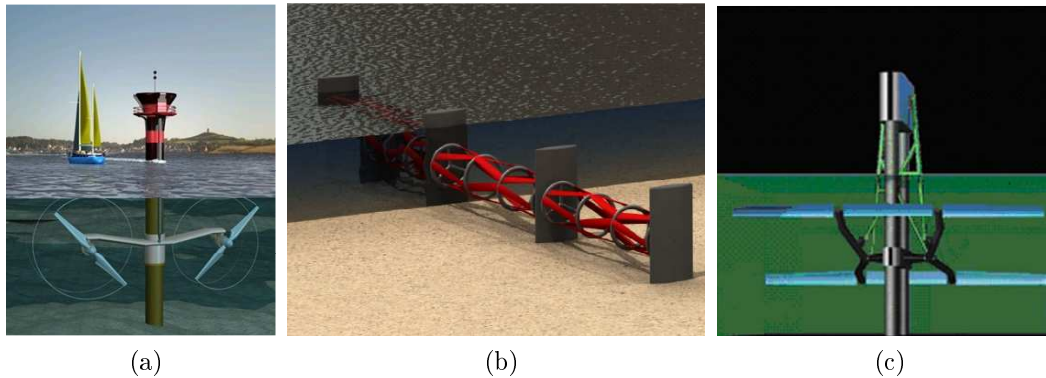


Figure 1.3: (a) MCT SeaGen horizontal axis turbine. Figure taken from Marine Current Turbines [2010]. (b) THAWT Darrieus type turbine. Figure taken from McAdam et al. [2009]. (c) Pulse tidal hydrofoil device. Figure taken from Pulse Tidal [2010].

Bondi [1982] and Prandle [1984]. It may also be possible to employ pumping strategies for barrages to obtain better efficiency and to match electricity demand better (MacKay [2007a]).

Two tidal barrages with rated capacity greater than 10 MW are currently in operation. The first is at La Rance, in France (240 MW), and the second is Annapolis in the Bay of Fundy (20 MW) (O'Rourke et al. [2010]). Larger developments proposed for the Bristol Channel in the UK, and the Bay of Fundy, in North America, have been delayed by concerns over the possible environmental impacts and the large capital cost involved in construction (WEC [2007]). Although attempts are being made to quantify the potential of tidal barrages around the North West of the UK and further sites have been proposed around the world (O'Rourke et al. [2010]), most recent interest has been centered on tidal stream devices.

### 1.1.3.2 Tidal Stream Devices

Tidal stream devices act superficially like wind energy devices to extract energy from moving tidal streams. Broadly, tidal stream devices can be classified into three types: horizontal axis turbines; Darrieus-type turbines; and, hydrofoils or hydroplanes. Figure 1.3 provides an example of each type. It appears that perhaps more than 50 different devices are currently in various stages of development (see O'Rourke et al. [2010] for a recent review). At present however, only Marine Current Turbines SeaGen device (Figure 1.3(a)), installed in the Strangford Lough, Ireland, has generated electricity for more than 1000 hours (Marine Current Turbines [2010]).

The best device(s) to use in the long term will have to be economic to construct and maintain, whilst also remaining hydrodynamically efficient and capable of covering a large proportion of the cross section of a given tidal stream. The motivation behind several of the tidal stream designs, including the Transverse Horizontal Axis Water Turbine (THAWT) developed at the University of Oxford (Figure 1.3b), has been to cover the cross sectional area of the tidal stream as completely as possible, with minimal foundations (McAdam et al. [2009]). More specifically, the rectangular cross section of the THAWT device, similar to the reciprocating hydrofoil design of Pulse Tidal, has better coverage than a circular horizontal axis turbine. An accurate comparison of the cost and efficiency of competing devices is clearly ideal, but has not yet been undertaken.

In practice it is expected that tidal stream devices will be employed as *fences* of turbines in constrained channels and inlets, where the optimal tidal power can be extracted with very few rows (Garrett and Cummins [2007]), or as either a fence or array (or *farm*) in areas that are less well bounded, such as around a headland (Blunden and Bahaj [2007b]). Understanding the flow field around an individual tidal device placed within an array is an ongoing research topic (see, for example, Myers and Bahaj [2010]). The majority of this thesis will be concerned with tidal fences modelled using the theory outlined in Chapter 2.

Present interest in tidal stream turbines, compared with tidal barrages, has stemmed from environmental considerations (WEC [2007]). By the nature of their operation tidal stream turbines should have less impact on natural tidal currents than barrages, allowing water to pass through them at all times. From an economic perspective, tidal stream devices can be installed sequentially, thereby reducing the initial capital investment characteristic of tidal barrages.

## 1.2 The Exploitable Tidal Stream Resource

The natural dissipation rate of 2 - 3 TW is not the size of the tidal resource that is available for human use. To estimate the exploitable tidal stream resource, which is a principal focus of this thesis, it is necessary to understand how coastal tides and tidal streams will change when energy is extracted. To date two approaches have been undertaken to calculate the exploitable tidal stream resource. The first has involved semi-empirical desk studies of

recorded and simulated natural undisturbed tidal currents, which has culminated in the publication of tidal stream resource assessments. The second has focused on theoretical models for simplified, or idealised, coastal geometries together with numerical simulations of energy extraction.

### 1.2.1 Tidal Stream Resource Assessments

Several recent studies, documented in Table 1.1, have produced estimates of the exploitable tidal stream resource on the European Continental Shelf and around North America. These estimates suggest that a useful contribution to both the UK and Canadian energy supply could be made from tidal energy extraction. In the UK for example, the 2.5 GW resource estimated by Black and Veatch Ltd [2005] represented around 6% of UK electricity demand in 2004. However, despite these promising numbers there has been considerable criticism by MacKay [2007b], Garrett and Cummins [2005], and others, of the methodology employed to determine the resource potential listed in Table 1.1. For example, the most recent of these studies, conducted by Black & Veatch Ltd [2005] in the UK and Triton Consultants Ltd. [2006] in Canada, estimate the tidal resource based on the undisturbed kinetic energy flux  $\rho |\mathbf{u} \cdot \mathbf{n}|^3 dA_C$ , integrated over a cross sectional area of flow  $A_C$ , at a particular coastal site, where  $\mathbf{u}$  is the depth-averaged tidal current vector and  $\mathbf{n}$  is the unit normal vector to  $A$ . To determine the tidal resource in Canada, Triton Consultants Ltd. [2006] simply summed up this undisturbed power flux at various sites, taking no account of the fact that tidal devices may have a feedback effect on natural tidal currents, which will act to reduce the energy flux. Black & Veatch Ltd [2005] attempted to account for the feedback effect of tidal devices by multiplying the undisturbed energy flux by a Significant Impact Factor (SIF) of 20%. This impact factor was informed from a quasi-steady analysis of a rectangular channel (Bryden et al. [2005] ) and was considered to be the amount of energy that could be extracted without significant changes to natural tidal currents. Unfortunately, the application of this SIF had two shortcomings. Firstly, the SIF was used to determine the tidal resource for a number of coastal sites, including sites like the Severn Estuary, which do not resemble quasi-steady rectangular channels. Secondly, as outlined by Garrett and Cummins [2005] and discussed further in Chapter 5, the natural kinetic flux does not explain the tidal forcing which generates the tidal currents in a tidal channel, and consequently bears no

Author	Data Source	Resource Estimate
Tidal Resource Assessments of the European Shelf		
European Commission [1996]	Navigational Charts	3.9 GW
Black & Veatch Consulting Ltd [2004]	Natural Tidal Flows	2.5 GW
Black & Veatch Ltd [2005]	Natural Tidal Flows	$2.1 \pm 0.5$ GW
Tidal Resource Assessments in North America		
Triton Consultants Ltd. [2006]	Natural Tidal Flows	42 GW*
Electrical Power Research Institute, EPRI [2006]	Natural Tidal Flows	15.7 GW

Table 1.1: Tidal Energy resource assessments for the European Shelf and North America over the last 15 years. For more detailed discussion on the European Shelf see Blunden and Bahaj [2007a]. \* Includes Hudson Strait, which accounts for 29.6 GW or 70%.

general relationship with the maximum tidal power that can be extracted or the effect on natural tidal currents as a result of energy extraction.

Because of this criticism, the estimates in Table 1.1 should be treated with caution. In particular, Karsten et al. [2008] have performed recent numerical simulations of energy extraction in the Minas Passage in the Bay of Fundy, Canada, representing tidal energy extraction as an additional depth-averaged shear stress. As pointed out by Karsten et al. this analysis, which explicitly accounts for the presence of tidal devices, calculated the energy potential of the Passage to be 9 GW, much higher than the 1.9 GW calculated by Triton Consultants Ltd. [2006] using the kinetic flux approach.

## 1.2.2 Theoretical Energy Potential

On the assumption that tidal oscillations at some arbitrary distance from a coastal site are fixed, such as a fixed tidal range either side of a channel or at the entrance to a bay, it is reasonable to expect that there will be an upper limit to the amount of energy that can be dissipated due to a combination of natural friction and tidal devices. This is because, as illustrated in Figure 1.4, if a particular site had a perfectly smooth seabed, slowly varying geometry and no tidal devices, natural tidal streams resulting from the oscillating tide would accelerate in and around land masses but dissipate little power<sup>1</sup> (Point A in Figure 1.4). At the opposite extreme, if a large number of tidal devices were distributed over the site, or if the natural seabed offered significant resistance to the flow, tidal streams would eventually reduce towards zero (Point B in Figure 1.4) and again no power could be dissipated at the site. Therefore, somewhere in between a maximum level of dissipation

<sup>1</sup>Here, and in Figure 1.4, power can be thought of as the power averaged over a tidal cycle.

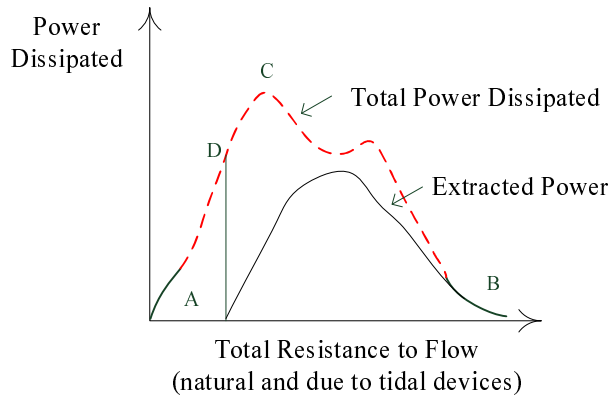


Figure 1.4: Dissipated power as a function of total resistance at a given coastal site. If the site is smooth with no tidal devices the dissipated power is small (point A). When a very large number of tidal devices are introduced natural tidal streams reduce and dissipated power again approaches zero (point B). In between a maximum should exist (point C). The natural dissipation at a real coastal site is indicated by point D. Note the power curve is drawn with two peaks to indicate that the form of the curve is site dependent and maybe complex.

should exist (Point C). In reality of course, a coastal site will have an arbitrary amount of friction and turbulence, and so will dissipate power naturally somewhere on the idealised power curve in Figure 1.4 (Point D) . From an energy extraction point of view it is the fraction of power extracted by devices when total friction is increased above these natural levels that is important. This fraction, indicated by the solid line in Figure 1.4, must also have a maximum value, which will define the theoretical tidal energy potential of the coastal site.

Consistent with this simple principle, Garrett and Cummins [2004, 2005] and Blanchfield et al. [2008b] have determined the theoretical optimum power dissipation, and the optimum power that can be extracted by in-stream tidal devices, for idealised coastal geometries that resemble a strait connecting two co-oscillating basins and a strait connecting one large oscillating basin to an enclosed bay (see Chapter 5 and 6 for further discussion). Unlike the resource assessments discussed in Section 1.2.1 the results from these two theoretical models have provided estimates of the optimum extractable power for a number of locations around North America, including the Minas Passage, Bay of Fundy (Karsten et al. [2008]) and the Johnstone Strait, Vancouver Island (Sutherland et al. [2007]), which have been shown to agree well with predictions by numerical models.

At the ocean scale Arbic and Garrett [2009] have employed the mechanical analogy of a coupled oscillator to describe the co-oscillation of the ocean and an adjacent continental shelf using a simplified analytical model. (At this scale an upper limit should also be

expected because gravitational forcing is essentially independent of the ocean tide.) Introducing natural friction, and artificial friction due to tidal devices, as a drag varying linearly with current velocity on the continental shelves, the optimum power that can be removed from the shallow shelf seas is estimated to be a fraction, possibly as high as 0.8, of the natural global dissipation rate (given as 2 - 3 TW in Section 1.1.2).

### **1.3 The Need for Further Research**

Existing theoretical models can be used to predict tidal stream energy extraction, but only for a small subset of idealised coastal geometries including a strait connecting two co-oscillating basins and a strait connecting one large oscillating basin to an enclosed bay (see Garrett and Cummins [2004, 2005], Blanchfield et al. [2008b]). Tidal stream energy extraction in estuaries or non-enclosed oscillating bays, around headlands and in two dimensional flow fields is clearly feasible, but has not yet been fully understood or assessed. Consequently it appears that a larger set of generic sites, which better represent the full variety of coastlines where tidal energy extraction may take place, require investigation.

Perhaps the most significant constraint to tidal stream energy will be environmental impacts that may result from energy extraction. For example, expert feedback to a research group established by UK Department of Business, Enterprise and Regulatory Reform (BERR), stated that “larger scale impact on the underlying resource of tidal energy converter (TEC) operation is an ongoing research question” (Edinburgh University [2007]). Although predicting and understanding environmental effects will require specialised insight, there is a pressing need to quantify changes to hydrodynamic quantities, from tidal energy extraction, which will influence these environmental effects.

### **1.4 Aims of this Thesis**

To understand how tidal devices will affect natural tidal currents, and to quantify better the tidal resource, an understanding of both the local field about a typical tidal energy device and the interaction of this local field with the far field tidal hydrodynamics of a coastal basin is required. With this in mind, this thesis sets out three objectives. The first two objectives are concerned with approximating the local field about an idealised tidal

device and the simulation (numerically) of the far field tidal hydrodynamics. The third objective is to investigate the amount of tidal energy that can be extracted by the idealised tidal devices, and the hydrodynamic impact of extracting this energy, from a set of generic coastal geometries.

### **1.4.1 Understanding the Local Field**

Linear momentum actuator disc theory (LMADT) provides a useful approximation to the complicated flow field about a wind turbine. The initial objective of this thesis was to apply the same theory to a tidal device, allowing for both the free surface boundary of a tidal stream, finite gravitational effects and the mixing process in the wake of a device. Ultimately a relationship for the momentum sink imparted by a particular geometry of tidal device in a uniform tidal stream is obtained, and the power available to the turbine, distinct to that extracted from the tidal stream, is defined together with a turbine efficiency.

### **1.4.2 Simulating Tidal Flows**

The shallow water equations, discussed in Chapter 3, have been used successfully to simulate tidal hydrodynamics in coastal waters for many years (many examples exist including, for example, Flather [1976] and the theoretical models discussed by Lamb [1932]). A number of numerical schemes to solve the non-linear shallow water system, both with and without turbulent diffusion terms, have been developed (see, for example Abbott [1979] and LeVeque [2002]). Of these schemes, finite element methods based on unstructured meshes offer particular advantages in coastal engineering applications. These advantages include an ability to conform to complex basin geometries, provide increased resolution in specified areas of the flow field, the straightforward application of boundary conditions and a theoretical background to quantify numerical error and undertake numerical convergence tests.

The second objective of this thesis is to develop a discontinuous finite element solution to the shallow water equations. This approach inherits the advantages of unstructured finite element methods, but has the additional advantage of conserving mass and momentum on an element by element basis (see, for example, Kubatco et al. [2009]). This local conservation is particularly important for tidal resource assessment to ensure that the

flow rate and momentum flux in the vicinity of a tidal device are computed accurately and consistently (Sutherland et al. [2007]). With this in mind two separate tasks have been undertaken:

1. The development of a numerical code, based on the discontinuous Galerkin finite element method, which has been validated for a number of linear and non-linear shallow water benchmark problems and verified against low Reynolds number incompressible flow experiments; and
2. Development of a numerical method to introduce a line sink of momentum due to a fence of tidal devices into a 2D depth-averaged numerical model, thereby allowing for the simulation of tidal energy extraction. In particular, it is suggested that this line sink of momentum can be defined by LMADT allowing for an estimate of the available power for a real fence of tidal devices defined by a blockage ratio and wake velocity coefficient or porosity.

### 1.4.3 Analysis of Generic Coastal Basins

There are many coastal sites around the world, generally located on the resonant continental shelves, which have large tidal currents. Although each of these sites may possess useful tidal energy, analysis of the tidal resource for every location would be labour intensive and involve the construction of a detailed numerical model in each case. Moreover the collection of bathymetric and input data, together with field observations for verification, would add significantly to the time and cost of analysis. As an alternative to this, the third main objective of this thesis is to investigate the tidal resource, both in terms of the maximum extracted and available power together with the hydrodynamic effects of extracting energy, for a number of generic coastal geometries. These generic geometries are defined in Chapter 3 to include: (a) strait between two oscillating water bodies; (b) oscillating bay or estuary; (c) strait between an island and a semi-infinite land mass; and (d) accelerated flow around a headland. A number of idealised forms of these generic basins, or *class* of basin, are investigated in Chapters 5-7 revealing that in each situation a limit to power extraction and available power exists because the tidal devices have a feedback effect on the local tidal stream which is dependent on the coastal geometry.

## 1.5 Thesis Outline

This thesis includes the analysis of the local flow field around a tidal device, development of a numerical solver to simulate tidal hydrodynamics, and an investigation into tidal energy extraction at different coastal sites. A brief literature review is included at the beginning of most chapters, rather than within one dedicated chapter.

Chapter 2 begins with a review of traditional actuator disc theory and its application to wind turbines. Extensions are outlined to traditional actuator disc theory to allow for application to tidal energy devices, which leads to an analytical expression for the momentum sink of a tidal device in a uniform tidal stream. Following this, Chapter 3 presents the SWEs, which are commonly used to simulate tidal hydrodynamics. Chapter 4 then describes the numerical solution of the SWEs using the Discontinuous Galerkin Finite Element Method. The incorporation of tidal devices within the numerical model as a line sink of momentum is discussed together with the problem of open boundary conditions in tidal models. Chapters 5, 6 and 7 investigate the generic coastal basins. In each chapter insight is gained from conducting numerical simulations of the SWEs and comparing the results with analytical models where relevant. Lastly, in Chapter 8 the main conclusions of this thesis are presented and suggestions for further work are made.

A survey of real coastal sites and details of the numerical solution of the SWEs are given in the Appendices.

# Chapter 2

## Approximating the Local Field

### 2.1 Introduction

In this chapter the local field about a tidal device in a uniform tidal stream is approximated by Linear Momentum Actuator Disc Theory (LMADT). The unbounded flow field applicable to wind turbines, and adopted in the traditional LMADT, is extended to include: 1) a pressure constraint; 2) a volume constraint; and, 3) a combined pressure-volume constraint, typical of a tidal turbine in a tidal stream of finite Froude number. Constraint 2 is a general case of that considered by Garrett and Cummins [2007]. Constraint 3 is an extended version of the case considered by Whelan et al. [2009], which accounts for mixing in the downstream wake of a tidal device. Importantly, allowing for this mixing leads to a measure of efficiency for a tidal energy device in a uniform tidal stream of non-zero Froude number, where efficiency is defined as the ratio of power *available* to the tidal device to the total power *extracted* from the tidal stream. Closely packed tidal devices, which occupy a large fraction of the tidal stream cross-section and have high-porosity, are shown to be most efficient for a given quantity of power extraction. Lastly, using the extended LMADT the effect of Froude number on the extracted power, efficiency and the local flow field are investigated. The chapter then concludes with a discussion of the limitations of actuator disc theory.

## 2.2 Linear Momentum Actuator Disc Theory

### 2.2.1 Application of LMADT to Wind Turbines

LMADT was first developed by Rankine [1865] and extended by Froude [1889] to analyze the flow field formed around a driving ship propeller. Several years later Lanchester [1915] and Betz [1920] adopted the same approach to model a wind turbine in uniform flow. For this application the key characteristic of the theory involved the introduction of an *actuator* disc, of porosity defined in terms of a velocity coefficient and capable of exerting only an axial thrust on the fluid, to approximate a real wind turbine. This ultimately allowed the complicated flow field about the turbine to be approximated by a much simpler flow field amenable to standard control volume techniques. The idealized flow field assumed by Lanchester and Betz on the basis of the actuator disc approximation is equivalent to that sketched in Figure 2.1(a), where a streamtube is drawn to enclose the fluid passing through the disc. This tube expands as it moves through the disc representing the reduction in velocity of the air in the steady flow. Intuitively, the rate of expansion of the streamtube increases, and consequently the upstream cross sectional area of fluid entering the streamtube reduces, as the disc becomes less porous.

Several interesting results can be determined from analysis of the simplified flow field in Figure 2.1(a) assuming that the fluid outside and within the streamtube is irrotational and incompressible. The most well known of these, which is discussed further in Section 2.3.1, is that the power removed by the actuator disc cannot exceed  $16/27$  of the kinetic flux passing through an equivalent cross-sectional area to that of the disc in the upstream fluid flow. This result indicates a theoretical upper bound to power extraction and is commonly referred to as the Lanchester-Betz limit<sup>1</sup>. Qualitatively the limit exists because, if the disc has low porosity and exerts a large force on the fluid, very little fluid will flow through the turbine and less than optimum power will be removed (where power is equal to the force exerted by the disc times the velocity of fluid passing through the disc). Conversely, if the retarding force of the disc is too small the flow velocity through the disc will be high, but again the product of thrust and velocity, and so the power removed by the turbine,

---

<sup>1</sup>van Kuik [2007] suggests the limit should be called the Lanchester-Betz-Joukowsky limit, to recognize the work completed independently by Joukowsky to derive the limit. We note this here, but refer to the limit as the Lanchester-Betz limit throughout the remainder of the thesis to avoid confusion with recent papers written on actuator disc theory.

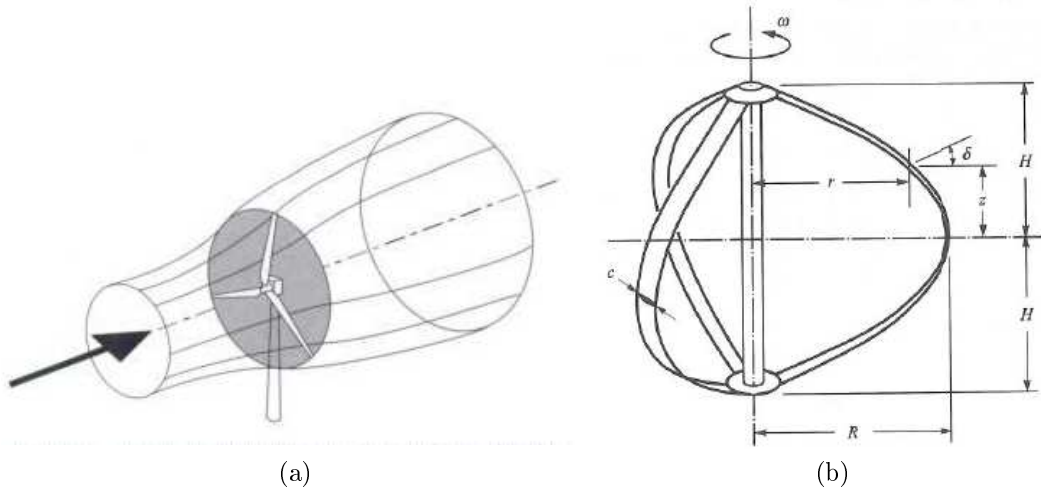


Figure 2.1: (a) Flow field through a horizontal axis wind turbine. The shaded disc is representative of the uniform porosity actuator disc. Figure taken from Burton et al. [2001]. (b) Schematic representation of a vertical axis wind turbine of Darrieus type. Figure taken from Paraschivoiu [2002].

will again be less than optimum. The Lanchester-Betz limit therefore represents an ideal solution, when the optimum thrust is applied and the extracted power is a maximum.

In modern wind turbine design the Lanchester-Betz limit and the underlying use of LMADT have proven to be very useful as a guide to power potential and as a qualitative diagnostic tool (Wilson [1980], Burton et al. [2001], van Kuik [2007]). Typical commercial wind turbines operate at up to 75% of the theoretical limit for some wind speeds<sup>2</sup>. The slight under performance, as compared to the theoretical limit, is a consequence of the simplified assumptions in the actuator disc approximation. For example, both horizontal axis turbines, depicted in Figure 2.1(a), and vertical axis turbines, depicted in Figure 2.1(b), introduce some component of swirl or tangential velocity into their wakes, which is not accounted for by the one dimensional streamwise analysis of the simple actuator disc theory (Glauert [1947]). This associated rotational energy in the real wake represents an additional loss of energy from the axial flow, thereby reducing the available power to the turbine (Burton et al. [2001]). Furthermore, and perhaps more importantly, real turbines also encounter frictional drag between the fluid and the rotating blades, in addition to aerodynamic losses, which add to the axial thrust exerted on the fluid but reduce the useful power available to the turbine (Wilson and Lissaman [1974]).

<sup>2</sup>See for example the wind turbine V52/850 at [www.vestas.com](http://www.vestas.com)

## 2.2.2 Application of LMADT to Tidal Devices

Based on the insight gained from the application of LMADT in wind turbine design, it is reasonable to expect that the theory might be equally beneficial for tidal energy devices, such as those outlined in Chapter 1 (Figure 1.4). The justification for this assumption is that, although the various tidal devices are markedly different in mechanical operation, the most efficient (or ideal) tidal device should still remove momentum from the flow in the streamwise direction and impart very little wasted rotational momentum into the wake. Therefore the introduction of an actuator disc, like that for a wind turbine, should provide a useful upper bound to power removal for tidal device developers to aspire towards (the word “turbine” and “actuator disc” will be used interchangeably hereafter, on the assumption that the turbine is approximated by an actuator disc).

However, early research into tidal energy devices indicated that the application of LMADT is not straightforward. For example, Fraenkel [2002] noted that the classic application of LMADT intended for wind turbines will only apply to tidal turbines when the flow boundaries are far from the turbine rotor. When the flow boundaries are sufficiently close to the rotor the assumptions made in standard actuator disc theory, which work well for the flow of air in an unbounded domain, are no longer relevant (Bryden et al. [2007]). In addition, simple open channel theory implies that the removal of energy from a sub-critical tidal flow will lead to a lowering of the free surface and an increase in fluid velocity downstream of the turbine, which is clearly at odds with the removal of kinetic energy observed in the wind turbine case (Houlsby et al. [2008]). To partly address these issues two recent papers have extended the Lanchester-Betz theory to a bounded flow, which is more representative of a tidal stream.

The first of these papers is due to Garrett and Cummins [2007] (hereafter GC07), and considers an analogy to the aeronautically similar case of an inverse propeller in a wind tunnel, or constant width flow field, considered previously for a standard propeller by Milne-Thomson [1966]. In the GC07 model the wind tunnel is formed by the parallel banks of the channel, the channel bed and the assumption of a fixed free surface (see Figure 2.2). The last of these boundaries requires that the deformation of the free surface is small compared with depth, or that the Froude number of the uniform flow is negligible, where the Froude number is defined as  $Fr = u/\sqrt{gh}$ , and  $u$  is the uniform depth-averaged



The second paper, produced more recently by Whelan et al. [2009] (hereafter W09), discusses an extension to the GC07 model of constant depth and volume. In particular W09 allow the free surface to deform, which removes the restriction on Froude number, and derive an implicit expression for the power coefficient that is dependent on the size, or blockage, of the turbines in the channel, the upstream Froude number of the uniform flow and the porosity of the turbines. Again the optimum power coefficient is shown to exceed the Lanchester Betz limit when the blockage ratio is finite, and to increase still further with increasing Froude number. However, the prediction of the power coefficient is restricted by the fact that the model only achieves physically admissible solutions for a subset of Froude numbers, blockage ratios and turbine porosity. W09 state that the loss of a physical solution is connected with the bypass flow becoming hydraulically critical, but provide no reasoning why. A more complete explanation is given here in Section 2.3.4. In addition, W09 do not introduce downstream mixing into their analysis, despite the fact that power is inevitably dissipated in downstream mixing. This dissipation must be introduced to understand the efficiency of a turbine in a tidal stream of non-zero Froude number. In addition, the introduction of mixing is also important when determining the relationship between upstream and downstream depth-averaged flow velocities and depths, as a function of turbine geometry and porosity. This relationship is useful in specifying the momentum sink due to a tidal device in a depth-averaged numerical model, as will be outlined in Chapter 4.

In summary, both GC07 and W09 provide useful extensions to LMADT. The former have accounted for the finite nature of the flow field, which allows for an analysis of downstream mixing, and the latter have accounted for gravitational effects and the formation of a free surface. The theoretical extensions that follow here in Section 2.3 form an extended summary of Housby et al. [2008] and effectively combine the work of GC07 and W09 to investigate an open channel flow with a deformable free surface and downstream mixing. An expression will be determined for the efficiency of a tidal turbine in a tidal stream of finite Froude number. Several additional results will also be obtained as a result of the systematic theoretical extensions.

## 2.3 Theoretical Extensions to LMADT

### 2.3.1 Unbounded Flow

The application of LMADT to an unbounded flow is well known in aerodynamics. Although the derivation is given in many text books (see, for example Burton et al. [2001]) the analysis will be reproduced briefly here to provide a basis from which to extend the theory to bounded flows in the subsequent sections.

The traditional theory considers the idealized flow field sketched in Figure 2.3 for an actuator disc of area  $A$ , placed in a uniform upstream flow of velocity  $u$ . Four stations are introduced to define the flow field: Station 1 located far upstream of the disc; Stations 2 and 3 located immediately upstream and downstream of the disc; and, Station 4 located far downstream of the disc. The main feature of Figure 2.3 is the control volume (denoted by dashed lines), which is drawn to coincide with a streamtube that bounds all the fluid which passes through the actuator disc (turbine flow), and assumes that the flow separates at the edge of the disc forming a singular surface where viscous forces are important. Both the fluid within the streamtube and the fluid outside (bypass flow) are considered to be steady, incompressible and inviscid, with viscous forces and rotational flow confined to the surface of the tube. To model the effect of the turbine on the flow field, the traditional theory introduces a momentum sink, or equivalently a thrust  $T$ , exerted by the disc on the air, and the flow through the disc is taken to be continuous in the streamwise direction to ensure continuity. To represent the average velocity in the stream tube and bypass flow, the coefficients  $\alpha_2$  and  $\alpha_4$  are introduced, where the coefficient  $\alpha_2$ , or the induction factor  $a_i = 1 - \alpha_2$ , can be related in practice to a particular turbine geometry and rotation speed via blade element theory (Wilson and Lissaman [1974]). At Station 4 the downstream static pressure is assumed to recover to that of upstream static pressure  $p$ . Lastly, to better understand the traditional theory and the extensions to bounded flows which follow, a pressure thrust  $X$  is introduced, which represents the net external force (equal and opposite) due to the pressure, above atmospheric, acting on the fluid within the streamtube over the surface of the streamtube (Milne-Thomson [1966]).

Continuity, conservation of energy and conservation of momentum can now be applied to the flow field to arrive at an analytical expression relating the power absorbed by the

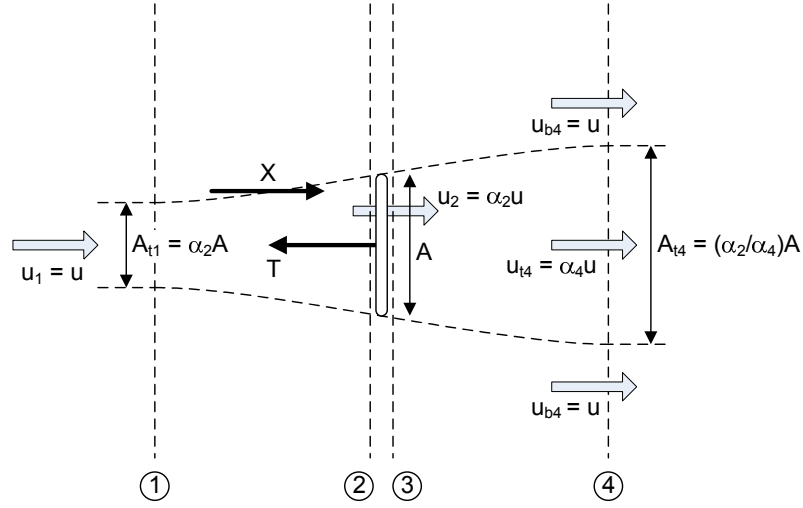


Figure 2.3: The classic actuator disc model for an unbounded flow. Figure taken from Houlby et al. [2008].

disc to the kinetic flux in the upstream flow. To begin, the Bernoulli equation is applied to the flow within the stream tube between Stations 1 and 2, and Stations 3 and 4, to give

$$p + \frac{1}{2}\rho u^2 = p_{2t} + \frac{1}{2}\rho\alpha_2^2 u^2, \quad (2.1)$$

and

$$p_{3t} + \frac{1}{2}\rho\alpha_2^2 u^2 = p + \frac{1}{2}\rho\alpha_4^2 u^2. \quad (2.2)$$

where the numerical subscripts indicate the appropriate averaged quantity at a given station in the flow field, and the subscript  $t$  indicates flow through the turbine. Combining Equation 2.1 and Equation 2.2 then gives an expression for the pressure change across the disc

$$\Delta p = p_{2t} - p_{3t} = \frac{1}{2}\rho u^2 (1 - \alpha_4^2). \quad (2.3)$$

This pressure is equivalent to the static pressure across the disc, so that

$$\frac{T}{A} = \frac{1}{2}\rho u^2 (1 - \alpha_4^2). \quad (2.4)$$

A second equation for the thrust can also be established by applying momentum flux conservation in the streamwise direction for the streamtube control volume in Figure 2.3

$$X - T = \rho u^2 A \alpha_2 (\alpha_4 - 1). \quad (2.5)$$

In the classical derivation it is assumed that there is no net change in the streamwise momentum of the bypass flow and so the force  $X$  is omitted, without detailed justification, leading to

$$\frac{T}{A} = \rho u^2 \alpha_2 (1 - \alpha_4). \quad (2.6)$$

Equation 2.4 and Equation 2.6 can then be equated to give the first well known conclusion of the classical analysis

$$\alpha_2 = \frac{1 + \alpha_4}{2}, \quad (2.7)$$

which implies that the flow through the disc is the average of the upstream and downstream flow. Interestingly this result indicates that the flow field is a single parameter family requiring the specification of  $\alpha_2$  or  $\alpha_4$ . Once either of these two variables has been defined the thrust is given directly by Equation 2.4 and the power removed by the turbine can be determined as

$$P = T\alpha_2 u = \frac{1}{2}\rho u^3 A \alpha_2 (1 - \alpha_4^2) = \frac{1}{2}\rho u^3 A \frac{(1 + \alpha_4)}{2} (1 - \alpha_4^2). \quad (2.8)$$

For convenience the dimensionless thrust coefficient  $C_T$  and the power coefficient  $C_P$ , which define the ratios of thrust to the integral of upstream dynamic pressure, and removed power to the upstream kinetic flux, respectively, are commonly introduced such that

$$T = \frac{1}{2}\rho u^2 A (1 - \alpha_4^2) = \frac{1}{2}\rho u^2 A C_T, \quad (2.9)$$

$$P = \frac{1}{2}\rho u^3 A \frac{(1 + \alpha_4)}{2} (1 - \alpha_4^2) = \frac{1}{2}\rho u^3 A C_P. \quad (2.10)$$

Maximum power is therefore removed by the turbine when the power coefficient is optimised with respect to, for example,  $\alpha_4$ . This optimization gives  $\alpha_4 = 1/3$ ,  $\alpha_2 = 2/3$ ,  $C_T = 8/9$  and  $C_P = 16/27$  which is the Lanchester-Betz limit.

The analysis above summarises the classic Lanchester-Betz derivation for a turbine, or actuator disc, in an unbounded flow. In retrospect two interesting points can be highlighted. First, it is clear that there is no justification made for the treatment of the pressure force  $X$ , acting on the body of fluid within the control volume depicted by the streamtube, which is neglected from the momentum balance for the streamtube. Secondly, the flow field in Figure 2.3 only extends to Station 4. However, far downstream from the turbine the wake of

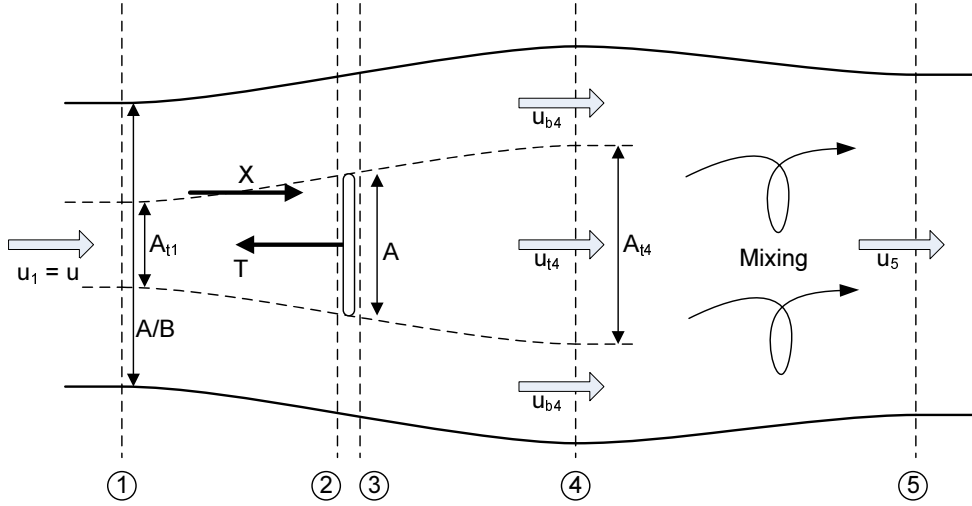


Figure 2.4: Flow field for an actuator disc placed in flow that has a constant pressure boundary. Figure taken from Houslyby et al. [2008].

a real fluid (with molecular viscosity) will eventually mix. Since the traditional unbounded case cannot be extended to include this mixing an analysis of a finite flow field is required.

### 2.3.2 Pressure Constrained Flow

The unbounded flow in Section 2.3.1 can be made finite by introducing a constant atmospheric pressure boundary, as shown in Figure 2.4. The finite boundary has a reference dimension of  $A/B$  measured at Station 1, where  $B \leq 1$  is the blockage ratio of the turbine. Station 5 is also introduced to define the location where complete mixing of the wake has occurred and the axial velocity is uniform.

In light of these alterations the analysis in Section 2.3.1 can be repeated. To begin, conservation of energy in the streamtube, and upstream and downstream of the turbine, leads again to Equation 2.3, and static equilibrium across the disc yields Equation 2.4. However, unlike the classical case, the presence of the constant pressure boundary now allows for a more precise investigation of the momentum change in the bypass flow. Writing the Bernoulli equation along the constant pressure boundary in Figure 2.4 (or any chosen streamline in the bypass flow) leads directly to the result  $u = u_{b4}$ . From continuity the cross-sectional area of the bypass flow therefore remains constant, from which it is clear that there is no change in the streamwise momentum for the bypass flow, implying that the applied force along the constant pressure boundary is equal to the negative of the force  $X$ . However, since the force acting along the pressure constrained boundary is constant and atmospheric by definition, it follows that the assumption  $X = 0$  in the traditional theory

is satisfactory. As a result the flow velocity through the turbine will again satisfy Equation 2.7 and the thrust and power also remain unaltered from Equation 2.4 and Equation 2.8 respectively. The optimum power results when  $\alpha_4 = 1/3$  for all blockage ratios.

In addition to clarifying the momentum change in the bypass flow, the second advantage in pursuing the constant pressure boundary is that an analysis of the wake mixing between Stations 4 and 5 can be undertaken. Applying momentum conservation over the mixing region gives

$$u^2 AB\alpha_2\alpha_4 + u^2 A(1 - B\alpha_2) = uAu_5, \quad (2.11)$$

so that rearranging for the uniform far downstream velocity gives

$$u_5 = u \left( 1 - \frac{B(1 - \alpha_4^2)}{2} \right). \quad (2.12)$$

Notably when  $B = 0$ , this result is consistent with the classical analysis that requires  $u_5 \rightarrow u$  (i.e. the vanishingly small area of slower turbine flow has a negligible effect on the average downstream flow velocity). Equation 2.12 can also be used to determine the power lost in the wake  $P_W$ , since

$$P_W = \frac{1}{2}\rho u^3 A\alpha_2\alpha_4^2 + \frac{1}{2}\rho u^3 A \left( \frac{1}{B} - \alpha_2 \right) - \frac{1}{2}\rho u \frac{A}{B} u_5^2,$$

so that

$$P_W = \frac{1}{2}\rho u^3 A\alpha_2(1 - \alpha_4)^2 \left( 1 - \frac{B(1 + \alpha_4)}{2} \right). \quad (2.13)$$

An efficiency measure for the turbine, defined as the power removed by the disc (or available to the turbine), to the total power extracted from the flow, then follows directly

$$\eta = \frac{P}{P + P_W} = \frac{(1 + \alpha_4)}{(1 + \alpha_4) + (1 - \alpha_4)(1 - B\alpha_2)}. \quad (2.14)$$

Therefore, for a turbine operating at maximum power ( $\alpha_4 = 1/3$ ) the power lost in the wake is  $P_W = P/2$  and the efficiency is  $2/3$  for  $B = 0$ , which corresponds to an unbounded flow. Consequently, in the classical Lanchester-Betz analysis a further 50% of the extracted power is dissipated in the wake as it mixes. Interestingly, maximum efficiency is achieved when  $\alpha_4 = \alpha_2 = 1$ , but then no power is produced by the turbine regardless of blockage.



pressure  $p - p_4$ , which presents an additional energy source to the turbine, can be obtained by considering the Bernoulli equation in the bypass flow, which leads to

$$p - p_4 = \frac{1}{2}\rho u^2 (\beta_4^2 - 1) = \frac{1}{2}\rho u^2 \left( \frac{(1 - B\alpha_2)^2}{(1 - B\alpha_2/\alpha_4)^2} - 1 \right). \quad (2.16)$$

Application of the Bernoulli equation either side of the turbine in the streamtube also yields the result

$$p_{2t} - p_{3t} = p - p_4 + \frac{1}{2}\rho u^2 (1 - \alpha_4^2), \quad (2.17)$$

so that combining Equation 2.17 and Equation 2.16 gives

$$p_{2t} - p_{3t} = \frac{1}{2}\rho u^2 \left( \frac{(1 - B\alpha_2)^2}{(1 - B\alpha_2/\alpha_4)^2} - \alpha_4^2 \right). \quad (2.18)$$

Satisfying static equilibrium across the disc therefore leads to

$$\frac{T}{A} = \frac{1}{2}\rho u^2 \left( \frac{(1 - B\alpha_2)^2}{(1 - B\alpha_2/\alpha_4)^2} - \alpha_4^2 \right). \quad (2.19)$$

Conservation of momentum flux in the streamwise direction for the combined bypass and turbine flow between Stations 1 and 4 produces a second equation in terms of the thrust

$$pA/B - p_4A/B - T = u^2 A \rho \alpha_2 (\alpha_4 - 1) + u^2 \rho A/B (1 - B\alpha_2) \left( \frac{(1 - B\alpha_2)}{(1 - B\alpha_2/\alpha_4)} - 1 \right). \quad (2.20)$$

Rearranging this expression leads to

$$p - p_4 = \frac{TB}{A} + \rho u^2 \frac{\alpha_2}{\alpha_4} \frac{B(1 - \alpha_4)^2}{(1 - B\alpha_2/\alpha_4)}, \quad (2.21)$$

which can be combined with Equation 2.16 and Equation 2.19 to give

$$\alpha_4^2 (2\alpha_2 - 1 - \alpha_4) + B\alpha_2 (2\alpha_4^2 + \alpha_2 - 3\alpha_4\alpha_2) = 0. \quad (2.22)$$

Equation 2.22 can be considered the constant volume equivalent to Equation 2.7 derived for the traditional LMADT. It illustrates that in the presence of a fixed volume constraint the solution for the flow is now a two parameter set: for a particular blockage  $B$ , the specification of either  $\alpha_2$  or  $\alpha_4$  will determine the remaining velocity coefficient and, via

Equation 2.15, the velocity in the bypass flow.

For an unbounded flow ( $B = 0$ ), Equation 2.22 reduces to  $\alpha_2 = (1 + \alpha_4)/2$ , which is consistent with the usual result. In the limit  $B \rightarrow 1$ , Equation 2.22 leads to a cubic expression that is consistent with  $\alpha_2 \rightarrow 1$  and  $\alpha_4 \rightarrow 1$ . For arbitrary  $B$ , rearranging Equation 2.22 yields

$$\alpha_2 = \frac{(1 + \alpha_4)}{(1 + B) + \sqrt{(1 - B)^2 + B(1 - 1/\alpha_4)^2}}. \quad (2.23)$$

With this definition of  $\alpha_2$  the power removed by the turbine follows directly from Equation 2.19

$$P = \frac{1}{2}\rho Au^3 \alpha_2 \left( \frac{(1 - B\alpha_2)^2}{(1 - B\alpha_2/\alpha_4)^2} - \alpha_4^2 \right). \quad (2.24)$$

For all choices of  $B$  it can be verified numerically that this expression is a maximum when  $\alpha_4 = 1/3$ , giving

$$P_{max} = \frac{1}{2}\rho Au^3 \frac{16}{27} \left( \frac{1}{1 - B} \right)^2. \quad (2.25)$$

The limit to power removed is therefore a function of the blockage ratio

$$C_P = \frac{16}{27} \left( \frac{1}{1 - B} \right)^2, \quad (2.26)$$

from which it is evident that the constant volume constraint allows for the extraction of more power by comparison to the unconstrained case. For small  $B$  this increase in power coefficient is approximated by the factor  $1 + 2B$  and will be important in the accurate comparison of turbine devices analysed in a finite numerical mesh, for example.

A physical interpretation of the additional power defined in Equation 2.25 can be obtained by appreciating that the parallel walls confining the flow field allow for a pressure drop across the actuator disc (GC07). Consequently a pressure head is available to the turbine and there is no change in kinetic energy across the flow field. This means that the kinetic efficiency in isolation, given by the usual power coefficient, may not be the most rational measure of performance and can exceed unity. Perhaps a better expression for the power coefficient might be

$$C_P^* = \frac{P}{\frac{1}{2}\rho u^3 A + uA\Delta p} = \frac{C_P}{1 + BC_T}, \quad (2.27)$$

which incorporates the pressure head and remains bounded for all blockage ratios.

It is also of some interest to note that an alternative rationalisation for the increased power, in place of the pressure drop across the disc, can be achieved by analysing the pressure thrust  $X$ . In particular, one might expect that this force should actively push fluid through the turbine when  $B > 0$  allowing for greater power removal. Pursuing this further, momentum conservation in the bypass flow (assuming that  $X$  acts to the left for the bypass flow) gives:

$$(p - p_4) A \left( 1/B - \frac{\alpha_2}{\alpha_4} \right) - X = u^2 A \rho (1/B - \alpha_2) \left( \frac{(1 - B\alpha_2)}{(1 - B\alpha_2/\alpha_4)} - 1 \right), \quad (2.28)$$

and substituting for  $p - p_4$  from Equation 2.16 then gives

$$X = \frac{1}{2} \rho u^2 A \frac{\alpha_2}{\alpha_4} (1 - \alpha_4) (\beta_4 - 1). \quad (2.29)$$

Since  $\alpha_4 < 1$  and  $\beta_4 > 1$  for a typical turbine it is clear that the pressure thrust is, in fact, positive and acts to force fluid through the turbine, as depicted in Figure 2.5, when  $B > 0$ . For  $B = 0$  Equation 2.15 gives  $\beta_4 = 1$  and so  $X = 0$  from Equation 2.29, which is in agreement with the traditional analysis.

Given that the flow field in Figure 2.5 is finite it is again possible to analyse downstream mixing effects. Writing the momentum equation between Stations 4 and 5 gives an expression for the pressure change in the wake

$$p_4 - p_5 = -\rho u^2 \frac{\alpha_2 B (1 - \alpha_4)^2}{\alpha_4 (1 - B\alpha_2/\alpha_4)}. \quad (2.30)$$

The power lost in the wake can be then written in terms of this pressure difference

$$P_W = \frac{1}{2} \rho u^3 A \alpha_2 \alpha_4^2 + \frac{1}{2} \rho u^3 A (1/B - \alpha_2) \beta_4^2 - (A/B) \left( \frac{1}{2} \rho u^3 - u (p_4 - p_5) \right). \quad (2.31)$$

Substituting for Equation 2.30 therefore leads to

$$P_W = \frac{1}{2} \rho u^3 A \alpha_2 (1 - \alpha_4)^2 \left( 1 + \frac{B\alpha_2 (1 - B\alpha_2)}{\alpha_4^2 (1 - B\alpha_2/\alpha_4)^2} \right). \quad (2.32)$$

It is readily seen that for  $B = 0$  this result agrees with the solution for the constant pressure

boundary under the same limit (Equation 2.13), while for  $B > 0$  the power loss is greater than that for the constant pressure case. The total power extracted from the channel is simple  $(p - p_5) u A_C = T u$ . Combining this with the power removed by the disc  $\alpha_2 u T$ , leads to a measure of efficiency of

$$\eta = \frac{P}{P + P_W} = \alpha_2. \quad (2.33)$$

So that for  $\alpha_2 = 1$  the efficiency is unity for all  $B$ , but again no power is extracted (as is readily seen from substituting for  $\alpha_4$  in Equation 2.24). Alternatively at optimal power extraction ( $\alpha_4 = 1/3$ ) it follows from Equation 2.23 that  $\alpha_2 = 2/[3(1 + B)]$ , so that the efficiency for optimal power extraction is

$$\eta = \frac{2}{3(1 + B)}. \quad (2.34)$$

Consequently, a loss in efficiency is encountered when compared to an unconstrained flow although, of course, more power in total is extracted by the turbine with a finite blockage.

### 2.3.3.1 Comparison to the results of Garrett and Cummins

The main results of the analysis discussed above for a constant volume boundary have been determined by GC07 in relation to a tidal turbine in a channel. For this application the flow field in Figure 2.5 is interpreted as a plan view of a channel, and the actuator disc is a considered to be a partial fence of turbines in the channel (see Figure 2.2). To enable this interpretation the deformation of the free surface is neglected and the pressure of the fluid is taken to be  $p = \rho g z$ , where  $z$  is a vertical coordinate<sup>3</sup>. Bed friction is ignored.

GC07 calculate both the optimal power removed by the turbine (Equation 2.25) and the efficiency of the turbine (Equation 2.33). However GC07 note that perfect efficiency leads to the trivial case of zero power removal and, therefore, they only consider the efficiency of a turbine operating at the maximum power coefficient. This leads to the derivation of Equation 2.34 and several other quantities for a device operating at optimum power coefficient, including the pressure change between Stations 1 and 4 (but with an incorrect

---

<sup>3</sup>This expression for the variation in pressure is appropriate if changes to the free surface elevation are small. This is because, for a hydrostatic fluid of depth  $h + a$ , where it is assumed  $a \ll h$ , the along-stream pressure force averaged over the depth  $h$  is  $\rho g h/2 + \rho g a + O(a^2/h)$ , so that  $\rho g a$  gives a good approximation to the variation in average pressure due to the height change  $a$ .

sign in GC07)

$$p - p_4 = \frac{4B(3-B)}{9(1-B)^2} \rho u^2, \quad (2.35)$$

the pressure change between Stations 4 and 5

$$p_5 - p_4 = \frac{8B}{9(1-B)} \rho u^2, \quad (2.36)$$

and the thrust coefficient, defined such that the thrust exerted by the turbine is

$$C_T = \frac{8(1+B)}{9(1-B)^2}. \quad (2.37)$$

(Note that in each of these relations GC07 use the parameter  $\epsilon$  to denote the blockage ratio  $B$  and the parameter  $C_D$  to denote  $C_T/2$ ).

To determine the validity of their model GC07 revisit the assumption of a negligible depth change, which is valid when  $(p - p_4)/\rho gh \ll 1$ , or

$$Fr^2 = \frac{u^2}{gh} \ll \frac{9(1-B)^2}{4B(3-B)},$$

where  $Fr$  is the Froude number. Although not calculated by GC07, it is also possible to calculate the error in mass flow across the entire flow field (from Station 1 to Station 5), associated with the assumption of small depth-change, by taking the change in pressure, divided by specific gravity, to be the downstream depth. This error is

$$\frac{\text{Continuity Error}}{A_c u} = \frac{p - p_5}{\rho gh} = Fr^2 \frac{4B(1+B)}{9(1-B)}, \quad (2.38)$$

where the upstream channel area is  $A_c = A/B$ . For a turbine fence operating at maximum power coefficient with a blockage ratio 0.5 in a flow of Froude number 0.15 this will lead to an error, relative to the upstream flow rate, of 1.5%. If multiple rows of turbines are used, allowing for complete mixing between rows, then this error will be compounded at each row if the Froude number is maintained.



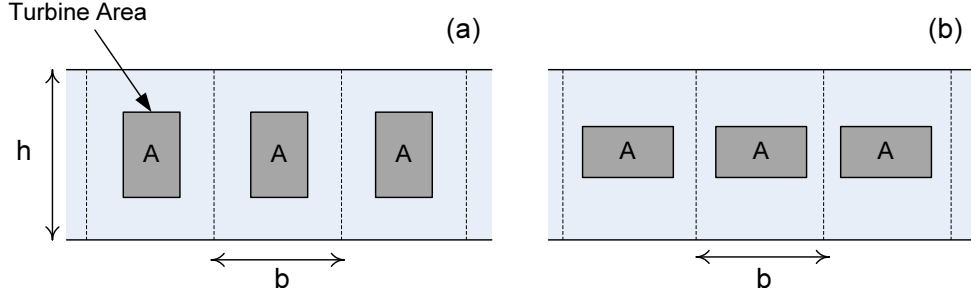


Figure 2.7: Stream-wise view of a section of two alternative tidal fences, (a) and (b), in a tidal stream of uniform flow with tidal devices placed periodically along the fence.

downstream depth and therefore lead to an increase in kinetic energy downstream. This is in contrast to the flow fields in the preceding sections where the extraction of energy led to a reduction, or no change, in downstream kinetic flux.

Lastly, three additional assumptions are required to analyse the flow field in Figure 2.6: (1) the pressure is taken to be hydrostatic at Stations 1, 4 and 5, (2) seabed friction is negligible, and (3) the seabed and channel walls remain straight and parallel to the tidal stream over the flow domain, or equivalently the spacing between devices within a fence remains regular. As in the traditional LMADT however, no conditions are placed on the geometry or position of the streamtube in the flow field and so the analysis that follows is indifferent to the shape of the turbines. This implies that both turbine geometries in Figure 2.7 for example, will be treated as equivalent by the theory.

To begin the analysis the Bernoulli equation is applied in the bypass flow to give

$$h + \frac{u^2}{2g} = h_4 + \frac{u^2 \beta_4^2}{2g}, \quad (2.39)$$

Likewise, application of the Bernoulli equation either side of the turbine in the stream tube yields

$$h + \frac{u^2}{2g} = h_{2t} + \frac{u^2 \alpha_2^2}{2g}, \quad (2.40)$$

and,

$$h_{3t} + \frac{u^2 \alpha_2^2}{2g} = h_4 + \frac{u^2 \alpha_4^2}{2g}. \quad (2.41)$$

Combining Equations 2.39-2.41 then gives an expression for the head drop across the turbine

$$h_{2t} - h_{3t} = \frac{u^2}{2g} (\beta_4^2 - \alpha_4^2), \quad (2.42)$$

which, from simple statics, can be used to determine the thrust across the turbine

$$\frac{T}{\rho g B b h} = \frac{u^2}{2g} (\beta_4^2 - \alpha_4^2). \quad (2.43)$$

A second equation for the thrust can be obtained by applying the momentum equation across the combined bypass and turbine flow between Stations 1 and 4

$$\frac{1}{2} \rho g b (h^2 - h_4^2) - T = \rho u^2 b h B \alpha_2 (\alpha_4 - 1) + \rho u^2 h b (1 - B \alpha_2) (\beta_4 - 1). \quad (2.44)$$

Eliminating  $T$  between Equation 2.43 and Equation 2.44 then gives

$$\frac{1}{2} \rho g b (h^2 - h_4^2) - \rho B b h \frac{u^2}{2} (\beta_4^2 - \alpha_4^2) = \rho u^2 b h B \alpha_2 (\alpha_4 - 1) + \rho u^2 h b (1 - B \alpha_2) (\beta_4 - 1). \quad (2.45)$$

Also, continuity between Stations 1 and 4 also leads to

$$h_4 = B h \frac{\alpha_2}{\alpha_4} + h \frac{(1 - B \alpha_2)}{\beta_4}, \quad (2.46)$$

or

$$\alpha_2 = \frac{\alpha_4 (h (1 - \beta_4) + \beta_4 (h - h_4))}{B h (\alpha_4 - \beta_4)}, \quad (2.47)$$

so that Equations 2.39, 2.45 and 2.46 can be combined to give, after some manipulation,

$$\alpha_2 = \frac{2(\beta_4 + \alpha_4) - (\beta_4 - 1)^3 (B\beta_4^2 - B\beta_4\alpha_4)^{-1}}{4 + (\beta_4^2 - 1)(\alpha_4\beta_4)^{-1}}. \quad (2.48)$$

This result can be viewed as the constant pressure-volume boundary equivalent to the traditional result defined by Equation 2.7 in Section 2.3.1 and the constant volume result defined by Equation 2.22 in Section 2.3.3. Comparing the different results it is immediately clear how the complexity of the analysis has escalated. With the addition of the pressure-volume boundary the flow field is now a three parameter set, whereby, for a given  $\beta_4$  and  $B$ , the specification of either  $\alpha_2$  or  $\alpha_4$  will define the thrust and power extracted by the turbine. Alternatively, the coefficient  $\beta_4$  can be related back to the upstream Froude number  $Fr$ , after eliminating  $h_4$  and  $\alpha_2$  in Equation 2.45 by making use of Equations 2.39 and 2.46, so

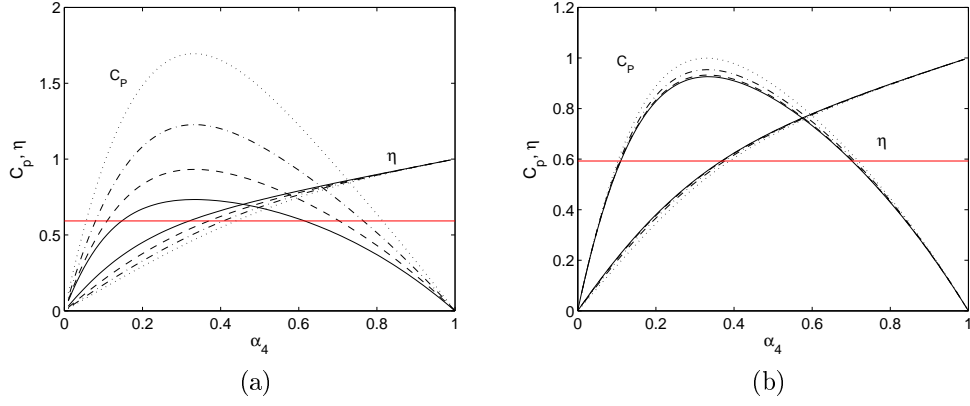


Figure 2.8: (a) Power coefficient and efficiency as a function of wake velocity coefficient  $\alpha_4$  for a pressure-volume constraint with  $Fr = 0.1$ , and varying blockage ratio:  $B = 0.1$  (solid line),  $B = 0.2$  (dash line),  $B = 0.3$  (dash-dot line),  $B = 0.4$  (dot-dot line). (b) Same as (a), but with  $B = 0.2$ , and varying Froude number:  $Fr = 0.01$  (solid line),  $Fr = 0.1$  (dash line),  $Fr = 0.2$  (dash-dot line),  $Fr = 0.3$  (dot-dot line). The horizontal line in both plots indicates the Lanchester-Betz limit.

that

$$\frac{Fr^2}{2}\beta_4^4 + 2\alpha_4 Fr^2 \beta_4^3 - (2 - 2B + Fr^2) \beta_4^2 - (4\alpha_4 + 2\alpha_4 Fr^2 - 4) \beta_4 + \left( \frac{Fr^2}{2} + 4\alpha_4 - 2B\alpha_4^2 - 2 \right) = 0. \quad (2.49)$$

Equation 2.49 is a quartic equation in  $\beta_4$ , which can be solved once the three parameters of Froude number  $Fr$ , blockage ratio  $B$  and the wake velocity coefficient  $\alpha_4$  have been defined. The thrust applied by the turbine  $T$ , and the power removed  $P = \alpha_2 u T$ , then follow directly from Equation 2.43

$$T = \frac{1}{2} \rho u^2 B b h (\beta_4^2 - \alpha_4^2) = \frac{1}{2} \rho u^2 B b h C_T, \quad (2.50)$$

and,

$$P = \frac{1}{2} \rho u^3 B b h \alpha_2 (\beta_4^2 - \alpha_4^2) = \frac{1}{2} \rho u^3 B b h C_P. \quad (2.51)$$

Figure 2.8 plots the power coefficient against the wake induction factor  $\alpha_4$  for several choices of Froude number and blockage ratio. It is clear from Figure 2.8 (a) that the maximum power coefficient increases with blockage ratio (indeed this relationship is monotonic, as can be readily verified numerically) and exceeds the Lanchester-Betz limit. Figure 2.8 (b) shows that the power also increases with the upstream Froude number. The physical

explanation for this increase follows from the arguments established for the constant volume boundary in Section 2.3.3; the finite volume constraint allows for a head difference to be established across the disc, which is augmented by the finite Froude number. Interestingly the maximum power occurs very close to  $\alpha_4 = 1/3$ , which is the optimum value in the constrained volume flow case.

An important point to highlight is that the actuator disc is removing potential energy from the flow and not kinetic energy. In fact, when the Froude number of the upstream flow is greater than zero the turbine increases the kinetic energy in the downstream flow, at the expense of a reduction in potential energy.

With respect to the flow field it is simple to show that the relationship between the velocity coefficients  $\alpha_2$  and  $\alpha_4$ , and consequently the thrust and power coefficients, are entirely consistent with those derived in Sections 2.3.1-2.3.3 under the appropriate asymptotic limits. Firstly, letting  $B \rightarrow 0$ , so that the flow field becomes equivalent to that of the traditional unbounded analysis, it follows that  $\beta_4 \rightarrow 1$  from Equation 2.46 and, since it can be shown numerically that  $(\beta_4 - 1)^3$  approaches zero faster than  $B$ , Equation 2.48 reduces to  $\alpha_2 = (1 + \alpha_4)/2$ , which is identical to the unbounded result given by Equation 2.7 in Section 2.3.1. Secondly, letting  $Fr = 0$ , so that the free surface deformation is zero (as can be readily seen from Equation 2.46) the quartic 2.49 reduces to the quadratic

$$(1 - B) \beta_4^2 - (2\alpha_4 - 2) \beta_4 + (2\alpha_4 - B\alpha_4^2 - 1) = 0, \quad (2.52)$$

and Equation 2.47 leads to

$$\beta_4 = \frac{1 - B\alpha_2}{1 - B\alpha_2/\alpha_4}, \quad (2.53)$$

Combining Equation 2.52 with Equation 2.53 it can be readily seen that the flow field is identical to that established for the constant volume boundary (Equation 2.22). The flow field is consistent, therefore, in the limit of small blockage to the constant pressure boundary flow and, in the limit of small Froude number, to the constant volume boundary flow.

Interestingly, for general values of  $B$  and  $Fr$  a physically admissible solution to the quartic Equation 2.49 does not always exist (Houlsby et al. [2008], Whelan et al. [2009]). This loss of a solution is typical for an open channel flow problem and usually implies the

onset of hydraulically critical flow at some point in the flow field (the simplest example is uniform flow over a smooth bump, see White [1994]). For the problem at hand it is easy to identify the reason for the loss of the physical solution by considering energy conservation within the bypass flow<sup>4</sup>

$$E_4 = \frac{u^2}{2g} + h = \frac{\beta_4^2 u^2}{2g} + h_4. \quad (2.54)$$

Critical bypass flow is consistent with the condition  $dE_4/dh_4 = 0$ , which on a plot of energy against depth defines the point at which the downstream depth  $h_4$  has become so small that energy is only just conserved in the bypass flow. Any further infinitesimal reduction in  $h_4$  will lead to a back up of the bypass flow and probably the onset of a hydraulic jump. Evaluating the derivative leads to

$$\frac{d}{d(h_4/h)} (\beta_4^2) = -\frac{2}{Fr^2}. \quad (2.55)$$

It is easily confirmed numerically that this equality holds at the point when physically admissible solutions to the quartic Equation 2.49 cease to exist, and so the onset of critical bypass flow is the limiting factor to the existence of physically admissible solutions. To better appreciate Equation 2.55 a contour plot of the velocity coefficient  $\alpha_4$ , in terms of the Froude number and blockage ratio at the onset of critical bypass flow, is given in Figure 2.9 (b). The range of admissible solutions reduces with the wake velocity coefficient. Furthermore, in the limit  $B \rightarrow 0$ , the bypass flow becomes critical when the upstream Froude number becomes critical. In the opposite limit  $B \rightarrow 1$ , critical flow is unavoidable for all non-zero Froude numbers.

### 2.3.4.1 Downstream Mixing

Since the flow is not uniform with depth at Station 4 downstream mixing is possible. Applying momentum conservation in the horizontal direction between Stations 1 and 5 leads to

$$\frac{1}{2}\rho gb (h^2 - (h - \Delta h)^2) - T = \rho bhu \left( \frac{uh}{h - \Delta h} - u \right). \quad (2.56)$$

---

<sup>4</sup>Of course momentum or energy conservation across another section of the flow field could be considered, but it turns out that these conservation relationships do not limit the solution space of the model.

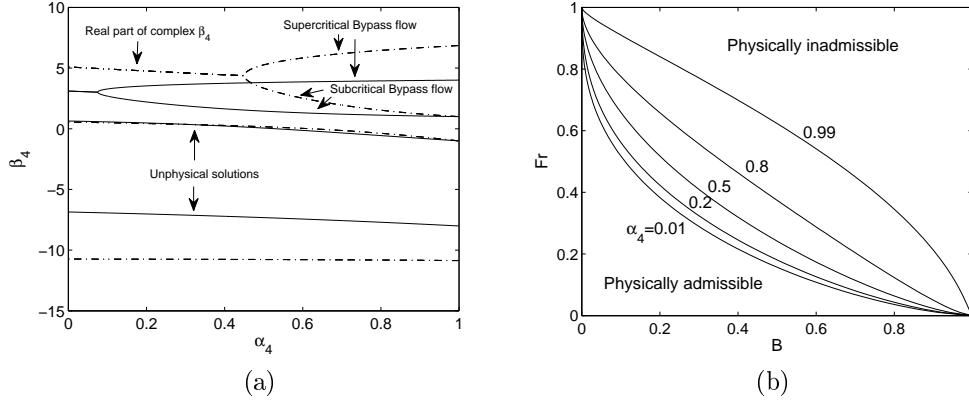


Figure 2.9: (a) Analysis of the roots to the quartic Equation 2.49. The example solution of Whelan et al. [2009] for  $Fr = 0.14$  and  $B = 0.64$  (dash-dot line), alternative case of  $Fr = 0.3$  and  $B = 0.2$  (solid line). (b) Allowable range of Froude number and blockage ratio to yield a physical solution for a range of velocity coefficient  $\alpha_4$  ( $\alpha_4$  labelled on the plot).

Substituting for the thrust coefficient and rearranging then gives

$$\frac{1}{2} \left( \frac{\Delta h}{h} \right)^3 - \frac{3}{2} \left( \frac{\Delta h}{h} \right)^2 + \left( 1 - Fr^2 + \frac{C_T B Fr^2}{2} \right) \frac{\Delta h}{h} - \frac{C_T B Fr^2}{2} = 0. \quad (2.57)$$

This is a cubic expression that can be solved for the downstream depth change that results from the operation of the turbine. Notably for zero Froude number the relative depth change tends to the solutions  $\Delta h/h \rightarrow 0, 1$  and  $2$ , with the former being the physically admissible solution. The power lost in the wake can be determined in terms of  $\Delta h$  from

$$P_W = \frac{1}{2} \rho u^3 B b h \alpha_2 \alpha_4^2 + \frac{1}{2} \rho u^3 b h (1 - B \alpha_2) \beta_4^2 - \frac{1}{2} \rho u^3 b h \left( \frac{h}{h - \Delta h} \right)^2 + h b u (h_4 - h_5) \rho g. \quad (2.58)$$

By combining Equation 2.58 with Equation 2.51, the total power lost in the channel, or *extracted* by the turbine(s), is then

$$P + P_W = \rho g u b h \Delta h \left( 1 - Fr^2 \frac{1 - \Delta h/(2h)}{(1 - \Delta h/h)^2} \right). \quad (2.59)$$

To a very good approximation this is simply the rate at which potential energy is being lost in the channel ( $\rho g u b h \Delta h$ ), with a small correction in brackets for the increase in downstream kinetic energy. A measure of efficiency, defined as the ratio of power *available* to the tidal device(s) to the total power extracted from the tidal stream, follows directly

from Equation 2.59,

$$\eta = \frac{P}{P + P_W} = \frac{P}{\rho g u b h \Delta h} \left( 1 - Fr^2 \frac{1 - \Delta h/2h}{(1 - \Delta h/h)^2} \right)^{-1}. \quad (2.60)$$

This is a very important equation for tidal devices and provides an indication of how effective a turbine is at using the energy that it extracts from the flow. Such a measure becomes especially relevant when, as discussed in Section 2.4, the power that can be extracted by a tidal fence is limited at an actual coastal site.

Several observations can be made about the measure of efficiency. Firstly, as  $Fr \rightarrow 0$ ,  $\eta \rightarrow \alpha_2$ , which agrees with the result obtained for a volume constrained flow (GC07 and Section 2.3.3). This result is easy to deduce from Equation 2.60 by first neglecting the term proportional to  $Fr^2$  and noting that the power can be written as  $P = (\alpha_2 u) T$ , so that

$$\eta \cong \frac{\alpha_2 u T}{\rho g u b h \Delta h}, \quad (2.61)$$

and second, by rearranging  $u$  times Equation 2.56 to give

$$u T = \rho g u b h \left( \Delta h - \frac{\Delta h}{2} \frac{\Delta h}{h} - Fr^2 \frac{h \Delta h}{h - \Delta h} \right) \cong \rho g u b h \Delta h, \quad (2.62)$$

which follows by ignoring terms proportional to  $Fr^2$  and  $\Delta h/h$  (since  $\Delta h/h \rightarrow 0$  when  $Fr \rightarrow 0$  from Equation 2.57). Substitution of Equation 2.62 into Equation 2.61 then leads to  $\eta \rightarrow \alpha_2$  as required.

For arbitrary Froude number, the effect of the free surface on efficiency is best appreciated through manipulation of Equation 2.60. Combining Equation 2.60 with the expression for power from Equation 2.51 and substituting for  $C_T B Fr^2/2$  from Equation 2.57 leads to

$$\eta = \alpha_2 \frac{(1 - \Delta h/(2h)) - Fr^2 (1 - \Delta h/h)^{-1}}{1 - Fr^2 (1 - \Delta h/(2h)) (1 - \Delta h/h)^{-2}}. \quad (2.63)$$

For small but finite Froude number and downstream depth change (i.e.  $Fr^2 (1 - \Delta h/h)^{-1} \ll 1$ ), which is realistic for many tidal flows, the efficiency can therefore be approximated as

$$\eta \approx \alpha_2 \left( 1 - \frac{1}{2} \frac{\Delta h}{h} \right). \quad (2.64)$$

On comparison with Equation 2.33 this indicates that the main effect of the non-zero Froude number and the associated relative depth change, is to reduce efficiency by a factor of  $(1 - \frac{1}{2}\Delta h/h)$ , as compared to that of a device with identical blockage ratio and turbine velocity coefficient placed in a flow with a rigid lid. Physically this result implies that the added constriction in downstream area caused by the deformed surface increases the speed of the bypass flow, relative to the turbine wake flow, and therefore introduces greater mixing losses.

## 2.4 Efficiency: Design Implications for Tidal Turbines

In the design of a row of wind turbines it can generally be assumed that the operation of devices will not have a significant effect on the upstream wind velocity. As a result mixing losses in the wake of the devices can have no effect on the power removed by the turbines and so the best turbines are those which maximise the power coefficient. By contrast, for tidal turbines the problem is more subtle since, as will be shown in Chapters 5-7, the power extracted by a tidal fence at a given coastal site (equal to the power removed by, or available to, the devices plus that lost in downstream mixing) can significantly affect tidal currents immediately upstream of devices. This feedback on the upstream velocity will be seen to ultimately limit the total power that can be extracted. Since the power that is available to a tidal device within the fence is defined by

$$\text{Power Available} = \eta \times \text{Power Extracted}, \quad (2.65)$$

it follows that at the limit of power extraction optimising device efficiency will recover the most available power. It is therefore of direct interest to understand what tidal devices will maximise efficiency.

To determine the most efficient devices it is useful to note that, for a given flow rate, upstream depth and downstream depth change, the force applied by the disc is fixed. It is then immediately evident from Equation 2.64 that devices with large  $\alpha_2$  will be most efficient, implying that one should design a device to have the highest possible  $\alpha_2$  whilst still achieving the given depth change and power extraction across the device. Furthermore, because  $B$  must increase with increasing  $\alpha_2$  to extract the required depth change (see

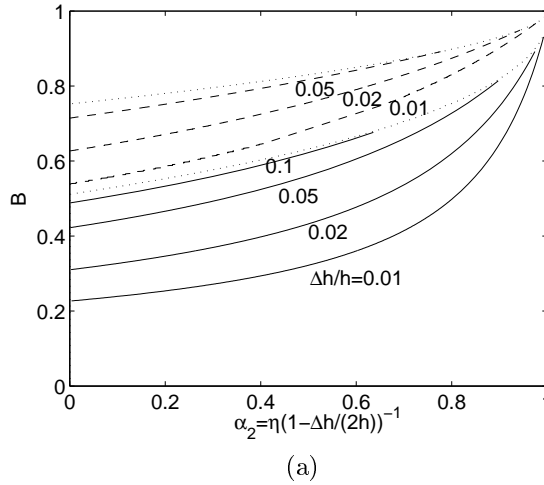


Figure 2.10: (a) Contours of dimensionless depth change, as a function of turbine velocity coefficient  $\alpha_2$ , and blockage ratio  $B$ .  $Fr = 0.05$  (dashed lines),  $Fr = 0.15$  (solid lines), cut-off condition (dotted line).

Figure 2.10 (a)), this is equivalent to the statement that devices with large blockage are most efficient or, more plainly, less power is lost in wake mixing when a large area of water is slowed by a small amount, than when a small area of water is slowed by a large amount. Alternatively, since the ratio of power coefficient to thrust coefficient is simply  $\alpha_2$ , the most efficient turbine can also be interpreted as the turbine which minimises the thrust coefficient for a given power coefficient.

It is useful to point out that maximising the efficiency of a tidal device is not the same as maximising the power coefficient. This is obvious from Figure 2.8, where the highest power coefficient does not achieve the highest efficiency. It should also be noted that there is a limit to how large  $\alpha_2$  and  $B$  can become to maximise efficiency. Using the model derived for pressure-volume constrained flow discussed in Section 2.3.2 the bypass flow becomes critical when the increase in  $\alpha_2$  and  $B$ , required to extract a given depth change, becomes too large (see Figure 2.10 (b)). Economic and serviceability constraints will also restrict the device blockage ratio at real tidal sites.

## 2.5 Effect of Finite Froude Number on Local Field

The step by step extensions to LMADT discussed in Section 2.3 have identified two actuator disc models that describe tidal energy devices in a uniform tidal stream. The first of these, identical to that of GC07, assumes a constant volume flow field and therefore pro-

vides an analytical approximation for the turbine thrust and downstream pressure change assuming that the Froude number is zero. The second model, similar to that of W09, but allowing for downstream mixing, considers a combined pressure-volume constrained flow field and provides an approximation for the thrust applied by a tidal device and the resulting downstream depth change when the Froude number is non-zero. In this section both of these two models are compared with an emphasis on the importance of the Froude number. In particular, the turbine performance, in terms of the thrust coefficient, the power coefficient and the efficiency are compared, followed by the differences in predicted flow fields described by the change in downstream depth.

Figures 2.11(a) and 2.11(c) display the thrust and power coefficient, respectively, as a function of the Froude number for several blockage ratios and a fixed wake velocity coefficient of  $\alpha_4 = 1/3$  (close to maximum power coefficient, see Figure 2.8). The vertical intercept of these individual curves ( $Fr = 0$ ) represent the power and thrust coefficient for the volume constrained flow analysed by GC07. It is evident that for small Froude number ( $Fr < 0.1$ ) the power and thrust coefficient change very little relative to the constant volume result. However, for larger Froude number, especially close to that when the bypass region becomes critical (dashed line), a substantial increase in the thrust and power coefficient of the tidal device results. This is more pronounced for larger blockage ratio. Figure 2.11(b) and 2.11(d) explore the effect of the wake velocity coefficient on these results for blockage ratios of  $B = 0.05$  and  $B = 0.4$ . For the smaller blockage ratio the change in power coefficient is minor for both power and thrust when  $\alpha_4$  is varied. For the larger blockage ratio the power coefficient reduces, as expected, when  $\alpha_4$  is either increased ( $\alpha_4 = 1/2$ ) or decreased ( $\alpha_4 = 1/6$ ). The thrust increases substantially when  $\alpha_4$  reduces, and the onset of critical flow occurs at lower Froude number, in agreement with Figure 2.9(b).

Perhaps the most interesting result of Figure 2.11 is the rate at which the thrust coefficient varies with Froude number. This suggests that if the blockage ratio of a tidal device remains relatively constant over a tidal cycle the equivalent depth-averaged drag force of a tidal device will be a time varying fraction of the time varying quantity  $\rho u^2 h$ .

The effect of Froude number on efficiency is evident in Figure 2.12(a), which plots the efficiency for turbines with varying blockage ratio and a wake velocity coefficient  $\alpha_4 = 1/3$ .

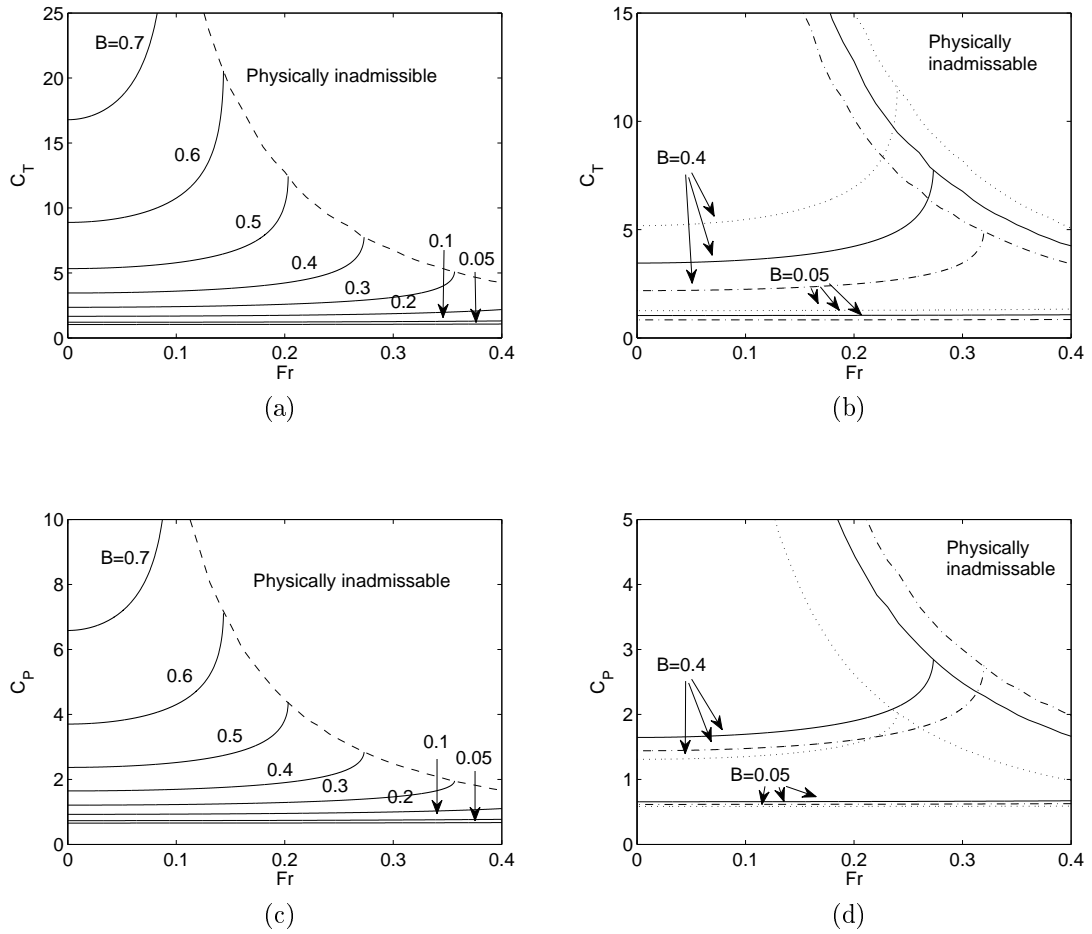


Figure 2.11: Plots of the thrust coefficient  $C_T$  and the power coefficient  $C_P$  against the upstream Froude number for various blockage ratios. (a)  $C_T$  against  $Fr$  where  $\alpha_4 = 1/3$ ; (b)  $C_T$  against  $Fr$  where  $\alpha_4 = 1/2$  (dash-dot line),  $\alpha_4 = 1/3$  (solid line) and  $\alpha_4 = 1/6$  (dotted line); (c)  $C_P$  against  $Fr$  where  $\alpha_4 = 1/3$ ; (d)  $C_P$  against  $Fr$  where  $\alpha_4 = 1/2$  (dash-dot line),  $\alpha_4 = 1/3$  (solid line) and  $\alpha_4 = 1/6$  (dotted line).

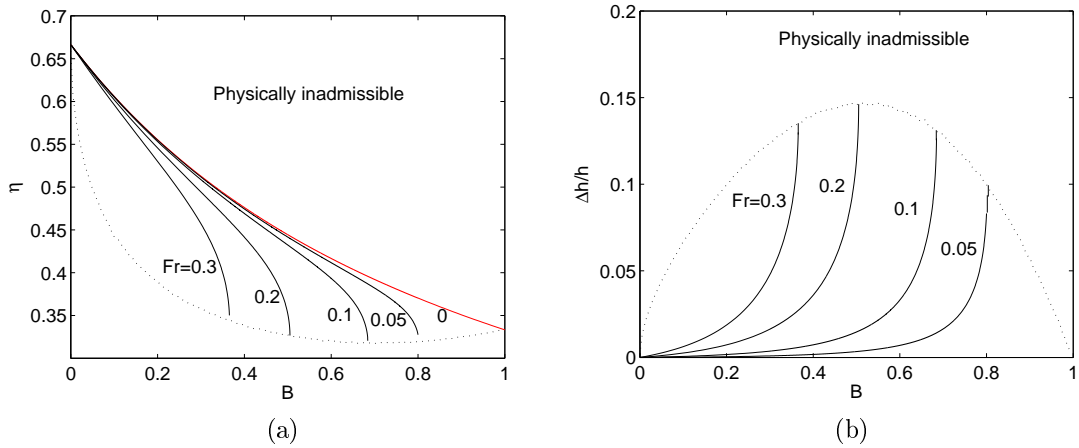


Figure 2.12: (a) Plot of efficiency against blockage ratio for tidal devices with wake velocity coefficient  $\alpha_4 = 1/3$ , and various Froude numbers (labeled on plot). (b) Plot of dimensionless downstream depth change against blockage ratio for tidal devices with wake velocity coefficient  $\alpha_4 = 1/3$ , and various Froude numbers (labeled on plot).

For higher Froude number the efficiency reduces below that of the constant volume flow ( $Fr = 0$ ), which is explained by the fact that the depth change is greater (Figure 2.12(b)). It is also clear that, holding  $\alpha_4$  fixed, the efficiency reduces as the blockage ratio increases regardless of the Froude number, but of course more power in total is being removed from the tidal stream, as is evident by the greater depth change in Figure 2.12(b).

Figure 2.13(a) plots the change in non-dimensional downstream depth change that results from an actuator disc of various blockage and fixed wake induction factor and upstream Froude number. It is obvious that significant downstream depth change can occur. For example, a depth change close to 5 % results at each fence of tidal devices when  $B \sim 0.45$  and  $Fr \sim 0.2$ . This change in depth would equate to 2 m in a flow depth of 40 m. Given the size of such a depth change it is interesting to compare these results with the constant volume results derived by GC07. Although the constant volume flow has by definition no change in area, a depth change can be implied from the change in pressure across the flow divided by specific gravity. Figure 2.13(a) plots this change in depth, for various blockage ratios, and compares them to that produced by the pressure-volume constrained flow. The agreement is surprisingly good despite the inconsistency in mass flow rate outlined in Equation 2.38.

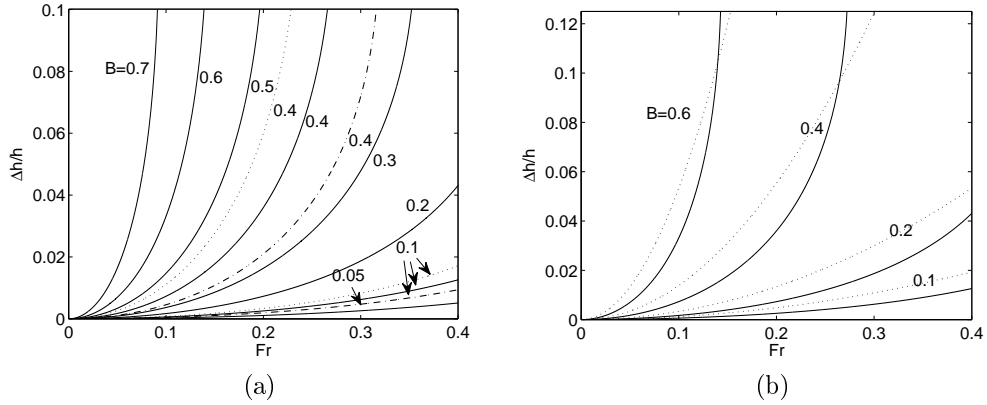


Figure 2.13: (a) Plot of  $\Delta h/h$ , as a function of Froude number, for various blockage ratios (labeled on the plot) based on a volume-pressure bounded flow. The wake velocity coefficient is  $\alpha_4 = 1/3$  (solid lines),  $\alpha_4 = 1/2$  (dash-dot line), and  $\alpha_4 = 1/6$  (dotted line). (b) Plot of  $\Delta h/h$ , as a function of Froude number, for various blockage ratios (labeled on the plot) based on a volume-pressure bounded flow (solid lines) and implied from the downstream pressure change in a constant volume bounded flow (dotted lines).

## 2.6 Discussion

### 2.6.1 Limitations of LMADT

It is useful at this stage to consider the limitations of LMADT in approximating the local flow field about a tidal energy device. The majority of these limitations are due to the one-dimensional nature of the theory, which is unable to account for two dimensional phenomena such as non-uniform upstream currents, changes in bathymetry, bed friction effects, drag forces due to the support structure or asymmetry in the placement of a tidal device in the water column. Over a long tidal fence, however, it would be expected that changes in the horizontal component of upstream velocity and the along fence bathymetry would have a minor effect on the theoretical result for a device placed within the fence provided that they change over a length scale much larger than the centre to centre spacing between turbines. If this is not the case, or when changes in the vertical velocity profile, bed friction or the asymmetric and irregular placement of turbines in the fence are deemed to be important detailed 3D numerical modelling and experimental work will be required to better understand the local field.

Actuator disc theory applies strictly to steady flows. By contrast, at tidal sites the motion is unsteady due to both long period variations in tidal stream velocity over a tidal cycle and shorter period variations in velocity due to free surface waves and turbulence.

Although LMADT gives no indication of the length scale of the local field (distance between Stations 1 and 5), recent experiments on porous discs suggest that mixing may occur over 20-30 device diameters ( $\sim O(10^2)$  m) for a low blockage device (Myers and Bahaj [2010]). At this length scale time varying velocity fluctuations of the order of the period of a tidal wave will be negligible. Shorter period variations will however remain important and will introduce added mass effects and dynamic inflow effects. These have been shown to increase the forces experienced by a tidal device (Whelan [2010]). They may also have some influence on the average momentum sink introduced by a device within a fence or the useful power extracted by a tidal device. Despite this observation these effects are not yet well understood and are overlooked in the Thesis.

Lastly, perhaps the most well known limitation of actuator disc theory is its inability to model correctly highly loaded turbines (i.e. turbines with small velocity coefficient  $\alpha_2$ ). For instance, when  $\alpha_2 < 1/2$  the traditional Lanchester-Betz theory will predict a reversed flow in the wake, which is clearly at odds with the turbulent wake that is produced in practice (Burton et al. [2001]). However, from the discussion in Section 2.4, efficient tidal turbines should typically aim to have large  $\alpha_2$  values and so this limitation should be unimportant.

## 2.7 Conclusions

The most important conclusion from this chapter is that power removed by a turbine(s) in an open channel flow can exceed the traditional power coefficient but the removed power is only a fraction of the total power extracted from the flow. This fraction can be increased by maximising the efficiency of the tidal devices within the fence, which is not the same as maximising the traditional power coefficient. In particular, devices with large blockage ratio and wake velocity coefficient will be the most efficient.

In Chapter 4 it will be shown how the momentum sink implied by LMADT for a particular tidal fence can be introduced into a 2D shallow water model to calculate power extraction. The efficiency from Equation 2.60 will then be used to determine the available power from tidal fence deployed in a range of different coastal basins in Chapters 5-7.

# Chapter 3

## Simulating Coastal Tidal Flows

### 3.1 Introduction

This chapter presents the Shallow Water Equations (SWEs), which are commonly employed to model tidal flows in coastal waters. The SWEs are first derived by vertically integrating the continuity and Navier Stokes equations. Next, the limitations of the two dimensional SWEs for modelling tidal flows, as compared to more complex three dimensional (3D) numerical models, is discussed. Chapter 3 concludes with the definition of a set of generic coastal basins, which will provide a framework for studying the effects of tidal energy extraction in later chapters. The relevance and generality of this set is discussed, with reference to a number of locations around the world that have been highlighted as having significant tidal energy potential.

### 3.2 The Shallow Water Equations

The SWEs have been used for many years to approximate the evolution of long waves in shallow water, one aim being to understand tidal hydrodynamics in coastal basins (see, for example, Lamb [1932]). The equations are valid when the horizontal scales of a time varying flow are much larger than the vertical scales, and can be derived by vertically integrating the continuity and Navier Stokes (NS) equations over the flow depth (see, for example, Falconer [1993]) or from a control volume analysis of a fluid element of infinitesimal plan area extending over the entire water depth (see, for example, Abbott [1979]). The former of these two approaches provides insight into the origin of the depth-averaged shear

stress terms and the depth-averaged dispersion coefficient. To benefit from this insight, a derivation, based on that of Falconer [1993] and Dean and Dalrymple [1984], will be presented briefly below.

The governing equations for an incompressible and Newtonian fluid constitute the continuity equation

$$\frac{\partial u_*}{\partial x} + \frac{\partial v_*}{\partial y} + \frac{\partial w_*}{\partial z} = 0, \quad (3.1)$$

and the associated Navier Stokes momentum equations

$$\frac{\partial u_*}{\partial t} + u_* \frac{\partial u_*}{\partial x} + v_* \frac{\partial u_*}{\partial y} + w_* \frac{\partial u_*}{\partial z} = X - \frac{1}{\rho} \frac{\partial p}{\partial x} + \frac{\mu}{\rho} \left( \frac{\partial^2 u_*}{\partial x^2} + \frac{\partial^2 u_*}{\partial y^2} + \frac{\partial^2 u_*}{\partial z^2} \right), \quad (3.2)$$

$$\frac{\partial v_*}{\partial t} + u_* \frac{\partial v_*}{\partial x} + v_* \frac{\partial v_*}{\partial y} + w_* \frac{\partial v_*}{\partial z} = Y - \frac{1}{\rho} \frac{\partial p}{\partial x} + \frac{\mu}{\rho} \left( \frac{\partial^2 v_*}{\partial x^2} + \frac{\partial^2 v_*}{\partial y^2} + \frac{\partial^2 v_*}{\partial z^2} \right), \quad (3.3)$$

and,

$$\frac{\partial w_*}{\partial t} + u_* \frac{\partial w_*}{\partial x} + v_* \frac{\partial w_*}{\partial y} + w_* \frac{\partial w_*}{\partial z} = Z - \frac{1}{\rho} \frac{\partial p}{\partial x} + \frac{\mu}{\rho} \left( \frac{\partial^2 w_*}{\partial x^2} + \frac{\partial^2 w_*}{\partial y^2} + \frac{\partial^2 w_*}{\partial z^2} \right), \quad (3.4)$$

where the velocity vector  $\mathbf{u}_* = (u_*, v_*, w_*)^T$ ,  $\mathbf{x} = (x, y, z)^T$ , the pressure is  $p$ , the density of the fluid is  $\rho$ , the dynamic viscosity is  $\mu$ , and the terms  $X$ ,  $Y$ , and  $Z$  represent body forces. (For a discussion and detailed derivation of the above equations see, for example, Massey [1998], Hughes and Brighton [1967] or Young et al. [2001].)

In shallow coastal basins the flow is generally turbulent (Taylor [1920], Jirka [2002]) and so the velocity field can be considered, using the Reynolds decomposition, to comprise a local mean velocity  $\bar{\mathbf{u}}_*$ , and a local fluctuating velocity  $\mathbf{u}'_*$ , such that

$$\mathbf{u}_* = \bar{\mathbf{u}}_* + \mathbf{u}'_*. \quad (3.5)$$

Over a time period  $T_f$ , which is long compared to the timescale of the fluctuations but short compared to the timescale of tidal motions, these components satisfy

$$\bar{\mathbf{u}}_* = \frac{1}{T_f} \int_t^{t+T_f} \mathbf{u}_* dt, \quad \text{and} \quad \overline{\mathbf{u}'_*} = \frac{1}{T_f} \int_t^{t+T_f} \mathbf{u}'_* dt = 0.$$

Introducing these velocity components into the continuity and NS Equations (3.1-3.4), and averaging the result over  $T_f$ , leads to the time-averaged continuity equation (Reynolds

[1895])

$$\frac{\partial \bar{u}_*}{\partial x} + \frac{\partial \bar{v}_*}{\partial y} + \frac{\partial \bar{w}_*}{\partial z} = 0, \quad (3.6)$$

and the time-averaged momentum equation (in the subsequent discussion only the  $x$  direction will be given for brevity)

$$\begin{aligned} \frac{\partial \bar{u}_*}{\partial t} + \bar{u}_* \frac{\partial \bar{u}_*}{\partial x} + \bar{v}_* \frac{\partial \bar{u}_*}{\partial y} + \bar{w}_* \frac{\partial \bar{u}_*}{\partial z} &= \bar{X} - \frac{1}{\rho} \frac{\partial \bar{p}}{\partial x} + \frac{1}{\rho} \frac{\partial}{\partial x} \left( \mu \frac{\partial \bar{u}_*}{\partial x} - \overline{\rho u'_* u'_*} \right) + \\ &\quad \frac{1}{\rho} \frac{\partial}{\partial y} \left( \mu \frac{\partial \bar{u}_*}{\partial y} - \overline{\rho u'_* v'_*} \right) + \frac{1}{\rho} \frac{\partial}{\partial z} \left( \mu \frac{\partial \bar{u}_*}{\partial z} - \overline{\rho u'_* w'_*} \right) \end{aligned}$$

The non-linear fluctuations  $\overline{u'_* u'_*}$ ,  $\overline{u'_* v'_*}$  and  $\overline{u'_* w'_*}$  in this expression indicate the effect of random fluctuations on the long term mean flow pattern, and are commonly known as the Reynolds, or turbulent, stresses. Using the Boussinesq eddy viscosity concept (Boussinesq [1877]), these stresses can be written in terms of the mean velocity components

$$-\overline{\rho u'_* u'_*} = \rho v_t \left( \frac{\partial \bar{u}_*}{\partial x} + \frac{\partial \bar{u}_*}{\partial x} \right), \quad -\overline{\rho u'_* v'_*} = \rho v_t \left( \frac{\partial \bar{u}_*}{\partial y} + \frac{\partial \bar{v}_*}{\partial x} \right), \quad -\overline{\rho u'_* w'_*} = \rho v_t \left( \frac{\partial \bar{u}_*}{\partial z} + \frac{\partial \bar{w}_*}{\partial x} \right), \quad (3.7)$$

where  $v_t$  is the turbulent eddy viscosity (which may vary with both position, time and Reynolds stress component). The eddy viscosity is generally much larger than the molecular viscosity  $\mu$ , due to turbulence and because the dispersive momentum transport by turbulent eddies is significantly larger than that possible by laminar diffusion. Neglecting the laminar contribution therefore leads to the momentum equation

$$\begin{aligned} \frac{\partial u_*}{\partial t} + u_* \frac{\partial u_*}{\partial x} + v_* \frac{\partial u_*}{\partial y} + w_* \frac{\partial u_*}{\partial z} &= X - \frac{1}{\rho} \frac{\partial p}{\partial x} + \frac{\partial}{\partial x} \left( v_t \left( \frac{\partial u_*}{\partial x} + \frac{\partial u_*}{\partial x} \right) \right) + \\ &\quad \frac{\partial}{\partial y} \left( v_t \left( \frac{\partial u_*}{\partial y} + \frac{\partial v_*}{\partial x} \right) \right) + \frac{\partial}{\partial z} \left( v_t \left( \frac{\partial u_*}{\partial z} + \frac{\partial w_*}{\partial x} \right) \right) \end{aligned} \quad (3.8)$$

where the over-bar symbols have been removed for convenience. (Each dependent variable hereafter now represents a locally time-averaged mean value.)

The body force terms, per unit mass, applicable for a rotating earth are simply

$$X = 2fv_*, \quad Y = -2fu_*, \quad \text{and,} \quad Z = -g, \quad (3.9)$$

where  $g$  is the acceleration due to gravity and  $f$  is the Coriolis parameter that results from

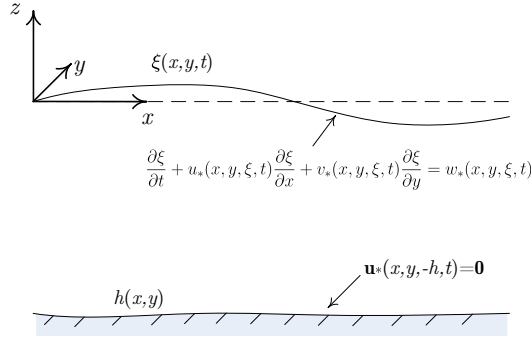


Figure 3.1: Definition sketch and co-ordinate system for the shallow water equations.

the Earth's rotation. It should be noted that equilibrium tidal forcing and self attraction and loading have been omitted from these terms, on the assumption that the coastal basins that will be investigated are sufficiently small, in horizontal extent, so that their effects are negligible.

Following the classical shallow water assumption, provided the horizontal scales of fluid motion are much larger than the fluid depth, as would be the case for very long waves over smooth bathymetry, the vertical accelerations of the fluid can be neglected. The vertical momentum equation then reduces to a balance between the pressure gradient and gravitational acceleration

$$\frac{1}{\rho} \frac{\partial P}{\partial z} - g = 0. \quad (3.10)$$

Integrating Equation 3.10 over the depth results in a hydrostatic pressure distribution

$$P = P_a + \rho g (\xi - z), \quad (3.11)$$

where  $P_a$  is the atmospheric pressure at  $z = \xi$  (see Figure 3.1).

Because vertical motions are assumed to be negligible it is efficient to integrate the continuity and momentum equations over the depth. Using Leibniz's rule, integration of the continuity Equation 3.6 leads to

$$\int_{-h_o}^{\xi} u dz + \frac{\partial}{\partial y} \int_{-h_o}^{\xi} v dz - u(x, y, \xi, t) \frac{\partial \xi}{\partial x} - u(x, y, -h_o, t) \frac{\partial h_o}{\partial x} - v(x, y, \xi, t) \frac{\partial \xi}{\partial y} - v(x, y, -h_o, t) \frac{\partial h_o}{\partial y} + w(x, y, \xi, t) - w(x, y, -h_o, t) = 0. \quad (3.12)$$

where the free surface is at  $z = \xi(x, y, t)$  and the seabed is at  $z = -h_o(x, y)$  (see Figure

3.1). A no slip boundary condition exists at the seabed

$$\mathbf{u}_*(x, y, -h_o, t) = \mathbf{0}, \quad (3.13)$$

together with a kinematic boundary condition at the free surface

$$\frac{\partial \xi}{\partial t} + u_*(x, y, \xi, t) \frac{\partial \xi}{\partial x} + v_*(x, y, \xi, t) \frac{\partial \xi}{\partial y} = w_*(x, y, \xi, t). \quad (3.14)$$

Introducing these boundary conditions into Equation 3.12 leads to the depth averaged continuity equation

$$\frac{\partial \xi}{\partial t} + \frac{\partial uh}{\partial x} + \frac{\partial vh}{\partial y} = 0, \quad (3.15)$$

where  $h = h_o + \xi$ , and the depth averaged velocities are defined as

$$u = \frac{1}{h} \int_{-h_o}^{\xi} u_* dz, \quad v = \frac{1}{h} \int_{-h_o}^{\xi} v_* dz.$$

Likewise, adding  $u_*$  times Equation 3.6 to the momentum equation 3.8 and integrating over the depth leads to (again only the  $x$  direction is shown for brevity)

$$\int_{-h_o}^{\xi} \left( \frac{\partial u_*}{\partial t} + \frac{\partial u_*^2}{\partial x} + \frac{\partial u_* v_*}{\partial y} + \frac{\partial u_* w_*}{\partial z} \right) dz = \int_{-h_o}^{\xi} f v_* dz - \frac{1}{\rho} \int_{-h_o}^{\xi} \frac{\partial P}{\partial x} dz + \int_{-h_o}^{\xi} \left[ \frac{\partial}{\partial x} \left( 2v_t \frac{\partial u_*}{\partial x} \right) + \frac{\partial}{\partial y} \left( v_t \left( \frac{\partial u_*}{\partial y} + \frac{\partial v_*}{\partial x} \right) \right) + \frac{\partial}{\partial z} \left( v_t \left( \frac{\partial u_*}{\partial z} \right) \right) \right] dz.$$

Employing Leibniz's rule and the boundary conditions Equation 3.13 and Equation 3.14, this expression can be rewritten as

$$\begin{aligned} \frac{\partial uh}{\partial t} + \frac{\partial \beta_{xx} u^2 h}{\partial x} + \frac{\partial \beta_{xy} uv h}{\partial y} &= fvh - \frac{1}{\rho} \int_{-h_o}^{\xi} \frac{\partial P}{\partial x} dz + \\ \frac{\partial}{\partial x} \int_{-h_o}^{\xi} 2v_t \frac{\partial u_*}{\partial x} dz - 2v_t \frac{\partial u_*}{\partial x} \Big|_{\xi} \frac{\partial \xi}{\partial x} - 2v_t \frac{\partial u_*}{\partial x} \Big|_{-h_o} \frac{\partial h_o}{\partial x} &+ \\ \frac{\partial}{\partial y} \int_{-h_o}^{\xi} v_t \left( \frac{\partial u_*}{\partial y} + \frac{\partial v_*}{\partial x} \right) dz - v_t \left( \frac{\partial u_*}{\partial y} + \frac{\partial v_*}{\partial x} \right) \Big|_{\xi} \frac{\partial \xi}{\partial y} &+ \\ v_t \left( \frac{\partial u_*}{\partial y} + \frac{\partial v_*}{\partial x} \right) \Big|_{-h_o} \frac{\partial h_o}{\partial y} + v_t \left( \frac{\partial u_*}{\partial z} \right) \Big|_{\xi} - v_t \left( \frac{\partial u_*}{\partial z} \right) \Big|_{-h_o} &, \end{aligned} \quad (3.16)$$

where  $\beta_{xx}$  and  $\beta_{xy}$  are momentum correction factors defined so that

$$\beta_{xx} = \frac{1}{hu^2} \int_{-h_o}^{\xi} u_*^2 dz, \quad \beta_{xy} = \frac{1}{huv} \int_{-h_o}^{\xi} u_* v_* dz. \quad (3.17)$$

Likewise the momentum equation in the  $y$  direction leads to the additional correction factor

$$\beta_{yy} = \frac{1}{hv^2} \int_{-h_o}^{\xi} v_*^2 dz. \quad (3.18)$$

If the vertical velocity profiles of  $u_*$  and  $v_*$  vary with depth these correction factors will differ slightly from unity. However in most practical applications this difference is ignored and  $\beta_{xx}$ ,  $\beta_{xy}$  and  $\beta_{yy}$  are taken to be unity (Falconer [1993]).

Traditionally Equation 3.16 is simplified through the introduction of two additional assumptions. The first is that the depth integration of the viscous terms can be rewritten as

$$\int_{-h_o}^{\xi} v_t \frac{\partial u_*}{\partial x} dz = v_T h \frac{\partial u}{\partial x}, \quad (3.19)$$

where  $v_T$  is introduced to define the depth averaged turbulent eddy viscosity. A similar definition is made for the integrals involving eddy viscosity multiplied by the velocity gradients  $\partial u_*/\partial y$ ,  $\partial v_*/\partial x$  and  $\partial v_*/\partial y$ . In practice there are several ways to define  $v_T$  (Elder [1959], Stansby [2006]), but in this thesis it will be taken as a constant value for simplicity.

Secondly, the viscous terms evaluated at the free surface and the seabed are parameterised. For example, at the free surface ( $z = \xi(x, y, t)$ ) it is assumed that viscous terms are related to surface shearing action, which can be described by a wind shear stress  $\tau_W$ . In the present thesis the wind shear terms will be ignored to simplify the analysis, however their inclusion in depth-averaged models is straightforward (see, for example Falconer [1993]). At the seabed, ( $z = -h_o(x, y)$ ) the viscous terms are assumed to represent frictional resistance between the seabed and the fluid flow. This seabed shear stress has a significant physical effect in coastal basins and is modelled with the introduction of a bed shear stress  $\tau_{x,b}$ , defined such that

$$\frac{\tau_{b,x}}{\rho} = v_t \left( \frac{\partial u_*}{\partial z} \right) \Big|_{-h_o} + 2v_t \frac{\partial u_*}{\partial x} \Big|_{-h_o} \frac{\partial h_o}{\partial x} + v_t \left( \frac{\partial u_*}{\partial y} + \frac{\partial v_*}{\partial x} \right) \Big|_{-h_o} \frac{\partial h_o}{\partial y}. \quad (3.20)$$

For a flat seabed this becomes

$$\frac{\tau_{b,x}}{\rho} = \nu_t \left( \frac{\partial u_*}{\partial z} \right) \Big|_{-h_o}. \quad (3.21)$$

The bed shear  $\tau_{b,y}$  is defined similarly from the momentum equation in the  $y$  direction.

Introducing the hydrostatic pressure defined by Equation 3.11, the definition of depth averaged eddy viscosity introduced in Equation 3.19 and, the bed shear stress given in Equation 3.20, the SWEs can be written as

$$\frac{\partial \xi}{\partial t} + \frac{\partial uh}{\partial x} + \frac{\partial vh}{\partial y} = 0, \quad (3.22)$$

$$\begin{aligned} \frac{\partial uh}{\partial t} + \frac{\partial u^2 h}{\partial x} + \frac{\partial uvh}{\partial y} &= fvh - gh \frac{\partial \xi}{\partial x} - \\ &\frac{\tau_{b,x}}{\rho} + \frac{\partial}{\partial x} \left( 2\nu_T h \frac{\partial u}{\partial x} \right) + \frac{\partial}{\partial y} \left( \nu_T h \left( \frac{\partial u}{\partial y} + \frac{\partial v}{\partial x} \right) \right), \end{aligned} \quad (3.23)$$

$$\begin{aligned} \frac{\partial vh}{\partial t} + \frac{\partial uvh}{\partial x} + \frac{\partial v^2 h}{\partial y} &= -fuh - gh \frac{\partial \xi}{\partial y} - \\ &\frac{\tau_{b,y}}{\rho} + \frac{\partial}{\partial x} \left( \nu_T h \left( \frac{\partial u}{\partial y} + \frac{\partial v}{\partial x} \right) \right) + \frac{\partial}{\partial y} \left( 2\nu_T h \frac{\partial v}{\partial y} \right). \end{aligned} \quad (3.24)$$

### 3.2.1 Bed Shear Stress

In practice the bed shear stress is usually defined empirically using a variety of models such as the Darcy-Weisbach equation, the Chézy equation and Manning's equation (see Soulsby [1997] for a review). Each of these approaches assumes a quadratic friction law of the form

$$(\tau_{b,x}, \tau_{b,y})^T = \rho \nu_t \left( \left( \frac{\partial u_*}{\partial z} \right) \Big|_{-h_o}, \left( \frac{\partial v_*}{\partial z} \right) \Big|_{-h_o} \right)^T = \rho C_d \mathbf{u} |\mathbf{u}|, \quad (3.25)$$

where  $\mathbf{u} = (u, v)^T$  and  $C_d$  is a drag coefficient that can be related to a Darcy-Weisbach resistance coefficient  $f_{DW}$ , the Chézy coefficient  $C$  and Manning's coefficient  $n$ , through the relationships

$$C_d = \frac{f_{DW}}{8} = \frac{g}{C^2} = \frac{gn^2}{h^{1/3}}. \quad (3.26)$$

Alternatively, if the turbulent tidal flow is assumed to have a logarithmic velocity profile of the form

$$\mathbf{u}_*(z) = \frac{u_f}{\kappa} \ln(z/z_o), \quad \text{with} \quad u_f = \left( \frac{|\tau_b|}{\rho} \right)^{1/2}, \quad (3.27)$$

where  $\kappa = 0.4$  is the von Kármán constant and  $z_o$  describes a roughness length, the drag coefficient according to Equation 3.25 can be defined as (Soulsby [1997])

$$C_d = \left( \frac{-\kappa}{1 + \ln(z_o/h)} \right)^2. \quad (3.28)$$

In practice the roughness parameter  $z_o$  can be calculated by adding the roughness due to skin friction  $z_{os}$  and the roughness due to form drag  $z_{of}$  (Soulsby [1997]). The former is dependent on the seabed conditions (Table 7 in Soulsby [1997] gives roughness lengths for various mixes of mud, sand and gravel). The latter can be estimated from the following empirical expression

$$z_{of} = \frac{\Delta_r^2}{\lambda_r}, \quad (3.29)$$

where  $\Delta_r$  is the height, and  $\lambda_r$  is the wavelength, of seabed undulations. In rocky tidal races these undulations may be related to boulders or other large debris and so the parameter  $z_{of}$  might be significant (Soulsby, personal communication, 2009).

### 3.2.2 Simplifications to the SWEs

If the horizontal scale of a tidal site is large and tidal currents vary smoothly over the length of the site simple scaling arguments suggest that the viscous terms, which involve second order spatial derivatives of the velocity field, can be neglected in the shallow water approximation to the momentum equation. This leads to the inviscid SWEs

$$\frac{\partial \xi}{\partial t} + \frac{\partial uh}{\partial x} + \frac{\partial uh}{\partial y} = 0, \quad (3.30)$$

$$\frac{\partial uh}{\partial t} + \frac{\partial u^2 h}{\partial x} + \frac{\partial uvh}{\partial y} = fvh - gh \frac{\partial \xi}{\partial x} + \frac{\tau_{b,x}}{\rho}, \quad (3.31)$$

$$\frac{\partial vh}{\partial t} + \frac{\partial uvh}{\partial x} + \frac{\partial v^2 h}{\partial y} = -fuh - gh \frac{\partial \xi}{\partial y} + \frac{\tau_{b,y}}{\rho}, \quad (3.32)$$

which constitute a weakly damped hyperbolic system of partial differential equations (Sobey [2008]). Of course, at any real coastal site turbulent viscosity will be important in the

vicinity of small scale features where the flow may separate, for example. However the resolution of a tidal model is often insufficient to represent these features. In such cases bed shear stress will then effectively parameterise the additional mixing losses (Sutherland [2007]).

If the amplitude of tidal oscillations is also small, with respect to the mean water depth, and the velocity field varies smoothly over a length scale of the order of a tidal wave, then the advection term becomes small relative to the remaining terms in the shallow water momentum balance. The continuity equation can then be linearised and the advection terms in the SWEs neglected, leading to (Lamb [1932])

$$\frac{\partial \xi}{\partial t} + h_o \frac{\partial u}{\partial x} + h_o \frac{\partial v}{\partial y} = 0, \quad (3.33)$$

$$\frac{\partial u}{\partial t} + g \frac{\partial \xi}{\partial x} = -\frac{\tau_{b,x}}{h_o \rho} + f v, \quad (3.34)$$

$$\frac{\partial v}{\partial t} + g \frac{\partial \xi}{\partial y} = -\frac{\tau_{b,y}}{h_o \rho} - f u. \quad (3.35)$$

### 3.3 Limitations of 2D Shallow Water Models

As mentioned in the first section of this Chapter, the SWEs have been used for many years to model tidal hydrodynamics with considerable success. However in certain situations the ability of 2D SWE models to simulate shallow flows is limited.

Stansby [2006] suggests that shallow water wake flows are one example where numerical simulation of the SWEs give poor predictions. The reason for this deficiency may arise from the assumption of a fixed vertical velocity profile in the SWEs, such that bed friction in shallow flows, which is related physically to the velocity gradients at the seabed, must instead be specified relative to the depth-averaged velocity and the assumed velocity profile (see Equation 3.25). As a result the velocity near the seabed in a depth-averaged model is implicitly assumed to be both in phase with, and a constant fraction of, the depth-averaged velocity at all times. However, this assumption appears to be violated in shallow water flows when large-scale horizontal mixing is important, as for shallow wake flows (Stansby [2006]). One example that has been investigated is flow in the wake of a small conical island, where 3D simulations indicate that the bed velocity gradients and the depth-averaged velocity differ substantially in phase and possibly in sign, resulting generally in increased bed shear

relative to that which would be predicted using depth average velocity (Stansby [2003]). Simulations of these flows using a 2D depth-averaged SWE model have been shown to give poor results unless the shallow wake is unsteady everywhere (Stansby [2006]). In particular a 2D model was reported to predict an unsteady wake, when experiments indicated a steady wake, and generally to underpredict the downstream extent of bubble wakes. Similar problems may result when simulating the far wake of tidal devices modelled using a 2D depth-averaged model.

More complex 3D numerical models avoid the problem of a fixed velocity profile by simulating the vertical variations in horizontal velocity directly. However, with these more advanced models care must still be taken in selecting an appropriate turbulence model to simulate accurately horizontal and vertical mixing, which then drives variation in vertical velocity profile and ultimately bed friction. Stansby [2003] proposed a mixing length model, based on the assumption that the shallow flow is everywhere turbulent. The application of this mixing length model to a 3D numerical model, assuming hydrostatic pressure, provided significantly better predictions of wake formation in the lee of a conical island with shallow slope.

It therefore appears that ideally a 3D numerical model, with a suitable turbulence model, should be used to model tidal energy extraction. However, since the focus of this thesis is to understand the potential of tidal energy for a variety of generic coastal basins, a more computationally efficient 2D numerical model is highly desirable. Furthermore, for some of the geometries to be investigated it is unlikely that details of the flow structure in regions of separated flow and perhaps in the localised wake behind a turbine fence (both areas with potential large-scale horizontal mixing) will have a first order effect on power potential or mean tidal currents. It would, however, be useful to confirm this with 3D models in future work.

### **3.4 Set of Generic Coastal Basin Geometries**

Recent tidal stream resource assessments (see Table 1, Chapter 1, and Blunden and Bahaj [2007a] for a review regarding the European shelf) have identified large tidal streams in excess of 2 m/s at a wide variety of different coastal sites. Although these sites tend to be

located on continental shelves that appear to be close to resonance and have large natural energy dissipation, the mechanisms that lead to large tidal streams at each site vary. For example, large tidal streams through the Pentland Firth are principally the result of a phase difference established across the strait as the tide propagates from the Atlantic Ocean into the North Sea, whereas in a large open bay, such as the Bristol Channel coupled to the European shelf, quarter wavelength resonance with the Atlantic Ocean tide is believed to generate amplified tidal range and streams (Heath, 1981). This apparent difference between sites suggests that site specific investigations are required to understand the tidal resource at each coastal location. However, in practice such investigations would require extensive numerical modelling and field observations, both of which are time consuming and expensive.

A useful compromise, pursued in this thesis, is to define a set of generic coastal sites, or coastal geometries, which cover the various locations where tidal streams are known to be large. The benefit from defining this set of geometries is that the general physics of each type of coastal location can be investigated, without site-specific anomalies, to provide an understanding of the hydrodynamic effects of tidal energy extraction.

Based on a survey of a large number of tidal sites, summarised in Appendix A, the set of generic sites illustrated in Figure 3.2 (which is an expanded version of Figure 1.6, Chapter 1) has been defined. These geometries have been chosen so that every tidal site documented in Appendix A can be classified into one of the four fundamental classes in Figure 3.2, or a combination thereof. Figure 3.3 summarises this classification.

The first class of site describes a strait between two oscillating water bodies. In the simplest example, considered in detail by Garrett and Cummins [2005], the tidal strait is isolated and no interconnected channels or straits are present (Figure 3.2(a-i)). The more complicated scenario (Figure 3.2(a-ii)) describes a strait with multiply connected sub channels, discussed in Chapter 5. Many real channels surveyed in Appendix A have this characteristic.

The second class of site concerns an oscillating bay from which two distinct groups can be defined, based on their geometry. The first group consists of enclosed bays which have a narrow inlet channel connecting the bay to a much larger basin or ocean (Figure 3.2(b-i)). As outlined in Chapter 6, tidal oscillations in these enclosed bays will accelerate

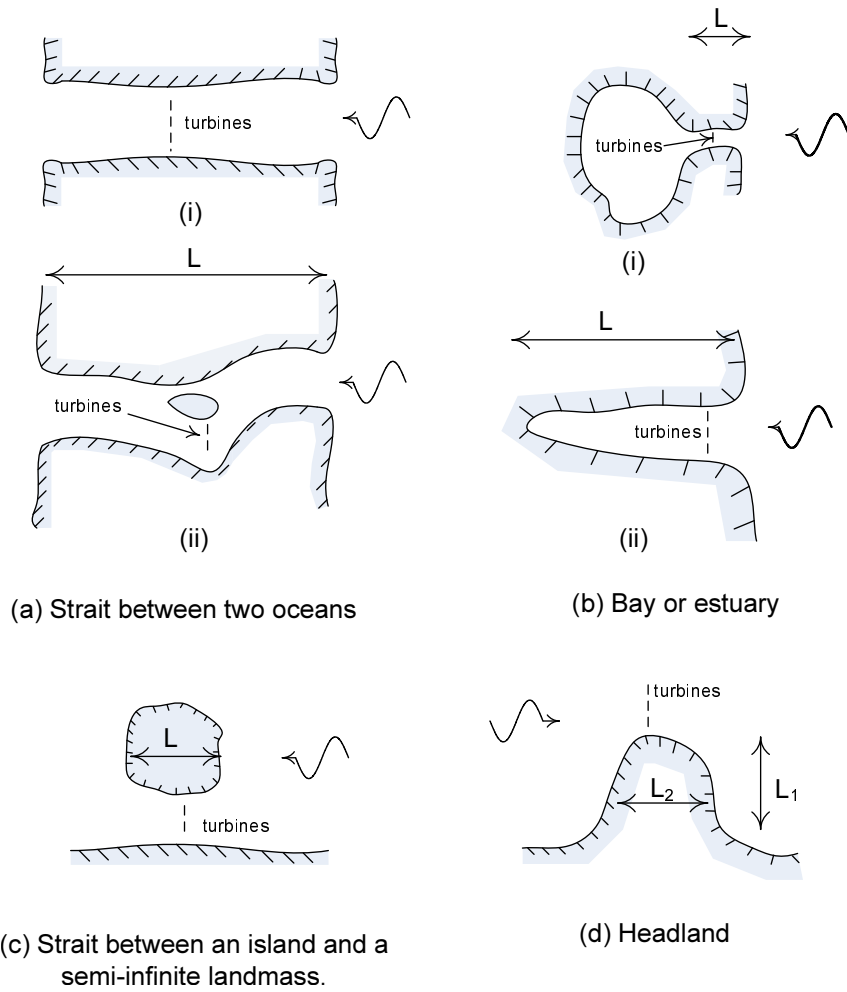


Figure 3.2: Four different classes of generic coastal sites. Sub groups are included for classes (a) and (b). (Extended version of Figure 1.6.) The lengths  $L$ ,  $L_1$  and  $L_2$  are referred to in Appendix A.

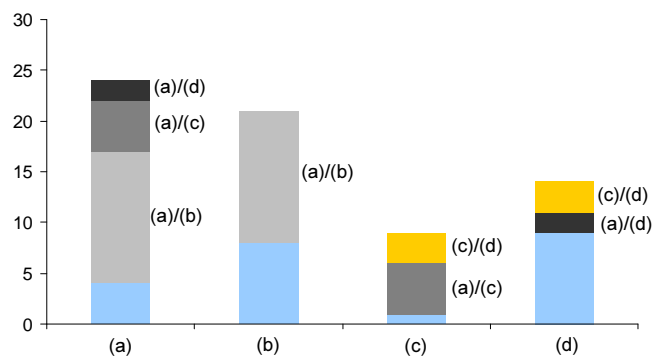


Figure 3.3: Prospective tidal sites surveyed in Appendix A, listed by site class. A number of sites represent a compound addition of more than one generic site.

tidal streams through the narrow inlet. In contrast, Figure 3.2(b-ii) describes non-enclosed bays or estuaries, such as for example the Bristol Channel. Tidal energy sites with this geometry tend to be very large in extent, and many establish quarter wavelength resonance with the semi-diurnal tide, as discussed further in Chapter 6.

Figure 3.2(c) outlines the third class of site which describes the occurrence of large tidal currents between an island and a much larger land mass. As discussed below, it can be considered as a limiting case of a tidal strait or network of tidal channels, and is considered in more detail in Chapter 5.

Lastly Figure 3.2(d) describes accelerated flow around headlands. Many examples of this coastal geometry exists around the UK, including Portland Bill in England and Duncansby Head in Scotland (see Appendix A). Chapter 7 investigates this geometry further.

### 3.4.1 Independence and Compound Sites

The generic sites in Figure 3.2 are not strictly independent and overlap under certain geometric limits. In particular, class (a-i) becomes equivalent to class (b-i) when the enclosed bay becomes very large (Blanchfield et al. [2008b]). Similarly class (a-i) becomes equivalent to class (c) when the island in the latter class is very large. Alternatively class (c) is similar to class (a-ii) when both the channel and the sub-channel not containing the tidal devices become very wide, or the island becomes small.

Compound sites may also be formed from the addition of one or more of the classes depicted in Figure 3.2. Chapter 6 discusses the compound addition of class (a) and class (b-i), which may occur when an enclosed bay is part of a larger multiply connected network of tidal channels. Locations such as the Alderney Race (see Appendix A) provide a good example of the compound addition of class (c) and class (d). Analysis of these sites are outside the scope of the present thesis.

# Chapter 4

## Numerical Solution of the Shallow Water Equations

### 4.1 Introduction

This chapter describes the numerical solution of the Shallow Water Equations (SWEs) using the Discontinuous Galerkin (DG) finite element method. The DG method is adopted because of its ability to achieve an arbitrarily high order of accuracy, handle complex geometry, and, importantly for tidal resource assessment, ensure conservation of mass on an element by element basis. Following a short literature review, the solution of the SWEs using the DG method is outlined. Next, the representation of tidal energy extraction within the resulting 2D numerical model is discussed and a line sink of momentum is implemented to represent a fence of tidal devices. It is suggested that the momentum sink associated with the tidal fence can be defined using Linear Momentum Actuator Disc Theory (LMADT). Lastly open ocean boundary conditions are discussed and a characteristic based open boundary condition, consistent with the well known Flather condition (Flather [1976]), is adopted to simulate the open boundary. Further detailed discussion of the DG numerical solution and extensive validation of a numerical solver called OxTide, which has been developed to perform the numerical analysis in the thesis, are given in Appendix B.

## 4.2 Characteristics of the DG Method

For complicated coastal domains, or when non-linear terms become important, the SWEs can rarely be solved analytically. As a result there is a substantial body of literature concerned with the numerical solution of the equations. Traditionally, the methods used to solve the equations have included Finite Differences (FD), Finite Volumes (FV), Finite Elements (FE) and the Method of Characteristics (MoC), among others. Although each of these methods have their own strengths and weaknesses the present thesis will be concerned with the relatively new application of the Discontinuous Galerkin (DG) method, which was first introduced in 1973 by Reed and Hill [1973] to model the neutron transport equation.

In effect the DG method combines the FE and FV numerical approaches (Cockburn and Shu [1998]). It therefore inherits various characteristics from both numerical methods, including: (1) the ability to model flows with strong advection; (2) compatibility with unstructured meshing, so as to model complex geometry and provide increased resolution within the flow field; (3) straightforward application of boundary conditions through a numerical flux; and, (4) a sound theoretical base to quantify numerical error and undertake numerical convergence tests. Despite these similarities the DG method is distinct from FV and FE methods in a number of important ways. Firstly, unlike continuous FE solutions of the Generalized Wave Equation (GWE) formulation of the SWEs<sup>1</sup>, the DG method conserves mass on an element by element basis. This is achieved because the continuity equation is satisfied in the weak sense for each individual element in the DG formulation (Dawson and Proft [2004]), whilst for the GWE the continuity equation is not solved directly and so residuals in mass can exist locally, even though conservation is ensured globally (Dawson and Proft [2004], Sutherland et al. [2007]). Local conservation is particularly important when simulating tidal energy extraction, where the local mass flux must be computed consistently to allow accurate representation of the momentum sink of a tidal device.

Secondly, unlike low order FV methods, the DG method can incorporate high-order elements in addition to high-order time stepping schemes. This has the advantage of reducing numerical diffusion in a similar manner to spectral FE models (see for example Ma [1993]

---

<sup>1</sup>The GWE was introduced because numerical solution of the primitive SWEs using continuous FE methods results in well-known unphysical oscillations (see, for example, Lynch and Gray [1979]).

and Iskandarani et al. [2005]) and will be important when accurately simulating complicated shallow flows around islands and tidal fences for example, provided that secondary flows are not important.

Despite these promising advantages, the well known downside of the DG method has been its computational cost compared with continuous FE methods. This additional cost is a direct result of the discontinuous polynomial basis functions used in the DG method, which introduce many more degrees of freedom than comparative continuous FE methods (Karniadakis and Sherwin [2005]). To overcome this disadvantage the development of quadrature free DG formulations (see, for example Atkins and Shu [1998], Hesthaven and Warburton [2008]) have helped to reduce slightly the computational disadvantage. In practical applications the adoption of parallel computation, which is easily achieved in the DG method because of the compact form of the mass matrix, can also be employed (Atkins [1997]). In fact, a simulation of the SWEs on a numerical mesh with approximately 160,000 elements conducted by Kubatco et al. [2009] demonstrated that a DG solver achieved better parallel efficiency than a continuous FE model when run on 256 and 1024 processors.

#### 4.2.1 Application of the DG Method to the SWEs

There has been a steady increase in the application of the DG method to the inviscid SWEs in recent years, beginning with the simulation of non-linear shock wave problems in both one and two dimensions (see, for example, Li and Liu [2001], Aizinger and Dawson [2002], Schwanenberg and Harms [2004], Kubatco et al. [2006a] and Kesserwani et al. [2008]). These earlier papers have tended to conclude two main findings: (1) the DG method is comparable with FV methods for capturing shock waves; and (2) the order of convergence of the DG method is  $n + 1$  for smooth solutions, where  $n$  is the order of the polynomial basis functions. Both of these two findings confirm that the DG method effectively combines useful aspects of FV and spectral FE methods.

High order applications of the method (up to  $n = 15$ ) have been presented by Eskilsson and Sherwin [2004] and Giraldo and Warburton [2008], and have illustrated the ability of the DG method to achieve spectral convergence for a number of test problems involving the linearised SWEs. This property has been confirmed both for unstructured and adaptive grids (see Giraldo and Warburton [2008] and earlier work for  $n < 5$  by Atkins and Shu

[1998]). For the non linear inviscid SWEs only qualitative comparisons have been made to analytical approximations and alternative numerical solutions. For this reason, in Appendix B (B.2.2) a quantitative comparison between the Method of Characteristics and the DG method is presented for a non-linear test problem.

To extend the DG to more practical problems the well balanced property of the SWE source terms has been investigated by Ern et al. [2008] and an extension including a morphodynamic model have been presented by Kubatco et al. [2006b]. A wetting and drying treatment has also been implemented by Bunya et al. [2009] and Ern et al. [2008]. Although the development of a wetting and drying routine is outside the scope of the present thesis, the well balanced nature of the numerical solver is demonstrated in Appendix B (B.2.4.2).

To date very little analysis has been undertaken for the viscous form of the SWEs using the DG method. Notable exceptions are by Schwanenberg and Harms [2004], who outline an application of the method to viscous equations, and by Bernard et al. [2009] who investigate shallow wake flows around islands. In the present thesis the numerical solution of the SWEs including viscous terms is outlined and verified with experimental results (see Appendix B.2.3).

### 4.3 Matrix form of the SWEs

The SWEs (introduced in detail in Chapter 3), may be written in matrix-form as

$$\frac{\partial \mathbf{U}}{\partial t} + \frac{\partial \mathbf{F}(\mathbf{U}, \mathbf{Q})}{\partial x} + \frac{\partial \mathbf{G}(\mathbf{U}, \mathbf{Q})}{\partial y} = \mathbf{S}(\mathbf{U}), \quad (4.1)$$

and,

$$\mathbf{Q} - \frac{\partial \mathbf{R}_x(\mathbf{U})}{\partial x} - \frac{\partial \mathbf{R}_y(\mathbf{U})}{\partial y} = 0, \quad (4.2)$$

where the vector  $\mathbf{U} = (h, uh, vh)^T$  contains the dependent variables and the vector  $\mathbf{Q} = (\frac{\partial u}{\partial x}, \frac{\partial u}{\partial y}, \frac{\partial v}{\partial x}, \frac{\partial v}{\partial y})^T$  parameterise the first order spatial derivatives. The flux vectors are given by

$$\mathbf{F}(\mathbf{U}, \mathbf{Q}) = \begin{bmatrix} uh \\ u^2h + gh^2/2 - 2h\nu_T \frac{\partial u}{\partial x} \\ uvh - h\nu_T \left( \frac{\partial v}{\partial x} + \frac{\partial u}{\partial y} \right) \end{bmatrix}, \quad \mathbf{G}(\mathbf{U}, \mathbf{Q}) = \begin{bmatrix} vh \\ uvh - h\nu_T \left( \frac{\partial v}{\partial x} + \frac{\partial u}{\partial y} \right) \\ v^2h + gh^2/2 - 2h\nu_T \frac{\partial v}{\partial y} \end{bmatrix}, \quad (4.3)$$

$$\mathbf{R}_x(\mathbf{U}) = \begin{bmatrix} \frac{uh}{h} \\ 0 \\ \frac{vh}{h} \\ 0 \end{bmatrix}, \quad \mathbf{R}_y(\mathbf{U}) = \begin{bmatrix} 0 \\ \frac{uh}{h} \\ 0 \\ \frac{vh}{h} \end{bmatrix}, \quad \text{and} \quad \mathbf{S}(\mathbf{U}) = \begin{bmatrix} 0 \\ -gh\frac{\partial z}{\partial x} - \frac{\tau_{x,b}}{\rho} + fvh \\ -gh\frac{\partial z}{\partial y} - \frac{\tau_{y,b}}{\rho} - fuh \end{bmatrix}, \quad (4.4)$$

where use has been made of the identities  $\partial\xi/\partial t = \partial h/\partial t$ , on the assumption of a fixed seabed, and  $gh\nabla\xi = \nabla(gh^2/2) - gh\nabla z$ , where  $\nabla z = -\nabla h_o$  is the seabed slope.

The inviscid SWEs, defined in Section 3.3.1 (Chapter 3), result when  $v_T = 0$ . The auxiliary Equation 4.2 is then redundant. For the linearised SWE defined in Section 3.3.2 (Chapter 3), the flux vectors are given by

$$\mathbf{F}(\mathbf{U}) = \begin{bmatrix} uh_o \\ gh_o h \\ 0 \end{bmatrix}, \quad \mathbf{G}(\mathbf{U}) = \begin{bmatrix} vh_o \\ 0 \\ gh_o h \end{bmatrix}, \quad (4.5)$$

where  $h_o(x, y)$  is the still water reference depth defined in Chapter 3 and the appropriate conserved variables become  $\mathbf{U} = (h, uh_o, vh_o)^T$ .

## 4.4 Discontinuous Galerkin Formulation of the SWEs

This section describes the application of the DG method to the SWEs. The formulation loosely follows the approach outlined by Schwanenberg and Harms [2004] and includes the treatment of viscous terms. As outlined in Section 4.3 the viscous SWEs are considered as a system of first order equations. This allows for polynomial approximations at  $n = 1$  (because the second order derivatives are now parameterised). When  $v_T = 0$  the equations are similar to those considered by Eskilsson and Sherwin [2004] and Giraldo and Warburton [2008].

To begin, an arbitrary two dimensional domain  $\Omega(x, y)$  is divided into a finite number of  $N_e$  non-overlapping elements defined over  $\Omega_e(x, y)$ . Across each of these elements an orthogonal projection of the shallow water system, into a polynomial space characterized by an arbitrary smooth polynomial  $\phi_i$ , is taken

$$\int_{\Omega_e} \left( \frac{\partial \mathbf{U}}{\partial t} + \frac{\partial \mathbf{F}(\mathbf{U}, \mathbf{Q})}{\partial x} + \frac{\partial \mathbf{G}(\mathbf{U}, \mathbf{Q})}{\partial y} - \mathbf{S}(\mathbf{U}) \right) \phi_i d\Omega_e = 0, \quad (4.6)$$

$$\int_{\Omega_e} \left( \mathbf{Q} - \frac{\partial \mathbf{R}_x(\mathbf{U}, \mathbf{Q})}{\partial x} - \frac{\partial \mathbf{R}_y(\mathbf{U}, \mathbf{Q})}{\partial y} \right) \phi_i d\Omega_e = 0. \quad (4.7)$$

An approximate solution  $\mathbf{U}_h$  is then sought which satisfies Equation 4.6 and Equation 4.7 for a range of polynomials  $\phi_i$ . As this range becomes larger the approximation will usually become more accurate. Notably because the approximation is sought on an element by element basis, conservation of mass is ensured within each computational element.

The DG finite element method seeks an approximation to the true solution within each element of the form

$$\mathbf{U}(x, y) \sim \mathbf{U}_h(x, y) = \sum_k^M \hat{\mathbf{U}}_k(x, y) \psi_k(x, y) = \sum_k^M \mathbf{U}_k(x, y) \ell_k(x, y), \quad (4.8)$$

with the associated auxiliary variables

$$\mathbf{Q}(x, y) \sim \mathbf{Q}_h(x, y) = \sum_k^M \hat{\mathbf{Q}}_k(x, y) \psi_k(x, y) = \sum_k^M \mathbf{Q}_k(x, y) \ell_k(x, y), \quad (4.9)$$

where the vectors<sup>2</sup>  $\{\hat{\mathbf{U}}_k\}$  and  $\{\hat{\mathbf{Q}}_k\}$  are a set of discrete time dependent modal coefficients, and the vectors  $\{\mathbf{U}_k\}$  and  $\{\mathbf{Q}_k\}$  are a set of discrete time dependent nodal coefficients. The set of polynomials  $\{\psi_k\}$  and  $\{\ell_k\}$  are the time independent two dimensional modal and nodal basis functions, respectively. In two spatial dimensions the polynomial degree of these approximations, denoted by  $n$ , is related to the number of basis functions, or degrees of freedom within an individual element,  $M$ . For example, for the triangular elements and basis functions used herein (see Appendix B.1.2)  $M = \frac{1}{2}(n+1)(n+2)$ .

Substituting the nodal or modal form of the approximation (for brevity the nodal approximation will be considered hereafter) into Equations 4.6 and 4.7, and integrating the flux terms by parts, then gives the semi-discrete equations

$$\begin{aligned} \frac{\partial}{\partial t} \int_{\Omega_e} \left( \sum_k^M \mathbf{U}_k \ell_k \right) \phi_i d\Omega_e - \int_{\Omega_e} \left( \frac{\partial \phi_i}{\partial x} \mathbf{F}(\mathbf{U}_h, \mathbf{Q}_h) + \frac{\partial \phi_i}{\partial y} \mathbf{G}(\mathbf{U}_h, \mathbf{Q}_h) \right) d\Omega_e + \\ \int_{\Gamma_e} (\mathbf{F}(\mathbf{U}_h, \mathbf{Q}_h) n_x + \mathbf{G}(\mathbf{U}_h, \mathbf{Q}_h) n_y) \phi_i d\Gamma_e = \int_{\Omega_e} \mathbf{S}(\mathbf{U}_h) \phi_i d\Omega_e \end{aligned} \quad (4.10)$$

---

<sup>2</sup>The brackets  $\{a_k\}$  are used throughout this Chapter to represent the column vector  $(a_1, \dots, a_M)^T$ ,  $k \leq M$ .

and,

$$\int_{\Omega_e} \left( \sum_k^M \mathbf{Q}_k l_k \right) \phi_i d\Omega_e + \int_{\Omega_e} \left( \frac{\partial \phi_i}{\partial x} \mathbf{R}_x(\mathbf{U}_h) + \frac{\partial \phi_i}{\partial y} \mathbf{R}_y(\mathbf{U}_h) \right) d\Omega_e - \int_{\Gamma_e} (\mathbf{R}_x(\mathbf{U}_h) n_x + \mathbf{R}_y(\mathbf{U}_h) n_y) \phi_i d\Gamma_e = 0, \quad (4.11)$$

where  $\mathbf{n} = (n_x, n_y)^T$  is the unit normal vector orientated out of the element  $\Omega_e$ , and  $\Gamma_e$  is the positively orientated boundary about  $\Omega_e$ .

In the DG approach continuity of the basis functions is not enforced between elements, in contrast to the standard continuous finite element approach. This implies that the boundary integrals in Equations 4.10 and 4.11, or more specifically the flux vectors in the integrands, are not uniquely defined. As a compromise the flux terms in these integrals are replaced by the numerical flux terms computed from the solution of a local Riemann problem at the interface. This choice naturally leads to consistency with first order FV schemes when  $n = 0$ . Stability of the numerical scheme, with the aid of slope limiters, can also be achieved in the presence of strong advection and numerical discontinuities (Eskilsson and Sherwin [2004]). However, for the simulations in this thesis no slope limiter was required.

Introducing the numerical fluxes  $\widehat{\mathbf{F}}$ ,  $\widehat{\mathbf{G}}$ ,  $\widehat{\mathbf{R}}_x$  and  $\widehat{\mathbf{R}}_y$ , Equations 4.10 and 4.11 become

$$\frac{\partial}{\partial t} \int_{\Omega_e} \left( \sum_k^M \mathbf{U}_k l_k \right) \phi_i d\Omega_e - \int_{\Omega_e} \left( \frac{\partial \phi_i}{\partial x} \mathbf{F}(\mathbf{U}_h, \mathbf{Q}_h) + \frac{\partial \phi_i}{\partial y} \mathbf{G}(\mathbf{U}_h, \mathbf{Q}_h) \right) d\Omega_e + \int_{\Gamma_e} \left( \widehat{\mathbf{F}}(\mathbf{U}_h, \mathbf{Q}_h) n_x + \widehat{\mathbf{G}}(\mathbf{U}_h, \mathbf{Q}_h) n_y \right) \phi_i d\Gamma_e = \int_{\Omega_e} \mathbf{S}(\mathbf{U}_h) \phi_i d\Omega_e, \quad (4.12)$$

and,

$$\int_{\Omega_e} \left( \sum_k^M \mathbf{Q}_k l_k \right) \phi_i d\Omega_e + \int_{\Omega_e} \left( \frac{\partial \phi_i}{\partial x} \mathbf{R}_x(\mathbf{U}_h) + \frac{\partial \phi_i}{\partial y} \mathbf{R}_y(\mathbf{U}_h) \right) d\Omega_e - \int_{\Gamma_e} \left( \widehat{\mathbf{R}}_x(\mathbf{U}_h) n_x + \widehat{\mathbf{R}}_y(\mathbf{U}_h) n_y \right) \phi_i d\Gamma_e = 0. \quad (4.13)$$

A unique set of discrete nodal coefficients  $\{\mathbf{U}_k\}$  and  $\{\mathbf{Q}_k\}$  can then be defined, provided that Equations 4.12 and 4.13 are satisfied for all  $\phi_i = l_k$ , as per the standard Galerkin approach. The result is a set of  $M$  Ordinary Differential Equations (ODEs) in time, per

element, for each conserved variable. The set can be summarized as

$$\frac{d}{dt} \{\mathbf{U}_k\} = \mathcal{M}^{-1} [\mathcal{B} + \mathcal{E} - \mathcal{S}], \quad \text{with} \quad \{\mathbf{Q}_k\} = \mathcal{M}^{-1} [\mathcal{A} - \mathcal{G}], \quad (4.14)$$

where  $\mathcal{M}$  is the mass matrix with elements

$$\mathcal{M}_{(i,k)} = \int_{\Omega_e} l_i l_k d\Omega_e, \quad \text{for } i, k \leq M, \quad (4.15)$$

and the elements of the remaining terms take the values

$$\mathcal{B}_{(i)} = \mathcal{B}_{(i)}^x + \mathcal{B}_{(i)}^y = \int_{\Omega_e} \left( \frac{\partial l_i}{\partial x} \mathbf{F}(\mathbf{U}_h, \mathbf{Q}_h) \right) d\Omega_e + \int_{\Omega_e} \left( \frac{\partial l_i}{\partial y} \mathbf{G}(\mathbf{U}_h, \mathbf{Q}_h) \right) d\Omega_e, \quad (4.16)$$

$$\mathcal{E}_{(i)} = \int_{\Omega_e} \mathbf{S}(\mathbf{U}_h) l_i d\Omega_e, \quad (4.17)$$

$$\mathcal{S}_{(i)} = \int_{\Gamma_e} l_i \left( \hat{\mathbf{F}}(\mathbf{U}_h, \mathbf{Q}_h) n_x + \hat{\mathbf{G}}(\mathbf{U}_h, \mathbf{Q}_h) n_y \right) d\Gamma_e, \quad (4.18)$$

$$\mathcal{A}_{(i)} = \int_{\Gamma_e} \left( \hat{\mathbf{R}}_x(\mathbf{U}_h) n_x + \hat{\mathbf{R}}_y(\mathbf{U}_h) n_y \right) l_i d\Gamma_e, \quad (4.19)$$

$$\mathcal{G}_{(i)} = \mathcal{G}_{(i)}^x + \mathcal{G}_{(i)}^y = \int_{\Omega_e} \left( \frac{\partial l_i}{\partial x} \mathbf{R}_x(\mathbf{U}_h) \right) d\Omega_e + \int_{\Omega_e} \left( \frac{\partial l_i}{\partial y} \mathbf{R}_y(\mathbf{U}_h) \right) d\Omega_e. \quad (4.20)$$

for  $i \leq M$ . Since each of the terms is solely a function of the nodal coefficients  $\{\mathbf{U}_k\}$  and  $\{\mathbf{Q}_k\}$ , Equation 4.14 is often written in the simplified form

$$\frac{d}{dt} \{\mathbf{U}_k\} = \mathbf{L}_U(\mathbf{U}_h, \mathbf{Q}_h), \quad \text{where} \quad \{\mathbf{Q}_k\} = \mathbf{L}_Q(\mathbf{U}_h). \quad (4.21)$$

The final stage in the DG formulation requires the solution of these ODEs. Since the mass matrix within the operator is compact, and can be decoupled for each element in the domain, integration of Equation 4.21 can be achieved efficiently by an explicit integration scheme such as that implemented in the Runge-Kutta discontinuous Galerkin (RKDG) method (Cockburn et al. [1989]). A third order RK method is used here to update the variables  $\{\mathbf{U}_k^{(p)}\}$  to  $\{\mathbf{U}_k^{(p+1)}\}$  over the time increment  $\Delta t$ . Second and fourth order time stepping were also used in the validation problems reported in Appendix B, and gave very similar results. Third order time stepping was ultimately selected as a compromise because it offers greater accuracy than second order time stepping, and is more computationally efficient than fourth order time stepping. The time stepping is achieved with the following

operations:

$$\{\mathbf{U}_k^{(1)}\} = \{\mathbf{U}_k^{(p)}\} + \Delta t \mathbf{L}_U(\mathbf{U}_h^{(p)}, \mathbf{Q}_h^{(p)}), \quad (4.22)$$

$$\{\mathbf{U}_k^{(2)}\} = \frac{3}{4}\{\mathbf{U}_k^p\} + \frac{1}{4}\{\mathbf{U}_k^{(1)}\} + \frac{1}{4}\Delta t \mathbf{L}_U(\mathbf{U}_h^{(1)}, \mathbf{Q}_h^{(1)}), \quad (4.23)$$

and,

$$\{\mathbf{U}_k^{p+1}\} = \frac{1}{3}\{\mathbf{U}_k^p\} + \frac{2}{3}\{\mathbf{U}_k^{(2)}\} + \frac{2}{3}\Delta t \mathbf{L}_U(\mathbf{U}_h^{(2)}, \mathbf{Q}_h^{(2)}), \quad (4.24)$$

where  $\{\mathbf{Q}_k^{(i)}\} = \mathbf{L}_Q(\mathbf{U}_h^{(i)})$  and the time step  $\Delta t$  is calculated as

$$\Delta t = \max_{\Omega} \left\{ \frac{h_m}{0.5n^2(\sqrt{u^2 + v^2} + \sqrt{gh})} \right\} \quad (4.25)$$

where  $h_m$  is a characteristic mesh dimension (taken to be the smallest vertex of an element). In practice Equation 4.25 ensures a CFL number of 0.5 when  $n = 1$  and includes a correction factor of  $n^2$  for larger  $n$ , as suggested by Karniadakis and Sherwin [2005]. It should be noted that other corrections for large  $n$  have been suggested in the literature (for example Kubatco (2006a) adopt  $2n + 1$ ). The object of this thesis was not to determine the most efficient correction and so a thorough comparison has not been undertaken. A comparison would comprise useful further work.

To solve Equation 4.21 at each time step a numerical solver called OxTide has been written in FORTRAN. The general layout of this code is similar to that used by Hesthaven and Warburton [2008] for hyperbolic conservation laws. Further details about the solver, including the choice of linear and isoparametric triangular elements, basis functions, formation of the spatial operators, and a series of validation and verification tests, are given in Appendix B.

Although the majority of the numerical code details are confined to Appendix B, two aspects of the numerical solver are especially important to tidal energy resource assessment and warrant explanation in the present chapter. The first involves the representation of tidal devices in a 2D depth averaged model and the second concerns the treatment of open boundary conditions.

## 4.5 Representing Tidal Turbines

Two methods can be adopted to introduce a momentum sink, caused by tidal energy extraction, into a depth-averaged numerical model of the SWEs. The first involves the specification of an additional bed shear stress term, whilst the second models tidal devices (on the assumption they are deployed as a tidal fence) as a line sink of momentum.

### 4.5.1 Additional Bed Shear Term

When the Froude number is small, the analysis of an actuator disc in a volume constrained flow (see Garrett and Cummins [2007] and Chapter 2) indicates that the depth-averaged drag force imparted by a disc scales with the velocity squared. More generally, many bluff bodies also obey a simple drag law that is quadratic in the flow rate (Pugh [1987]). Therefore it seems rational as a first approximation to model tidal energy devices by a drag force that is quadratic in the flow rate. Adopting this approach the natural bed shear stress coefficient  $C_d$  in the vicinity of tidal devices is augmented to

$$C_{Tot} = C_d + k_t, \quad (4.26)$$

where  $k_t$  is the thrust coefficient of the tidal devices, per unit area of seabed. It then follows from Equation 4.26 that the instantaneous power extracted by the tidal devices  $P$  is (Sutherland et al. [2007])

$$P = \frac{k_t}{C_d + k_t} P_t, \quad (4.27)$$

where  $P_t$  is the instantaneous total power dissipated due to  $C_{Tot}$ .

The use of Equation 4.26 to model tidal devices has been adopted in several studies on tidal energy extraction in the literature. For example, Sutherland et al. [2007] and Karsten et al. [2008] use Equation 4.26 to determine the power potential of the Johnstone Strait, Canada, and the Minas Passage, Canada. Blunden and Bahaj [2007b] also adopt Equation 4.26 to model tidal energy extraction at Portland Bill in the UK.

As the studies by Sutherland et al. [2007] and Karsten et al. [2008] illustrate, the introduction of additional bed shear for modelling tidal energy extraction is useful to determine the theoretical maximum power that can be extracted at a particular coastal site. How-

ever it is difficult to relate the thrust coefficient  $k_t$  to a particular configuration of tidal device or an array of devices, and so the available power is unknown. Blunden and Bahaj [2007b] have attempted to assign the coefficient based on a case study of a yawed horizontal axis marine current turbine and a hypothetical array design. However they admit that verification of that approach is needed.

### 4.5.2 Line Sink of Momentum

A key advantage of the linear momentum actuator disc theory (LMADT) presented in Chapter 2 is that it provides a theoretical argument that links a tidal device, defined by a blockage ratio and wake velocity coefficient (see Chapter 2 for definitions), to the thrust that the device should impart in a uniform flow. The theory also allows for a distinction to be made between the power extracted by the fence and the power available to the devices. For these reasons it is of practical interest to define tidal devices within a 2D depth-averaged numerical model using LMADT.

In this section it is argued that a fence of tidal devices can be modelled as a line sink of momentum defined by LMADT in a 2D shallow water model. To explain how this can be achieved two typical scenarios for the deployment of a tidal fence are discussed. The work effectively builds on the use of LMADT in 1D shallow water models, considered previously by Draper [2008] and Polagye et al. [2008].

#### 4.5.2.1 Simple Scenario

The simplest scenario for the deployment of a tidal fence is represented in Figure 4.1 (a), which depicts a fence of devices that extends completely across a narrow channel. In this situation one would expect that a time varying tidal stream confined to the channel will pass through the fence, separate around the perimeter of any devices, and then mix to reform a mean velocity profile, similar in shape to that upstream, over some mixing region of length  $l_v$  (the mixing region is denoted by the shaded region in Figure 4.1(a)). Limited experimental evidence that is available for porous discs suggest that the length of this mixing region may be roughly of the order of 20 tidal device diameters (Myers and Bahaj [2010]), or perhaps 200 - 300 m for a 10-15 m diameter axial flow turbine. However further investigation is needed into the effects of ambient turbulence, device turbulence, device

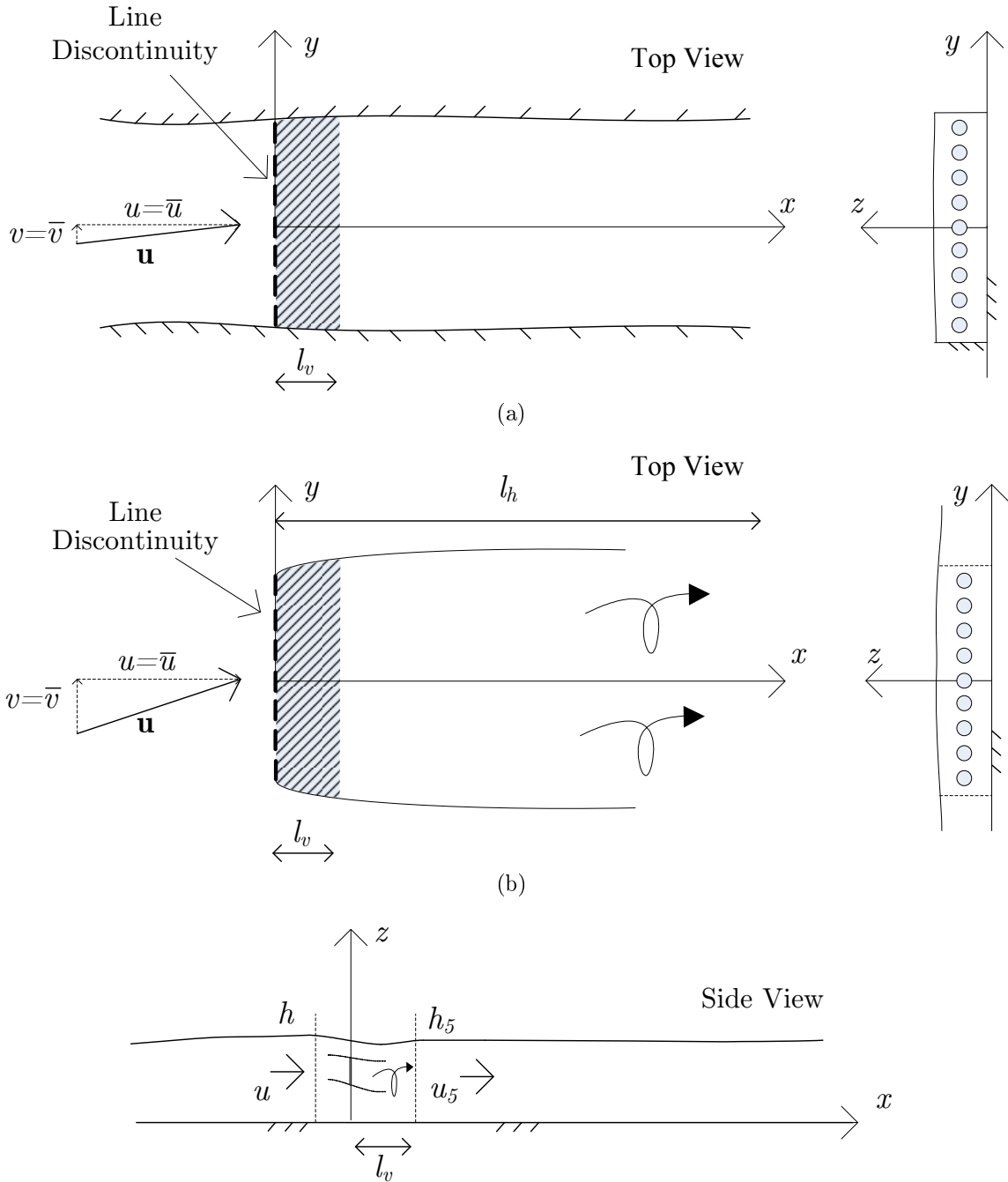


Figure 4.1: Plan view of a fence of tidal turbines in (a) Simple Scenario: a confined channel and (b) Unbounded Scenario: a general 2D flow. The upstream velocity is  $\mathbf{u}$ , having components  $\bar{u}$  and  $\bar{v}$ , normal and tangential to the turbine fence, respectively.

blockage ratio and device shape.

LMADT can be used to define the energy and momentum sink within the shaded region at each point along the fence. For this to be appropriate a number of assumptions are required, including: (1) periodicity in the placement of the devices within the fence; (2) quasi-steady flow over the length  $l_v$  (i.e. the thrust of the turbines must dominate bed friction and inertia forces locally), and (3) slowly varying device blockage ratio, device porosity, channel depth, and depth-averaged velocity, along the fence relative to the center-to-center spacing between devices  $b$ . Provided these assumptions are valid the perturbation in depth and velocity across the region  $l_v$ , at a given point along the fence, will be similar to that between Stations 1-5 in Figure 2.6 (Chapter 2) and is therefore a known function of the local upstream Froude number, device blockage ratio and wake velocity coefficient, at each point along the fence.

From the perspective of numerical modelling, since  $l_v$  will often be much smaller than the mesh discretisation in a 2D depth-averaged model (of the order of kilometers, and perhaps larger for a high order code), introducing the perturbation in depth and velocity implied by LMADT as a line discontinuity offers a useful approach to account for a tidal fence in a 2D depth-averaged model. No numerical or experimental evidence is presented in this thesis to justify this approach, but it is noted that a similar approach has been adopted for a line of diffusers, each with diameter smaller than the water depth, discharging into shallow water (see Lee and Jirka [1980], Lee and Greenberg [1984]). In that situation satisfactory results were achieved in treating the diffusers as a line source of momentum in a 2D depth-averaged framework.

#### 4.5.2.2 Unbounded Scenario

Figure 4.1(b) now illustrates a more complicated scenario in which the fence of turbines is deployed in a laterally unbounded 2D flow. In this situation it is suggested that the flow field about the fence can be split into two fields: (1) a near field extending over the distance  $l_v$  and (2) a far field extending over a distance  $l_h$ , which will be dependent on the extent of the tidal fence and so will generally be much larger than  $l_v$ . Within the near field the flow structure should be similar to that in Figure 4.1 (a), at least towards the center of the fence. In the far field region behind the fence the extraction of momentum by the tidal devices

will lead to a depth-averaged wake with velocity lower than that in the surrounding tidal stream. Generally actuator disc theory cannot be used to describe the energy extraction of the entire fence over this far field length scale because the upstream flow may not be uniform, there might be substantial bed roughness and changes in bathymetry, or the length scale may be too large to validate the assumption of steady flow. However, provided the assumptions presented in Section 4.5.2.1 are valid over the near field LMADT can be used to define the perturbation in depth and velocity at the fence. This amounts again to the assumption that the change in depth and velocity across the fence is a function of the local Froude number, device blockage ratio and wake velocity coefficient at each point along the fence. By analogy to experiments on a line of diffusers and similar flow structures in shallow flows (Lee and Jirka [1980], Lee and Greenberg [1984] and Jirka [2002]), the mixing of the far field in the wake of a fence will result from shear generated turbulence, and will be dependent on the bed roughness, bathymetry and, as mentioned above, the length of the fence. These parameters will typically vary between different locations and it is expected they can be accounted for reasonably well in the depth-averaged numerical model, subject to the limitations of 2D models discussed in Chapter 3.

#### 4.5.2.3 Numerical Implementation of a Line Sink of Momentum

The introduction of a line sink of momentum into the DG method (and any piecewise constant FV method more generally) can be achieved with a modification to the numerical flux passing through a fence. For example, consider Figure 4.2(a) which displays the interface between two elements  $A$  and  $B$  that border a fence of tidal devices. With respect to element  $A$ , the values  $h_L$ ,  $\bar{u}_L$ ,  $h_R$  and  $\bar{u}_R$  represent the depth and normal component of velocity just inside and just outside the element, respectively, at a computational point along the element edge. If the turbine acts as a line sink of momentum the flux out of element  $A$ ,  $F(h_L^*, \bar{u}_L^*, \bar{v}_L^*)$ , and the flux into element  $B$ ,  $F(h_R^*, \bar{u}_R^*, \bar{v}_R^*)$ , need to be adjusted to represent the loss of momentum, where the interface values  $h_L^*$ ,  $\bar{u}_L^*$ ,  $h_R^*$  and  $\bar{u}_R^*$  represent the solution to a local Riemann problem (see Figure 4.2(b)).

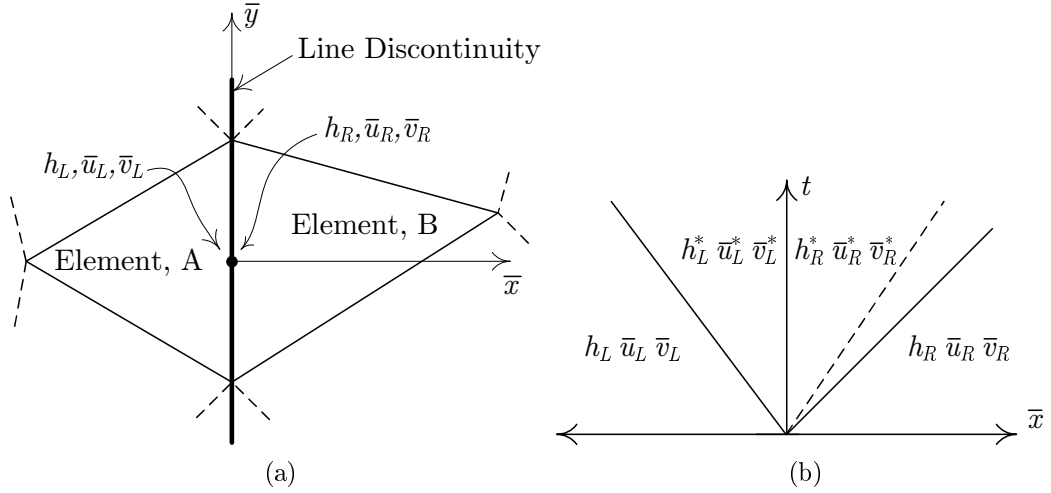


Figure 4.2: (a) Location of flux calculation for two elements either side of a line sink of momentum. (b) Linearised characteristic lines along a coordinate normal to the line discontinuity in sub-critical tidal flow. The solid lines are rarefaction waves and the dashed line represents the contact discontinuity for the tangential velocity.

Provided the flow is assumed to remain sub-critical at the location of the turbine fence, the interface values should satisfy the conditions

$$I^+ = \bar{u}_L + 2c_L = \bar{u}_L^* + 2c_L^*, \quad (4.28)$$

$$I^- = \bar{u}_R - 2c_R = \bar{u}_R^* - 2c_R^*, \quad (4.29)$$

and,

$$(c_L^*)^2 \bar{u}_L^* = (c_R^*)^2 \bar{u}_R^*, \quad (4.30)$$

where  $c_{(L,R)}^* = \sqrt{gh_{(L,R)}^*}$ . Equations 4.28 and 4.29 are based on zero order extrapolation of Riemann invariants along left and right going characteristic lines, and Equation 4.30 ensures conservation of mass across the momentum discontinuity. To uniquely define the interface values a fourth condition needs to be defined to describe the momentum sink. Any number of choices is possible. Perhaps the most convenient approach is to specify the change in depth across the discontinuity. Adopting LMADT the sink is then defined by (c.f. Equation 2.52, Chapter 2)

$$\frac{1}{2} \left( \frac{\Delta h^*}{h^*} \right)^3 - \frac{3}{2} \left( \frac{\Delta h^*}{h^*} \right)^2 + \left( 1 - Fr^2 + \frac{C_T B Fr^2}{2} \right) \frac{\Delta h^*}{h^*} - \frac{C_T B Fr^2}{2} = 0, \quad (4.31)$$

where the blockage ratio  $B$ , Froude number  $Fr$  and depth  $h^*$  are defined relative to the depth and velocity upstream of the line sink,  $\Delta h^*$  is the absolute difference in the interface

depth  $|h_R^* - h_L^*|$ , and the thrust coefficient  $C_T$  is obtained from the specification of a wake velocity parameter  $\alpha_4$ . In practice, because Equation 4.31 requires the solution of a cubic it is more efficient in a numerical code to work with a polynomial approximation to Equation 4.31 of the form:  $\Delta h^*/h^* = p(Fr, B, \alpha_4)$ . A function describing the downstream celerity in terms of the upstream celerity is then

$$g(z) = z\sqrt{1 - p(Fr, B, \alpha_4)}, \text{ where } \begin{cases} z = c_L^*, Fr = (I^+ - 2z)/z, B = Ag/z^2; \text{ for } \bar{u}_L > 0, \\ z = c_R^*, Fr = -(I^- + 2z)/z, B = Ag/z^2; \text{ for } \bar{u}_L < 0, \end{cases} \quad (4.32)$$

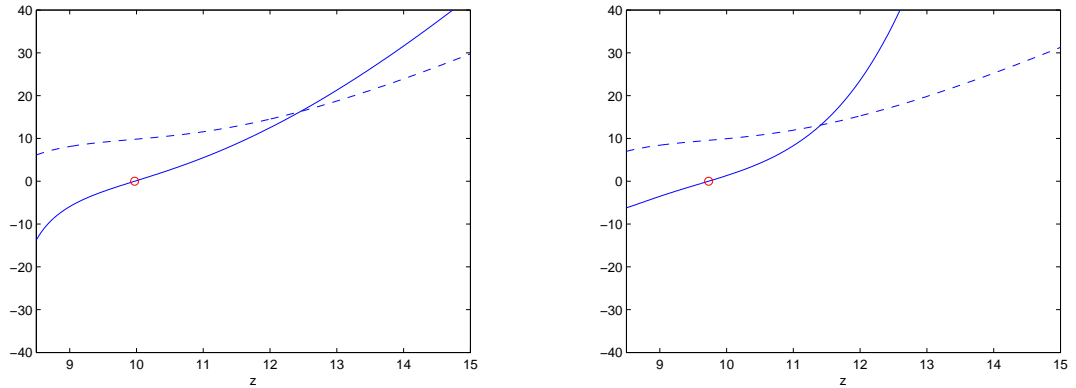
with the condition on  $\bar{u}_L$  defining the upstream values.

Combining Equations 4.28-4.30 with Equation 4.32 leads to the non-linear equation

$$G(z) := \begin{cases} I^+ - 2z - \left(\frac{g(z)^2}{g(z)^2 - z^2}\right) [I^+ - I^- - 2(z + g(z))], & z = c_L^*; \text{ for } \bar{u}_L > 0, \\ I^+ - 2g(z) - \left(\frac{z^2}{z^2 - g(z)^2}\right) [I^+ - I^- - 2(g(z) + z)], & z = c_R^*; \text{ for } \bar{u}_L < 0, \end{cases} \quad (4.33)$$

which must satisfy the condition  $G(z) = 0$ .

In this thesis Equation 4.33 is solved numerically using the Newton-Raphson method. The function  $G(z)$  is generally smooth and monotonic in the region of the root and so convergence, from an initial guess of  $z = \max(c_L^*, c_R^*)$ , is usually rapid (Figure 4.3).



(a)  $h_L = 10, h_R = 9, u_L = 1$  and  $u_R = 1.11$ .

(b)  $h_L = 9, h_R = 10, u_L = -1.11$  and  $u_R = 1$ .

Figure 4.3: Convergence to the required root for  $G(z)$ . The solid line represents  $G(z)$ , the dashed line represents  $g(z)$ , and the circle is the location of the root.

No direct adjustment is required for the tangential velocity components in the flux either side of the fence because it is assumed that the devices will not exert a force in the tangential direction. This is consistent with the classical actuator disc analysis. The

tangential velocity used to compute the numerical flux is determined relative to the contact wave speed as defined in the HLLC method (see Toro et al. [1994] and Appendix B.1.4.1). A direct result of this assumption is that, in the horizontal plane, a depth-averaged tidal stream approaching oblique to a fence will refract through the fence.

It should also be noted that the assumption that devices do not exert a force in the direction parallel to the fence introduces a distinction between the line sink of momentum introduced in Section 4.5.2.3 and the conventional method of an additional bed roughness noted in Section 4.5.1. More specifically, the additional bed roughness will introduce a shear stress in the direction of the local velocity vector, and therefore does not account for any directionality in the resistance of the fence. To overcome this the added bed roughness could alternatively be modified to act on the component of the velocity normal to the fence (i.e.  $\tau = \rho k_t \bar{u} |\bar{u}|$ , where  $\bar{u}$  is the component normal to the fence), but it would then have to be modelled as a separate sink term in the momentum equations as opposed to a simple augmentation of the natural bed friction.

#### 4.5.2.4 Edge of the Fence

For a tidal fence in an unbounded flow (i.e. Figure 4.1) the thrust applied by the devices will drop from a finite value to zero at the edge of the fence. This represents an unbounded shear stress on the fluid at the edge of the fence and will introduce singular behaviour in the velocity field similar to that discussed by Sorensen et al. [1998] and van Kuik [2003] concerning the numerical simulation of an actuator disc. This behaviour presents a problem numerically because it prohibits numerical convergence. To circumvent this problem a smoothing function was applied to remove the singularity at the edges of the fence. This smoothing function was implemented by replacing Equation 4.32 with

$$g(z) = z\sqrt{1 - \Phi p(Fr, B, \alpha_4)}, \quad \text{for } \Phi = \begin{cases} -2\left(\frac{|x'|}{\delta L_f}\right)^3 + 3\left(\frac{|x'|}{\delta L_f}\right)^2 & , |x'| < \delta L_f \\ 1 & , |x'| \geq \delta L_f \end{cases}, \quad (4.34)$$

where  $x'$  is the shortest distance to the edge of the fence,  $L_f$  is the length of the fence and  $\delta$  is a constant that defines the smoothing. For arbitrarily small but finite  $\delta$ , a smooth solution and numerical convergence can be achieved. In this thesis a value of  $\delta = 1/40$  is generally used. It is anticipated that in future work a value of  $\delta$  may be informed from more

detailed modelling of tidal devices orientated within a fence, whereby a physical reduction in depth change is expected towards the edge of the fence.

### 4.5.3 Example Calculations

#### 4.5.3.1 Steady Flow Through a Tidal Fence: Simple Scenario

Two examples were used to test the algorithm in Section 4.5.2. The first considered the simple scenario of a fence in a confined channel shown in Figure 4.4(a), with the location of a turbine fence illustrated by the vertical line down the middle of the domain. The extent of the channel was 400 m×1000 m and the depth was set to 10 m. A constant volume flow rate was used at the upstream (left) boundary (increasing gradually from 0 to full flow rate over 2000 s) and the downstream (right) boundary depth was held fixed at 10 m. The bed friction coefficient was set to  $C_d = 5 \times 10^{-3}$ .

To test the algorithm over different parameter values several flow rates were simulated, giving a range of Froude numbers. The momentum sink of the fence was defined by specifying the depth change across the fence using a polynomial approximation (both a linear approximation and a 10th order polynomial approximation without odd terms) to the depth change implied by LMADT (Equation 4.31) for a specified fixed blockage ratio, wake induction factor  $\alpha_4$ , and the simulated local Froude number immediately upstream of the fence at each computational point.

Figure 4.4 (b) illustrates the depth discontinuity at steady state. A comparison of this simulated depth change, to that intended for the momentum sink based on the simulated Froude number, is shown in Figure 4.4 (c). It is evident that in each case the numerical algorithm simulates the specified depth change satisfactorily at steady state. Figure 4.4 (d) illustrates that this is also the case prior to steady state.

#### 4.5.3.2 Steady Flow Through a Tidal Fence: Unbounded Scenario

The second example considers a tidal fence that does not extend over the full width of the channel. The example numerical domain is shown in Figure 4.5 (a) with the turbine fence located symmetrically around the horizontal centerline of the channel and extending one quarter of the channel width. The extent of the channel was 4 km×10 km and the depth was set to 1.0 m with a bed friction coefficient of  $C_d = 5 \times 10^{-4}$ . Again a constant

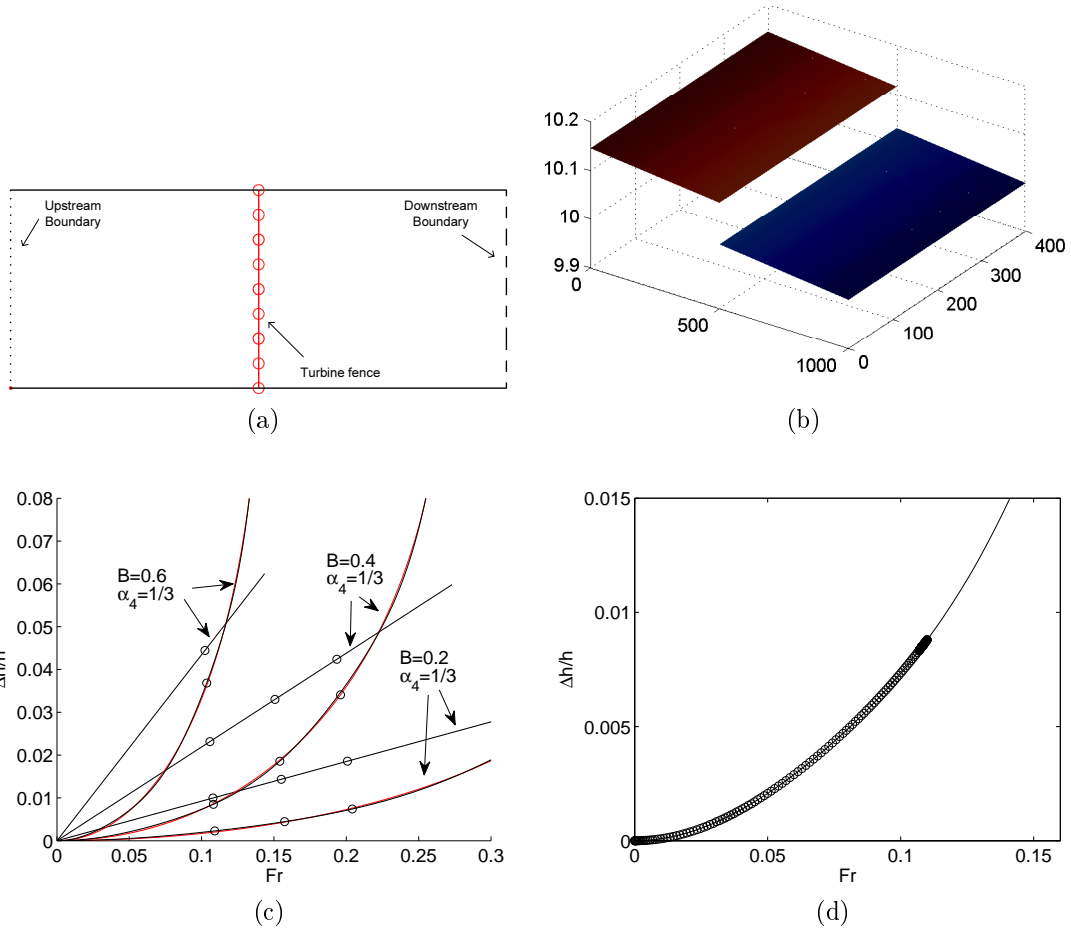


Figure 4.4: (a) Numerical domain with a central line of turbines modelled as a line sink of momentum. (b) Example solution for depth at steady state: the discontinuity in depth is evident across the turbine fence. (c) Linear and 10th order polynomial approximations to the depth change, as a function of Froude number, implied from LMADT for various blockage ratios and wake velocity coefficients (full LMADT solution shown in red). The circles represent simulated depth changes across the discontinuity in the numerical model at steady state. (d) Variation of depth change with Froude number across the line sink at various times prior to steady state. Circles represent simulated depth change and solid line a 10th order polynomial used to define the line sink.

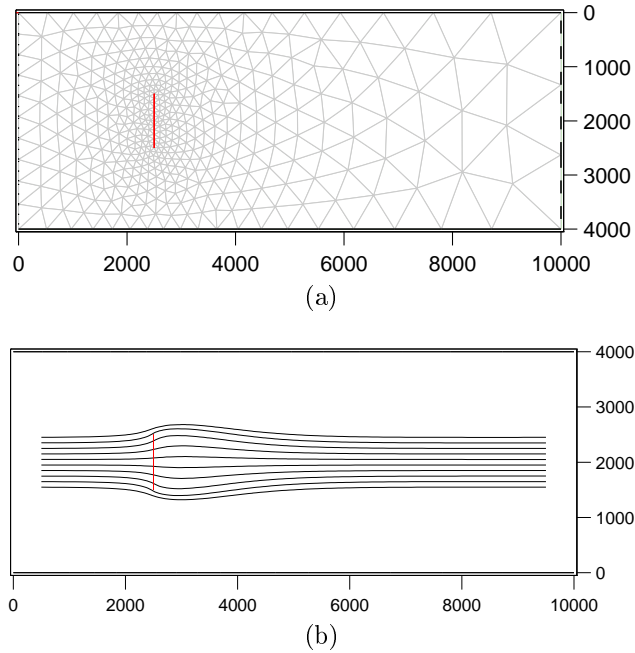


Figure 4.5: (a) Numerical mesh used for the unbounded turbine fence. (b) Example streamlines through a turbine fence with devices having blockage  $B = 0.6$  and  $\alpha_4 = 1/3$ . The channel has  $C_d = 5E - 4$ ,  $h = 10$  m and a turbine blockage ratio within the fence of 0.6.

volume flow rate was used at the upstream (left) boundary (increasing gradually from 0 to full flow rate over 10000 s) with the flow rate set to give an upstream Froude number of approximately 0.15. The downstream (right) boundary depth was held fixed at 1.0 m. Devices within the turbine fence were characterised by  $\alpha_4 = 1/3$  and a blockage ratio of 0.6, and the depth change across the fence, as a function of the simulated Froude number, was specified using a 10th order polynomial approximation to LMADT. A value of  $\delta = 1/40$  was used to smooth the singularity at the edges of the fence (see Equation 4.34).

The effect of the momentum sink on the local flow at steady state is illustrated in Figure 4.5 (b), which presents streamlines through the fence when elements of order  $n = 5$  are used. In this particular example the streamlines are steady and contract smoothly downstream of the device because the bed friction is sufficiently high to avoid wake instability. At higher blockage or lower bed friction an unsteady wake results (not shown). Figures 4.6 (a) and (b) illustrate the depth change across the fence, with the latter figure comparing the simulated depth change to that intended for the momentum sink based on the simulated Froude number along the fence. The agreement is satisfactory. The power extracted by the fence and the flow rate through the fence are shown in Figures 4.6 (c) and (d) for various polynomial order  $n$ . Convergence under  $n$  refinement is evident.

It is interesting to note that the flow field in Figure 4.5 looks very similar to that

assumed for an actuator disc in a constant volume flow field in Chapter 2, where the disc represents the entire fence. It is therefore interesting to compare the power extracted by the entire fence in the channel to the power predicted by that theory. Taking the blockage ratio to be  $B = 0.25$ , which is the ratio of fence to channel width, the theory in Chapter 2 predicts a maximum power coefficient of 1.05 at which point the average velocity through the disc is 0.53 of that in the upstream flow. The comparable values for the simulated fence are 1.3 and 0.64 (where the velocity through the fence is the value immediately upstream of the fence, averaged along the fence). The simulated power extracted by the fence is therefore higher than the maximum predicted by the theory. The reason for this additional power is due to bed friction, which helps to retard the bypassing of fluid around the fence and thereby allows for a greater extraction of power. This conclusion was confirmed by reducing the bed friction to  $C_d = 1 \times 10^{-5}$  and repeating the simulation for device blockage ratios of  $B = 0.5$ , 0.6 and 0.7. The total power extracted by the fence as a function of the flow rate through the fence for these cases is plotted in Figure 4.7 when  $t = 80000$  s. At this point in time the extracted power was still oscillating around the values shown in Figure 4.7, but only with a variation of  $\pm 0.05 \times 10^4$  W. The simulated extracted power is in reasonable agreement with theory.

## 4.6 Open Boundary Conditions

Artificial boundaries that separate a numerical coastal domain from a connecting body of water are commonly referred to as open boundaries. In coastal hydrodynamic models it is common to specify fixed time series elevations, obtained either from a larger numerical model or observations, along these open boundaries (Blayo and Debreu [2005]). However, as pointed out by Garrett and Greenberg [1977], if a substantial disturbance occurs within the coastal region, due to the operation of tidal devices for example, then the elevations and fluxes across the open boundary will alter from those in the undisturbed state. In that case an allowance needs to be made at the open boundary to accommodate these changes. If no correction is made, gross errors may occur when the disturbance excites a resonant mode within the coastal domain (Rainey [2009]).

Provided the disturbances at the edge of an open boundary are of small amplitude

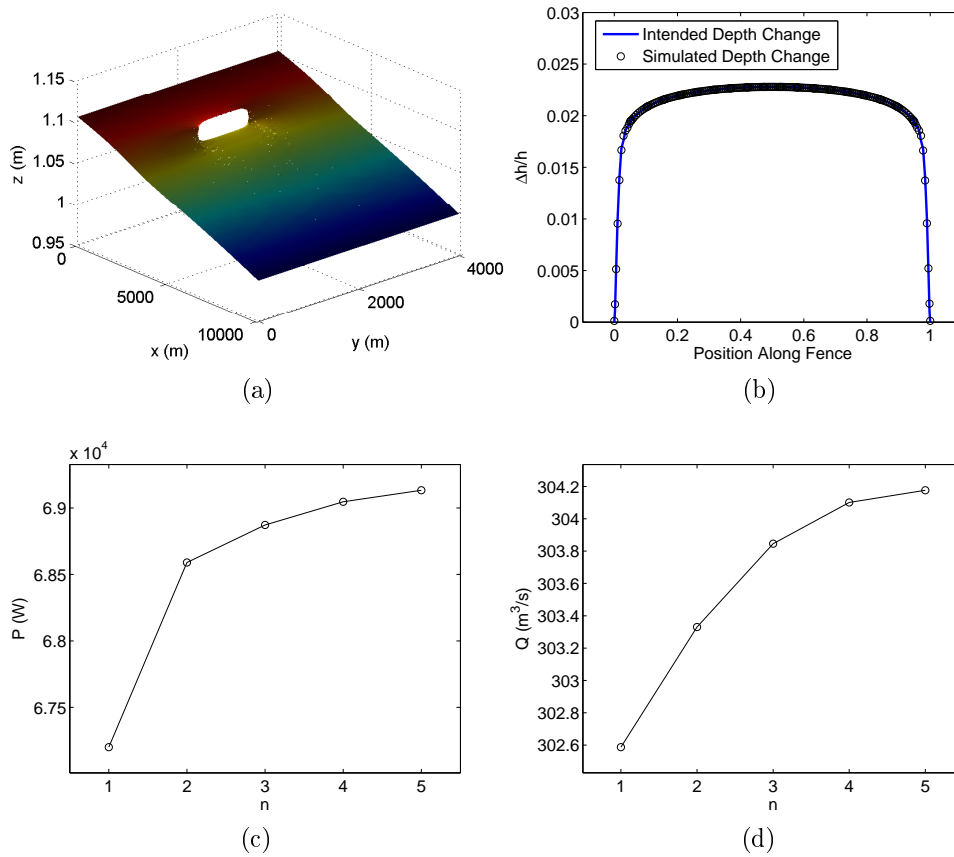


Figure 4.6: (a) 3D view of the depth in the channel. (b) Simulated depth change along the fence. (c) Power extracted by the fence for various polynomial orders  $n$ . (d) Total flow rate through the fence for various polynomial orders  $n$ .

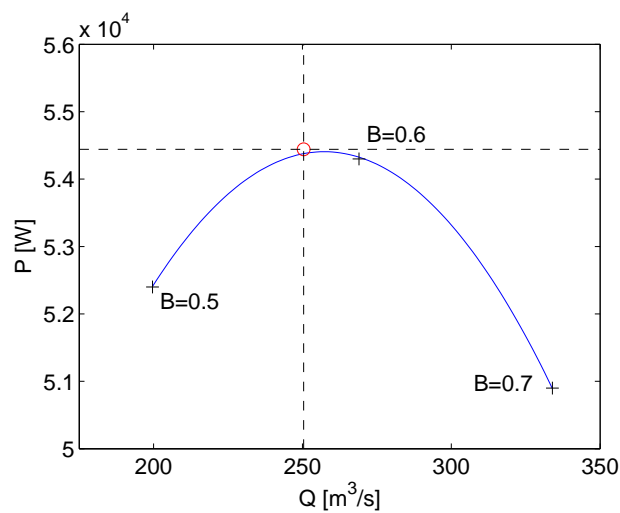


Figure 4.7: (a) Total extracted power by the fence in Figure 4.5 (a), for three different device blockage ratios when the bed friction was set to  $C_d = 1 \times 10^{-5}$ . The red circle indicates the predicted power extraction based on LMADT, taking the entire fence to be an actuator disc in a constant volume flow.

relative to fluid depth (i.e. linear) it is useful to consider the solution at the open boundary as the sum of two parts: (i) an elevation and velocity time series that represents the natural conditions at the boundary of the coastal domain, and (ii) deviations from the natural boundary conditions that result when artificial changes are made within the coastal domain. In practice Part 2 is neglected if the numerical model is only used to simulate natural tides or when it is argued that the open boundary is located in very deep water (Figure 4.8(a)) compared with the location of the disturbance. This second argument follows from the theory of long wave propagation over a large abrupt depth change, where propagating scattered waves from a coastal disturbance into deeper water will have very low transmission coefficient across the step, and so have minimal effect on the natural elevations and fluxes at the open boundary (see Mei [1989] and the discussion by Arbic and Garrett [2009]).

In the absence of a significant continental shelf, as shown in Figure 4.8(b), or for cross-shelf boundaries, a more general approach is required to account for both Parts 1 and 2. Provided that the boundary separates the numerical domain from a semi-infinite connecting ocean of constant depth then an appropriate boundary treatment is one that will absorb, or radiate, the Part 2 component (Chapman [1985], Martinsen and Engedahl [1987] and Rainey [2009]). Numerical implementation of this radiation condition is discussed in Section 4.6.0.4, and a clamped boundary condition, suitable when Part 2 is negligible, is discussed in Section 4.6.0.3.

For more general situations, where the connecting ocean is neither constant in depth or semi-infinite, the specification of numerical boundary conditions can become ambiguous. For example, if the connecting ocean is not constant in depth then scattered waves due to Part 2 might reflect from depth discontinuities external to the numerical domain and re-enter the shallow coastal region. If the connecting ocean is not semi-finite (as is indeed the case in the real world) disturbances due to Part 2 may excite the normal modes of the finite ocean (see Garrett and Greenberg [1977] for further discussion). In either of these two situations a larger numerical model would be required.

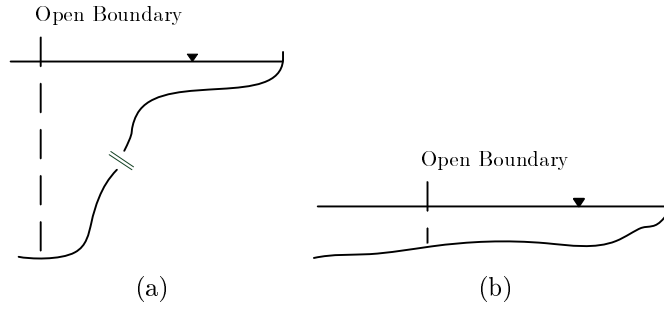


Figure 4.8: The open boundary for two hypothetical coastal regions. (a) Open boundary located in the deep ocean bounding a shallow shelf. (b) Open boundary located adjacent to an ocean of moderate and constant depth.

### 4.6.0.3 Clamped Boundaries

Boundary conditions in the DG formulation enter weakly through the evaluation of the numerical flux. At an open boundary specification is required of the depth and velocity components exterior to the numerical domain (see Appendix B.1.5). These exterior values will be referred to as  $\mathbf{U}_b = (h_b, u_b h_b, v_b h_b)^T$ .

For a clamped boundary consider, for example, a prescribed time series of depth  $h(\mathbf{s}, t)$ , where the open boundary is defined along a positively orientated (anti-clockwise) curve  $\mathbf{s}$  and the flow is sub-critical. At a discrete point  $\mathbf{s}(b)$  along  $\mathbf{s}$ , the velocity normal to the boundary can be calculated from the numerical solution inside the domain and the assumption of either mass conservation (see, for example Aizinger and Dawson [2002]), or, the conservation of the Riemann invariant along the right going characteristic line normal to the boundary (see, for example Liang and Borthwick [2009] and Figure 4.9). Pursuing the second of these options the external boundary condition at a particular computational time step  $t_i$ , becomes

$$h_b = h(\mathbf{s}(b), t_i) \quad \text{and} \quad \bar{u}_b = \bar{u}_{in} + 2 \left( \sqrt{gh_{in}} - \sqrt{gh_b} \right). \quad (4.35)$$

This will ensure that the computed depth at the boundary is clamped to the prescribed time series. In a similar manner the flow rate, velocity or another useful quantity, could be clamped at the boundary.

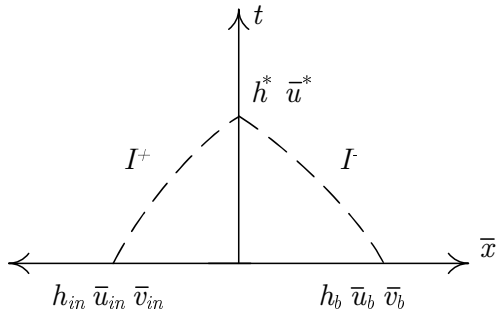


Figure 4.9: 1D Riemann problem in the direction  $\bar{x}$ , directed outward normal to the computational boundary. The subscript *in* refers to the solution within the boundary, and *b* refers to the specified values external to the boundary.

#### 4.6.0.4 Radiation Boundaries

A substantial body of literature has been established on the use of radiation, or open, boundary conditions for hyperbolic and parabolic systems. Two particular numerical approaches have seen significant development. The first includes characteristic-based boundary conditions, shown by Blayo and Debreu [2005] to be consistent with, for example, radiation methods based on the Sommerfeld condition, characteristic invariants and the Flather [1976] condition (also see Chapman [1985] and the references cited therein). The second approach consists of absorbing layers such as Perfectly Matched Layers (PML) and Flow Relaxation Schemes (FRS) (see Martinsen and Engedahl [1987], Lavelle and Thacker [2008] and the references cited therein). In the present work a characteristics-based approach has been adopted and will be discussed here.

Ignoring source terms in the vicinity of the boundary, a set of Riemann invariants  $I^\pm = \bar{u} \pm 2\sqrt{gh}$  exist along the projected characteristic lines normal to the boundary (Figure 4.9). If advective terms are also ignored, as is appropriate in deep water or when the disturbances are of small amplitude, these invariants further reduce to  $\bar{u} \pm (h - h_o)\sqrt{g/h_o}$ , where  $h_o$  is the mean water depth. Thus for a positively orientated boundary  $I^+ = \bar{u}_{in} + (h_{in} - h_o)\sqrt{g/h_o}$  then defines the information leaving the numerical domain and  $I^- = \bar{u}_b - (h_b - h_o)\sqrt{g/h_o}$ , the information entering. An important observation, and the basis for the accuracy of the characteristics approach used here, is that linear waves propagating out of the domain normal to the boundary will not contribute in any way to  $I^-$ . This is simply because the velocity of a linear wave traveling normal to the boundary is given by  $\bar{u}_b = (h_b - h_o)\sqrt{g/h_o}$  so that its contribution to  $I^-$  once it leaves the computational domain is zero. A practical approach to the boundary condition is therefore to specify  $\bar{u}_b$  and  $h_b$  using Part 1 of the

solution at the boundary only, because any superimposed normal radiating waves will not effect the computation of  $I^-$  (in practice the Part 1 values could be obtained by (a) first running a simulation without any disturbance using a boundary condition clamped to known elevations so as to obtain the Part 1 fluxes, or (b) as may be appropriate in very deep water, by simply setting  $h_b$  equal to the observed elevation and  $\bar{u}_b = \bar{v}_b = 0$ ). Following changes to the internal domain additional scattered waves will then exit through the boundary and, crucially, if these waves are propagating close to normal to the boundary, they will radiate efficiently.

For small amplitude disturbances this characteristic boundary condition is consistent with the well known Flather condition (Flather [1976]), which has been shown to produce satisfactory results for a wide variety of coastal problems in practice (see, for example, Nycander and Doos [2003]).

## 4.6.1 Example Calculations

### 4.6.1.1 Radiation in 1D

The first test problem undertaken was similar to that adopted by Modave et al. [2009] and simulates the radiation of an initial Gaussian mound having the form

$$\xi(x, y, t) = \exp[-(x + L/4)^2/(3h)^2] \quad \text{and} \quad u(x, y, 0) = \xi(x, y, t)\sqrt{g/h_o},$$

in otherwise still water of depth  $h_o = 100$  m, defined in a domain  $(x, y) \in [-L, 0] \times [0, L/10]$ , where  $L = 1000$  km. The left boundary of the domain ( $x = -L$ ) was set as a reflective boundary and at the right boundary of the domain ( $x = 0$ )  $\bar{u}_b = h_b = 0$ . A structured triangular mesh with  $h_m = L/20$  was adopted. The purpose of the test was to determine the effectiveness of the characteristic boundary condition to radiate waves out of the domain. The energy density within the domain at any time is

$$E = \int_{-B/2}^{B/2} \int_{-L/2}^0 \left( \frac{1}{2}g\xi^2 + \frac{1}{2}hu^2 \right) dx dy. \quad (4.36)$$

An exact solution will have zero energy in the wake of the radiated wave. It is clear in Figure 4.10 that the boundary condition works satisfactorily. The  $L2$  norm of the energy  $E$  at

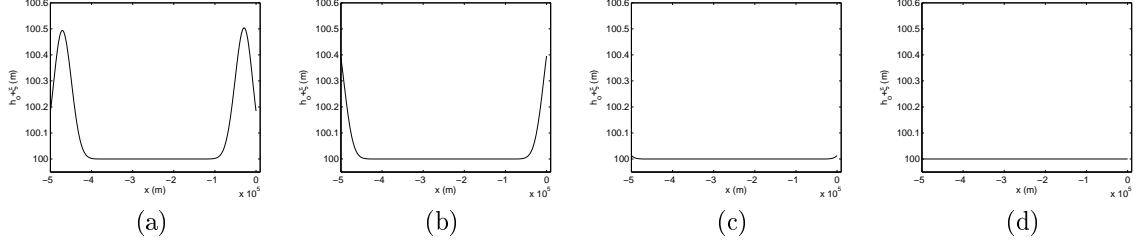


Figure 4.10: Snapshots of a radiating wave computed using the characteristic boundary condition ( $n = 3$ ). (a)  $t = 0.44t_f$ , (b)  $t = 0.53t_f$ , (c)  $t = 0.61t_f$ , (d)  $t = 0.70t_f$ .

$t_f = (L/2)/\sqrt{gh}$  is  $1.85 \times 10^{-2}$ ,  $1.98 \times 10^{-5}$ , and  $2.08 \times 10^{-8}$ , for  $n = 1, 2$  and  $3$ , respectively.

This indicates spectral convergence towards the true solution with polynomial refinement.

#### 4.6.1.2 Harbour Resonance

This test problem considers the response of a rectangular bay of constant depth to an incoming wave  $\xi_i = (A/2)\cos(kx + \omega t)$ , where  $k = \omega/\sqrt{gh_o}$  is the wave number and  $h_o$  is the depth (see Figure 4.11(a) for geometry). An approximate analytical solution to this problem, valid for small amplitude linear waves, has been obtained by several authors (see, for example, Miles [1971], Mei [1989]). Using the method of matched asymptotic expansions Mei [1989] gives

$$\xi = \operatorname{Re} \left\{ A\Lambda_1 \cos(k(x+L))e^{-j\omega t} \right\} \quad \text{for } x < 0, \quad (4.37)$$

$$\xi = \operatorname{Re} \left\{ \left( A\cos(kx) + A\Lambda_2 H_0^{(1)}(k\sqrt{x^2 + y^2}) \right) e^{-j\omega t} \right\} \quad \text{for } x > 0, \quad (4.38)$$

where  $H_0^{(1)}$  is a zero order Hankel function of the first kind, and

$$\Lambda_1 = \frac{1}{\cos(kL) + (2ka/\pi)\sin(kL)\ln(2\gamma ka/\pi e) - jkasin(kL)}, \quad (4.39)$$

$$\Lambda_2 = \Lambda_1 jkasin(kL). \quad (4.40)$$

The second term in Equation 4.38 represents a scattered wave radiating from the mouth of the bay with an amplitude that is a function of the incoming wave frequency. To accurately simulate the bay response over a range of frequencies this radiated wave must be allowed to propagate through the open boundary. To model the problem using the DG method the mesh depicted in Figure 4.11(b) was used. The bay had geometry  $a/L = 0.1$ , the water depth was set to  $h_o = 10$  m and  $A/h_o = 2.5 \times 10^{-3}$  to ensure small amplitude (linear)

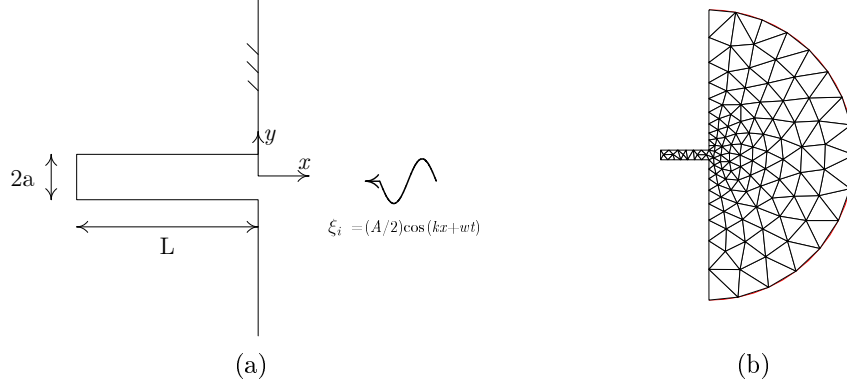


Figure 4.11: (a) Geometry for the harbour oscillation validation test and (b) Example numerical mesh.

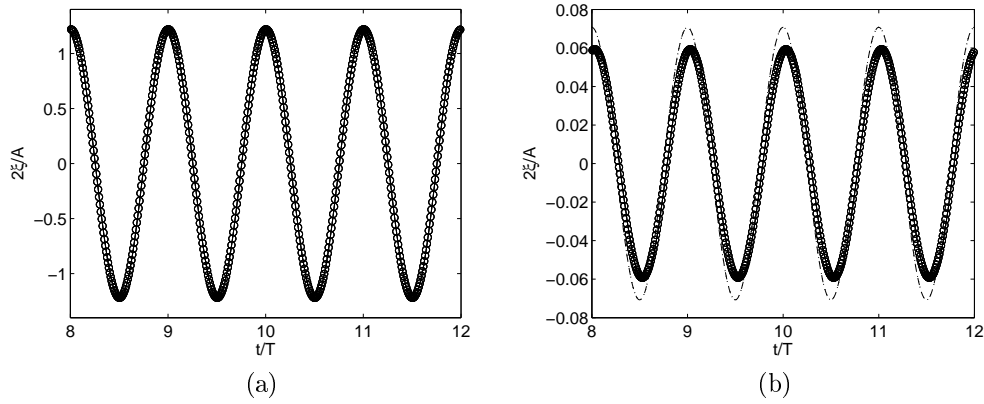


Figure 4.12: Elevation time series at (a) the end of the bay  $(-L, 0)$ , and (b) at the open boundary  $(R, 0)$ , when  $kL = 0.5$ . Approximate analytical solution: solid line; numerical solution: circles. The solution  $(h_b, u_b)$  that would exist without the harbour present is shown as the dashed line in figure (b).

behavior. The radius of the curved outer boundary of the numerical mesh  $R$ , was normally set to  $3L$  and the depth and velocity normal to the boundary were set to

$$h_b = h_o + \text{Re} \left\{ A \cos(k(x + L)) e^{-j\omega t} \right\}, \quad u_b = \text{Re} \left\{ \frac{jgk}{\omega} A \sin(k(x + L)) e^{-j\omega t} \right\}, \quad v_b = 0, \quad (4.41)$$

to define the elevation and velocity that would exist at the boundary in absence of the rectangular bay. Consequently this simulation tests the ability of the characteristic boundary condition to radiate scattered waves associated with the existence of the bay. The remaining coastal boundaries were treated as slip reflective walls.

Figures 4.12 (a) and (b) compare the free surface elevation for  $kL = 0.5$  at two locations within the domain: the end of the bay  $(-L, 0)$  and the open boundary  $(0, R)$ . Agreement between the numerical model and the approximate analytical solution is satisfactory in

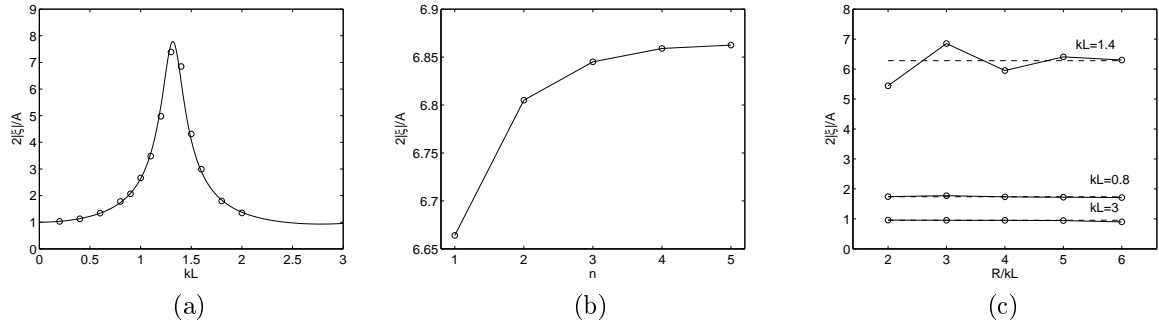


Figure 4.13: (a) Response curve for the harbour oscillation test problem. Solid line: approximate analytical solution; Circles: numerical solution. (b) Numerical convergence under  $n$  refinement for  $kL = 1.4$ . (c) Bay response as a function of the location of the open boundary condition. Dashed line: approximate analytical solution; Circles Numerical solution.

both examples. As required, the elevation at the open boundary differs from the externally prescribed values to account for the radiation of the scattered wave from the harbour mouth. Figure 4.13 compares the numerical results with the analytical solution for various length of bay. The simulations and the analytical solution agree well over most of the response curve. Close to the first resonant mode there is small disagreement, even after refinement and convergence of the numerical solution (Figure 4.13(b)). However exact agreement is not expected given that the approximate analytical solution assumes  $ka \ll 1$ .

The results presented in Figure 4.13 (a) should, of course, be independent of the placement of the open boundary. Figure 4.13 (c) presents the bay response when the open boundary is located at several different distances from the mouth of the bay. There is variation in the bay response, especially for the bay closest to resonance ( $kL = 1.4$ ). Far from resonance, the convergence properties are better (i.e.  $kL = 0.8, 3$ ). The channels, bays and headlands modelled numerically in the remaining chapters constitute systems that are far from resonance and so the present boundary condition will be satisfactory.

## 4.7 Conclusions

The solution of the SWEs using the DG method has been outlined and a numerical solver developed to simulate tidal hydrodynamics in coastal basins. Extensive validation of the numerical solver has been undertaken for linear, non-linear and viscous test problems, with the results presented in Appendix B. The validation tests highlight the excellent properties

of the DG method. The importance of open boundary conditions in numerical simulations of tidal energy extraction have been discussed and a characteristic based open boundary condition has been shown to give satisfactory results for 1D and 2D test problems.

A new method to introduce fences of tidal devices into a depth-averaged numerical model has been implemented numerically as a line sink of momentum. An appealing aspect of this new method is that the properties of the tidal devices can be related, by LMADT, to the actual momentum sink imparted in the coastal basin. It is however acknowledged that experimental or numerical verification is required for this new approach.

# Chapter 5

## Tidal Channel

### 5.1 Introduction

This chapter begins with a summary of the tidal channels in Appendix A and a review of the existing literature concerning the analysis of energy extraction from a tidal channel. Numerical simulations are then presented for an idealised tidal channel with energy extraction introduced, as discussed in Chapter 4, using a line sink of momentum to represent a fence of devices modelled using actuator disc theory. The simulation results show that the maximum extracted power is achieved for a range of device blockage ratio and wake velocity coefficient, however the available power is maximised if the devices have large blockage ratio and a high wake velocity coefficient (i.e. large, closely packed turbines slowing a large cross-section of tidal stream). Simulations are also presented for variable channel geometry and for multiply connected channels, with the extracted power interpreted in the latter case using an electrical analogy. Overall, the maximum simulated energy extraction is in good agreement with a theoretical model due to Garrett and Cummins [2005] for isolated channels over the full range of channel dimensions. For multiply connected channels the model of Garrett and Cummins [2005] is less appropriate and an alternative model is presented which is more applicable when the total flow rate through the multiply connected channels is largely unaffected by the introduction of a tidal fence.

## 5.2 Tidal Channel Sites

A significant number of the coastal sites surveyed in Appendix A resemble a tidal channel connecting two bodies of water which oscillate with different phase or amplitude. These channels are generally narrow (Figure 5.1 (a)), vary over an order of magnitude in length and have a natural Froude number in the range 0.1-0.3 (Figure 5.1 (b)). To summarise the basic dynamics within each channel the flow through the channel can be considered one dimensional so that the shallow water momentum equation reduces to

$$-g \frac{\partial \xi}{\partial x} = \frac{\partial u}{\partial t} + u \frac{\partial u}{\partial x} + \frac{C_d |u| u}{h}, \quad (5.1)$$

where  $x$  is the along channel coordinate,  $u$  is cross-sectional average channel velocity,  $\xi$  is the free surface height above mean water level and  $C_d$  is the depth-averaged drag coefficient. Consequently, if the velocity within the channel has a characteristic maximum  $U$ , and varies from this maximum to zero over the length of the channel  $L$  and over a tidal period proportional to  $\omega^{-1}$ , simple scale analysis can be used to determine the importance of the terms on the right hand side of Equation 5.1,

$$-g \frac{\partial \xi}{\partial x} = \underbrace{U \omega \frac{\partial u'}{\partial t'}}_A + \underbrace{\frac{U^2}{L} u' \frac{\partial u'}{\partial x'}}_B + \underbrace{\frac{U^2 C_d |u'| u'}{h_d}}_C, \quad (5.2)$$

$$(5.3)$$

where  $h_d$  is the mean depth in the channel and the terms involving primes are of order one. The three terms on the right hand side of Equation 5.2 balance the surface slope on the left hand side, which drives flow through the channel. The ratio of the relevant right hand terms is given by

$$\frac{A}{B} = \frac{1}{K_c} = \frac{\omega L}{U}, \quad \text{and} \quad \frac{C}{B} = C'_d = \frac{C_d L}{h_o} \quad (5.4)$$

The first of these two ratios explains the importance of acceleration relative to advection in balancing the seabed slope within a channel of length  $L$  and depth  $h_o$  and is equal to the inverse of the Keulegan Carpenter number  $K_c$ . The second ratio explains the importance of seabed friction relative to advection and describes an effective bottom drag  $C'_d$ , or stability number (Jirka [2002], Signell and Geyer [1991]). Figure 5.1 (c) plots these dimensionless numbers for each of the channels surveyed in Appendix A. There is a good scattering over

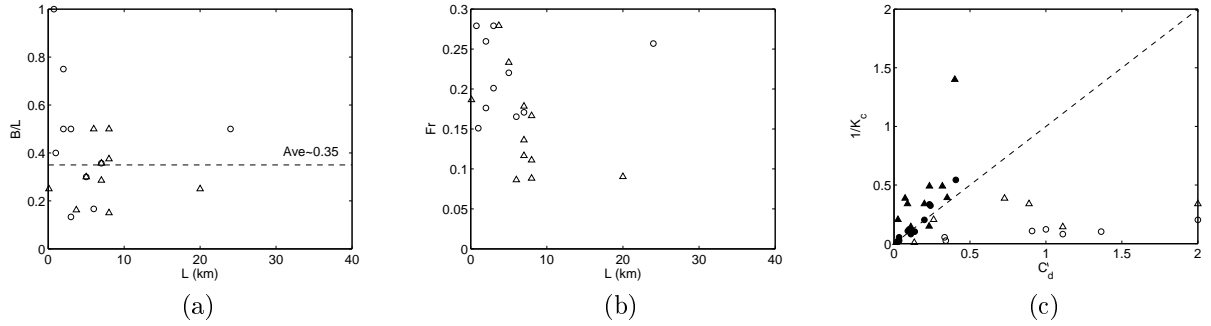


Figure 5.1: Summary of class a tidal sites in Appendix A. (a) Aspect ratio and geometry. (b) Froude number as a function of channel length. (c) Key dimensionless numbers. The solid and hollow markers assume  $C_d = 0.001$  and  $0.01$ , respectively. North American sites (triangles), UK sites (circles). Where both Spring and Neap tides are listed in Appendix A, Spring tides are used.

both ratios, indicating that tidal energy extraction may occur at sites with moderate acceleration and drag ( $1/K_c \gtrsim 0.5$ ,  $C'_d \gtrsim 0.5$ ), significant drag forces ( $1/K_c \lesssim 0.5$ ,  $C'_d \gtrsim 0.5$ ), and advection dominated flow ( $1/K_c \lesssim 0.5$ ,  $C'_d \lesssim 0.5$ ). The last two of these regimes describe quasi-steady flows, in which acceleration is unimportant and the time varying head difference across the tidal strait is in phase with the velocity.

## 5.3 Background

### 5.3.1 Early Analysis and Resource Assessments

Early analysis of energy extraction from a channel between two large bodies of water focused exclusively on quasi-steady flow (see Bryden et al. [2005], Bryden and Couch [2006, 2007] and Bryden et al. [2007]). In that work the one dimensional momentum and continuity equations were used, in the quasi-steady limit, to define the steady flow rate  $Q$  within a uniform rectangular channel. The effects of energy extraction were considered as a simple bed roughness, modelled as a fraction of the local kinetic flux over an increment of channel length, and the inlet and outlet of the channel were assumed to conserve energy and depth, respectively.

Figure 5.2 (a) illustrates an example solution for the depth and velocity along a channel with energy extraction calculated by Bryden et al. [2005]. A visible result is that the extraction of energy leads to an increase in “speed” and kinetic energy across the extraction zone, which is consistent with a reduction in specific energy in an open channel flow (Chapter 2;

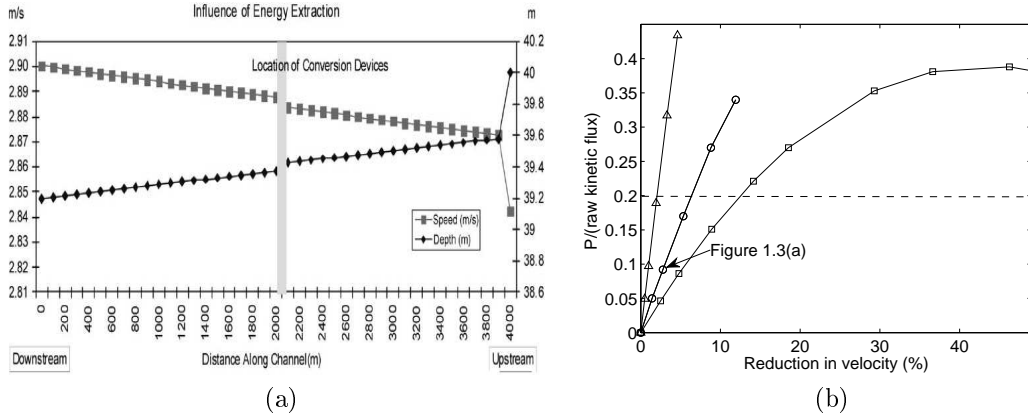


Figure 5.2: (a) Depth and velocity in a steady channel when 10% of local kinetic energy is extracted by a device. Channel dimensions given in Bryden et al. [2005]. (b) Reduction in flow rate as a function of extracted power. Solid-circle: channel displayed in subfigure (a); Solid-triangle: as in (a) but with 4 times the channel length and 15% larger bed roughness. Solid-square: as in (a) but with one quarter the channel length and 40% smaller bed roughness.

Young et al. [2001]). To investigate the effect of energy extraction on the natural velocity within the channel Figure 5.2 (b) plots various levels of power extraction, normalised by the *raw* kinetic flux (raw implying flux in the undisturbed channel) against the reduction in average velocity within the channel. The variation in power extraction is achieved by varying the amount of local kinetic flux removed over the extraction zone. As noted by Bryden et al. [2005] the velocity within the channel reduces below that of the undisturbed state as energy extraction increases.

Based on these results Bryden et al. [2005] suggested that 10% of the raw undisturbed kinetic flux could be extracted “without causing undue modification to the flow characteristics”. Black & Veatch Ltd [2005] assumed that up to 20% of the raw kinetic flux could be extracted from a number of different coastal sites and used this estimate, or Significant Impact Factor (SIF), to calculate that the tidal resource potential of UK coastal waters is  $2.1 \pm 0.5$  GW.

Although the development of a SIF was a novel attempt to account for the feedback effect of tidal energy extraction on tidal streams, its use to estimate resource potential has been criticized by many authors (see, for example MacKay [2007b] and Garrett and Cummins [2005]). The main reason for this criticism is that there is no clear reason why the raw kinetic flux should provide any general indication of the maximum power that can be extracted from a channel or, perhaps more importantly, the change in flow rate

that results from energy extraction. The first of these deficiencies is discussed in the next section and demonstrated with numerical simulations in Section 5.4, whilst the second can be easily illustrated by considering two channels with slightly different parameters to that analysed by Bryden et al. [2005]. For example, using the model outlined in Bryden et al. [2005], Figure 5.2 (b) plots (i) a channel that is four times shorter with 40% small Manning bed roughness coefficient, and (ii) a channel that is four times longer with 15% larger Manning bed roughness coefficient. Substantially different changes in velocity result for an extraction of power equal to 20% of the natural kinetic flux. In particular, the long channel experiences flow reduction of 2% when extracting at the SIF, whereas the channel analysed by Bryden et al. [2005] and the short channel experience 6% and 13%, flow reductions.

### 5.3.2 Theoretical model due to Garrett and Cummins

An alternative theoretical model of energy extraction from a tidal channel has been developed by Garrett and Cummins [2005] (hereafter GC05). Unlike the quasi-steady analysis discussed above, this model accounts for a time varying tidal stream and is applicable to a channel of slowly varying cross-sectional area separating two large basins of water (Figure 5.3). To describe the flow within the channel the 1D shallow water approximation to the momentum equation is rewritten

$$\frac{\partial u}{\partial t} + u \frac{\partial u}{\partial x} + g \frac{\partial \xi}{\partial x} = -F_{GC}, \quad (5.5)$$

where  $F_{GC}$  is now a force, per unit mass, associated with bed friction and tidal devices. To form the model, GC05 assume (i) the channel length is short, compared to the tidal wavelength, so that the flow rate  $Q$  is constant with position along channel; (ii) the Froude number and tidal range are small so that, to the leading order, depth and velocity become functions of position only; (iii) the tidal elevations in the adjoining basins are unaltered by changes in the channel flow which result when turbines are added, and (iv) the channel length, or the cross-sectional area at exit, does not vary in time. Based on these assumptions Equation 5.5 can be integrated along the channel length to give

$$c \frac{dQ}{dt} - g\xi_o = - \int_0^L F_{GC} dx - \frac{1}{2} |u_e| u_e, \quad (5.6)$$

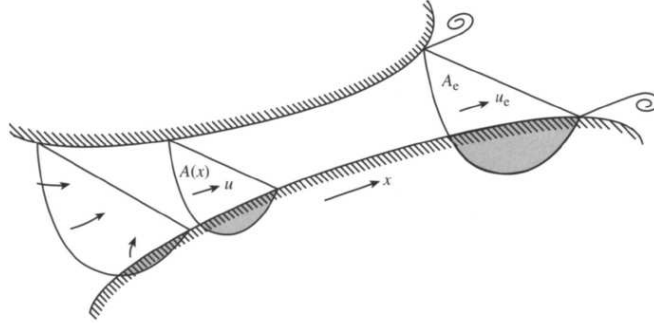


Figure 5.3: A channel connecting two basins with different elevations. Taken from Garrett and Cummins [2005].

where  $c = \int_0^L A_c^{-1} dx$ ,  $A_c(x)$  is the channel cross sectional area,  $\xi_o(t)$  is the sea level difference between the two adjoining basins (taken to be  $\xi_o = a \cos(\omega t)$ , where  $a$  is the amplitude of the tide and  $\omega$  is the frequency) and  $u_e$  is the exit velocity at the downstream end of the channel. The last term in Equation 5.6 arises from integration of the non-linear advection term in Equation 5.5 and the assumption that the tidal flow enters smoothly upstream and exits as a jet into the ocean. This term is effectively the velocity head (multiplied by  $g$ ) at the channel exit.

Within the channel the drag due to natural bed friction is modelled as  $C_d u^2/h$ , where  $C_d$  is the bed friction coefficient, and the force applied by tidal devices is, in the standard case, taken to be a function of the flow rate squared, so that

$$\int_0^L F_{GC} dx = \int_0^L \frac{C_d u^2}{h} dx + \int_0^L F_t dx = \left( \int_0^L \frac{C_d}{h} dx + \delta_1 \right) |Q| Q, \quad (5.7)$$

where  $F_t$  is the component of  $F_{GC}$  due to tidal devices and  $\delta_1$  is an arbitrary constant related to the devices. In this sense the devices are considered as a “roughness”, distributed arbitrarily over the tidal channel. The average power extracted over a tidal cycle is then

$$P = \rho Q \int_0^L F_t dx = \rho \delta_1 \overline{|Q| Q^2}, \quad (5.8)$$

and Equation 5.6 can be written as

$$g a \cos \omega t = c \frac{dQ}{dt} + (\delta_0 + \delta_1) |Q| Q, \quad \text{where} \quad \delta_0 = \int_0^L \frac{C_d}{h A_c^2} dx + \frac{1}{2} \left( \frac{1}{(A_c)_e} \right)^2. \quad (5.9)$$

The form of Equation 5.9 is physically meaningful, indicating that the driving head is balanced by a combination of acceleration and velocity head at the channel exit combined

with natural and artificial drag. GC05 introduce the non-dimensional variables  $t = \omega^{-1}t'$ ,  $Q = ga(c\omega)^{-1}Q'$ ,  $\delta_0 = \lambda_0(c\omega)^2(ga)^{-1}$  and  $\delta_1 = \lambda_1(c\omega)^2(ga)^{-1}$ , so that Equation 5.9 becomes

$$cost' = \frac{dQ'}{dt'} + (\lambda_0 + \lambda_1)|Q'|Q'. \quad (5.10)$$

Conveniently  $\lambda_0$  in Equation 5.10 now represents the ratio of drag losses and velocity head at exit to acceleration, normalised by the amplitude of the driving tide. The value of this term therefore defines the dynamic balance in the channel. In particular for large  $\lambda_0$  acceleration is relatively small and the flow is quasi-steady.

GC05 solve Equation 5.10 for all values of  $\lambda_0$  and determine the turbine drag parameter  $\lambda_1$  that optimizes the non-dimensional extracted power. Qualitatively a maximum exists because, for  $\lambda_1 = 0$  no turbine power is extracted, but for  $\lambda_1 \gg 1$  the flow is choked ( $Q' \rightarrow 0$ ), and again no power is extracted. Returning to dimensional variables, a convenient representation of the maximum average power available  $\bar{P}_{max}$ , is shown by GC05 to be

$$\bar{P}_{max} = \gamma\rho g a Q_{max}, \quad (5.11)$$

where  $Q_{max}$  is the peak flow rate over the tidal cycle in the undisturbed channel and  $\gamma$  is a multiplier that depends on  $\lambda_0$ , as shown in Figure 5.4(b). Equation 5.11 is a particularly useful representation of the extracted power because Figure 5.4 (a) shows that the range in  $\gamma$  is very small for most values of  $\lambda_0$ . GC05 point out that choosing a value of  $\gamma = 0.22$  provides a good approximation regardless of whether the channel is acceleration dominated ( $\lambda_0 \rightarrow 0$ ) or quasi-steady ( $\lambda_0 \gg 0$ ). However a more exact estimate can be obtained if the phase lag between the driving tide and the dominant harmonic of the peak flow rate is known (Figure 5.4(b)).

An important conclusion is that the form of the maximum average power, given by Equation 5.11, is not generally related in any simple way to the undisturbed kinetic flux in the channel, but rather the rate of work done by the driving tide. In fact GC05 note the maximum average power only becomes a constant fraction of the natural kinetic flux if the velocity head at exit is much larger than natural drag losses and acceleration (i.e. the channel is advection dominated). In this situation the natural driving amplitude is proportional to the velocity squared at the exit of the channel, based on simple energy

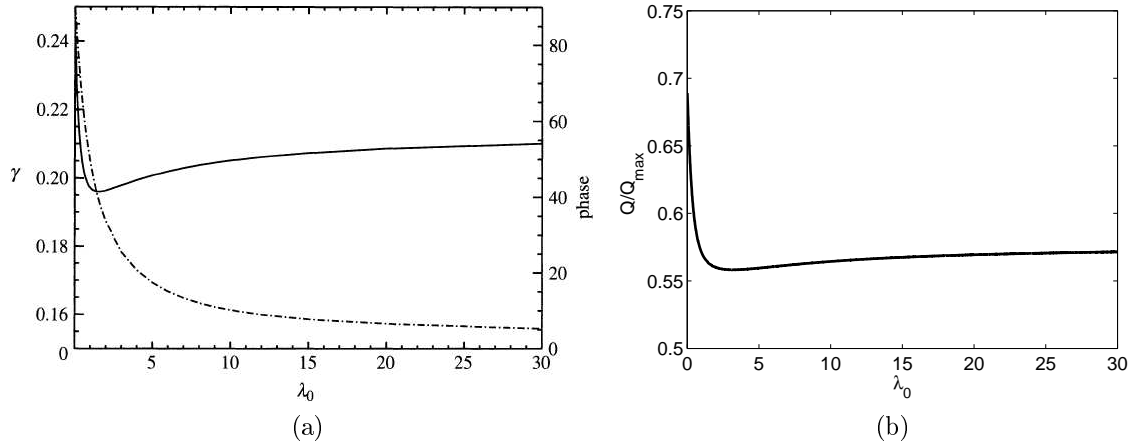


Figure 5.4: (a) Multiplier  $\gamma$  as a function of the non-dimensional natural drag  $\lambda_o$  (solid line). Phase lag between the forcing tide and the channel flow rate (dash line). Figure taken from Garrett and Cummins [2005]. (b) Flow rate at the point of maximum power extraction, normalised by undisturbed flow rate, as a function of the non-dimensional natural drag  $\lambda_o$ .

arguments, and GC05 show that

$$\bar{P}_{max} = 0.38 \left( \frac{1}{2} \rho (A_c)_e \overline{|u_e|^3} \right),$$

or 0.38 times the undisturbed flux at the end of the channel.

### 5.3.2.1 Including the Local Field in a Uniform Tidal Channel

The model of GC05 predicts the power that can be extracted from a channel as the drag due to turbines  $\lambda_1$  is varied. Garrett and Cummins [2007] suggest that this drag can be related to a fence (or fences) of tidal devices modelled using LMADT provided the channel walls are parallel and the flow is uniform and quasi-steady over the mixing length scale associated with the devices within the fence. Based on these assumptions Garrett and Cummins [2007] equate the thrust (per cross sectional area of channel) to that obtained for  $N$  rows of actuator discs, having a blockage  $B$  and operating at wake velocity coefficient  $\alpha_4$ ,

$$\int_0^L F_t dx = N \frac{C_T B}{2} u^2 = \delta_1 Q |Q|, \quad \text{where (c.f. Equation 2.19)} \quad C_T = \frac{(1 - B\alpha_2)^2}{(1 - B\alpha_2/\alpha_4)^2} - \alpha_4^2, \quad (5.12)$$

and (c.f. Equation 2.23)

$$\alpha_2 = (1 + \alpha_4) \left[ (1 + B) + \sqrt{(1 - B)^2 + B(1 - 1/\alpha_4)^2} \right]^{-1} \quad (5.13)$$

The power extracted is then compared directly with the power estimated from the theoretical model of GC05

$$\bar{P} = \rho Q \int_0^L F_i dx = N \frac{C_T B}{2} \rho A_C u^3, \quad (5.14)$$

The available power to the devices within the fence therefore follows from Equation 5.14 as,

$$\bar{P}_a = \eta \bar{P} = \alpha_2 \bar{P}. \quad (5.15)$$

This last result importantly establishes a link between the available and extracted power for tidal devices deployed within a tidal channel. It is surprising that Garrett and Cummins [2007] only explored this expression for devices operating at maximum power coefficient (i.e.  $\alpha_4 = 1/3$ ) and when the power extracted from the channel is a maximum. Under these conditions the available power is

$$\bar{P}_a = \alpha_2 \bar{P}_{max} = \frac{2}{3(1+B)} \gamma \rho g a Q_{max}. \quad (5.16)$$

Devices that operate at maximum power coefficient (i.e.  $\alpha_4 = 1/3$ ) are however not the most efficient (see Chapter 2). Efficient devices with large blockage and  $\alpha_4$  can introduce the same thrust as those at maximum power coefficient (i.e. the same  $C_T B/2$ ) and from Equation 5.14 the same power extraction, but recover more available power. This is discussed further in Section 5.4.1.3 and in Vennell [2010].

The application of LMADT assumed in Equation 5.14 requires that the Froude number is small, so that the drag force associated with the fence is quadratic in the flow rate. However, for the more realistic pressure-volume constrained analysis in Chapter 2 the thrust coefficient was shown to vary with Froude number, and so the drag force associated with tidal devices may not necessarily behave quadratically with the flow rate in a real tidal channel. This is also investigated further in Section 5.4.1.3.

### 5.3.3 Numerical Resource Assessment

Several site-specific numerical simulations of tidal energy extraction have been documented in the literature. Relevant to a tidal channel, Sutherland et al. [2007] studied energy extraction from tidal straits east of Vancouver Island, Canada, using a 2D depth-averaged model. In that study several scenarios are considered, including the extraction of energy from Johnstone Strait which provides a useful cross validation to the model of GC05 discussed previously. Using a uniform bed roughness to simulate energy extraction within the Strait, Sutherland et al. computed a maximum average power that agreed with Equation 5.11 to within 10%; the discrepancy being due to the slight increase in driving amplitude across the Strait following the addition of added roughness. In two further scenarios, energy extraction from multiply connected channels is investigated. Due to the ability of the flow to divert away from the channel with energy extraction, the simulated power was found to be significantly lower than predicted by the theory of GC05.

Idealised numerical modelling has also been undertaken by Bryden et al. [2007] and Polagye and Malte [2011]. In the first of these studies flow around an island is considered using a 2D numerical model. The results show that flow does indeed divert away from the channel with energy extraction, although no general conclusions are given. Polagye and Malte [2011] consider a range of 1D tidal channels including: serial constrictions, multiply connected networks and branching networks. A detailed comparison is made with the theoretical model of GC05 showing that generally the model is adequate for serial constrictions, although there is sensitivity to the tidal amplitude across the constriction with energy extraction. The model is again found to be less useful for multiply connected channels.

## 5.4 Numerical Simulations

### 5.4.1 Idealised Channel

To explore the relevance of the theoretical model of GC05 described in Section 5.3.2, and to investigate the available power for a turbine fence, numerical simulations have been undertaken using the idealised channel geometry illustrated in Figure 5.5. In total 12 cases are considered (see Table 5.1), covering the different channel geometries in Appendix A and

Case	$L$ [km]	$W$ [km]	$h_o$ [m]	$C_d$	$A$ [m]	$A/h_o$	$\sigma$	$Fr$	$\omega L/U$	$C_d L/h$
5-1	6	1.2	40	0.0025	0.7	0.01	52 <sup>o</sup>	0.21	0.25	0.375
5-2	6	1.2	80	0.01	1.75	0.02	20 <sup>o</sup>	0.15	0.2	0.8
5-3	6	1.2	25	0.0025	0.4	0.02	42 <sup>o</sup>	0.13	0.4	0.6
5-4	6	1.2	25	0.01	1.1	0.04	15 <sup>o</sup>	0.13	0.4	2.4
5-5	20	4	80	0.0025	1.5	0.02	68 <sup>o</sup>	0.11	0.90	0.625
5-6	20	4	80	0.01	4	0.05	28 <sup>o</sup>	0.13	0.75	2.5
5-7	20	4	35	0.0025	1.7	0.05	50 <sup>o</sup>	0.10	0.95	1.4
5-8	20	4	35	0.01	2.5	0.07	21 <sup>o</sup>	0.11	0.90	5.7
5-9	1	0.2	80	0.0025	0.5	0.01	34 <sup>o</sup>	0.19	<0.1	<0.1
5-10	1	0.2	80	0.01	0.6	0.01	14 <sup>o</sup>	0.16	<0.1	0.1
5-11	1	0.2	10	0.0025	0.15	0.02	15 <sup>o</sup>	0.21	<0.1	0.2
5-12	1	0.2	10	0.01	0.3	0.03	8 <sup>o</sup>	0.17	<0.1	1.0

Table 5.1: List of different test cases undertaken for the idealised channel geometry. In all cases  $R_i = W$  and  $\sigma$  is the phase lag of the flow rate behind the tidal forcing. The last three columns represent non-dimensional ratios in the channel prior to the installation of turbines, where  $U$  is the maximum velocity in the tidal channel and  $Fr = U/\sqrt{gh_o}$ .

a similar range in the dimensionless ratios  $K_c$  and  $C'_d$ . The different cases are grouped into intermediate (1-4), long (5-8) and short (9-12) channels, with each channel length allowing for variations in depth and bed friction coefficient.

In the numerical simulations the tide is introduced as a linear incident wave  $\xi_i = (A/2)\cos(\omega t - kx)$  at the left open boundary, where  $A$  would be the amplitude of the tide at  $x = 0$  if the channel did not exist and non-linear effects were negligible,  $k = \omega\sqrt{gh_o}$  is the wave number,  $h_o$  is the uniform mean depth, and  $\omega$  is the frequency of the tide, taken to be 0.00014 rad/s to represent the principal M2 component. To implement the tide numerically at the open boundary, the sum of the incident tidal wave and its reflection, in the absence of the channel, are specified using a characteristic non-reflecting boundary condition (i.e.  $h_b = h_o + A\cos(\omega t)\cos(kx)$ ,  $u_b = \sqrt{g/h_o}h_b$  and  $v_b = 0$ ). At the right open boundary  $h_b = h_o$  and  $u_b = v_b = 0$ . Each simulation commenced from quiescent initial conditions, with the amplitude of the incident wave ramped-up over two tidal periods according to

$$A(t) = A \left( -2 \left( \frac{t}{2T} \right)^3 + 3 \left( \frac{t}{2T} \right)^2 \right), \quad t < 2T, \quad (5.17)$$

where  $T = 2\pi/\omega$  is the tidal period. Generally 8 tidal periods were simulated, with steady periodic flow achieved typically after 3-4 tidal periods. Energy extraction was introduced with a line sink of momentum defined along  $x = L/2$ ,  $|y| \leq W/2$ , representative of a fence of tidal turbines extending completely across the channel. The amplitude of the incoming

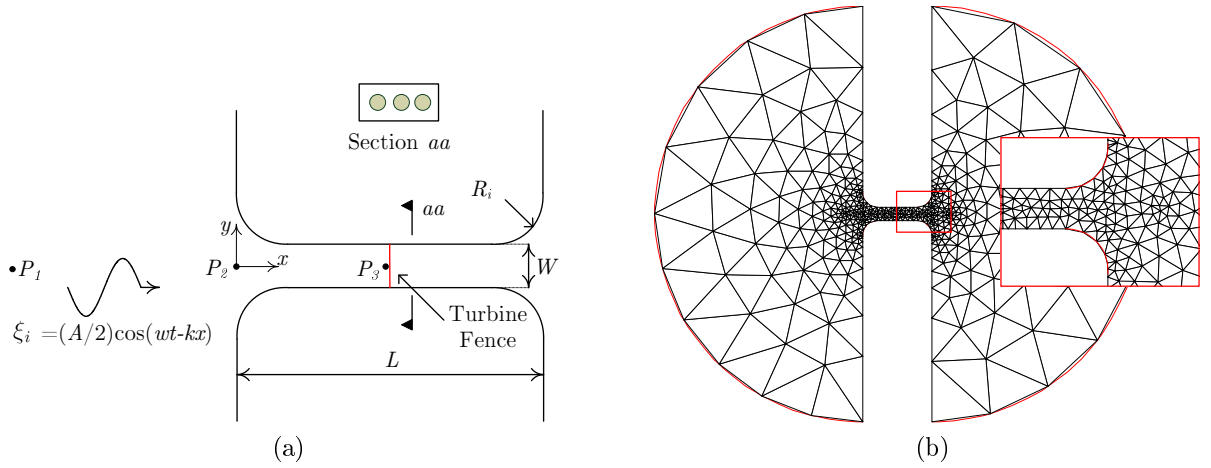


Figure 5.5: (a) Idealised geometry of a tidal channel. (b) Example numerical mesh. Elements of order  $n = 3$  were used. Curved isoparametric elements were adopted along the inlets of the channel and around the open boundaries (red lines). The open boundary is located a distance of  $4L$  from the opening of the channel and the  $P_1$ ,  $P_2$  and  $P_3$  are located at  $(-4L, 0)$ ,  $(0, 0)$  and  $(L/2, 0)$ , respectively.

tide was adjusted to ensure that the Froude number remained within the realistic range observed in Figure 5.1 (b). Bed friction and the seabed elevation were kept uniform over the domain. Coriolis acceleration was neglected (since most real channels are narrow). Viscous terms were omitted, based on the arguments in Chapter 3.

#### 5.4.1.1 Undisturbed Flow

The theoretical model of GC05 makes several assumptions about the natural flow through a tidal channel. To investigate these assumptions snapshots of the velocity component  $u$ , together with a profile of depth along  $y = 0$ , are presented at the point of high tide in the left basin in Figure 5.6 for cases 5-4,5,11 before devices are installed. These three cases are representative of moderate acceleration/drag, drag dominated and advection dominated tidal channels, respectively. In Figure 5.6 the velocity fields for cases 5-4 and 5-5 are similar, indicating smooth acceleration and deceleration of fluid into and out of the channel. In contrast, the velocity field in case 5-11 resembles more of an orifice-type flow with a prominent velocity jet at the channel exit. This implies advection of the flow at the channel exit and an associated loss of “velocity head” to the channel, as accounted for in the model of GC05. For all three cases the variation in velocity and depth throughout the uniform section of channel is small, implying that the flow rate along the channel is constant to very good approximation, as suggested by GC05.

The elevation profiles for the different channels illustrate a reduction in elevation over the channel length, with the greatest slope evident for case 5-4, which has the largest frictional drag coefficient. For case 5-11 there is a noticeable change in depth at the inlet and outlet of the channel. This change is dependent on the channel geometry and is consistent with a head drop of the order of  $(\Delta |\mathbf{u}|)^2 / 2g$  over the contraction and expansion in channel cross-section at the ends of the channel, where  $\Delta |\mathbf{u}|$  is the difference in the instantaneous velocity magnitude at the channel opening and inside the uniform section of channel. A similar head drop also results for the other two channels, but is less noticeable because, for case 5-4, the magnitude of the head drop is a much smaller fraction of the tidal amplitude while, for case 5-5, the velocity through the channel is not close to a maximum at the time of high tide.

The natural dynamic balance within each of the channels in the natural state can be inferred from the phase lag of the channel flow rate behind the maximum difference in elevation across the channel (GC05). This phase lag  $\sigma$  is recorded in Table 5.1 for each of the cases simulated. For the longer and deeper channels (cases 5-1,3,5,7), when acceleration is expected to be important, the phase lag is above  $30^\circ$ . For short, shallow and rough channels (i.e. cases 5-4,9:12) the phase lag falls below  $15^\circ$  and the flow is closer to quasi-steady as expected.

It should be noted that the flow for case 5-11, illustrated in Figure 5.6 (e), is not symmetric about the  $x$  axis because the flow is unsteady as it exits into the basin. This unsteady flow is a result of the fact that, at the reduced geometric scale of case 5-11, there is insufficient net drag due to bed friction to stabilise the jet of water exiting into the basin. In contrast, for cases 5-5 and 5-5 bed friction acts over a much larger scale (and the bed friction coefficient is larger for case 5-5) to stabilise the flow as it exits into the basin. This ensures a symmetric snapshot of velocity contours in Figures 5.6 (a) and (c).

#### 5.4.1.2 Power Extraction

For each of the cases listed in Table 5.1 between 8 and 10 simulations were run with a tidal fence deployed across the full width of the channel. In each simulation the fence was modelled using LMADT with a fixed wake velocity coefficient of  $\alpha_4 = 1/3$  and a fixed blockage ratio. To map out an extracted power curve the blockage ratio was varied between

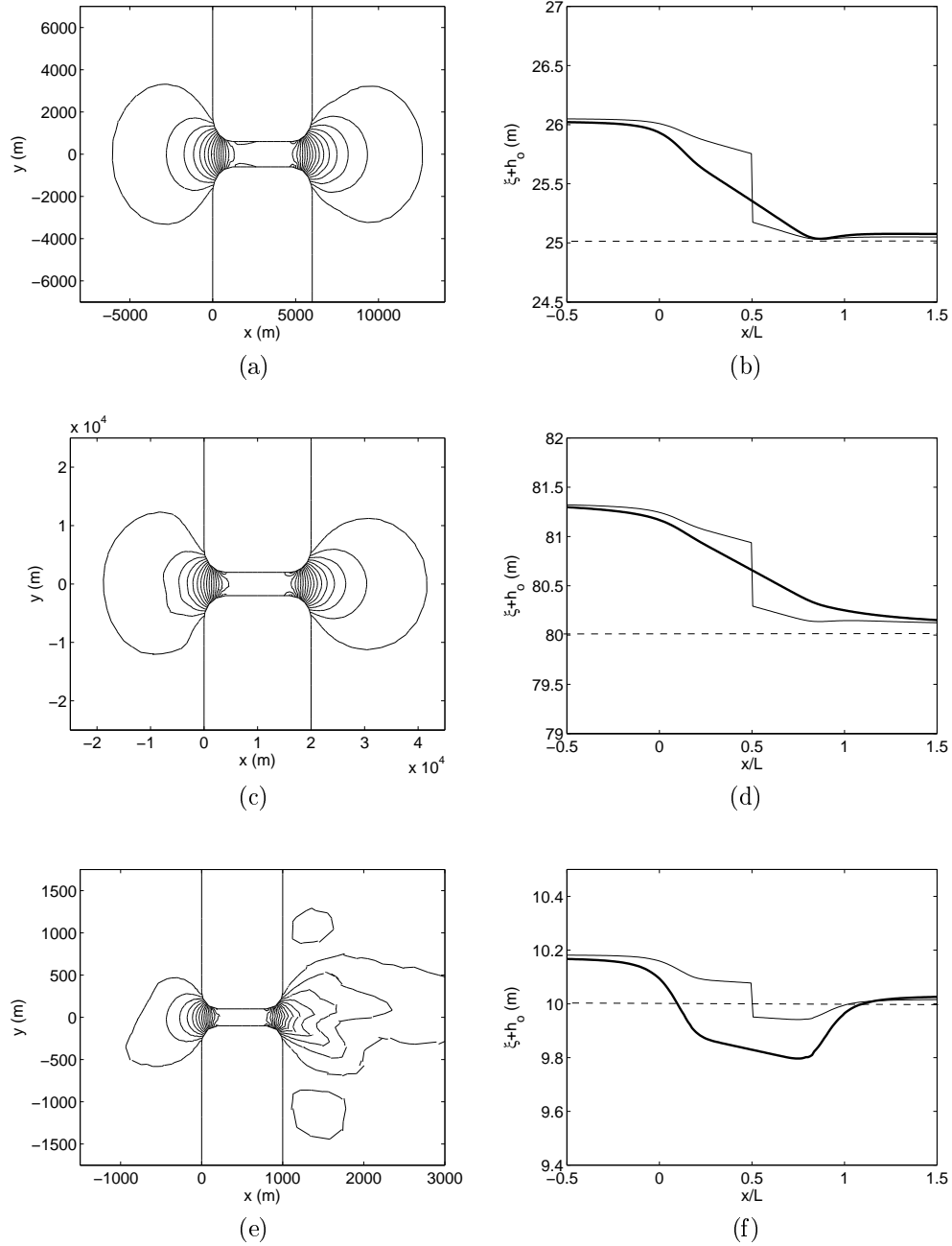


Figure 5.6: Contours of velocity component  $u$ , spaced equally at 20 increments between maximum and minimum, for (a) case 5-4, (c) case 5-5, (e) case 5-11, at  $t/T = 8$ . The flow is from left to right. Depth profile along  $y = 0$  shown for (b) case 5-4, (d) case 5-5 and (f) case 5-11. Thick solid line: natural elevation; Thin solid line: elevation close to maximum power extraction; Dashed line: still water depth.

runs, allowing for a change in turbine thrust or depth-averaged drag coefficient.

**Example Case: Case 5-1** Figure 5.7 (a) plots the power extracted by the turbine fence together with the power available to the fence and the total power dissipated in the channel for case 5-1. The basic shape of the extracted power curve is illustrative of all the cases examined and shows the effect of increasing the effective drag coefficient of the turbine fence; initially there is an increase in extracted power until eventually the turbines begin to slow the flow rate to such an extent that a reduction in extracted power results. The total power dissipated within the channel peaks for the same reason, but at a higher flow rate, whereas the power dissipated due to natural bed friction, which is proportional to the velocity cubed within the channel, reduces monotonically throughout. The maximum power extraction is 190 MW, which is achieved when the peak velocity in the channel is 1.8 m/s, or 55 % of the peak velocity in the natural state, and the turbines block  $\sim 70$  % of the channel cross-section. However, at this blockage ratio and wake velocity coefficient the efficiency of the devices within the fence is approximately 44% over the tidal cycle, meaning that only 84 MW is available for use, with the remaining 106 MW lost in wake mixing behind the devices.

With reference to Table 5.2 the maximum extracted power is significantly smaller than the undisturbed time-averaged kinetic flux (370 MW) and the time-averaged natural power dissipation within the channel (270 MW). In contrast, combining the natural flow rate through the channel ( $1.56 \times 10^5 \text{ m}^3/\text{s}$ ) and the driving amplitude across the channel (0.53 m, measured between the points  $(-4L, 0)$  and  $(5L, 0)$ ), with the phase lag of the flow rate behind the tidal forcing given in Table 5.1, the model of GC05 predicts a maximum power extraction of 175 MW. This is in better agreement with the simulated result. Furthermore, at maximum power extraction the model of GC05 predicts that the channel flow rate will be  $\sim 56$  % of that in the natural state, which is also in very good agreement.

To explore the simulated changes to the natural tidal hydrodynamics Figure 5.7 (b) plots the amplitude in elevation at the points  $P_1$ ,  $P_2$  and  $P_3$  as the fence blockage ratio increases. The change in elevation amplitude at  $P_1$  is small, as assumed in the model of GC05. There is a more noticeable reduction in amplitude at point  $P_3$ , indicating that with less flow through the channel the drawdown in depth, associated with the change in velocity head at the channel entrance and exit, is reduced. For point  $P_2$  there is also a reduction

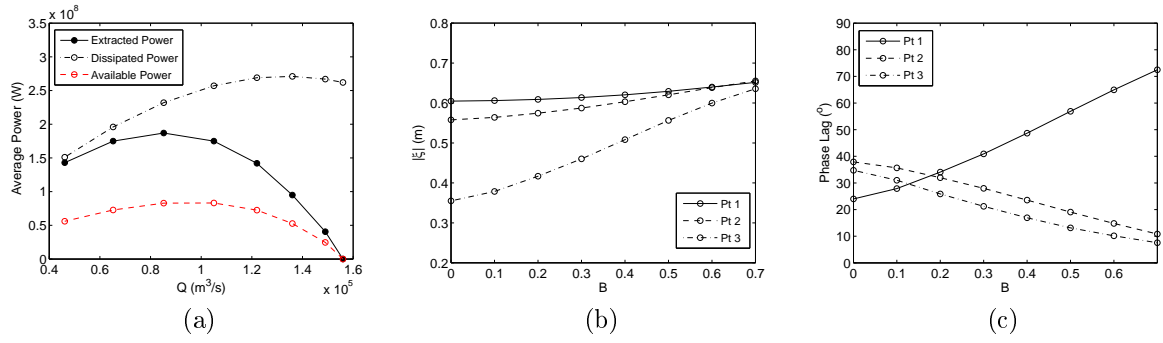


Figure 5.7: (a) Extracted power, total power dissipated in the channel due to turbines and natural bed friction and available power, as a function of normalised flow rate, for case 5-1. (b) Amplitude of M2 elevation at points  $P_1$ ,  $P_2$  and  $P_3$ , with varying blockage ratio. (c) Phase lag of M2 velocity behind M2 elevation at points  $P_1$ ,  $P_2$  and  $P_3$ , with varying blockage ratio.

because the reduced flowrate through the channel leads to less “sucking and blowing” of the channel in the adjoining water connecting the channel to the basins. Close to maximum power extraction approximately 2/3 of the driving amplitude, or head, is lost at the turbine fence (see Figure 5.6), which is again in agreement with the model of GC05. Figure 5.7 (c) illustrates the phase difference between the elevation and velocity at the three points. The lag at both  $P_2$  and  $P_3$  reduces towards zero with increasing blockage ratio as the turbine fence forces the flow closer to a quasi-steady regime. The phase lag at  $P_1$  approaches  $90^\circ$ , which is close to the expected value that would exist in the absence of the tidal channel.

**Extraction for all Cases** Table 5.2 summarises the energy extraction for all 12 cases. Across the full range of dynamic regimes Table 5.2 illustrates that the natural kinetic flux and the natural power dissipation provide a very poor indication of the power that the tidal fence can extract. For example, the natural dissipation overpredicts the power potential in all channels, measuring four times larger than the extracted power for the roughest channel case 5-8 (largest  $C'_d$ ), and just 10% larger than the smoothest channel case 5-9 (smallest  $C'_d$ ). The natural flux significantly over-predicts the extractable power for the short smooth channels (case 5-9:11), where the driving elevation across the channels is small, and significantly under-predicts the extractable power for the longer rougher channels (case 5-4:8), where the driving elevation across the channels is large.

Comparing the maximum power extracted from each channel to that predicted by the model of GC05 ( $\overline{P}_{GC}$  in Table 5.2) there is very good agreement for cases 5-1:8,12 but a noticeable under-prediction of power by GC05 for the smaller advection dominated channel

Case	Natural Flow			Maximum Power						
	$\gamma$	$a$ (m)	$Q_{max}$ (m <sup>3</sup> /s)	$\bar{P}$ (MW)	$\bar{P}/\bar{P}_{GC}$	$\bar{P}/\bar{P}_f$	$\bar{P}/\bar{P}_d$	$C_{d,eff}$	$Q/Q_{max}$	$\Delta a/a_0$
5-1	0.2	0.53	1.6E+5	190	1.10	0.52	0.70	1.1	0.54	1.1
5-2	0.2	1.3	3.9E+5	985	1.18	0.71	0.47	4.5	0.54	1.17
5-3	0.2	0.30	5.7E+4	35	1.10	0.81	0.67	3.1	0.52	1.09
5-4	0.2	0.95	6.3E+4	115	1.06	1.9	0.41	2.9	0.53	1.06
5-5	0.2	1.3	1.0E+6	2600	1.0	1.3	1.0	2.7	0.58	0.98
5-6	0.2	3.4	1.2E+6	8950	1.04	2.4	0.48	5.9	0.54	1.04
5-7	0.2	1.4	4.1E+5	1200	1.05	1.6	0.57	2.8	0.54	1.01
5-8	0.2	4.4	4.4E+5	3900	1.02	4.2	0.37	6.0	0.56	1.01
5-9	0.2	0.15	8.2E+4	25	2.21	0.05	0.87	0.41	0.50	2.01
5-10	0.21	0.27	7.1E+4	40	1.51	0.14	0.54	0.61	0.53	1.57
5-11	0.2	0.10	4.0E+3	0.8	1.21	0.24	0.48	0.79	0.55	1.19
5-12	0.21	0.25	3.2E+3	1.8	1.03	1.0	0.52	2.31	0.56	1.08

Table 5.2: Summary of power potential for numerical cases 5-1:12.  $\bar{P}_f$  and  $\bar{P}_d$  are the time average kinetic flux and natural power dissipation in the channel. The ratio  $\Delta a/a_0$  is the amplitude of the tidal forcing at maximum power extraction (measured between points  $(-4L, 0)$  and  $(5L, 0)$ ) divided by that in the undisturbed flow.

cases 5-9:11. This under-prediction of power is, however, proportional to the increase in amplitude of the driving tide across the channel when turbines are introduced, and suggests that for the smaller channels the driving tide needs to be measured much further from the channel mouth to be independent of the tidal devices, so as to obtain accurate predictions. Therefore, although Equation 5.11 appears to provide a very good prediction of the power that can be extracted from a given channel, one limitation of its application in practice is that the driving amplitude may need to be observed ambiguously far from the entrance and exit of the channel (which may be hard to define) in order to make accurate predictions (see also the study of the Minas Passage by Karsten et al. [2008]).

Comparing across the different channel lengths in Table 5.2, it can be seen that substantially more power can be extracted from the longer channels (cases 5-5:8). This is because a larger driving tidal elevation exists to accelerate the flow through the longer channels to achieve the required peak tidal current in the natural state. Consequently there is more power driving the longer channels, which can be used to do work on the tidal devices within the channel leading to a greater power extraction. Likewise, comparing channels of the same length and depth, more power can be extracted from channels with greater bed friction because a larger driving amplitude is again required in the natural state to overcome the drag forces and achieve the required peak tidal currents. For channels of the same length and friction factor, Table 5.2 indicates that more power can be extracted from

deeper channels, which is consistent with a larger flow rate in the undisturbed channel and again a greater driving power in the natural state.

Table 5.2 also records the effective depth-averaged drag coefficient  $C_{d,eff}$  (computed when  $F_r = 0$ ) at maximum power extraction. (For reference, when  $\alpha_4 = 1/3$  and  $F_r = 0$ , blockage ratios of 0.3 and 0.6 give  $C_{d,eff} = 0.35$  and 2.7, respectively.) It is clear that for the longer channel cases (i.e. cases 5-5:8 with moderate  $K_c$  and  $C'_d$ ) and the rough channels with large natural drag (i.e. cases 5-2:4 with large  $C'_d$ ), the effective turbine drag required to extract the maximum power is larger. This is consistent with the need for a larger turbine drag to decelerate the larger mass of accelerating fluid flowing through a long channel and to compete with the large natural bed friction in a rough channel, respectively. In contrast, for very short and smooth channels (cases 5-9:11) the required blockage ratio is sufficiently low that the maximum extracted power might be removed in practice with only one tidal fence (Garrett and Cummins [2008]).

Figures 5.8 (a) and (c) display the time variation in power extraction, normalised by the maximum instantaneous power, for all cases. It is clear that the time series of extracted power close to maximum extraction, and when the peak flow rate in the channel is 90% of the natural conditions, are asymmetric about the flood and ebb tide. This asymmetry is a result of the manner in which the tide was introduced solely in the left basin and the non-linearity inherent in the shallow water equations, which generates shallow water over tides in velocity (i.e. higher harmonics at a multiple of the driving frequency) within the channel (Figures 5.8 (b) and (d)). The even harmonic overtides in particular are responsible for the asymmetry in power extraction (Friedrichs and Aubrey [1988]) and their amplitude generally increases when the driving tidal amplitude is large relative to the mean depth in the channel. However, even for long rough channels such as case 5-4, which has the largest driving amplitude relative to the mean depth, the asymmetry in power extraction is only small. Furthermore, the asymmetry reduces with energy extraction (compare Figure 5.8(a) with 5.8(c)), which is due to the fact that although the amplitude of the first odd harmonic, which arises from the quadratic bed friction and drag from the turbines, slightly increases in relative amplitude with energy extraction, the first even harmonic, which is most responsible for asymmetry, reduces.

It is also interesting to note that the extracted power is noticeably 'peaky' over the tidal

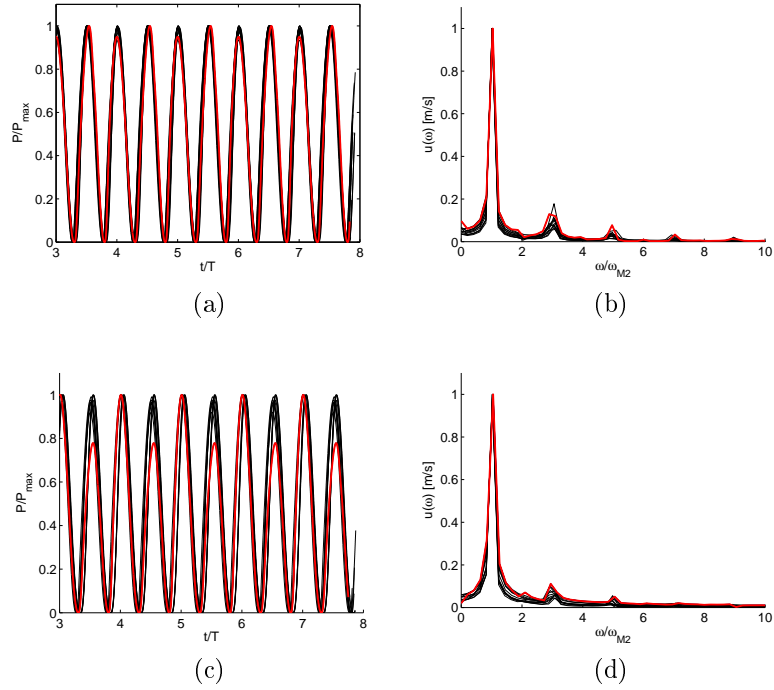


Figure 5.8: (a) Time series of power extraction close to maximum power extraction and (b) frequency spectrum of velocity in the channel, normalised to the M2 component, close to maximum power extraction. Figures (c) and (d) are equivalent to (a) and (b), but for a power extraction that results in approximately a 10% reduction in natural flow rate. All 12 cases are shown with case 5-8 represented by red.

period in Figures 5.8 owing to the time dependence of extraction on the cube of the flow rate. This will have implications for device developers who will need to choose between a device with high rated power to remove all of the power, or a lower rated device to extract power at a higher capacity factor.

Lastly, the changes to the natural flow rate at maximum power extraction for each of the cases in Table 5.2 agree well with the model of GC05 and generally indicate a 40-50% reduction. In some situations this reduction may be perceived to be environmentally unacceptable, however fortuitously the shape of the power curve illustrates that significant power can still be extracted whilst maintaining flow rates well above values at maximum extraction (Garrett and Cummins [2004] and Sutherland et al. [2007]). Across the different cases, between 40-50% of the maximum power extraction can be removed when the flow rate in the channel is reduced by only 10%.

#### 5.4.1.3 Available Power

The results presented in the previous section simulated energy extraction for a fence of turbines with variable blockage ratio and a fixed wake velocity coefficient of  $\alpha_4 = 1/3$ , so

that the fence was operating close to the maximum power coefficient (Chapter 2). For case 5-1 in particular, this meant that only 44% of the extracted power was available to the turbine. However based on the efficiency arguments outlined in Chapter 2 there is no reason why the wake velocity coefficient could not be set at higher values, to increase device efficiency and maximise the power available to devices. To investigate this further Figure 5.9 presents the power that is extracted by a fence of various wake velocity coefficients, together with the maximum Froude number in the channel, for case 5-1. Although the actuator disc theory in Chapter 2 indicates that the depth averaged turbine thrust  $C_{d,eff}$  will vary over the tidal cycle with Froude number by an amount dependent on the particular fence blockage ratio and wake velocity coefficient, it is evident in both figures that when the results are plotted against the depth-averaged effective drag ratio of the fence,  $C_{d,eff} = C_T B/2$  (computed using  $Fr = 0$ ), the different curves are very similar regardless. The curves are also consistent with that obtained using LMADT for an actuator disc in a constant volume flow to define the fence, which ensures that the effective drag coefficient is independent of Froude number and constant over the tidal cycle (dark black circles in Figure 5.9). As such, the time variation in thrust coefficient, introduced by the variation in Froude number over the tidal cycle (see Figure 2.11, Chapter 2), appears to have little bearing on the extracted power. Consequently many different device configurations (i.e. blockage and wake velocity coefficient), each giving the same  $C_{d,eff}$  when  $Fr = 0$ , can extract the maximum extractable power. This result was consistent for all the channels in Table 5.1.

A convenient conclusion from Figure 5.9 (a) is that, for any combination of  $B$  and  $\alpha_4$ , it is possible to interpolate the extracted power from the unique curve in Figure 5.9 and subsequently, after computing the efficiency from Equation 2.64 (Chapter 2) assuming  $Fr = 0$ , obtain an estimate of the available power. As an example, Figure 5.10 plots contours of extracted and available power (normalised by the maximum extractable power) as a function of the blockage ratio and wake velocity coefficient for case 5-1. These plots, which are similar to those presented recently by Vennell [2010], illustrate clearly that although the maximum extracted power can be achieved for any wake velocity coefficient, the largest proportion of the maximum extracted power is available to a tidal fence of devices with large wake velocity coefficient and large blockage ratio. This is because devices with large

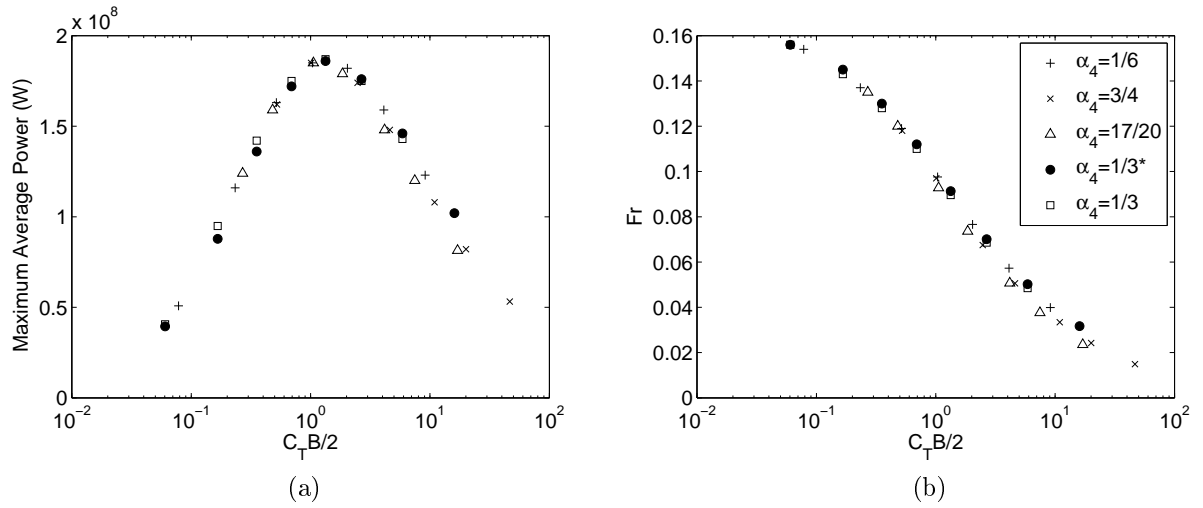


Figure 5.9: (a) Extracted power as a function of  $C_{d,eff} = C_T B/2$ . (b) Froude number as a function of  $C_{d,eff} = C_T B/2$ .  $C_{d,eff}$  is calculated using a  $Fr = 0$ . The \* indicates a fence modelled using LMADT for a constant volume flow.

$B$  and  $\alpha_4$  are efficient and provide sufficient thrust to extract maximum power. In practice these efficient fences would be formed with devices of large cross-sectional area and small centre to centre spacing.

Fixing the blockage ratio at 0.5 for case 5-1, Figure 5.10 illustrates that the available power is maximised when devices operate with a wake velocity coefficient close to 0.6, giving an efficiency of roughly 73%. Interestingly at this point the power extracted by the fence is only between 80-90 % of the maximum extractable power highlighting the distinction between maximising the available power and the extracted power discussed in Chapter 2. For comparison, if the wake velocity coefficient was set close to 0.35 almost all of the extractable power could be extracted but then the efficiency of the devices would reduce to 42% because of a reduction in wake velocity coefficient, reducing the overall available power. In agreement with Vennell [2010] there is therefore clearly a need to select, or “tune”, the wake velocity coefficient to maximise the available power for a given channel and turbine fence blockage ratio. Only for a fence with very large blockage ratio, where the appropriate wake velocity coefficient is close to unity, or for a fence with very small blockage ratio, where the back effect on the flow is small and the appropriate wake velocity coefficient is 1/3 in agreement with the classic Betz analysis, is the choice of velocity coefficient obvious.

To investigate the available power over the range of tidal channels Figure 5.11 illustrates contours of the extracted and available power, divided by the maximum extractable power, for cases 5-3,7,9. These channels have a dynamic balance that is drag dominated,

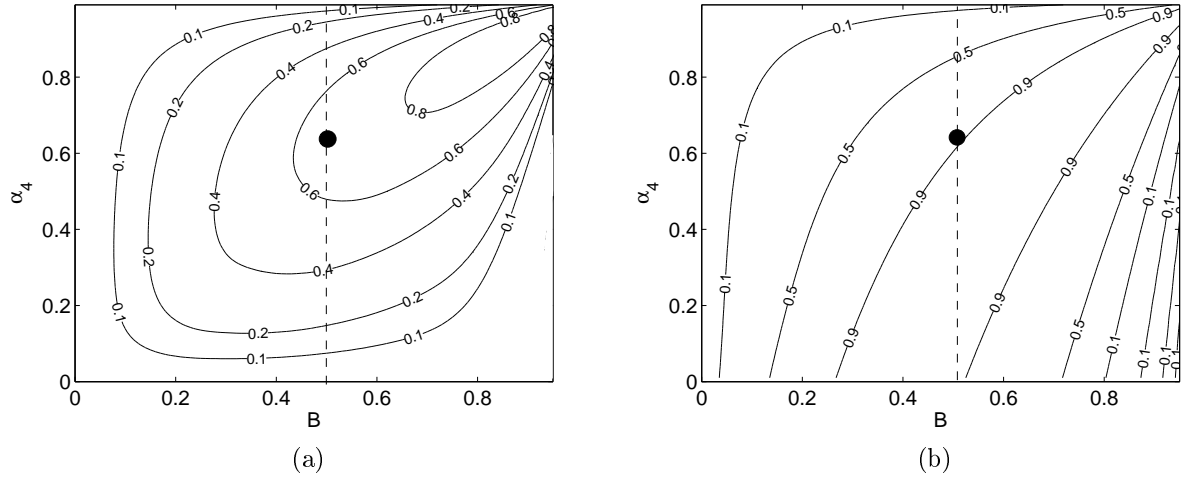


Figure 5.10: (a) Contours of available power, normalised by the maximum extractable power, plotted as a function of blockage ratio and wake velocity coefficient for case 5-1. (b) Same as for (a), but contours of extracted power, normalised by maximum extractable power. Black dot indicates location of optimum available power for a turbine fence with  $B = 0.5$ .

acceleration/drag dominated, and advection dominated, respectively. In all three cases it is evident that a turbine fence with a blockage ratio of 0.5 can extract the maximum extractable power, however the available power is maximised when less than this maximum power is extracted. Interestingly for case 5-9 the fraction of the maximum extractable power available to the devices at a blockage ratio of 0.5 is much higher than for cases 5-3,7. This can be explained by the fact that a greater effective drag coefficient  $C_{d,eff}$  is required to achieve the maximum extracted power in cases 5-3,7 (see Table 5.2) so that a much lower wake velocity coefficient, and consequently a lower device efficiency, is required to operate at maximum power extraction and a given fraction thereof. In practice this result implies that a large fraction of the extracted power will not be available in a long or rough channel when only one fence of moderately blocked turbines is used. In contrast, for a short advection dominated channel (i.e. case 5-9) not only can the maximum extracted power be achieved with one fence but, since devices within the fence operate efficiently at maximum power, and a given fraction thereof, a large proportion of the extracted power is available to the fence.

Lastly, because most of the extracted power is available to the devices when the blockage ratio is large it is useful to investigate how large the devices can become before the bypass flow, passing between the devices in the fence, becomes hydraulically critical. Taking case 5-1 as an example, the nature of the bypass flow can be determined for a fence of given

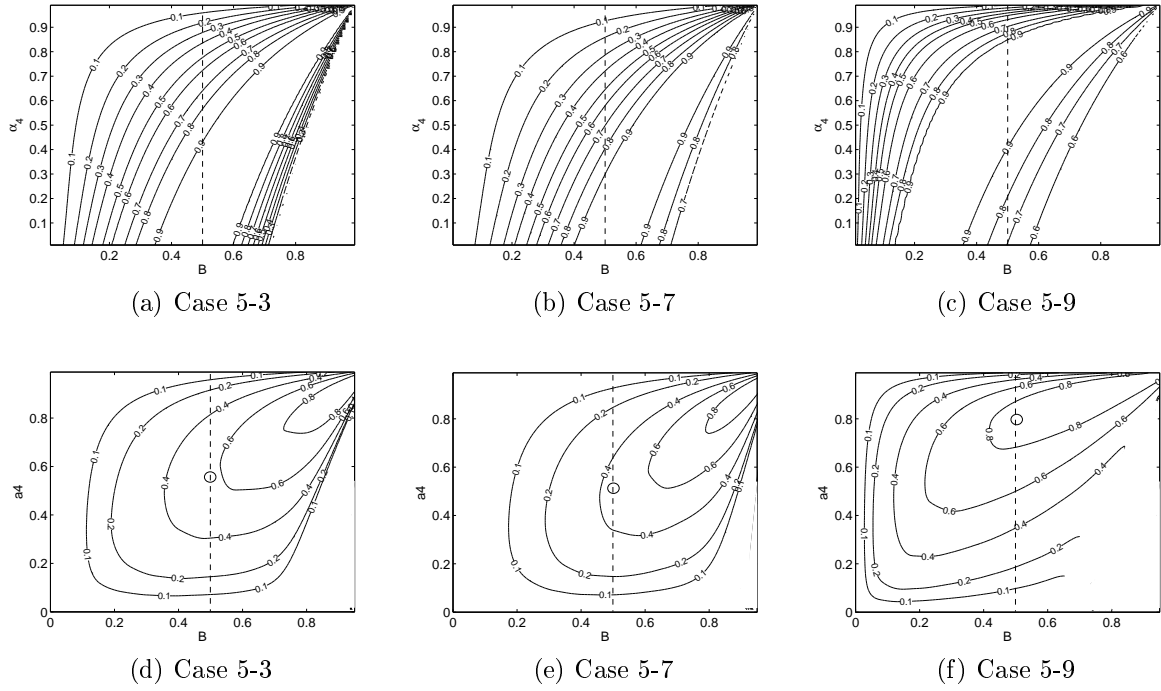


Figure 5.11: Extracted power divided by maximum extractable power (a-c). Available power divided by maximum extractable power (d-f). Dots locate maximum available power.

blockage ratio and wake velocity coefficient by interpolating the Froude number from 5.9 (b) and comparing the result with Figure 2.9 (b) in Chapter 2. Undertaking these calculations it was found that critical bypass flow did not occur until  $B > 0.95$ , regardless of the wake velocity coefficient. For cases 5-2 and 5-6, which require much larger effective fence drag coefficients at maximum power extraction, critical bypass did not occur until  $B > 0.9$ . The reason for this is that the addition of a turbine fence acts to reduce the flow rate and Froude number in the channel, thereby reducing the possibility of critical bypass flow. For longer and rougher channels the reduction in flow rate for a given turbine fence is smaller, but even in those cases only at impractically high blockage ratio is the reduction in Froude number insufficient to maintain sub critical flow. It is also important to note that when multiple fences are introduced subcritical bypass flow will be even less likely.

#### 5.4.1.4 Alternative Representation of Turbines

For each channel case energy extraction was also simulated using an added bed roughness within the channel. An example comparison to the line sink of momentum for case 5-1 is presented in Figure 5.12. It is clear that the extracted power and reduction in flow rate is indifferent to the use of a line sink of momentum or added bed roughness. This result was

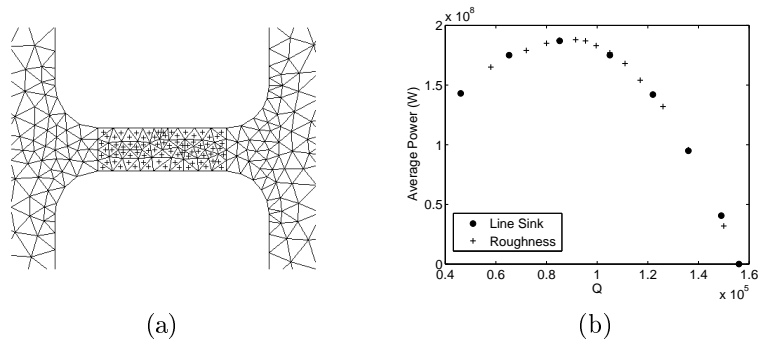


Figure 5.12: (a) Elements within the channel with added bed roughness indicated by crosses. (b) Power extraction for case 5-1 using bed roughness and a line sink of momentum.

representative of all the cases in Table 5.1.

## 5.4.2 More Complex Geometry

### 5.4.2.1 Permutations of case 5-1

To investigate the effect of variable geometry on power extraction six geometric permutations of case 5-1 have been analysed, as shown in Figure 5.13. The first three permutations involve variations in coastline and the last three consider variations in bathymetry.

Comparing the first three permutations, which are all driven by the same ocean tide, it is interesting to observe in Table 5.3 the effect of the geometry on the natural flow rate through the channels. For instance, in cases 5-1 a,c the flow rate is higher than in the reference case 5-1 because both the width of the channel, averaged over the channel length, is larger, and because the reduced velocity over most of the seabed area within the channel implies a reduced drag force due to bed friction. In contrast, case 5-1 b contains a bend and is longer than the reference case, which results in a greater effective resistance to the flow and a smaller natural flow rate. Importantly, these differences in natural flow rate directly impact the power potential of the different geometries, as can be seen in Table 5.3, because when the channel geometry offers less impedance to the flow the fixed driving elevation of the tide can do relatively more work on the tidal fence placed within the channel. If one was to construct an artificial tidal channel of constant depth to extract energy, the channel should be slowly converging like case 5-1 a and made as wide as possible whilst still maintaining the driving elevation across its length.

Across all three coastline permutations the agreement between the simulated power

extraction and that predicted by the model of GC05 is generally good. The slight under-estimation of power in cases 5-1 a,c can be reconciled by the change in driving amplitude with the addition of devices.

An advantage of the 2D simulations over the 1D analytical model of GC05 is that the variation in flow rate and power extraction across the fence can be simulated directly. Figure 5.14 displays the time series of power extraction, close to maximum extraction, at three locations along the fence for cases 5-1 a,c. For case 5-1 a the power extraction is greatest on the inside of the bend where the flow must accelerate to satisfy continuity. For case 5-1 c the power on the northern end of the fence is lower and asymmetric over the tidal cycle. This is because tidal flow from left to right advects through the narrow gap in the channel leading to lower velocities and lower power extraction on the northern end of the fence, compared with flow from right to left. If viscosity was included in the model together with a no-slip boundary at the coastline, separation of the flow passing through the constriction might be expected to enhance this asymmetry in power extraction along the fence. Although not pursued here, simulations of this nature would allow the distribution of turbines along the fence to be optimised.

For the three permutations in bathymetry differences in natural flow rate are also evident in Table 5.3. For cases 5-1 d,e in particular, the natural flow rate is reduced because the average cross-sectional area of channel is smaller and because the bed friction force, per unit depth, increases as the channel depth reduces. In contrast, for case 5-1 f the flow rate is slightly increased, compared with the reference case. Since the driving elevation is similar for all three bathymetry the variations in natural flow rate are again consistent with the power potential of the channels. The simulated power extraction matches the predictions of GC05 very well accounting for the small back effect on the driving tide.

#### **5.4.2.2 Flow around an Island**

Flow around an island situated near to a semi-infinite coastline, as shown in Figure 5.15, resembles one of the four classes of basin proposed in Chapter 3. If the island is small compared with the tidal wavelength a significant flow rate between the island and coastline will occur only if the background tidal velocities away from the island are also large, as may be the case for an island within a channel discussed in the next section. For larger islands

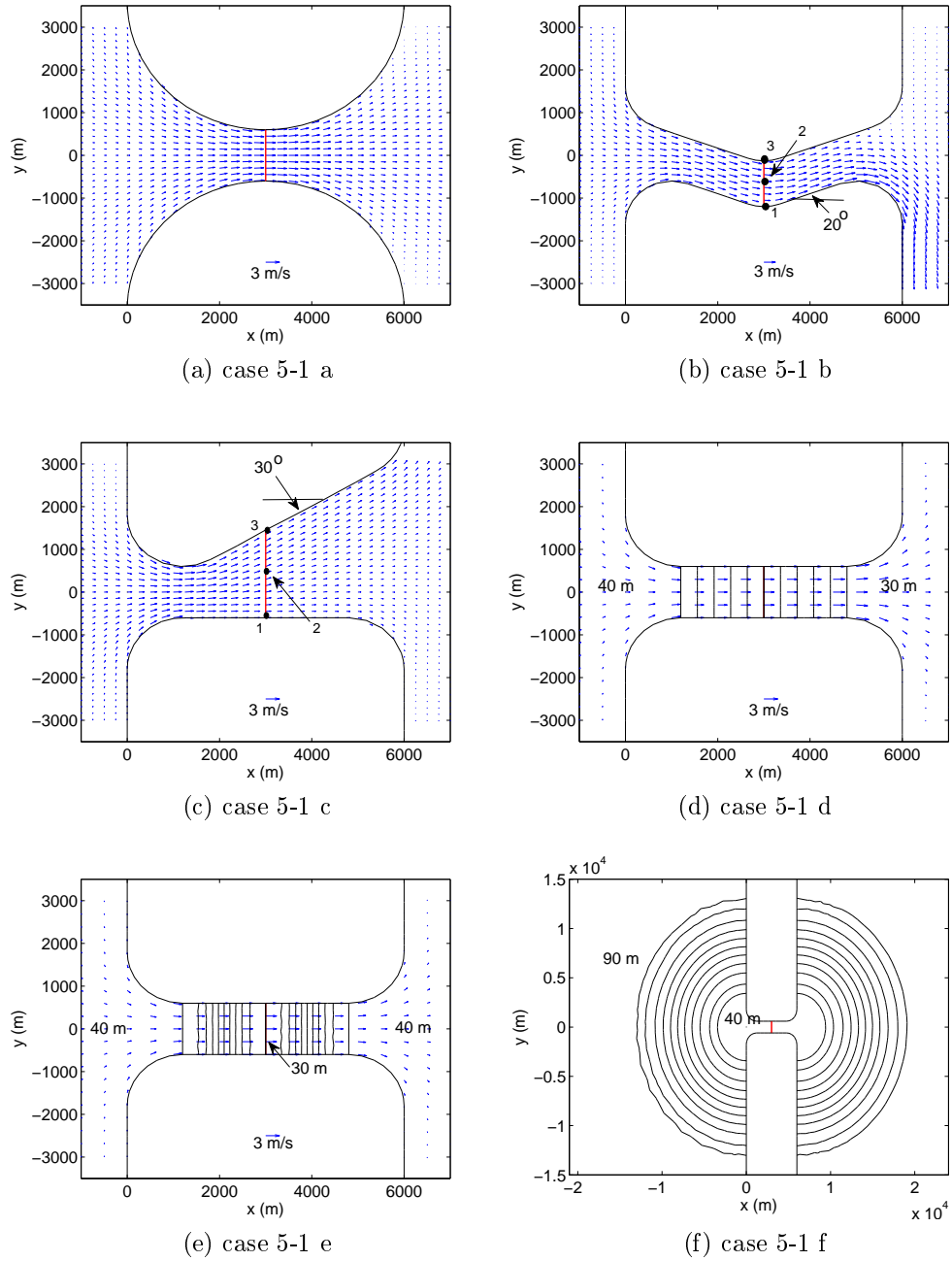


Figure 5.13: Velocity field at time of highest tide in the left basin for geometric and bathymetric permutations of case 5-1. All snapshots are taken when the blockage ratio of the fence is close to the optimum blockage ratio for power extraction. Solid lines in (d,e,f) indicate equal contours of bathymetry. Velocity vectors not shown for (f).

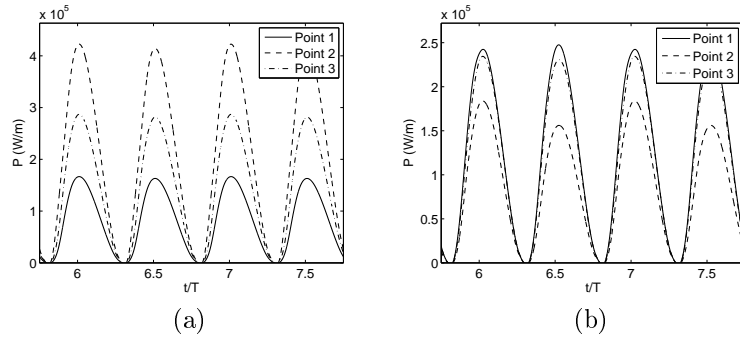


Figure 5.14: Power extraction, per unit width, at three locations along the turbine fence for (a) case 5-5b, and (b) Cases 5-5c. The points are defined in Figure 5.13.

Case	Undisturbed Flow				Maximum Power		
	$\sigma$	$\gamma$	$a$ (m)	$Q_0$ (m <sup>3</sup> /s)	$\bar{P}$ (MW)	$\bar{P}_{GC}$ (MW)	$\Delta a/a_0$
5-1a	50	0.2	0.54	2.0E+5	230	200	1.1
5-1b	45	0.2	0.49	1.4E+5	150	145	1.1
5-1c	45	0.2	0.54	2.0E+5	230	200	1.1
5-1d	45	0.2	0.54	1.3E+5	160	140	1.1
5-1e	45	0.2	0.54	1.4E+5	170	150	1.1
5-1f	45	0.2	0.57	1.7E+5	210	190	1.1
5-1	52	0.2	0.53	1.6E+5	190	170	1.1

Table 5.3: Natural flow conditions and maximum power extraction for the various channel geometries shown in Figure 5.13. Case 5-1 is included for reference.

significant flow rates in the strait can result when a phase difference is established around the island. This is characteristic of the island considered here, which has dimensions given in Figure 5.15, and could be thought of as a very crude representation of the Orkney Isles located adjacent to the Scottish mainland. To investigate the power potential of the island geometry, numerical simulations have been undertaken with tidal forcing introduced as a linear M2 progressive tidal wave traveling from left to right (i.e.  $h_b = h_o + (A/2)\cos(\omega t - kx)$ ,  $u_b = \sqrt{g/h_o}h_b$  and  $v_b = 0$ , where  $A = 3.5$  m). Figure 5.15 (b) illustrates lines of constant phase around the island in the natural state, spaced at  $15^\circ$  intervals, that result from this tidal forcing. The difference in elevation either side of the strait, shown in Figure 5.15 (c), leads to a maximum tidal velocity of 2 m/s through the strait. The peak velocity lags the maximum elevation difference across the strait by  $68^\circ$ .

Modelling a tidal fence across the centre of the channel as a line sink of momentum, the maximum power extraction was simulated as 4.25 GW when the fence reached an effective drag coefficient of  $C_{d,eff} \approx 9.3$  (i.e. a blockage ratio of 0.75 when  $\alpha_4 = 1/3$ ). This optimum drag coefficient is similar to the long channel cases listed in Table 5.1 and implies that

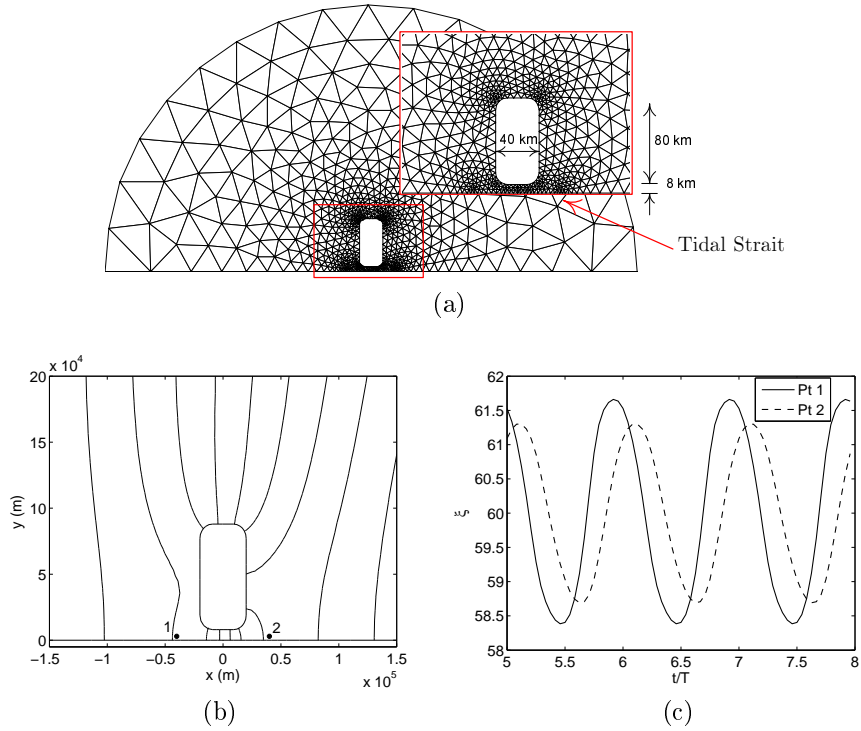


Figure 5.15: (a) Numerical mesh used to simulate flow around an island located close to a semi-infinite coastline. The depth was set to 60 m and  $C_d = 0.0025$  across the whole region. (b) Elevation co-phase lines, spaced at intervals of  $15^\circ$ . (c) Time series of elevation at two points either side of the Island Strait.

the majority of the strait's power will only be available to a single fence if the fence is filled with devices having an unrealistically high blockage ratio. This would suggest that realistically many fences (or farms) are needed to extract power efficiently from a similar coastal geometry, such as the Pentland Firth.

Taking the driving amplitude as the difference in natural elevation between the points 1 and 2 in Figure 5.15, and the undisturbed flow rate to be  $9.7 \times 10^5 \text{ m}^3/\text{s}$ , the theoretical model of GC05 predicts a maximum extracted power of 3.2 GW. The difference between this prediction and the simulated power can be explained almost entirely by the change in the driving amplitude as turbines are introduced into the channel; the amplitude at maximum power extraction is 1.3 times larger than the natural driving amplitude. Allowing for this discrepancy it is apparent that the model of GC05 satisfactorily explains the basic physics of the Strait. Equally, it is apparent that the flow will not bypass around the island and limit the power potential at this geometric scale.

Lastly, it is of interest to investigate the far field effects of energy extraction within the strait. Figure 5.16 displays the M2 elevation amplitude in the natural state together with the difference in elevation amplitude when a fence is operated at maximum power

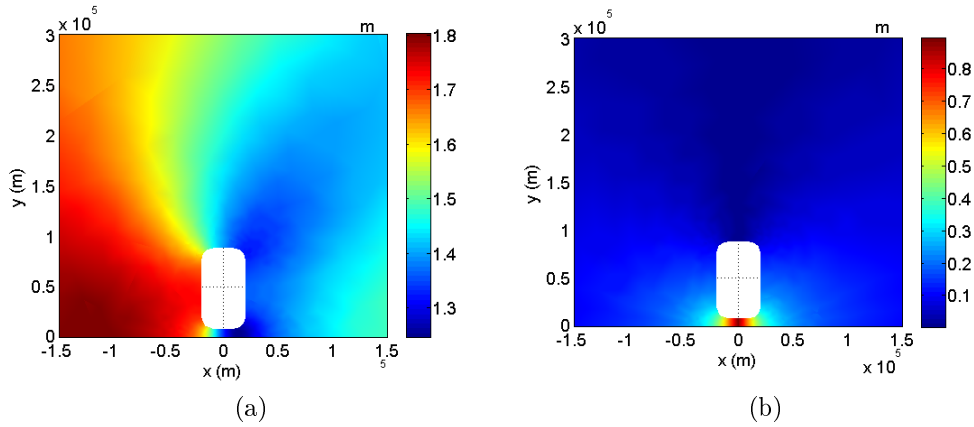


Figure 5.16: (a) Natural M2 elevation amplitude. (b) Change to the M2 elevation amplitude when a tidal fence is operating at maximum power extraction.

extraction. Although the depth change is large within the strait, the change in amplitude is less than 0.1m (less than 10% of the natural elevation) over the majority of the flow field.

### 5.4.3 Multiply Connected Channels

Many tidal channels are either complicated by the presence of small islands or form part of large multiply connected channels (see, for example, UK1, UK2, US6; Appendix A). In these channels the theoretical model of GC05 will tend to overpredict the extracted power because the tidal flow can bypass around the island or subchannel when a turbine fence begins to extract power (Sutherland et al. [2007], Polagye and Malte [2011]). In this section, the theoretical model of GC05 is interpreted using an electrical analogy. An extended electrical analogy is then used to interpret simulations of multiply connected channels.

#### 5.4.3.1 An Electrical Interpretation

The flow rate through an isolated channel, in the presence of energy extraction, is given by GC05 to be (c.f. Equation 5.9)

$$\rho g a \cos(\omega t) = \rho c \frac{dQ}{dt} + \rho \delta_0 |Q| Q + \rho \delta_1 |Q| Q. \quad (5.18)$$

An interpretation of this equation can be achieved by reference to an electrical circuit analogy. A similar analogy has been used by many researchers to solve problems involving the shallow water equations in channels (see, for example, Miles [1971], Lighthill [1978] and

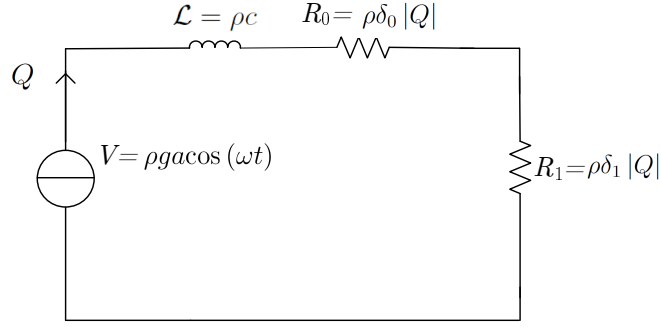


Figure 5.17: Equivalent electric circuit for an isolated tidal channel.

Rainey [2009]). Using the electrical analogy the dynamic pressure  $\rho g a \cos(\omega t)$  is analogous to the alternating voltage  $V$  and the flow rate  $Q$  is analogous to the alternating current  $I$ . Equation 5.18 can then be compared to the differential equation

$$V = \mathcal{L} \frac{dI}{dt} + RI + \mathcal{C} \int I dt, \quad (5.19)$$

which describes the alternating current in an electric circuit comprised of an inductance  $\mathcal{L}$ , capacitance  $\mathcal{C}$ , and resistance  $R$ . The acceleration of water through the channel therefore represents an inductance with  $\mathcal{L} = \rho c$ , the natural bed friction and velocity head at the channel exit represent a non-linear resistance  $R_0 = \frac{8}{3\pi} \rho \delta_0 |Q|$  and the tidal devices represent an additional non-linear resistance  $R_1 = \frac{8}{3\pi} \rho \delta_1 |Q|$ . The equivalent electrical circuit for the isolated channel is shown in Figure 5.17.

An advantage of the electrical analogy lies in the simple interpretation of Figure 5.17. For instance, the assumption made by GC05 that the elevation in the connecting ocean is independent of the action of the turbines requires that the voltage across the channel is fixed. As a result, introducing tidal devices will increase  $R_1$  and the total impedance of the circuit ultimately reducing the current in the circuit. The electrical analogy therefore highlights the feedback effect of tidal devices on the flow rate through the channel, so that the existence of a maximum power dissipation across the resistor  $R_1$  is readily demonstrated. The electrical circuit also explains that a higher natural flow rate, for a given driving elevation or voltage, is achieved in wide and deep channels (discussed in Section 5.4.2) because they have a lower natural impedance and resistance. Furthermore, the optimum resistance for  $R_1$  in the circuit must increase when either the imaginary or real part of the natural impedance increases, in agreement with the increased effective drag coefficient required in the long and rough channels documented in Table 5.2.

The electrical circuit also highlights that both the natural flow rate and the driving amplitude are required to fully describe the impedance of the channel in the natural state so that the effect of an additional resistance in the form of tidal turbines can be predicted. As such it is no surprise that the undisturbed kinetic flux in the channel (which only describes the current in the circuit) and the natural power dissipated in the channel (which only describes the time-average product of the flow rate and resistance  $R_0$ ), do not give good estimates of the power that can be extracted from the channel. In contrast, the formula of GC05 involves both the amplitude and the flow rate, completely describing the power driving the channel in the undisturbed state.

To extend the model of GC05 to a multiply connected channel, with a total length much smaller than the tidal wavelength, the 1D shallow water approximation to the momentum equation can be integrated along each subchannel. With reference to the multiply connected channel shown in Figure 5.18, the integrated equations are then

$$\rho g (\xi_1 - \xi_4) = \rho (c_1 + c_4) \frac{dQ_1}{dt} + \rho (\delta_{0,1} + \delta_{0,4}) |Q_1| Q_1 + \rho g (\xi_2 - \xi_3), \quad (5.20)$$

$$\rho g (\xi_2 - \xi_3) = \rho c_2 \frac{dQ_2}{dt} + \rho \delta_{0,2} |Q_2| Q_2 + \rho \delta_1 |Q_2| Q_2, \quad (5.21)$$

$$\rho g (\xi_2 - \xi_3) = \rho c_3 \frac{dQ_3}{dt} + \rho \delta_{0,3} |Q_3| Q_3, \quad (5.22)$$

where,  $Q = Q_1 + Q_2$ ,  $c_i$  and  $\delta_{0,i}$  describe the geometry and natural resistance in each subchannel,  $\delta_1$  is related to the tidal devices placed in subchannel 2, and  $\xi_2$  and  $\xi_3$  are the average tidal elevation in the connecting channel either side of the multiply connected subchannels. In a similar manner to the isolated channel this system of equations can be represented by the electrical circuit given in Figure 5.5 (b): two subchannels represent separate impedance in parallel and connected in series to a third impedance defining the connecting channel. If subchannel 3 had subchannels of its own,  $\delta_{0,3} |Q_3|$  and  $\rho c_3$  may define the effective resistance and inductance, respectively.

#### 5.4.3.2 Voltage and Current Limit

With reference to the electrical circuit two limiting conditions for the subchannels clearly present themselves. The first is the condition in which the voltage or driving tidal elevation across the subchannels is constant, whilst the second is the condition when the total flow

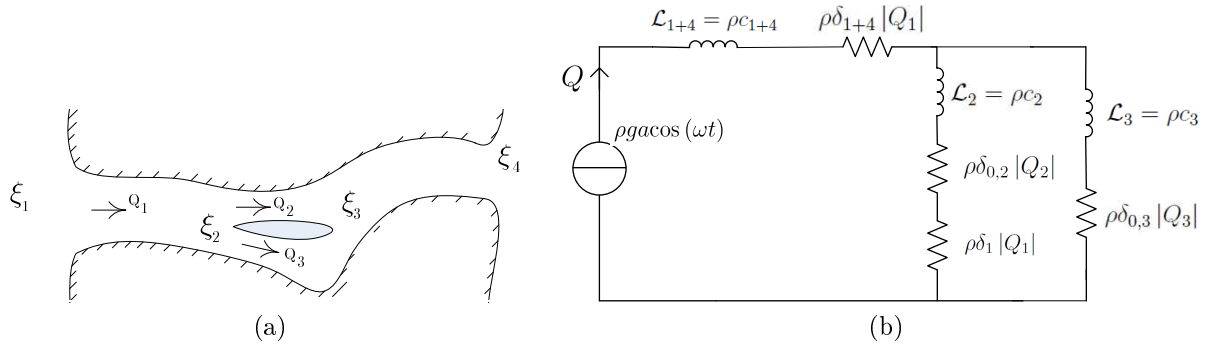


Figure 5.18: (a) Sketch of a multiply connected channel. (b) Equivalent electric circuit for the multiply connected channel.

rate through the subchannels is constant. The occurrence of these two limiting conditions is dependent on the relative impedance of the subchannels to that of the connecting channel. When  $c_2, c_3 \gg c_1 + c_4$  and  $\delta_{0,2}, \delta_{0,3} \gg \delta_{0,1} + \delta_{0,4}$ , the constant voltage limit is appropriate, while for  $c_2, c_3 \ll c_1 + c_4$  and  $\delta_{0,2}, \delta_{0,3} \ll \delta_{0,1} + \delta_{0,4}$  the constant total current limit is appropriate.

To explore the two limiting conditions Figure 5.19 presents the energy extracted from two different multiply connected channels when a fence of tidal turbines (with  $\alpha_4 = 1/3$ ) is deployed in one subchannel. In each set of simulations the channels have a uniform mean depth of 40 m, a bed roughness coefficient of  $C_d = 0.0025$  and a driving tidal amplitude of 0.7 and 1.5 m, for the channels in Figures 5.19 (a) and (c), respectively. (The boundary conditions are identical to those employed for the idealised channels.)

Using the electrical analogy, the channel in Figure 5.19 (a) describes the constant voltage limit, since the connecting channel is non-existent. The elevation or voltage across each subchannel is approximately constant and, as would be expected, the model of GC05 predicts the maximum extractable power well (Figure 5.19 (b)). The flow rate in the subchannel not containing the turbines is increased by just 6% at maximum power extraction.

Figure 5.19 (c) describes the second limiting condition in which the connecting channel is very long compared with the subchannels, such that its impedance is expected to be much greater. This is confirmed in Figure 5.19 (d) which illustrates that the total flow rate through the channels only reduces by 12% at the point of maximum power extraction (the change in phase of the total flow rate behind the tidal forcing is just  $4^\circ$ ). Figure 5.19 (d) also illustrates that the model of GC05 significantly overpredicts the maximum power extraction (where  $a$  is taken over the entire channel and  $Q_{max}$  is measured in the

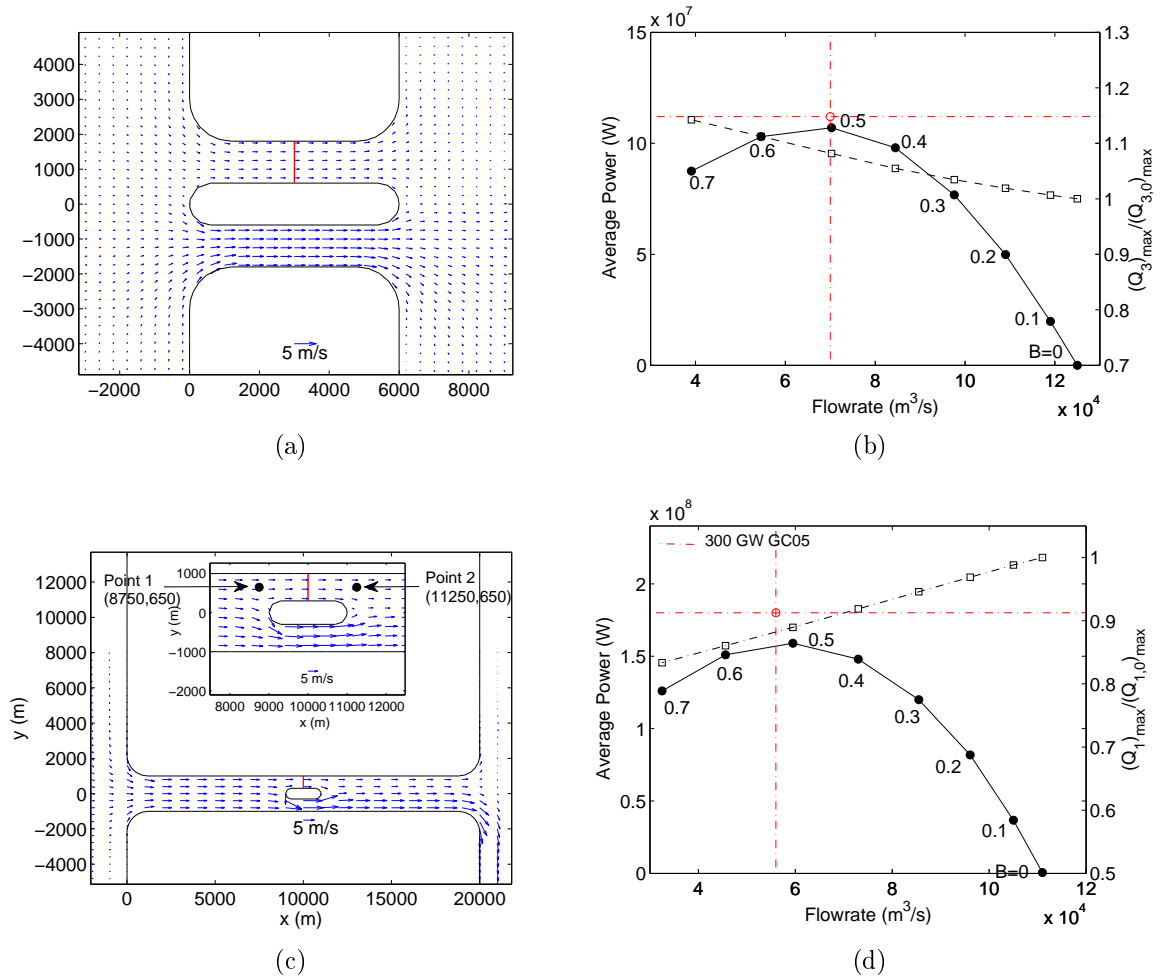


Figure 5.19: (a) Multiply connected channel with negligible connecting channel. Velocity vectors are at high tide and maximum power extraction. (b) Left axis, solid line: Extracted power for the channel in (a); right axis, dashed line: Maximum flow rate, normalised by the undisturbed maximum flow rate, in the subchannel without turbines. Cross hairs locate the predicted power and flow rate due to the model of GC05. (c) Multiply connected channel with long shallow connecting channel. (d) Left axis, solid line: Extracted power for the channel in (c); Right axis, dashed line: Maximum total flow rate, normalised by the undisturbed maximum flow rate, through the channel. Cross hairs locate the predicted power and flow rate consistent with Equation 5.27.

subchannel with the turbines), because the flow is able to bypass to the subchannel without devices.

For the limiting case of fixed total current, or tidal stream flowrate, a more accurate prediction of the power potential might be obtained by revisiting the basic physics. For example, equating the voltage across the subchannels and neglecting inductance (as would be realistic if the subchannels are short and shallow), provides an estimate for the relative resistance of the channels in terms of the readily observed natural flow rates

$$\frac{\delta_{0,2}}{\delta_{0,3}} = \left( \frac{(Q_{3,0})_{max}}{(Q_{2,0})_{max}} \right)^2. \quad (5.23)$$

Where, for convenience, the maximum flow rates over the tidal cycle  $(Q_{2,0})_{max}$  and  $(Q_{3,0})_{max}$  are used. Now, assuming  $Q_1$  does not change with the introduction of turbines, the flow rate through the subchannel in the presence of a tidal fence, or some arrangement of devices, is given by

$$Q_2 = Q_1 \left[ 1 + \left( \frac{\delta_{0,2}}{\delta_{0,3}} + \frac{\delta_1}{\delta_{0,3}} \right)^{1/2} \right]^{-1}, \quad (5.24)$$

with the turbines contributing an additional bed roughness to the channel. The instantaneous power extracted by the turbines then follows as

$$P = \rho \delta_1 |Q_2| Q_2^2 = \rho \delta_1 |Q_1| Q_1^2 \left[ 1 + \left( \frac{\delta_{0,2}}{\delta_{0,3}} + \frac{\delta_1}{\delta_{0,3}} \right)^{1/2} \right]^{-3}. \quad (5.25)$$

Comparing the extracted power to the reference power dissipated naturally in the subchannel  $P_{ref} = \rho g Q_{2,0} (\xi_{2,0} - \xi_{3,0}) = \rho \delta_{0,2} |Q_{2,0}| Q_{2,0}^2$ , gives the fraction

$$\frac{P}{\rho g Q_2 (\xi_{2,0} - \xi_{3,0})} = \frac{P}{\rho \delta_2 |Q_{2,0}| Q_{2,0}^2} = \frac{\delta_1}{\delta_{0,3}} \frac{\delta_{0,3}}{\delta_{0,2}} \left( \frac{1 + \left( \frac{\delta_{0,2}}{\delta_{0,3}} \right)^{1/2}}{1 + \left( \frac{\delta_{0,2}}{\delta_{0,3}} + \frac{\delta_1}{\delta_{0,3}} \right)^{1/2}} \right)^3. \quad (5.26)$$

This expression has a maximum  $\gamma_2$ , as  $\delta_1/\delta_{0,3}$  is varied, which is dependent on the ratio  $\delta_{0,2}/\delta_{0,3}$ . Figure 5.20 plots  $\gamma_2$  together with the maximum flow rate in the subchannel at maximum extraction, divided by the maximum flow rate without energy extraction. As  $\delta_{0,2}/\delta_{0,3} \rightarrow \infty$  the flow can bypass the devices easily and  $\gamma \rightarrow 2/3^{3/2}$  with  $(Q_2)_{max} / (Q_{2,0})_{max} \rightarrow 1/3^{1/2}$ , but, of course, the natural flow rate will be small. In the opposite limit, when  $\delta_{0,2}/\delta_{0,3} \rightarrow 0$ ,  $\gamma_2$  is unbounded and  $(Q_2)_{max} / (Q_{2,0})_{max} \rightarrow 1/3$ . In this

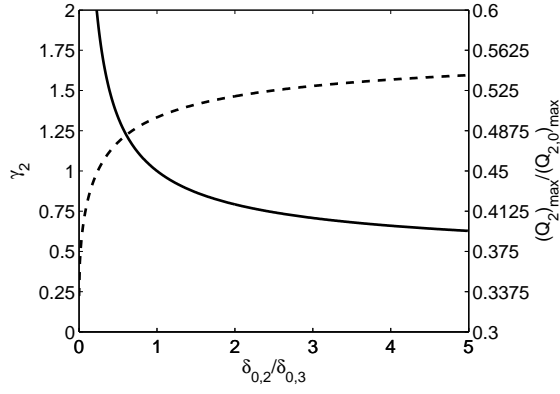


Figure 5.20: Left axis, solid line: Variation of  $\gamma_2$  with the relative resistance between both subchannels. Right axis, dashed line: Flow rate at maximum power extraction, relative to that in the natural state, as a function of the relative resistance between both subchannels.

limit, however, the assumption that the flow rate  $Q_1$  is independent of the devices becomes less likely.

The instantaneous maximum power can now be written as  $P_{max} = \gamma_2 \rho g (\xi_{2,0} - \xi_{3,0}) Q_{2,0}$ . Therefore, assuming a sinusoidal driving tide  $\xi_{2,0} - \xi_{3,0} = a_2 \cos(\omega t)$  in the natural state,  $(\xi_{2,0} - \xi_{3,0}) Q_{2,0}$  can be written as  $a_2 (Q_{2,0})_{max} |\cos(\omega t)|^{3/2}$  so that the maximum power averaged over a tidal cycle is simply

$$\overline{P_{max}} = 0.56 \gamma_2 \rho g a_2 (Q_{2,0})_{max}. \quad (5.27)$$

Conveniently this expression can be evaluated using just the natural flow rates in the channel and the driving amplitude  $a_2$ . For the subchannel in Figure 5.19 (c) taking  $a_2$  to be the driving amplitude between the points 1 and 2, and adopting  $\gamma_2 = 1$  because both subchannels have the same flow rate in the natural state, leads to a significantly better prediction than the model of GC05 (see Figure 5.19 (d)). This estimate is however still an overestimate of the simulated maximum power extraction because the simulated total flow rate through the subchannels has reduced.

#### 5.4.3.3 Intermediate Cases

Figure 5.21 displays the power extracted from a channel with an island located in three different positions. When the island is located in the center of the channel (Figures 5.21 (a) and (b)) the extracted power is smaller than that predicted by both the model of GC05 and Equation 5.27. This can be explained in the first case by the increase in flow rate

through the subchannel without tidal devices and, in the second case, by the reduction in total flow rate through the channel, respectively.

Translating the island to the left (Figures 5.21 (c) and (d)) results in a very similar power extraction to the geometry in Figure 5.21 (a). This is consistent with the compact length of the channel, relative to the tidal wavelength, which implies that only the total impedance of the connecting channel is relevant and not the distribution of impedance at either end of the subchannels.

Translating the island within the channel cross section (Figures 5.21 (e) and (f)) leads to an increase in power potential. Using the electrical analogy, this additional power can be explained by the increase in impedance of the subchannel not containing the turbines (i.e. both the inductance and resistance increase with a reduction in cross-sectional area) and the reduction in the natural impedance of the subchannel with the turbines. It is also useful to note that the proportion of flow bypassing the devices reduces so that the model of GC05 provides a better approximation than for the other two island locations, whereas Equation 5.27 provides a worse approximation.

For all intermediate cases, when the impedance's in the subchannel and connecting channel are comparable, both the model of GC05, and Equation 5.27 will overpredict the maximum power extraction, with the lower of the two predictions providing the better estimate. However, an even better estimate might be possible if an accurate observation of the phase and magnitude of the flow rate through each channel can be made, together with the phase and amplitude of the driving tide across the whole channel and the subchannels in the natural state. This would provide sufficient information to calibrate each inductor and resistor in the electric circuit shown in Figure 5.18.

## 5.5 Conclusions

For energy extraction in isolated channels the model of GC05 provides a very good prediction of maximum extraction across a range of dynamic regimes, provided that an accurate measure of the driving amplitude across the channel can be obtained. The natural power dissipation and the kinetic flux do not give a satisfactory prediction of the extracted power across the range of dynamic regimes found in practice.

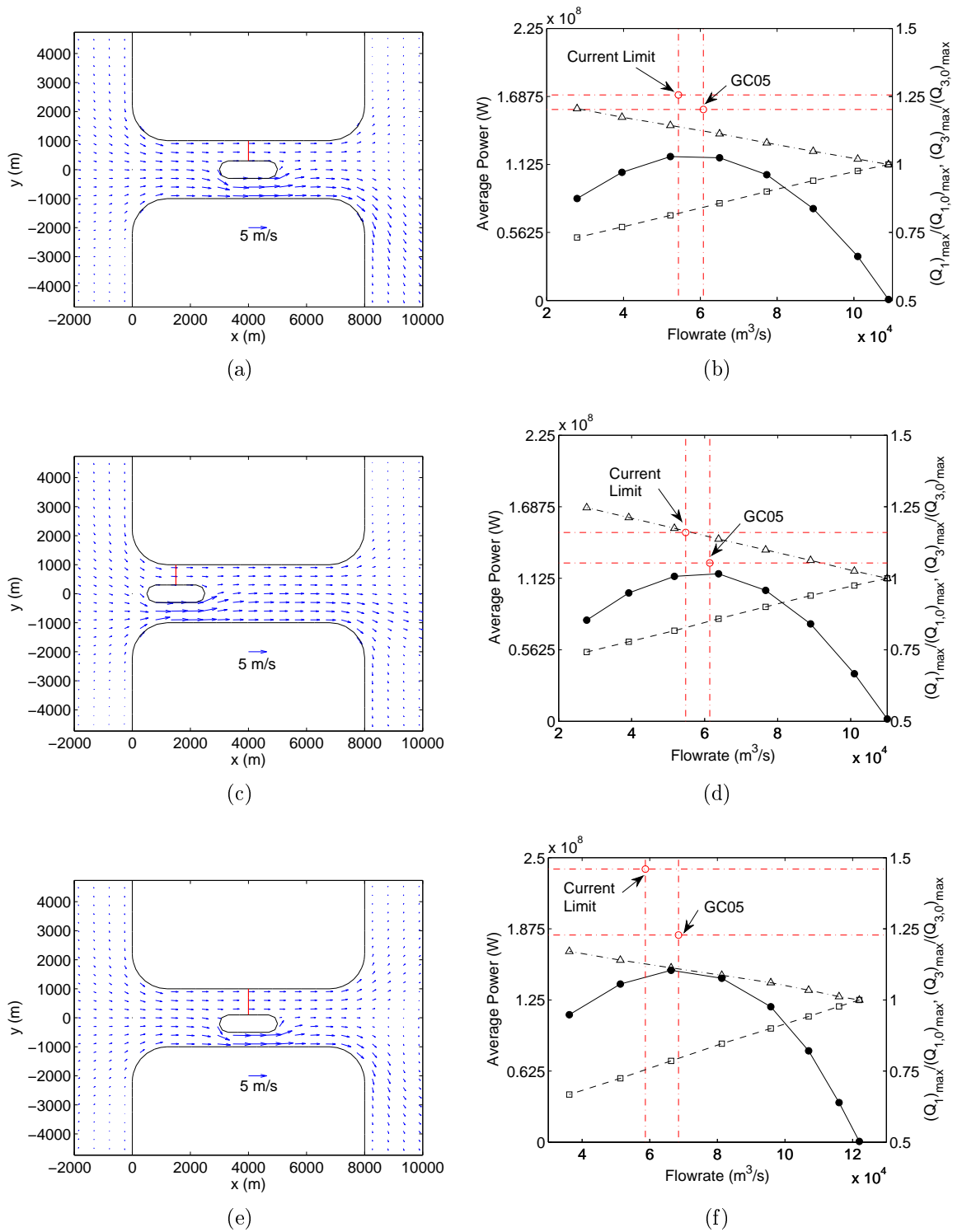


Figure 5.21: (a) Tidal channel containing an island. A uniform bed roughness of  $C_d = 0.0025$  and a uniform depth 40 m are specified. The driving tide has amplitude 0.7 m. (b) Left axis, solid line: Extracted power; Right axis, dashed line: Maximum total flow rate through both subchannels, normalised by the undisturbed value; Right axis, dash-dot line: Maximum flow rate through the subchannel without turbines, normalised by the undisturbed value. Cross hairs locate the predicted power and flow rate using the model of GC05 and Equation 5.27. Figures (c,e) similar to (a), Figures (d,f) similar to (b).

In agreement with Vennell [2010] the fraction of extracted power available to a tidal fence increases as the blockage ratio and wake velocity coefficient of the fence increase. Generally, shorter advection dominated channels can achieve a higher fraction of the maximum extractable power in the channel when a single fence of given blockage ratio is deployed.

The shape of a tidal channel, for a given driving tide, can effect the maximum extractable tidal power. Channels that are wide and deep provide the least impedance to the flow, thereby increasing the power that can be extracted by tidal devices. Simulations of energy extraction close to a large island, forming a crude representation of the Orkney Isles, UK suggest that many tidal fences will be required to remove the extractable power efficiently.

The model of GC05 is less accurate for multiply connected channels when the tidal devices are deployed in a subchannel that has an impedance which is a small fraction of the connecting channel impedance. A revised model has been proposed that appears to provide a better estimate in this situation.

# Chapter 6

## Oscillating Bay

### 6.1 Introduction

The first part of this chapter concerns enclosed tidal bays, where tidal devices might be deployed in a narrow channel connecting the bay to a larger sea or ocean. An existing theoretical model developed by Blanchfield et al. [2008b] is reviewed and compared to numerical simulations of both an idealised and complicated enclosed bay geometry. A modification to the theoretical model of Blanchfield et al. [2008b] is then discussed to account for wetting and drying in the enclosed bay. Wetting and drying is shown to introduce asymmetry into power extraction over a tidal cycle but have little effect on maximum power extraction.

The second part of the chapter considers non-enclosed bays, which have no obvious narrow constriction in coastline to place tidal devices. Using a one dimensional analytical model, the power that can be extracted by a tidal fence, and the power available to the fence, is explored for various non-enclosed bay geometries. It is shown that the optimum location to place a tidal fence along the bay is dependent on the number of devices installed within the fence and the channel geometry.

### 6.2 Distinction Between Bays

It is convenient to outline two subgroups of tidal bays observed in Appendix A. In the first group (see US 11, US 14; Appendix A) significant tidal currents result in a narrow passage between an *enclosed bay* and a larger sea. In contrast, in the second group of bays (see

UK 19, US 13; in Appendix A), which have a *non-enclosed* geometry, there is no narrow channel to accelerate tidal streams and so significant tidal currents will result when the tidal range at the head of the bay is very large or when quarter wavelength resonance is established with the tidal forcing at the mouth of the bay. In this chapter enclosed bays will be considered first, followed by non-enclosed bays.

## 6.3 Enclosed Bay

### 6.3.1 Existing Theoretical Model

A theoretical model has been developed by Garrett and Cummins [2004], with revisions by Blanchfield et al. [2008b] and Karsten et al. [2008], to determine the tidal power potential of a narrow isolated channel connecting an oscillating enclosed bay to a larger sea (see Figure 6.1 (a)). The assumptions of the theoretical model are similar to those adopted for a channel connecting two very large bodies of water presented by Garrett and Cummins [2005] and discussed in Section 5.3.2, Chapter 5. To describe the flow rate through the channel the shallow water approximation to the momentum equation is integrated along the channel length to give

$$g(\xi - \xi_b) = c \frac{dQ}{dt} + (\delta_0 + \delta_1) |Q| Q, \quad \text{with} \quad c = \int_0^L A_c^{-1} dx, \quad (6.1)$$

where  $Q$  is the flow rate in the channel,  $L$  is the channel length,  $A_c$  is the cross sectional area of the channel,  $\delta_0$  parameterises the drag from tidal devices and  $\delta_1$  parameterises losses due to bed friction and velocity head at the channel exit. The key difference between Equation 6.1 and the model of Garrett and Cummins [2005], is that the surface slope across the channel is now represented by  $\Delta\xi = \xi - \xi_b$ , where  $\xi$  is the tidal elevation in the open sea and  $\xi_b$  is the elevation in the enclosed bay. The second of these elevations is no longer taken to be independent of the flow rate through the channel, but is instead determined by mass conservation in the bay:

$$\frac{d\xi_b}{dt} = \frac{Q}{S_0}, \quad \text{or} \quad \xi_b = \frac{1}{S_0} \int Q dt, \quad (6.2)$$

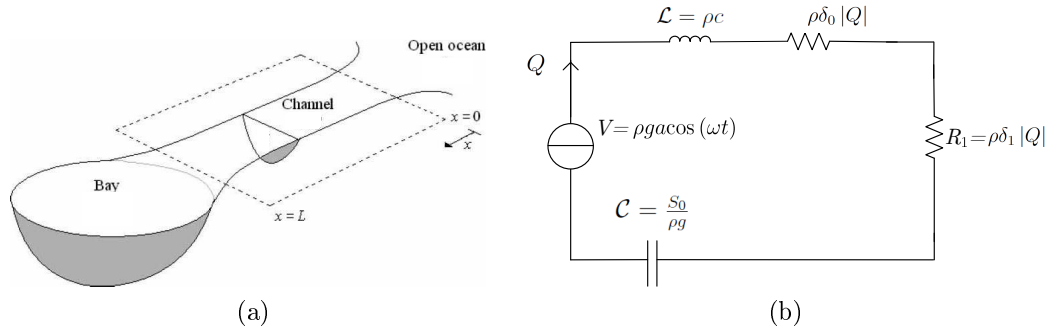


Figure 6.1: (a) Schematic of channel linking an open sea to an enclosed bay, taken from Blanchfield et al. [2008b]. (b) Equivalent electrical circuit describing the flow rate through the channel.

where  $S_0$  is the surface area of the bay. Equation 6.2 assumes that the surface area of the bay is constant with elevation and that the elevation within the bay is spatially uniform. The latter of these two assumptions requires that both the horizontal scale of the enclosed bay is small relative to a tidal wavelength and the connecting channel is narrow compared with the bay surface area (Miles [1971]).

Equation 6.1 and 6.2 constitute a non-linear system of equations that describe the flow rate in the connecting channel. Taking the driving tide in the adjoining sea to be  $\xi = a \cos(\omega t)$  and combining the mass and momentum equations leads to the expression

$$\rho g a \cos(\omega t) = \rho c \frac{dQ}{dt} + \rho (\delta_0 + \delta_1) |Q| Q + \frac{1}{(S_0/\rho g)} \int_0^t Q dt. \quad (6.3)$$

Equation 6.3 can be interpreted using the electrical analogy discussed in Chapter 5, with the equivalent electrical circuit given in Figure 6.1 (b). In particular, it is apparent that the bay introduces a capacitor,  $\mathcal{C} = \frac{S_0}{\rho g}$ , into the circuit: with a change in pressure in the bay (voltage across the capacitor) excess water (charge) is stored (Lighthill [1978]). The remaining impedance of the inlet channel includes an inductance  $\mathcal{L} = \rho c$ , due to the acceleration term in the momentum equation, and a non-linear resistance  $R = \rho (\delta_0 + \delta_1) |Q|$ , due to bed friction, exit head loss and tidal devices. From the perspective of power extraction it is clear using the electrical analogy that despite the addition of the bay there must still be a resistance  $\rho \delta_1 |Q|$  that will optimise the power removed by tidal devices, provided the voltage input into the circuit is fixed (independent elevation in the connecting sea).

Blanchfield et al. [2008b] non-dimensionalise the non-linear system of equations 6.1 and

6.2. They set  $\lambda_{0,1} = \delta_{0,1}(\omega c)^2/(ga)$ ,  $\xi = a\xi'$ ,  $\xi_b = a\xi'_b$ ,  $Q = Q'ga/(\omega c)$  and  $t = \omega^{-1}t'$  to give

$$\cos(t') = \frac{dQ'}{dt'} + (\lambda_0 + \lambda_1)|Q'|Q' + \xi'_b, \quad (6.4)$$

and,

$$\frac{d\xi'_b}{dt'} = \beta Q', \quad \text{where} \quad \beta = \frac{g}{\omega^2 c S_o}, \quad (6.5)$$

where the new non-dimensional parameter  $\beta$  describes the geometry of the bay relative to the connecting channel. As pointed out by Blanchfield et al. [2008b] in the limit of  $\beta \rightarrow 0$  the system of equations 6.4 and 6.5 become equivalent to those discussed in Chapter 5 to describe the flow rate through a channel connecting two large basins. As discussed in Chapter 3, the coastal sites denoted by class (a), and the enclosed bays denoted by class (b), are therefore equivalent when the enclosed bay is very large ( $S_o \rightarrow \infty$ ), or the channel cross section is very small ( $A_c \rightarrow 0$ ).

The non-linear system 6.4 and 6.5 can be solved numerically for the flow rate, bay elevation and, subsequently, the time averaged non-dimensional power extracted by the tidal devices ( $\overline{P'} = \lambda_1 \overline{|Q'|^3}$ ) for different values of  $\lambda_0$  and various bay geometries defined by  $\beta$ . Example results are presented in Figure 6.2 (a) with the extracted power described by  $\gamma$ , where

$$\overline{P}_{max} = \gamma \rho g a Q_{max}, \quad (6.6)$$

with  $\rho g a$  the dynamic pressure in the connecting sea and  $Q_{max}$  the maximum flow rate through the connecting channel in the undisturbed state. It is evident in Figure 6.2 (a) that, as for the channel between two large water bodies, the variation in  $\gamma$  is small, ranging between 0.19 and 0.26, though  $a$  now refers to the amplitude of the ocean tide not the elevation difference across the channel. To inform the environmental effects of energy extraction Figure 6.2 (b) presents the ratio  $\Lambda = a_b/a$ , at maximum power extraction to that in the natural state  $*_0$ . When natural friction is large ( $\lambda_0 \gg 1$ ) this ratio is approximately 0.57, while for negligible natural friction ( $\lambda_0 \rightarrow 0$ ) it varies between 0.5 and 0.75 for the geometries shown.

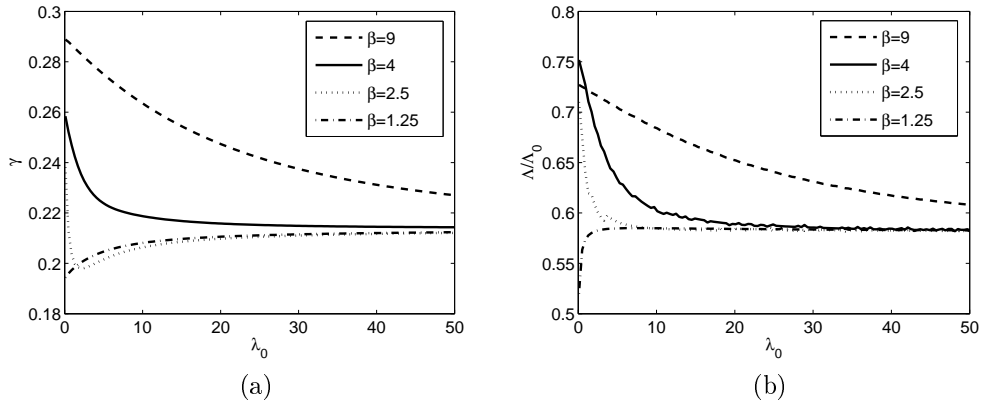


Figure 6.2: (a) Maximum average power, in terms of  $\gamma$ , for an enclosed bay. (b) Amplitude ratio  $\Lambda$  at maximum power extraction relative to that in the natural state. Values of  $\beta$  are labelled.

### 6.3.2 Numerical Simulations

In this section numerical simulations of an idealised enclosed bay, depicted in Figure 6.3, are compared to the analytical model of Blanchfield et al. [2008b] and the available power is explored. A more complicated bay geometry is then analysed to highlight the shortcomings of the Blanchfield et al. [2008b] model and the usefulness of the electrical analogy in interpreting the extracted power.

#### 6.3.2.1 Extraction from an Idealised Bay

Simulations of an idealised enclosed bay connected to a larger sea via a channel with dimensions identical to the tidal channel case 5-1 (Chapter 5) are now discussed. In all simulations the open ocean boundary condition, driving tide and the line sink of momentum representing the turbine fence are modelled in the same way as outlined in Chapter 5.

To give an overview of power extraction from the channel Figure 6.4 (a) presents the power extracted by a fence of devices, with a wake induction factor of  $\alpha_4 = 1/3$ , for case 6-4 (see Table 6.1). The power extracted by the fence initially increases as the blockage ratio increases, but then reduces because the devices slow the channel flow rate. Figure 6.4 shows that the fence also acts to increase the phase lag between the elevation in the bay and the open ocean, and to reduce the tidal range in the bay. Both of these effects are consistent with the electrical analogy as the turbine resistance increases. For instance, the reduction in tidal range within the bay implies a reduction in voltage across the capacitor, whereas the phase lag in the tidal range within the bay corresponds to an increase in the

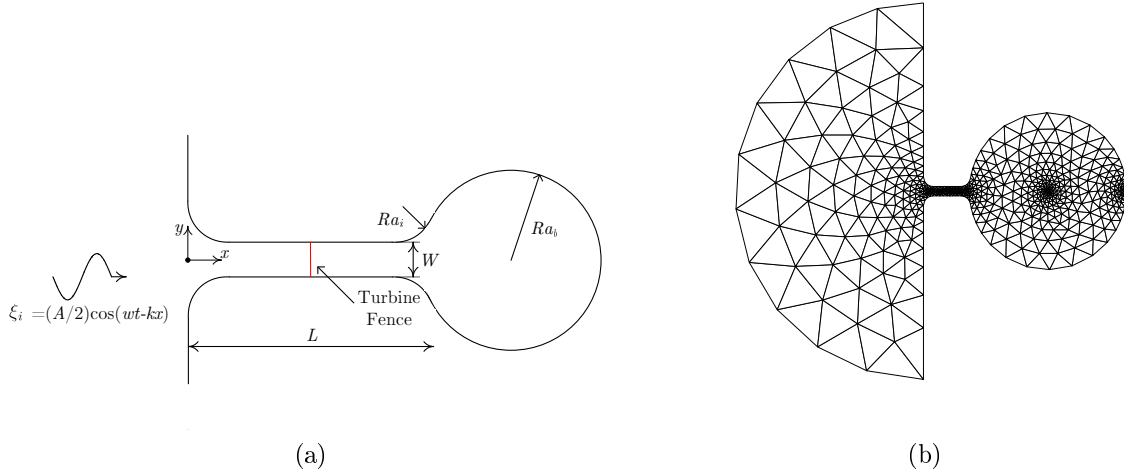


Figure 6.3: (a) Idealised geometry of an enclosed bay. (b) Example numerical mesh. Elements of order  $n = 3$  were used together with curved isoparametric elements along the inlets of the channel and around the open boundaries. The open boundary is located a distance of  $4L$  from the opening of the channel.

Case	Undisturbed Flow							Maximum Power		
	$Ra_b$ [km]	$A$ [m]	$Q_{max}$ [m <sup>3</sup> /s]	$\Lambda_0$	$\sigma$	$\beta$	$\lambda_0$	$C_{d,eff}$	$\bar{P}$ [MW]	$\bar{P}_B$ [MW]
6-1	20	0.7	8.7E+4	1.3	9°	4	1.3	2.7	130	120
6-2	10	0.7	3.2E+4	1.1	1°	8.5	1.3	16	55	55
6-3	5	0.7	8.2E+3	1.0	0.05°	27	1	330	14	15
5-1	$\infty$	0.7	2.0E+5	-	-	0	-	1.1	190	209
6-4	20	1.4	1.7E+5	1.3	17°	4	2.7	1.9	480	475
6-5	10	2	9.1E+4	1.1	4°	8.5	4.1	6	450	440
6-6	5	4	4.8E+4	1.0	0.5°	27	6	85	390	440

Table 6.1: List of enclosed bays analysed.  $A$  refers to the amplitude of the driving tide (see Chapter 5),  $Q_{max}$  is the maximum undisturbed flow rate in the channel,  $\Lambda_0$  is the amplitude ratio  $a_b/a$  in the natural state (with  $a_b$  recorded at the center of the bay),  $\sigma$  is the phase lag of the bay tide behind the ocean tide in the natural state, and  $C_{d,eff}$  is the effective depth-averaged drag coefficient of the fence.  $P_B$  is the power predicted by the model of Blanchfield et al. [2008b]. All bays have  $C_d = 0.0025$  and  $Ra_i = 1.2$  km.

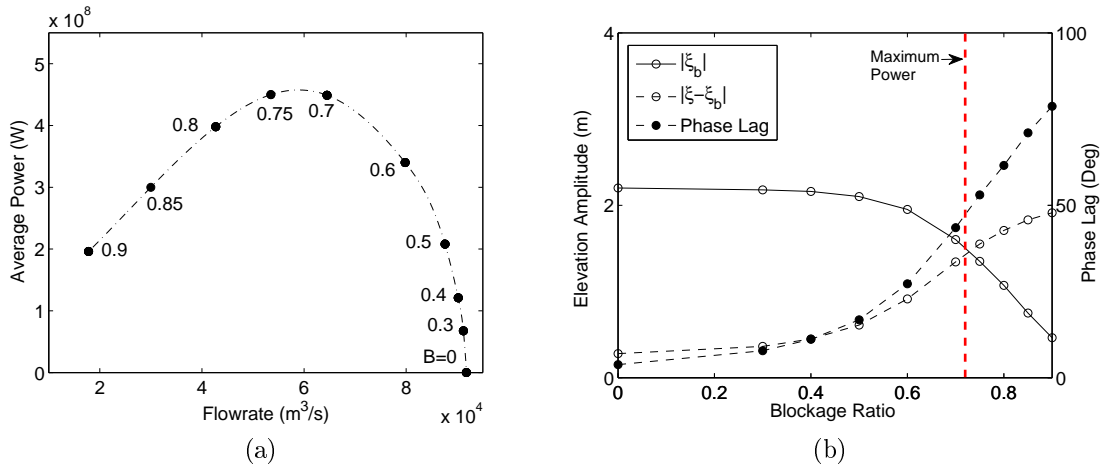


Figure 6.4: (a) Power extraction as a function of natural flow rate through the inlet channel for case 6-4. (b) Amplitude of tidal elevation at the center of the bay  $|\xi_b|$ , amplitude of elevation difference across the channel  $|\xi - \xi_b|$ , and phase lag of the the bay tide behind the ocean tide, as a function of fence blockage ratio (when  $\alpha_4 = 1/3$ ) for case 6-4.

effective impedance of the bay and channel.

Table 6.1 summarises undisturbed flow and simulated power extraction for a range of idealised bays. In each case the simulated maximum extracted power is compared quantitatively with the model of Blanchfield et al. [2008b] by first solving Equation 6.3 for the flow rate, based on the non-dimensional drag coefficient,  $\lambda_0$ , and the bay geometry term,  $\beta$ , for each bay. (These latter values are chosen so that the simulated undisturbed tidal amplitude in the bay to that in the ocean,  $\Lambda_0$ , and the phase lag of the bay tide behind the ocean tide,  $\sigma_o$ , match that predicted by Equation 6.3.) The simulated and theoretical maximum power extraction agree to within 5 % in each case. The simulated changes in elevation in the bay also agree to the same degree with those predicted by the theoretical model (not shown).

Comparing across the different bays in Table 6.1 it is interesting to observe the relationship between the bay surface area and power extraction. For example in cases 6-1:3 and 5-1, which are driven by a similar driving tidal amplitude, the power potential reduces with bay surface area. This can be explained by the fact that the capacitance of the bay is smaller for small surface area, leading to an increased impedance and consequently a reduced channel flow rate in the natural state. Physically it implies that a bay with small surface area can respond quickly to the driving tide, thereby reducing the phase lag and elevation difference across the channel, which drives the flow against the tidal devices (note also that for a very large bay, so that  $\beta \rightarrow 1$ , Helmholtz resonance will result at which

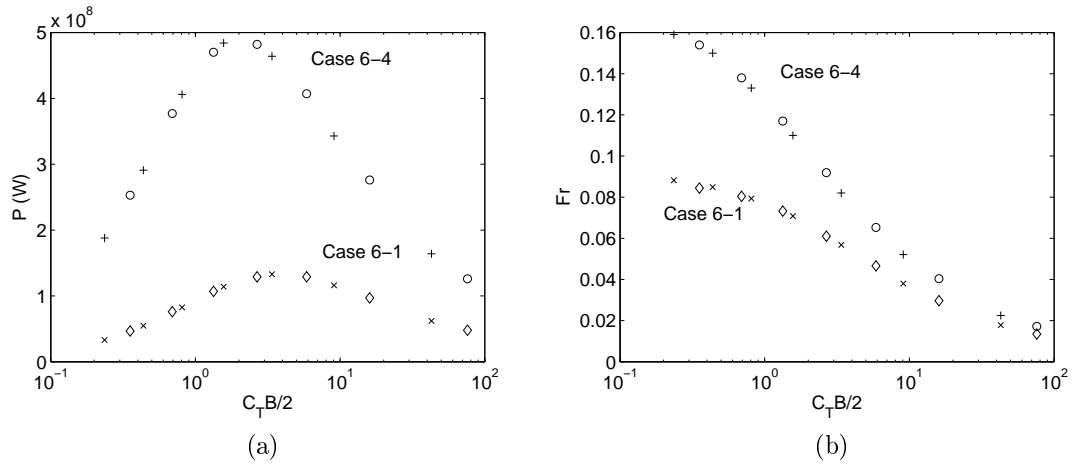


Figure 6.5: (a) Extracted power as a function of depth-averaged turbine drag coefficient  $C_{d,eff} = C_T B/2$ . (b) Froude number as a function of  $C_{d,eff} = C_T B/2$ , calculated for  $Fr = 0$ .  $C_{d,eff}$  is calculated using maximum Froude number over the tidal cycle. Circles and diamonds are for  $\alpha_4 = 1/3$ , crosses and x's are for  $\alpha_4 = 1/3$ .

point the flow rate through the inlet will be at its largest). It is also evident in Table 6.1 that a larger resistance must be applied by the fence at maximum power extraction for the smaller bays (i.e. higher  $C_{d,eff}$ ). This is because a higher resistance is required to compete with the large capacitance of the smaller bays.

Comparing cases 6-1:3 with 6-4:6 it is evident that the natural flow rate also increase when the offshore tidal amplitude increases. This is simply because the increased offshore driving tide can do more work on the tidal devices. The resistance of the turbines,  $C_{d,eff}$ , required to extract maximum power reduces as the driving amplitude increases.

### 6.3.2.2 Available Power

Figure 6.5 displays the extracted power and maximum Froude number over a tidal cycle for cases 6-1 and 6-4 when a turbine fence with wake velocity coefficient of  $\alpha_4 = 1/3$  and  $\alpha_4 = 1/2$  is installed. For both cases the curves formed by the different wake velocity coefficients are very similar. This result is equivalent to that obtained for tidal channels in Chapter 5 and again suggests that the extracted power, and changes to the natural hydrodynamics, are dependent only on the effective drag coefficient of the fence (i.e.  $C_{d,eff}$  calculated when  $Fr = 0$ ) and not the particular choice of wake induction factor and blockage ratio. This is consistent with the variation in thrust coefficient with Froude number over the tidal cycle having negligible effect on power extraction.

For all values of blockage ratio and wake velocity coefficient the available power to a

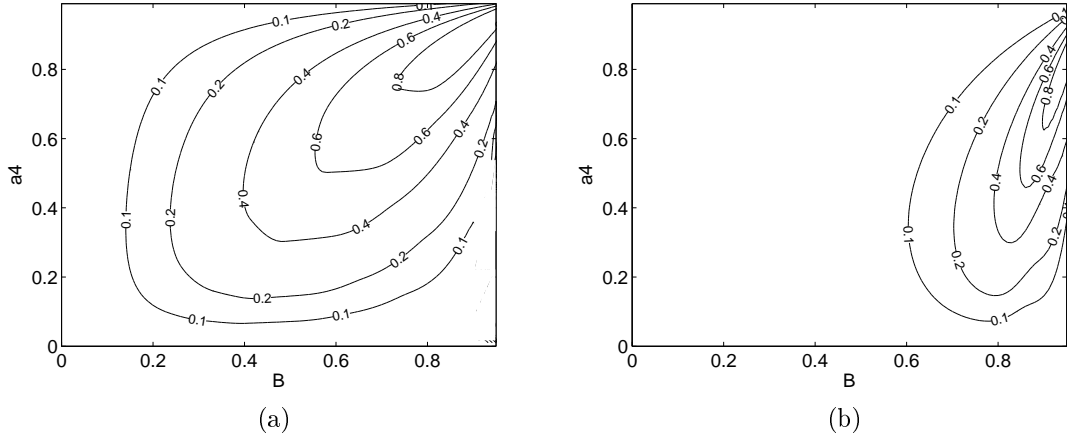


Figure 6.6: Available power, divided by the maximum extractable power from the inlet, for (a) Case 6-1 and (b) Case 6-3.

tidal fence is shown in Figure 6.6 for cases 6-1 and 6-3. It is again evident, as shown in Chapter 5, that the available power can be maximised when tidal devices with large blockage ratio, small center-to-center spacing and low wake velocity coefficient are used. Comparing Figures 6.6 (a) and (b), it is also evident that for a fixed blockage ratio a higher fraction of the maximum extractable power is available at a larger wake velocity coefficient for case 6-1, which has a much larger bay surface area. This result highlights that for a given driving tide not only can more power be extracted from the inlet to a bay with large surface area, but, because a lower effective drag is required by the fence at maximum power extraction and a fraction thereof (i.e. lower  $C_{d,eff}$  in Table 6.1), the devices within the fence can be more efficient.

The fraction of the extractable power available to a fence, of given blockage ratio, also increases when the connecting bay has a larger surface area. This result is not shown graphically here, but can be anticipated by comparing the effective turbine resistance  $C_{d,eff}$  for bays of different bay surface area in Table 6.1.

### 6.3.2.3 More Complex Bay Geometry

In practice geographically complicated bays and channel networks might be considered for tidal energy extraction (see for example Polagye and Malte [2010] and sites around Admiralty Inlet (Appendix A, US 7)). As an example of a complicated site Figure 6.7 (a) considers an enclosed bay that is connected to the open ocean by two parallel inlet channels. (This could be thought of as a compound addition of a class b and class c coastal

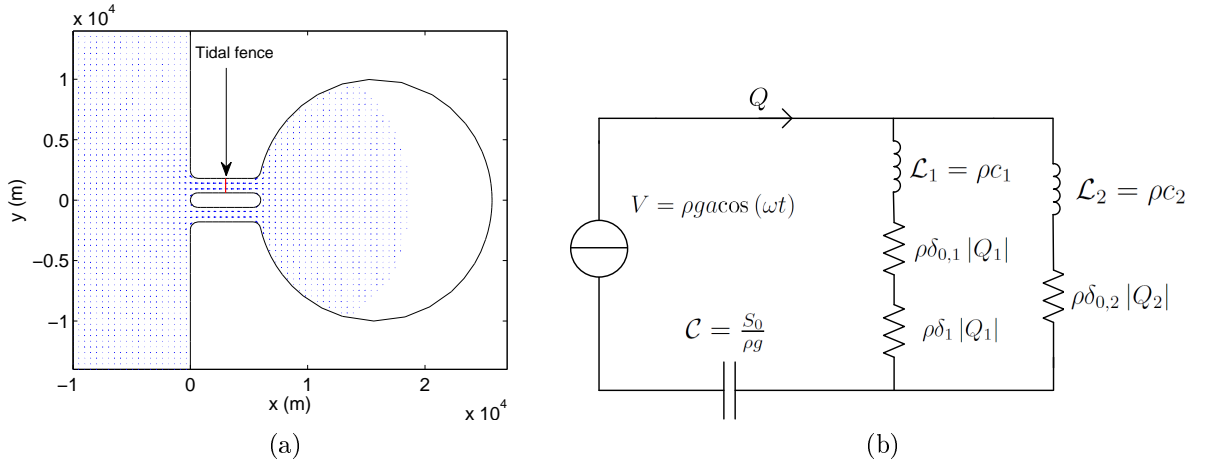


Figure 6.7: (a) Enclosed bay connected to an adjoining ocean by two parallel channels. The ocean extent, depth and bed friction are identical to the enclosed bays summarised in Table 6.1. The offshore amplitude was set to 0.7 m. (b) Equivalent electric circuit (the circuit is formed in a similar manner to the parallel channels in Section 5.4.3, Chapter 5).

site, discussed in Chapter 3.) In the natural state the amplitude of the open ocean tide for this bay measures 0.69 m, and the flow rate through the upper channel is  $1.65 \times 10^4$   $\text{m}^3/\text{s}$ . Using Equation 6.6, with  $\gamma = 0.21$  as an approximation, then gives a predicted maximum power extraction of 280 MW. Figure 6.8 (a) illustrates that this is significantly larger than the simulated power that can be extracted from the upper channel. The simple theoretical model of Blanchfield et al. [2008b] thus provides a very poor indication of the power potential for this more complicated geometry.

To understand the power extraction from the multiply connected bay it is useful to consider the equivalent electrical circuit given in Figure 6.7 (b), which shows the capacitance of the enclosed bay connected in series to two parallel impedance representing the entrance channels. In the electrical circuit it is clear that the addition of a tidal fence will increase the overall effective impedance of the circuit, but only until the effective impedance of the channels are equal to that in the undisturbed channel. If the enclosed bay has a small surface area (i.e. small capacitance and large impedance compared with the channels) the addition of turbines may have very little effect on the total flow rate in the circuit and the voltage across the capacitor. The electrical analogy therefore predicts that the change in tidal range and phase within the bay will remain unaltered, despite the introduction of the fence, if the bay surface area is sufficiently small. This appears to be the case in Figure 6.8 (b) where, in fact, the bay tidal range actually increases very slightly with the introduction of a fence. Consequently the driving elevation across the channel and the

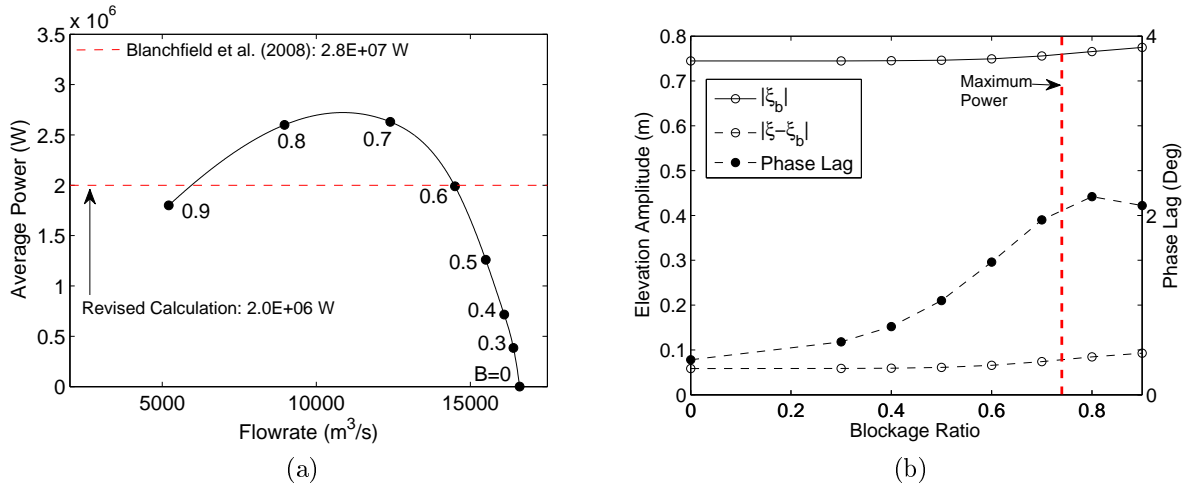


Figure 6.8: (a) Extracted power from the subchannel in Figure 6.7. (b) Bay elevation amplitude  $|\xi_b|$ , amplitude of elevation difference across the channel  $|\xi - \xi_b|$ , and phase lag of the the bay tide behind the ocean tide, as a function of fence blockage ratio (when  $\alpha_4 = 1/3$ ).

phase lag between the bay and ocean tide cannot increase significantly with the addition of turbines, drastically limiting the power potential.

Since the elevation in the bay and ocean are unaffected by the introduction of the tidal fence it would appear that a more appropriate estimate of the power potential can be calculated, as in Chapter 5, by replacing  $a$  in Equation 6.6 with the amplitude of the elevation difference between the ocean and the bay. This amplitude is 0.059 m and is significantly smaller than that in the open ocean alone. Using this revised formula, and a value of  $\gamma = 0.21$ , gives an estimated maximum extracted power of 20 MW, much closer to the simulated result.

The bay in Figure 6.7 highlights the difficulty of estimating the tidal response in more realistic channel geometries. The simple analytical model of Blanchfield et al. [2008] for an enclosed bay and Garrett and Cummins [2005] for a tidal channel are not generally appropriate to estimate the maximum extracted power of turbine fence placed subchannel. Applying an electrical analogy, such as that presented here, and in Section 5.4.3 (Chapter 5), together with numerical simulations provide a more rational approach to assess the resource for complicated geometries.

### 6.3.3 Enclosed Bay with Wetting and Drying

Large tidal currents are generally found at coastal locations with large tidal range and, as a result, significant inter-tidal area (land that is wet at high tide and dry at low tide). The Minas Basin in the Bay of Fundy, which is connected to the Bay of Fundy by the Minas passage, provides one well known example having a surface area at high water that can be three times greater than at low water (Prandle [1984] and Gregory et al. [1993])<sup>1</sup>. It is therefore of some interest to understand the effect that extracting tidal energy might have on the extent of inter-tidal area and, conversely, the effect wetting and drying might have on tidal dynamics and energy extraction.

The theoretical model described in Section 6.3.1 can be extended to include wetting and drying for a coastal site resembling an inlet to an enclosed bay. This can be achieved by defining a bay surface area that is a function of elevation within the bay (see Figure 6.9 (a)),

$$S(\xi_b) = S_o \left( 1 + \frac{\xi_b}{h_e} \right)^\alpha, \quad (6.7)$$

where the parameters  $h_e$  and  $\alpha$  describe the bathymetry of the bay and  $S_o$  is the bay surface area at still water level. Boon and Byrne [1981] and Maas [1997] have used a similar expression for the surface area to study the morphodynamic response of coastal inlet systems and the nonlinear Helmholtz response of tidal basins, respectively. Using Equation 6.7, the continuity Equation 6.2 can be updated and non-dimensionalised, in a similar manner to Equation 6.5, to give

$$\frac{d\xi'_b}{dt'} = \beta Q' (1 + \phi \xi'_b)^{-\alpha}, \quad (6.8)$$

where  $\phi = a/h_e$  and  $\alpha$  now describe the importance of wetting and drying. When  $\phi = 0$  or  $\alpha = 0$ , Equation 6.8 becomes identical to the original model of Blanchfield et al. [2008b].

The system defined by Equations 6.4 and 6.8 can be solved numerically to investigate the effect of wetting and drying. However one caveat with the numerical solution is that for a lightly damped system (i.e. small  $\lambda_T = \lambda_0 + \lambda_1$ ) the non-linearity introduced by Equation 6.8 can lead to multiple solutions (Maas, 1997), consistent with the bent response curve

---

<sup>1</sup>In the UK Townend [2005] has also calculated that the surface area of mean high water to mean low water maybe as high as 4.5, averaged across 150 estuaries. However many of these estuaries do not resemble enclosed bays.

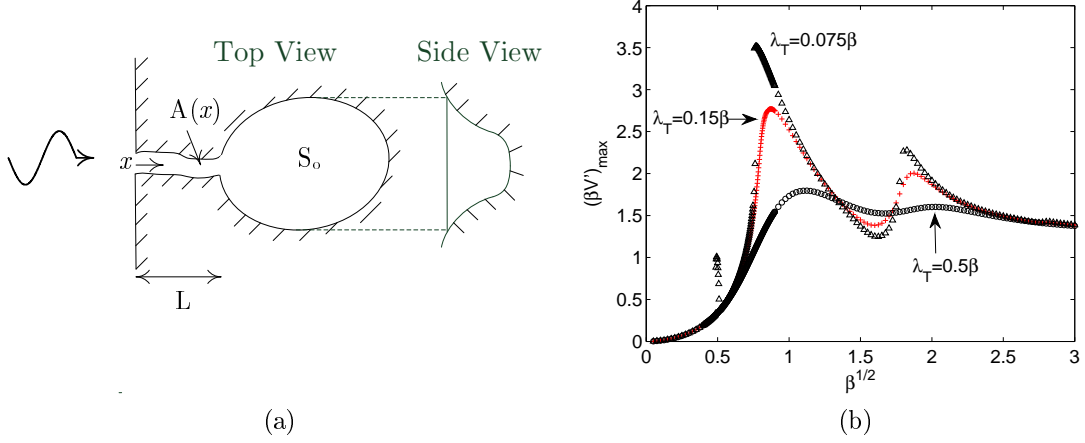


Figure 6.9: (a) An enclosed bay with sloping sides. (b) Response curve (for Equation 6.10) describing the dynamics of an enclosed bay with wetting and drying when  $\alpha = 1$  and  $\phi = 0.5$ . The jump phenomenon, consistent with multiple solutions, is evident for  $\lambda_T = 0.075\beta$ .

observed in, for example, the Duffing equation (Stoker [1950]). To explain this difficulty it is useful to rescale  $t' \rightarrow \beta^{-1/2}t'$ , and introduce the variable  $V'$ , defined by  $Q' = dV'/dt'$ , so that Equations 6.4 and 6.8 can be combined to give (Maas, 1997)

$$\cos(\beta^{-1/2}t') = \frac{d^2\beta V'}{dt'^2} + \beta^{-1}(\lambda_0 + \lambda_1) \left| \frac{d\beta V'}{dt'} \right| \frac{d\beta V'}{dt'} + \phi^{-1} \left[ (1 + (\alpha + 1)\phi\beta V')^{1/(\alpha+1)} - 1 \right]. \quad (6.9)$$

For small  $\phi$  the last term can be approximated by its Taylor series, leading to

$$\cos(\beta^{-1/2}t') = \frac{d^2\beta V'}{dt'^2} + \beta^{-1}(\lambda_0 + \lambda_1) \left| \frac{d\beta V'}{dt'} \right| \frac{d\beta V'}{dt'} + \beta V' - \frac{\phi}{2} (\beta V')^2 + \frac{\phi^2}{2} (\beta V')^3, \quad (6.10)$$

when  $\alpha = 1$ . A response curve, in terms of the maximum value of  $\beta V'$  plotted against  $\beta^{1/2}$ , for Equation 6.10 is given in Figure 6.9 (b) for various choices of  $\beta^{-1}\lambda_T$ . For  $\phi \leq 0.5$  and  $\alpha = 1$ , only values of  $\lambda_T \gtrsim 0.15\beta$  produce a smooth response curve without the jump phenomenon characteristic of multiple solutions. In the following analysis Equation 6.10 will be used to describe the dynamics in the connecting channel and all enclosed bays will lie within the range of unique solutions (i.e.  $\lambda_T \gtrsim 0.15\beta$ ,  $\phi \leq 0.5$  and  $\alpha = 1$ ).

### 6.3.3.1 Example Parameter Values

Equation 6.10 involves three parameters:  $\lambda_T$ ,  $\beta$  and  $\phi$ . Example values for the first two parameters have been listed in Table 6.1. In addition, Karsten et al. [2008] have estimated

$\beta \approx 7.6 - 13$  and  $\lambda_0 \approx 9.8 - 11.5$  for the Minas Passage, Bay of Fundy (US 11, Appendix A), and Blanchfield et al. [2008a] have obtained  $\beta \approx 1.45$  and  $\lambda_0 \approx 8$  for Masset Sound, Hadai Gwaii (US 5, Appendix A). The remaining parameter  $\phi$  is related to the change in surface area of the bay and can be determined from detailed hypsometric curves when  $\alpha \neq 1$  (a plot of basin area with depth) or, alternatively for  $\alpha = 1$ , by estimating  $h_e$  from high, mean and/or low water tidal data (Maas [1997]). As an example, for the Minas Basin the ratio of elevation amplitude in the Bay of Fundy to the basin is  $a_b/a \approx 1.1$  (Karsten et al., 2008), and the maximum surface area is approximately  $1.5S_0$ . Consequently, taking  $\alpha = 1$  gives  $\phi \approx 0.5$ . This value will be adopted as an upper bound in the following discussion.

### 6.3.3.2 Flow Dynamics

The addition of wetting and drying has a noticeable effect on the dynamics within the connecting channel. For example, Figure 6.10 presents the flow rate and the bay surface area for an enclosed bay with  $\lambda_0 = 10$ ,  $\alpha = 1$ ,  $\beta = 4$  and values of  $\phi = 0$  and  $0.5$ . It is evident that as wetting and drying become significant ( $\phi = 0.5$ ), the flow rate becomes larger on the ebb tide (negative flow rate) and the duration of the flood tide (positive flow rate) increases, implying an ebb-dominant channel (Friedrichs and Aubrey [1988]). This asymmetry can be explained by the fact that when  $\phi = 0.5$  changes in the bay elevation are slowest near high tide. Therefore there is a large lag between the elevation in the connecting sea and the bay near high tide, resulting in a slower turn to the ebb tide. At low tide the lag between the connecting sea and bay is smallest, and so the turn to flood tide is much quicker, cutting the ebb tide duration short. Since the total time of the ebb tide is therefore reduced, larger ebb currents occur to ensure mass conservation, as observed in Figure 6.10 (a). In Figure 6.10 (b) it is also evident that for  $\phi = 0.5$  the surface area at high tide is approximately three times larger than that at low tide and the surface area at low tide is proportionally smaller than that at high-tide, due to the non-linearity introduced by the sloping bay.

### 6.3.3.3 Power Extraction and Inter-Tidal Area

Because the variable bay surface area introduces asymmetry into the flow rate the power dissipated by tidal devices and bed friction, which is dependent on the velocity cubed,

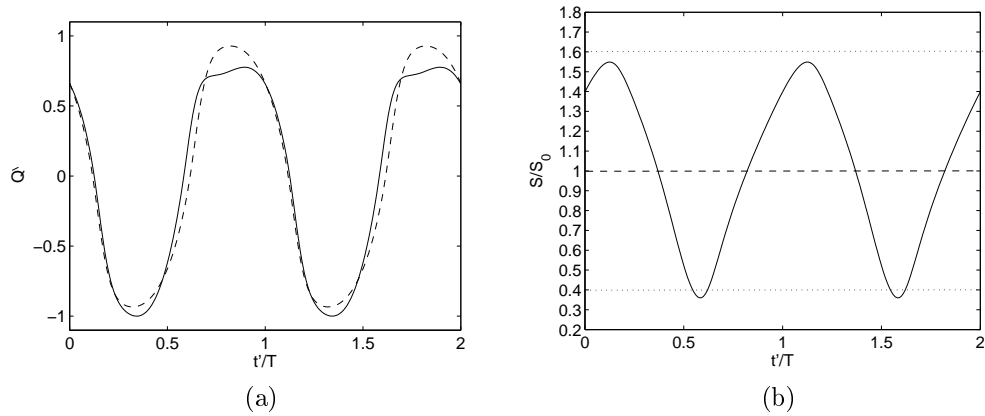


Figure 6.10: (a) Flow rate and (b) surface area, for an enclosed bay with natural friction defined by  $\lambda_0 = 10$ , and bay geometry defined by  $\alpha = 1$ ,  $\beta = 4$  and  $\phi = 0$  (dash line) and  $\phi = 0.5$  (solid line). The flow rate is normalised by the maximum absolute flow rate for  $\phi = 0.5$ . The two horizontal dotted lines in (b) highlight the asymmetry in maximum and minimum surface area.

may be asymmetric over the tidal cycle. This is illustrated in Figure 6.11 for a range of parameter values. The asymmetry is most prominent when  $\lambda_T$  is small, as would be the case for a long deep channel with low natural drag, small driving amplitude and very few tidal devices. In contrast, at higher values of  $\lambda_T$  the increased damping reduces the amplitude of oscillations in the bay and consequently reduces the effect of wetting and drying on the channel dynamics. It also is evident in Figure 6.11 that asymmetry increases with the bay geometry parameter  $\beta$ . This is because the bay surface area is small relative to the connecting channel cross-sectional area, so that a given volume flow rate into the channel leads to relatively larger tidal range in the bay and increased wetting and drying. The results in Figure 6.11 are also consistent with Figure 6.12, which plots the amplitude of the first harmonic over tide in the bay elevation, relative to the principal response, for various values of  $\beta$  and  $\lambda_T$ . For increasing  $\beta$  and small  $\lambda_T$ , the amplitude of the first harmonic increases (in fact as  $\lambda_T \rightarrow 0$  the amplitude of the second harmonic peaks close to  $\beta = 4$  consistent with superharmonic resonance). The interaction of this first (even) harmonic over tide with the principal tidal constituent causes the tidal asymmetry (Speer and Aubrey [1985]).

Since the asymmetry in power extraction is most pronounced for low  $\lambda_T$ , asymmetry will be most prominent for smaller deployments of tidal devices. For larger installations of devices it is of interest to investigate whether wetting and drying has any influence on the maximum power potential. Figure 6.13 (a) displays the non-dimensional maximum

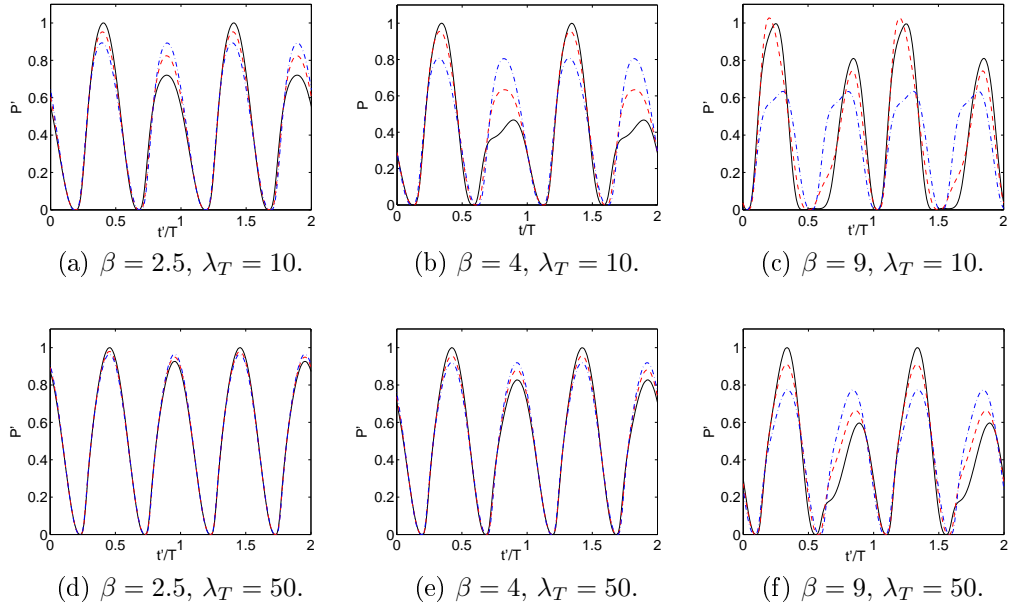


Figure 6.11: Non-dimensional power ( $\bar{P}/(\rho g^2 a^2/(\omega c))$ ), normalised by the maximum non-dimensional power obtained when  $\phi = 0.5$ , for a range of different bays. In each case  $\alpha = 1$  and three values of  $\phi$  are plotted:  $\phi = 0$  dash-dotted line;  $\phi = 0.2$  dashed line; and,  $\phi = 0.5$  solid line.

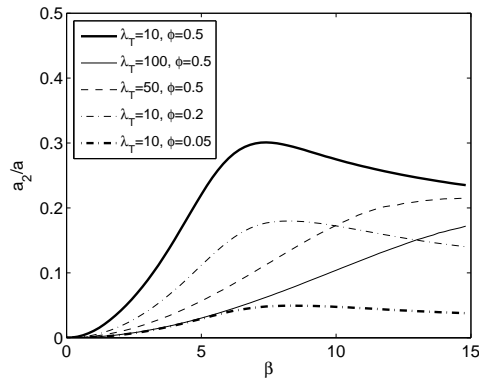


Figure 6.12: Magnitude of the first (even) harmonic over tide in elevation  $a_2$ , relative to the amplitude  $a$ , at the tidal forcing frequency for various values of  $\beta$ ,  $\lambda_T$  and  $\phi$ . In all cases  $\alpha = 1$ .

extracted power for three different bay geometries. Only when  $\lambda_0$  is small is there any noticeable dependence on  $\phi$ , but this is still less than 10%. For larger  $\lambda_0$  the effect of wetting and drying is nullified because the amplitude in the bay is damped.

Figure 6.13 (b) displays the power potential in terms of  $\gamma$ , calculated as  $\bar{P}_{max}/\rho gaQ_{max}$ , for a bay with  $\beta = 4$  and various  $\phi$ . It is evident that  $\gamma$  can reduce significantly with  $\phi$ . This is because  $\gamma$  is defined relative to the maximum flow rate within the channel, which is amplified by the wetting and drying. Consequently, although wetting and drying has little effect on the power potential, its effect on the ebb flow rate can lead to significant reduction in  $\gamma$ . Caution must therefore be taken in estimating maximum power extraction based on Equation 6.6 with an approximate  $\gamma = 0.22$  and the undisturbed maximum flow rate in bay with wetting and drying, suggested by Blanchfield et al. [2008b]. A much more consistent prediction could be made by using the average of maximum ebb and flood flow rate in Equation 6.6.

Figure 6.13 (c) displays the maximum inter-tidal area at maximum power extraction  $\Lambda_s = S_{max} - S_{min}$ , as a ratio of the intertidal area in the natural state  $\Lambda_{s,0}$  (when  $\phi > 0$ ), together with tidal range at maximum power extraction as a ratio of the range in the natural state  $\Lambda$  (when  $\phi = 0$ ). For small values of  $\lambda_0$  it can be seen that the inter-tidal area at maximum power extraction is a smaller fraction of the natural intertidal area. This is because the non-linearity associated with the changing bay surface area amplifies the natural tidal range and the natural inter-tidal area by a relatively larger amount than that at maximum power extraction. However, the effect of wetting and drying is again reduced for larger values of  $\lambda_0$ . In fact, a very close approximation for the change in inter-tidal area can be obtained from the change in tidal range for a bay with constant surface area. This is evident in Figure 6.13 (c) by the agreement between  $\Lambda/\Lambda_0$  and  $\Lambda_s/\Lambda_{s,0}$ , regardless of  $\phi$ , when  $\lambda_0$  is large.

#### 6.3.3.4 Discussion

A simple extension to the model of Garrett and Cummins [2004] to allow for wetting and drying in the enclosed bay illustrates that wetting and drying does not have a significant effect on the power potential of a channel linking an ocean to an enclosed bay. However, at lower levels of power extraction wetting and drying can introduce time asymmetry into the

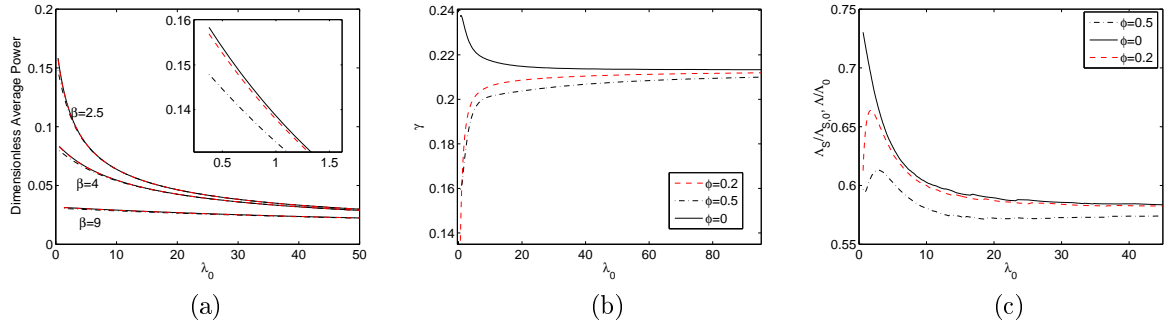


Figure 6.13: (a) Maximum non-dimensional time-average power ( $\overline{P_{max}} / (\rho g^2 a^2 / (\omega c))$ ) for various bay geometries. Solid line:  $\phi = 0$ ; Dashed line:  $\phi = 0.2$ ; Dash-dot line:  $\phi = 0.5$ . (b)  $\gamma$  for a bay with  $\beta = 4$ . (c) Change in bay surface area  $\Lambda_s$  (when  $\phi > 0$ ) and change in bay tidal elevation  $\Lambda$  ( $\phi = 0$ ) for a bay with  $\beta = 4$  at maximum power compared with natural conditions.

available power. This asymmetry may have implications for device developers looking to develop uni- or bi-directional devices and suggests that numerical models should account for wetting and drying to reflect accurately the tidal dynamics.

With respect to simulating the dynamics in the channel, the extended model assumes implicitly that  $a/h_c \ll 1$  (i.e  $c$  and  $\lambda_T$  are independent of time) and  $a/h_e \sim O(1)$ , where  $h_c$  is a typical depth in the channel and  $h_e$  is the effective depth in the bay. The model is therefore valid when  $h_e \ll h_c$ , as would be the case for a bay with large tidal flats and a deep connecting channel. In future work it will be necessary to consider an enclosed bay with  $a/h_c \sim O(1)$  and  $a/h_e \sim O(1)$ , which may occur for some bays such as the Minas Passage. When  $a/h_c$  is large, the flow through the channel can become flood dominant, or at least oppose the ebb-dominance introduced by wetting and drying (Speer and Aubrey [1985]).

## 6.4 Non-Enclosed Bays

Unlike the enclosed bays discussed above, non-enclosed or open bays have no identifiable inlet or constriction in width at their mouth to accelerate tidal streams. The large tidal currents observed in practice must therefore be attributed to either a significant driving elevation outside the bay or a resonant co-oscillation with the driving tide at the mouth of the bay. A typical example of the first scenario is the Cumberland Basin, Canada (see US 13, Appendix A), whilst the Bristol Channel, UK (Heath [1981]) is an example of the

second scenario.

Historically observed tidal resonance, and more generally the approximate tidal dynamics within many real non-enclosed bays, have been well explained using analytical models based on the one dimensional (1D) linearised shallow water equations. For example, Taylor [1921] produced remarkably accurate predictions of the observed tides in Bristol Channel using an inviscid 1D analytical model of a bay with linearly reducing depth and width. Likewise Hunt [1964] achieved equally good predictions using a similar 1D model for the Thames Estuary, allowing for an exponential reduction in width towards the head of the estuary. More recently, 1D models that account for frictional losses via a simple linearised bed friction coefficient have also been shown to give satisfactory predictions for a range of different estuaries (Prandle and Rahman [1980], Prandle [1985] and Robinson [1980]).

To understand better the tidal energy potential of non-enclosed bays Robinson and Perry [1980] extended a 1D model based on the linearised shallow water equations to include a tidal barrage represented as a perturbation in depth proportional to the local average velocity. Using this approach they demonstrated that a limit to power extraction exists for both rectangular and triangular shaped estuaries, and obtained a solution for the optimum resistance of the barrage. Their results were based on the assumption that tidal oscillations at the mouth of the bay are fixed. More recently Rainey [2009] has extended the analysis of Taylor [1921] to investigate the power that can be extracted by a tidal barrage at different positions along the Severn Estuary. Rainey [2009] showed that the extracted power typically increases as the barrage is moved towards the head of the bay, on the assumption that long waves radiated from the barrage can propagate uninhibited into deeper ocean. (However the free radiation of waves from the barrage, proposed by Rainey [2009], is unlikely once the reflected waves reach the shelf edge where reflection may result. Ideally a 2D numerical model, which includes a non-reflecting boundary condition beyond the shelf, is needed to investigate the power potential correctly.)

Although the studies of Rainey and Robinson et al. provide insight into the power extraction from open bays, their analyses were restricted to tidal barrages modelled by an arbitrary linear resistance. The available power to tidal devices installed within, say, a tidal fence was therefore not considered. In the remainder of this chapter, a simple 1D analytical model, following Lamb [1932], is developed to approximate tidal elevation and

velocity along a narrow open bay of variable geometry. A turbine fence of tidal devices is introduced into the model using linear momentum actuator disc theory (LMADT) and both the extracted and available power are calculated, under the assumption of a fixed open ocean boundary condition, for various bay geometries. The open ocean boundary is held fixed on the assumption that tides beyond, say, the continental shelf for a long bay or the mouth of the bay for a short bay, are unaltered with energy extraction. Ideally a numerical model is required to better investigate this for actual cases, in which details regarding the geometry beyond the bay must be accurately represented to determine how the elevation at the open ocean boundary reacts to energy extraction.

### 6.4.1 1D Model

Assuming that a non-enclosed bay is sufficiently narrow that Coriolis forces can be neglected and the tidal range within the bay is small compared to the depth, Lamb [1932] showed that tidal oscillations in the bay can be approximated by the shallow water mass and momentum equations

$$\frac{\partial \xi}{\partial t} + \frac{1}{b} \frac{\partial (bhu)}{\partial x} = 0, \quad \text{and} \quad \frac{\partial u}{\partial t} + g \frac{\partial \xi}{\partial x} + C_d \frac{|u|u}{h} = 0, \quad (6.11)$$

where  $u(x, t)$  describes the one dimensional cross-sectional averaged velocity,  $\xi(x, t)$  is the free surface elevation,  $C_d$  is the natural bed friction coefficient, and the channel geometry is described by the functions  $b(x)$  and  $h(x)$  that define the breadth and depth of the bay respectively (see Figure 6.14).

On the assumption that the elevation and velocity in the bay are dominated by a single tidal constituent with frequency  $\omega$ , the non-linear friction term in the momentum equation can be linearised without significant loss of accuracy (Hunt [1964]) so that solutions to Equations 6.11 are of the form  $\xi = \text{Re} \{ \xi_o e^{j\omega t} \}$  and  $u = \text{Re} \{ u_o e^{j\omega t} \}$ . Linearising the non-linear friction term with respect to the temporal oscillations and combining the mass and momentum equations then gives

$$\frac{d^2 \xi_o}{dx^2} + \frac{(b\kappa)_x}{b\kappa} \frac{d\xi_o}{dx} + \frac{\xi_o}{\kappa} = 0, \quad \text{with} \quad \kappa = \frac{gh^2}{\omega^2 h - j(8/3\pi)C_d \omega |u_o|}, \quad (6.12)$$

where the subscript indicates differentiation with respect to  $x$ . For a bay of length  $L$ , with

its head located at  $x = \epsilon L < L$ , the relevant boundary conditions for Equation 6.12 are

$$\xi(L) = a \cos(\omega t), \quad \text{and} \quad \frac{d\xi(\epsilon L)}{dx} = 0, \quad (6.13)$$

which imply a driving tide of amplitude  $a$  at the mouth of the bay and zero velocity at the head of the bay.

In practice there are many choices available for the bay geometry. However in the present work the following functions are considered

$$h(x) = h_o \left(\frac{x}{L}\right)^{m_1} \quad \text{and} \quad b(x) = b_o \left(\frac{x}{L}\right)^{m_2} \quad \text{with} \quad m_1, m_2 \geq 0, \quad (6.14)$$

where the mouth of the bay has reference dimensions  $h_o$  and  $b_o$ . In the absence of friction ( $C_d = 0$ ) a number of classical solutions have been obtained for various values of  $m_1$  and  $m_2$  (see Lamb [1932] for  $(m_1, m_2) = (0, 0), (1, 0)$  and  $(0, 1)$ , and Taylor [1921] for  $(m_1, m_2) = (1, 1)$ ). For arbitrary values of  $m_1$  and  $m_2$ , in the presence of bed friction, it is convenient to introduce non-dimensional variables  $x' = x/L$ ,  $t' = \omega t$ ,  $\xi' = \xi/a$ ,  $h' = h/h_o$ ,  $b' = b/b_o$  and  $u' = (h_o/a)u/\sqrt{gh_o}$ . Equation 6.12 then becomes

$$\Phi(\xi'_o) = \frac{d^2 \xi'_o}{dx'^2} + \left[ \frac{2m_1 + m_2}{x'} - \frac{m_1 \kappa'}{x'} \right] \frac{d\xi'_o}{dx'} + \frac{l^2}{x'^{m_1 \kappa'}} \xi'_o = 0, \quad \text{with} \quad \kappa' = \left( \frac{x'^{m_1}}{x'^{m_1} - j \lambda'_0 |u'_o|/l} \right), \quad (6.15)$$

where  $\lambda'_0 = 8/(3\pi)(C_d L/h_o)(a/h_o)$  describes an effective drag coefficient, normalised by the tidal amplitude to depth ratio, and  $l = \omega L/\sqrt{gh_o}$  describes the non-dimensional length of the bay. The boundary conditions become

$$\xi'_o(1) = 1, \quad \text{and} \quad \frac{d\xi'_o(\epsilon)}{dx'} = 0. \quad (6.16)$$

Following the specification of these two parameters the elevation along the bay can be solved numerically over the complete range of geometries defined by Equation 6.14.

To simplify the analysis in the following sections it will be assumed that  $\lambda'_0 = \lambda'_0 |u'_o|$  is constant along the length of bay. Furthermore, the head of the bay will be set at  $\epsilon = 0.001$  to avoid the numerical difficulties which result at  $x = 0$  for some bay geometries in the presence of friction. In the discussion of analytical solutions a value of  $\epsilon = 0$  will be

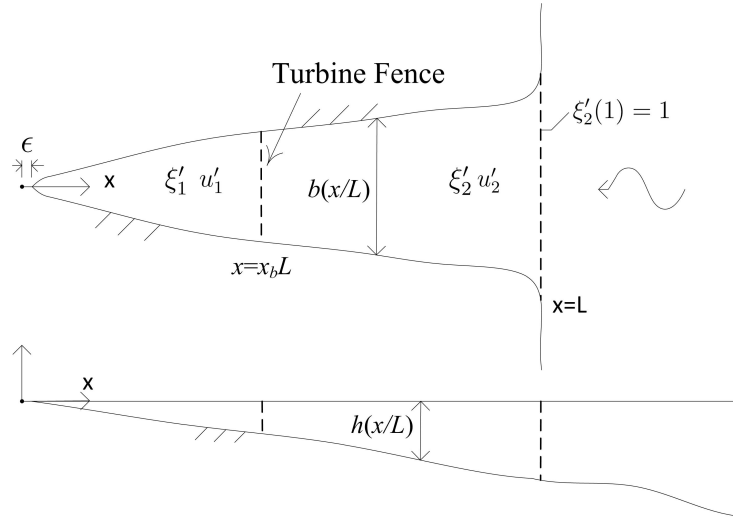


Figure 6.14: Sketch of a non-enclosed open bay with variable geometry.

assumed.

#### 6.4.1.1 Natural Resonance

It is well known that for a bay of constant depth and width, resonance will result when the bay length is equal to one quarter of the wavelength of the driving tide (where the driving tidal wavelength is  $2\pi\sqrt{gh_o}/\omega$ ). By solving Equation 6.15 with  $C_d \cong 0$  the computed response for various bay geometries are given in Figures 6.15 (a)-(c), with the bay response defined as the elevation amplitude at the head of the bay divided by that at the mouth. As expected, when  $m_1 = 0$  the response is a maximum close to  $l = \pi/2$ , which coincides with the classic result (see Figure 6.15 (a)). However, for variable geometry the equivalent “quarter wavelength” can alter considerably from this value. In particular, a reducing depth slows the wave speed so that a shorter bay will resonate, while a reducing width increases the wave speed due to continuity, and therefore increases the resonant bay length. The net result for a bay with  $m_1 = m_2 = 1$ , similar to that of the upper reaches of the Bristol Channel (Taylor [1921]), is a resonant length of  $l \approx 1.9$ , or 1.2 times the equivalent length for a rectangular bay. It is useful to bear these results in mind in the following analysis.

#### 6.4.1.2 Introducing Tidal Devices

Tidal devices can be introduced into the simple 1D analytical model as a tidal fence that extends completely across the bay (Figure 6.14). Furthermore, LMADT can be used to describe devices within the tidal fence provided the length scale over which vertical mixing

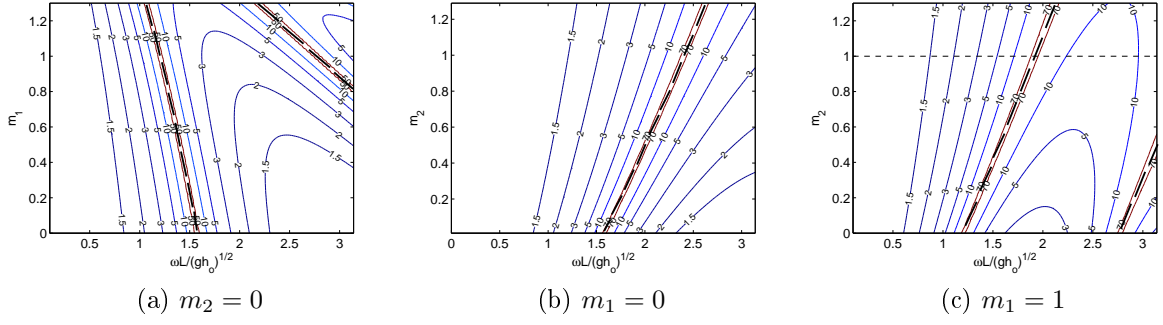


Figure 6.15: Elevation response for an open bay with various values of  $m_1$  and  $m_2$ . The dashed line in (c) coincides with a bay that has  $m_1 = m_2 = 1$ . The thick dark lines correspond to unbounded elevation response. (See Equation 6.14 for definition of  $m_1$  and  $m_2$ .)

occurs in the wake of the fence is small compared to the characteristic tidal wavelength and variation in bay geometry. Assuming this is the case, and that the Froude number is small everywhere in the bay, the perturbation in depth across the fence can be given as a function of the continuous velocity through the fence:

$$\Delta\xi = \frac{\Delta p}{\rho g} = \frac{C_T B}{2g} |u| u, \quad (6.17)$$

where  $C_T$  is the thrust coefficient and  $B$  is the blockage ratio of devices within the fence assuming the Froude number is small (see Section 2.3.3, Chapter 2). This expression can be linearised without significant loss in accuracy provided that the elevation and velocity within the bay are dominated by a single constituent and non-dimensionalised, leading to

$$\Delta\xi' = \frac{8}{3\pi} \frac{C_T B}{2} \frac{a}{h_o} |u_o'| u', \quad (6.18)$$

In terms of non-dimensional variables the elevation along a bay with a tidal fence prescribed by LMADT then becomes

$$\Phi(\xi_1') = 0, \quad \text{for } x' \leq x_b, \quad \text{and} \quad \Phi(\xi_2') = 0, \quad \text{for } x_b \leq x' \leq 1, \quad (6.19)$$

with the relevant boundary conditions at the turbine fence ( $x' = x_b$ )

$$u_1'(x_b) = u_2'(x_b) \quad \text{and} \quad \xi_1'(x_b) - \xi_2'(x_b) = \lambda_1' |u_2'(x_b)| u_2'(x_b). \quad (6.20)$$

where  $\lambda'_1 = 8/(3\pi)(C_T B/2)(a/h_o)$  and,  $\xi'_1, \xi'_2, u'_1$  and  $u'_2$  are the complex elevation and velocity either side of the fence (i.e.  $\xi'_o = \xi'_1 \cup \xi'_2$  and  $u'_o = u'_1 \cup u'_2$ ; see Figure 6.14). To close the problem a no-flow boundary can be specified at the head of the bay and the elevation specified at the mouth of the bay, such that

$$\xi'_2(1) = 1, \quad \text{and} \quad \frac{d\xi'_1(\epsilon)}{dx'} = 0. \quad (6.21)$$

## 6.4.2 Maximum Power Extraction

### 6.4.2.1 Inviscid Case

To explore the maximum power that can be extracted by a tidal fence situated somewhere along a non-enclosed bay it is instructive first to consider the simple case of a rectangular bay ( $m_1 = m_2 = 0$ ) with no natural friction ( $\lambda'_0 = 0$ ) and turbine fences modelled as a fixed linear resistance (i.e. let  $\lambda'_1 = \lambda'_1 |u'_2(x_b)|$  be constant). A closed-form solution to Equation 6.19 is then (Robinson and Perry [1980])

$$\xi'_1 = A_1 \cos(x'l); \quad \xi'_2 = A_2 \cos(x'l) + B_2 \sin(x'l), \quad \text{and} \quad (6.22)$$

$$u'_1 = -jA_1 \sin(x'l); \quad u'_2 = -j(A_2 \sin(x'l) - B_2 \cos(x'l)), \quad (6.23)$$

where the coefficients are

$$A_1 = A_2 - B_2 \cot(x_b l), \quad (6.24)$$

$$A_2 = \sec(l) - B_2 \tan(l), \quad (6.25)$$

$$B_2 = \frac{\lambda'_1 \sin^2(x_b l)}{\lambda'_1 \sin(x_b l) \cos((1-x_b)l) - j \cos(l)}. \quad (6.26)$$

It is convenient to explore this solution in terms of the elevation amplitude on the ocean side of the fence, relative to that at the mouth of the bay,

$$\mathcal{A} = \left| \frac{\xi'_2(x_b)}{\xi'_2(1)} \right| = \left| \frac{\lambda'_1 \sin(x_b l) - j \cos(x_b l)}{\lambda'_1 \sin(x_b l) \cos((1-x_b)l) - j \cos(l)} \right|, \quad (6.27)$$

which describes, in part, the effect that a turbine fence will have on the natural tidal range within the bay. In terms of this measure, when there are no tidal devices within the fence

( $\lambda_1^* = 0$ ) it can be seen that the relative tidal range varies along the bay according to

$$\mathcal{A} = \mathcal{A}_1 = \left| \frac{\cos(x_b l)}{\cos(l)} \right|, \quad (6.28)$$

which increases towards the head of the bay when  $l < \pi/2$  and is unbounded for all values of  $x_b$  when the non-dimensional length approaches  $l = \pi/2$  at which point the bay resonates. In the opposite extreme, when many tidal devices are placed within the tidal fence so as to create a tidal barrier ( $\lambda_1^* \gg 1$ ), the tidal range behaves like

$$\mathcal{A} = \mathcal{A}_2 = \left| \frac{1}{\cos((1 - x_b)l)} \right| \quad (6.29)$$

which has a resonant response when the distance between the barrier and the mouth approaches a quarter wavelength  $(1 - x_b)l = \pi/2$ , while, for bay lengths less than this, the range increases monotonically as the barrier is moved towards the head.

In between the two extremes of no devices and many devices the tidal range on the ocean side of the fence varies between Equation 6.28 and Equation 6.29. Provided that  $l < \pi/2$ , it is easy to show that

$$\mathcal{A}_1 \leq \left| \frac{\lambda_1^* \sin(x_b l) - j \cos(x_b l)}{\lambda_1^* \sin(x_b l) \cos((1 - x_b)l) - j l \cos(l)} \right| \leq \mathcal{A}_2, \text{ for all } \lambda_1^* \text{ and } x_b \in (0, 1), \quad (6.30)$$

which implies a monotonic reduction in tidal range on the ocean side of the fence, as compared to natural conditions, when the fence is placed at any position along the bay. The only exceptions being at the head or mouth of the bay where neither an increase or decrease in range results compared with natural conditions. For longer bays,  $l > \pi/2$ , the result is not so simple. For example, the addition of tidal devices can act to increase the elevation on the ocean side of the fence when the distance between the mouth and fence approaches  $\pi/2$ . In this sense the addition of the barrier effectively ‘‘tunes’’ the bay closer to resonance. However, when a fence is not placed at this resonant location an decrease in range occurs if the fence is placed towards the middle of the bay. The region over which this decrease occurs is bounded by the roots of the expression  $\tan(l) + (1 + \cos^2(x_b l)) / (\sin(x_b l) \cos(x_b l)) = 0$ .

To explore the power potential of the simple bay, the power extracted by the tidal fence

can be written as

$$P = \rho g \Delta \xi(x_b L) (b(x_b L) h(x_b L) u(x_b L)) \quad (6.31)$$

where  $\Delta \xi(x_b L)$  is the change in elevation across the fence and  $u(x_b L)$  is the velocity through the fence. This can be non-dimensionalised so that

$$P' = \frac{P}{a^2 \rho g \sqrt{g h_o b_o}} = (\xi_1'(x_b) - \xi_2'(x_b)) b' h' u_2'(x_b) = b' h' \lambda_1' |u_2'(x_b)| (u_2'(x_b))^2. \quad (6.32)$$

Keeping  $\lambda_1^* = \lambda_1' |u_2'(x_b)|$  constant, it therefore follows from Equations 6.22 and 6.23 that the non-dimensional power time-averaged over a tidal cycle can be written for the rectangular bay as

$$\overline{P'} = \frac{1}{2} \lambda_1^* |u_2'(x_b)|^2 = \frac{1}{2} \lambda_1^* \mathcal{A}^2 \left| \frac{1}{\lambda_1^* - j \tan^{-1}(x_b l)} \right|^2, \quad (6.33)$$

which illustrates that the extracted power is dependent on the location and resistance of the turbine fence. For very short bays  $l \ll \pi/2$ , it follows from Equation 6.27 that  $\mathcal{A} \sim 1$ , so that

$$\overline{P'} \approx \frac{1}{2} \lambda_1^* \left| \frac{1}{\lambda_1^* - j \tan^{-1}(x_b l)} \right|^2. \quad (6.34)$$

This has a maximum as  $\lambda_1^*$  is varied of  $\overline{P'}_{max} = \frac{1}{4} \tan(x_b l)$  and, given  $l \ll \pi/2$ , implies that the maximum power increases almost linearly with the distance of the fence from the head of the bay. Figure 6.16 (a) plots the maximum power extracted by a fence located at all positions along a rectangular bay with  $l$  equal to 0.5. It is evident that the increase in power is close to linear and, as a result, the maximum power extraction is at the mouth of the bay. It also useful to note that the optimum resistance of the fence is given by  $\lambda_{1,max}^* \sim \tan^{-1}(x_b l)$ , which reduces like  $1/(x_b l)$  with distance from the head for a short bay.

For longer bays the power from Equation 6.33 can be rewritten in full as

$$\overline{P'} = \frac{1}{2} \lambda_1^* \left| \frac{\sin(x_b l)}{\lambda_1^* \sin(x_b l) \cos((1 - x_b)l) - j \cos(l)} \right|^2. \quad (6.35)$$

If  $l > \pi/2$ , the left term in the denominator of this expression is zero when the fence is placed one quarter wavelength from the mouth of the bay. The extracted power is then unbounded for large  $\lambda_1^*$ , as shown in Figure 6.16 (b).

In summary, based on the analysis of a simple rectangular bay it is apparent that for bays shorter than the resonant length the tidal range will reduce with the addition of tidal

fences and the extracted power increases with distance from the head of the bay so that the best place to position a fence is at the mouth of the bay. For longer bays, the tidal range and power increase significantly when the fence is approximately one quarter wavelength from the mouth of the bay. Away from this resonant location power extraction is reduced and a resulting increase or decrease in tidal range depends on the particular location of the fence.

Figure 6.16 (c) and (d) show that similar results hold for other bay geometries. For shorter bays (Figure 6.16 (c)) the power increases monotonically towards the mouth of the bay. The increase is almost linear when  $m_2 = 0$ . When  $m_2 > 0$  the power increases faster but is smaller than for  $m_2 = 0$ , reflecting both the change in size and the absolute size of the bay surface area enclosed by the fence. These results can be borne out of more complicated analytical solutions for different integer values of  $m_1$  and  $m_2$  and is consistent with the importance of surface area in an enclosed bay discussed in Section 6.3. For the longer bays (Figure 6.16 (d)) an unbounded extraction is evident at a location along the bay that is dependent on the particular resonant length of each bay. It should also be noted that the results in Figure 6.16 are identical when  $\lambda'_1$  is held constant, as opposed to  $\lambda_1^*$ .

It is of considerable interest to compare the maximum extracted power to the rate at which potential energy is stored and dissipated within the channel, which can be approximated in the absence of extraction by the maximum flow rate at a given point along the bay  $Q_o = b'(x)h'(x)|u(x)|$  multiplied by the maximum dynamic pressure  $p_o = \rho g |\xi(x)|$ . This metric is of particular interest because it has been used, with considerable success, to summarise the power potential in short channels and inlets (Garrett and Cummins [2005, 2008]). Figure 6.17 (a) plots the parameter  $\gamma$ , equal to the maximum extracted power divided by the potential energy stored and dissipated shoreward of the tidal fence, given at each point along the bay by

$$\gamma = \frac{\lambda'_1 b'(x_b) h'(x_b) |u'_2(x_b)|^3}{p_o(x_b) Q_o(x_b)}, \quad (6.36)$$

for a range of different bay length and geometry. It is evident that for short bays this parameter is approximately 0.25 at all points along the bay, which agrees well with the analysis of a frictionless inlet to an enclosed bay discussed by Blanchfield et al. [2008b]. For longer bays, however, the parameter is only similar to this value close to the mouth and

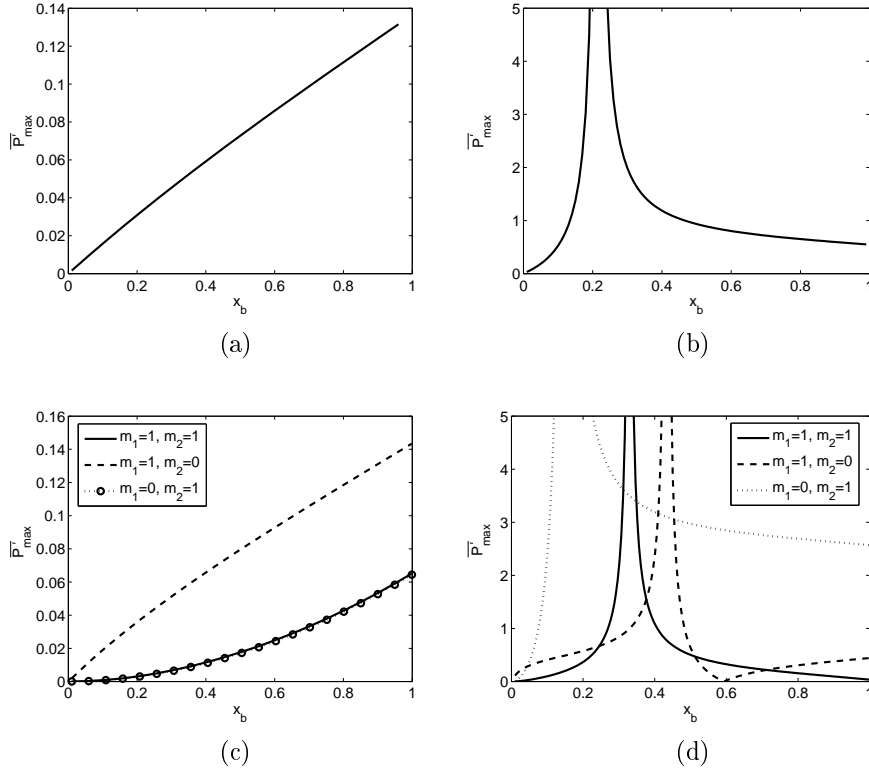


Figure 6.16: Maximum average power extraction at various positions along an open bay. (a) Rectangular bay of length  $l = 0.5$ , (b) Rectangular bay of length  $l = 2$ , (c) Various bay geometry ( $l = 0.5$ ), (d) Various bay geometry ( $l = 2.5$ ).

head of the bay where there is no change in tidal range with the introduction of a fence. Away from these locations the parameter can increase close to where the extracted power and change in elevation is a maximum along the bay and also where the tidal range in the natural state is small (i.e. at an elevation node point). Towards the middle of a long bay the parameter may decrease well below 0.25 because of the reduction in tidal range that can result from the introduction of the fence. It would thus appear that a constant value of  $\gamma \sim 0.25$  is not as successful at predicting the power potential of a resonant non-enclosed bay, when a tidal fence is located at certain positions along the bay, as it is for frictionless inlets and short channels.

#### 6.4.2.2 Including Natural Dissipation

In the preceding section the variation in power extraction along the bay was analysed in the absence of natural friction. Actual bays, of course, have natural dissipation and this can be accounted for in the analytical model via  $\lambda_0^*$ . Figure 6.18 plots the maximum extracted power for a fence situated at various locations along a rectangular bay ( $m_1 = m_2 = 0$ )

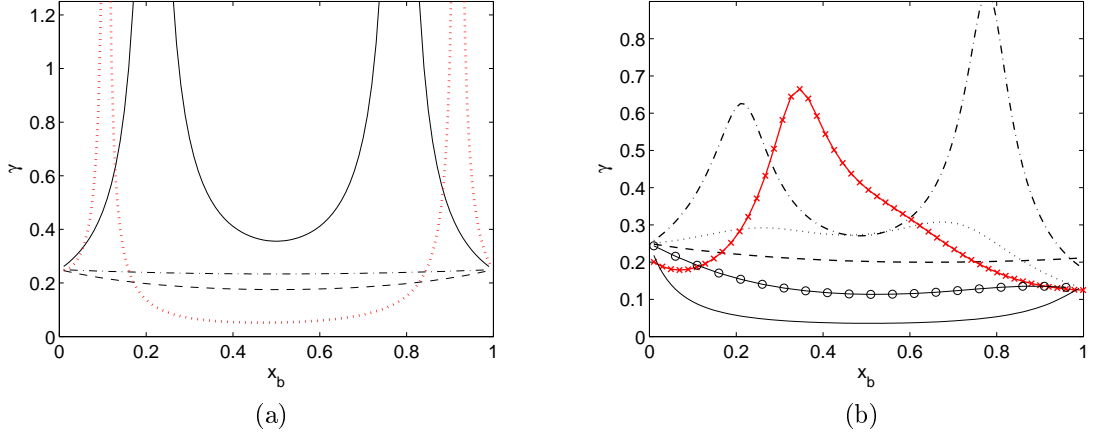


Figure 6.17: (a) Parameter  $\gamma$  computed for various positions along a frictionless open bay. Solid line:  $m_1 = m_2 = 0$ ,  $l = 2.0$ , dashed line:  $m_1 = m_2 = 0$ ,  $l = 1.0$ , dash-dot line:  $m_1 = m_2 = 0$ ,  $l = 0.5$ , and dotted line:  $m_1 = m_2 = 1$ ,  $l = 2.5$ . (b) Same as (a) but for an open bay with bed friction. Solid line:  $m_1 = m_2 = 0$ ,  $l = 1.5$ ,  $\lambda_0^* = 0.25$ , solid circle line:  $m_1 = m_2 = 0$ ,  $l = 1.5$ ,  $\lambda_0^* = 1$ , dashed line:  $m_1 = m_2 = 0$ ,  $l = 0.5$ ,  $\lambda_0^* = 1$ , dash-dot line:  $m_1 = m_2 = 0$ ,  $l = 2.5$ ,  $\lambda_0^* = 0.25$ , dotted line:  $m_1 = m_2 = 0$ ,  $l = 2.5$ ,  $\lambda_0^* = 1$ , and solid cross line:  $m_1 = m_2 = 1$ ,  $l = 2.5$ ,  $\lambda_0^* = 0.25$ .

and triangular bay ( $m_1 = m_2 = 1$ ) for different levels of natural friction  $\lambda_0^*$ . The extracted power in each figure is compared with the time average non-dimensional natural power dissipation within the channel  $\overline{P}'_d$ , which is equal to the time average flux of power entering through the mouth of the bay:

$$\overline{P}'_d = b'(1)h'(1)\overline{\xi'_2(1)u'_2(1)} = \int_0^1 \lambda_0^* b' \overline{(u'_o)^2} dx' + \overline{P}', \quad (6.37)$$

where  $\overline{P}'$  is the time average of power extracted by the turbine fence (Equation 6.32).

Figures 6.18 (a)-(d) represent short bays, with a length below that required for resonance. For these bays it is clear that increasing natural friction leads to a decrease in extracted power at all points along the bay. This is to be expected, since the turbine fence must now compete with natural friction to extract power. However, as noted by Robinson and Perry [1980], the amount of power that can be extracted from the bay can still exceed that dissipated naturally without a turbine fence (which is equal to the total dissipation when  $x_b = 0$ ) by several orders of magnitude. This is in fact to be expected since, in the limit of no natural dissipation, the extracted power was shown in the previous section to be greater than zero and so in that case infinitely larger than the natural dissipation. Less expectantly, Figures 6.18 (a)-(d) also show that for a fence placed at the mouth of the bay

more total power is dissipated (due to both natural bed friction and the fence) in each of the bays when the natural friction is lower. This implies that a tidal fence, which represents a concentrated friction along the bay, can extract power more effectively, when positioned towards the mouth of the bay, than a distributed roughness over the whole bay.

Figures 6.18 (e)-(h) represent bays that are longer than resonant length. What is immediately evident in these plots is that the presence of friction ensures that the extracted power is now bounded for a fence placed a quarter wavelength from the mouth of the bay. However, unless the friction is large, this resonant location is still the optimum place to deploy fences along the bay. (To provide some perspective on the friction parameter, a bay with length 350 km, drag coefficient of 0.0025, depth 80 m and average current amplitude 1.5 m/s, would have an equivalent damping of  $\lambda_0^* \sim 0.3$  and the effective length would be  $l \sim 1.7$ .) As was the case for short bays, the natural dissipation due to bed friction correlates poorly with the maximum extracted power across the different bays and fence locations. However, unlike for a short bay, the introduction of a turbine fence may now lead to an increase in dissipation due to bed friction if the fence tunes the bay closer to resonance (i.e. Figures (e), (g) and (h)).

For the inviscid bays it was shown that the ratio  $\gamma$ , which is equal to maximum extracted power divided by the product of maximum natural dynamic pressure and flow rate, varied considerably along the length of the bay. It is now useful to investigate this parameter in the presence of friction<sup>2</sup>. Figure 6.17 (b) shows, for a number of bays, there is considerable variation in  $\gamma$  along the bay when the total bay length is comparable to, or greater than, the resonant length for realistic values of natural friction. The reason for the variation is, as in the inviscid case, due to the fact that the tidal range seaward of the fence changes with the addition of devices and so the rate at which potential energy is stored or dissipated in the natural state no longer provides as good an indication of the power that can be extracted. Although linear bed friction is adopted here, a similar variation to this would be found with a representation of bed friction that varies quadratically with velocity.

---

<sup>2</sup>It should be noted, however, that the natural friction considered here varies linearly with velocity (i.e.  $\lambda_0^*$  is constant). For reference, the equivalent result of Blanchfield et al. [2008b] for an enclosed bay in the limit of large linear natural friction is  $\gamma \rightarrow 0.125$ , which is less than the value of  $\gamma = 0.21$  obtained when the friction is taken to vary with the velocity squared.

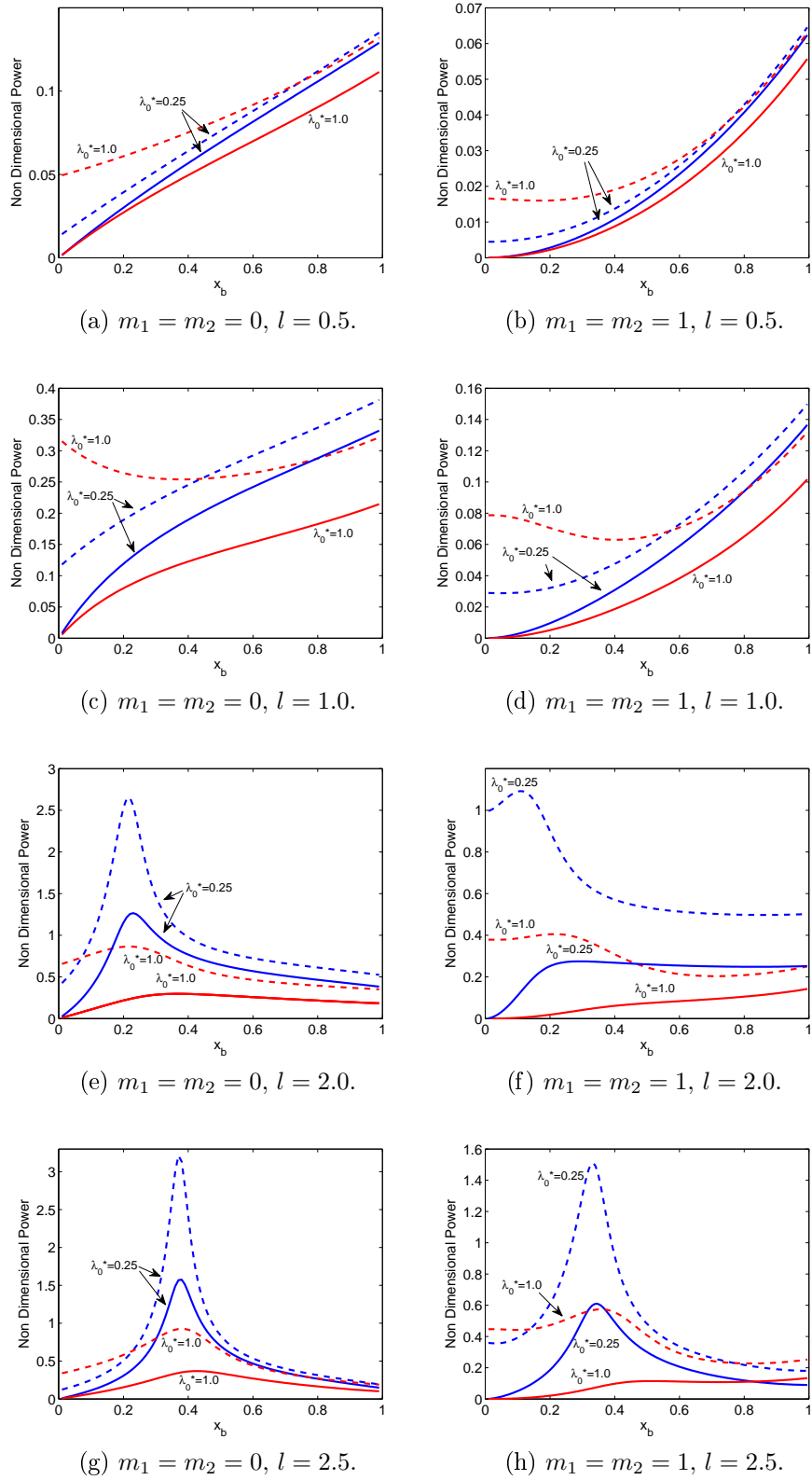


Figure 6.18: Maximum extracted power (solid lines) and total dissipated power due to bed friction and tidal fence (dashed lines) for a range of non-enclosed bays.

### 6.4.3 Maximum Available Power

Using LMADT to relate the resistance of the turbine fence to the devices within it, the power extracted by the fence can be written as

$$\overline{P'} = \frac{1}{2} \lambda'_1 b' h' |u'_o(x_b)|^3 = r \frac{C_T B}{2} b' h' |u'_o(x_b)|^3, \quad \text{with} \quad r = \frac{8}{6\pi} \frac{a}{h_o}, \quad (6.38)$$

so that the total available power to devices within the fence is simply

$$\overline{P'_a} = \eta \overline{P'} = \alpha_2 r \frac{C_T B}{2} b' h' |u'_o(x_b)|^3, \quad (6.39)$$

where  $\alpha_2$ , which defines the velocity through the devices, is equivalent to the device efficiency on the assumption that the Froude number is small (see Chapter 2) and  $r$  parameterises the non-dimensional amplitude. From Equation 6.39 it is possible to calculate the available power, for a given value of  $r$  (defined in Equation 6.38), as a function of the device blockage ratio and turbine velocity coefficient at any point along a bay. As an example Figures 6.19 (a) and (b) plot contours of the available power, normalised by maximum extractable power, for a turbine fence positioned half way along a short triangular bay when  $r$  is taken to be 0.1 and 1.0, respectively. These plots are similar to those presented recently by Vennell [2010] for a rectangular channel. The thick dark lines in both figures illustrate the maximum available power as a function of the blockage ratio. It is clear that as the blockage ratio increases the maximum available power increases, which is consistent with the devices becoming more efficient. However for small blockage ratio the devices can not achieve the maximum level of power extraction and therefore yield the most power, in the limit of zero blockage, when they maximise the power coefficient ( $\alpha_2 \rightarrow 2/3$ ) as opposed to the efficiency. The available power is then a very small fraction of that which could be extracted with a highly blocked fence and is equal to 0.59 times the natural kinetic flux.

Comparing Figures 6.19 (a) and (b) it is evident that more of the maximum extracted power is available, for a given blockage ratio, when a higher value of  $r$  is used. This is a general result for all bays and arises because the extracted power, for a given bay, is dependent on the resistance  $\lambda'_1$ : larger values of  $r$  ensure that the velocity in the bay is larger and so a reduced thrust (i.e. smaller  $C_T B/2$ ) is required by the devices at any level of power extraction. For a fixed blockage ratio, the ratio of thrust to power coefficient

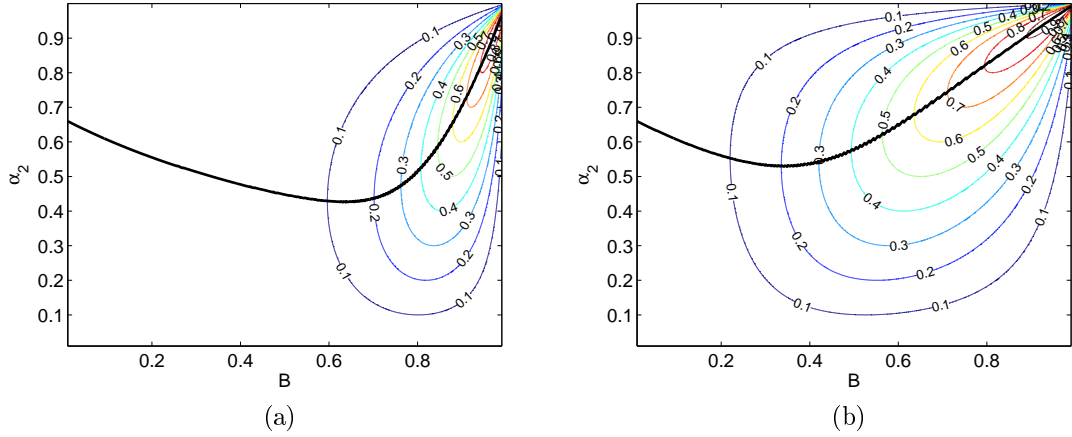


Figure 6.19: Contours of maximum available power, normalised by the local maximum extracted power, plotted as a function of blockage ratio and wake induction factor  $\alpha_4$ . The turbine fence is position half way along a triangular bay ( $m_1 = m_2 = 1$ ) with  $l = 1$  and  $\lambda_0^* = 0$ . (a)  $r = 0.1$ , (b)  $r = 1$ . The thick dark line indicates the maximum available power for a given blockage ratio.

(equal to  $1/\alpha_2$ ) must reduce implying an increase in device efficiency and available power.

#### 6.4.3.1 The Optimum Location to Place a Fence

In practice the area (or the number) of tidal devices within a fence will be constrained for economic reasons. An important question then concerns the best location to deploy a fence of limited devices along the bay to maximise the available power. The answer to this question is not immediately obvious because, for a bay with variable cross-sectional area, placing turbines towards the head of the bay will increase the blockage ratio and fence efficiency, but will also reduce the maximum extracted power. To explore this trade-off further, Figure 6.20 presents contour plots of the maximum available power (i.e. optimised velocity coefficient  $\alpha_2$ ) for tidal fence of various blockage ratio positioned at different locations along the several bays. Superimposed on these plots are lines corresponding to turbine fence with a fixed number of devices or turbine area (each bay has  $r = 0.1$ ).

Initially ignoring the lines of constant fence area, what is clear from all of the plots is that, for a fixed location along the bay, the highest fraction of extractable power is available when a fence with large blockage ratio is used. In contrast, for fixed fence blockage ratio, the highest fraction of extractable power occurs at various positions along the bay, depending on the particular bay. For example, for the shorter bays ( $l = 1$ ) the available power is optimised with a fence placed at the mouth regardless of the blockage ratio. If a fence of

given blockage ratio is not placed at the mouth of a short bay then the available power reduces as the fence is moved towards the head of the bay. This reduction is fastest for a bay with reducing width (i.e.  $m_2 > 0$ ) because the surface area of the bay enclosed by the fence and the extracted power reduces faster with distance from the mouth. In terms of the longer bays ( $l = 2$ ), the most available power is achieved at a distinct location within the bay where the extracted power is maximised, provided that the fence blockage ratio is close to unity (i.e. Figure 6.20 (g)). If the blockage ratio is less than unity there is shift in the optimum location of the turbine fence towards the location of maximum undisturbed kinetic flux within the bay as  $B$  reduces smoothly to zero (dark chained lines in Figures 6.20 (g,h) locates the optimum location along the bay based on available power).

With respect to the effects of bed friction, Figures 6.20 (d,e) illustrate that for shorter bays additional bed friction generally reduces the available power at all locations along the bay for a given blockage ratio. This is consistent with the need for a higher turbine thrust coefficient to overcome the increased bed friction and extract a given quantity of power, thereby reducing the device efficiency and the available power. For the longer bays, comparing Figures 6.20 (g) and (h) illustrates that bed friction can have a significant effect on the available power at any point along the bay because it can alter the position of maximum power extraction along the bay. Increasing the friction coefficient to  $\lambda_0^* = 0.5$  moves the location of maximum available power, for a highly blocked fence, to the mouth of the bay.

Returning to the realistic constraint of fences with a fixed number of devices, the dashed lines in all of the plots in Figure 6.20 show that, despite the location of maximum power extraction along the bay, more power is available to the fence when it is moved away from the mouth of the bay: the gain in efficiency due to the increased blockage experience by the devices outweighs any reduction in extracted power that may result. Consequently the optimum location to place a tidal fence is dependent on the geometry of the bay and the number of devices that are used to construct it, as opposed to simply the location of maximum power extraction.

For short bays the increase in available power achieved by moving a fence with a fixed number of devices away from the mouth of the bay is greater when the contraction in the channel cross-section is associated with a reduction in depth rather than width (Figure 6.20

(c)). This is because the extracted power reduces faster when the width varies, limiting the available power despite the increase in efficiency achieved by the devices. When the depth and width reduce at a faster rate (compare Figures 6.20 (d) and (e)), both the efficiency of the fence and consequently the available power increases more rapidly as the devices are moved away from the mouth of the bay (Figure 6.20 (f)).

For the longer bays there can be a significant gain in available power by optimally siting a limited number of devices in the bay because both the fence efficiency and the maximum power can increase as the devices are moved away from the mouth. This is illustrated in Figure 6.20 (i), where the normalised available power approaches unity when  $\lambda_0^* = 0.15$  if a fence which has a blockage ratio at the mouth of the bay equal to 0.025 (line 3-4 in Figure 6.20 (i)) is moved to  $x_b \approx 0.2$ .

## 6.5 Conclusions

Numerical simulations of an isolated enclosed bay agree well with the theoretical model of Blanchfield et al. [2008]. However, for more complex enclosed bays, such as an enclosed bay with two inlet channels, the model of Blanchfield et al. [2008] can lead to significant errors. Numerical simulations or alternative theoretical models are required to predict the maximum extraction in those cases.

Accounting for wetting and drying in the model of Blanchfield et al. [2008] illustrates that the variation in bay surface area has little effect on the maximum power that can be extracted from an isolated enclosed bay, but can lead to asymmetry in power extraction over a tidal cycle.

The tidal range in an open bay will typically decrease with the addition of a tidal fence, however if the bay is longer than a resonant length (an equivalent quarter wavelength) and the fence is placed approximately one quarter wavelength from the mouth of the bay, then an increase may result. Similarly the extracted power is a maximum at the mouth of the bay unless the bay is longer than the resonant length and does not have excessive bed friction, in which case the extracted power is greatest when the fence is also placed approximately one quarter wavelength from the mouth of the bay.

The available power at all points along a non-enclosed bay is greatest when a fence

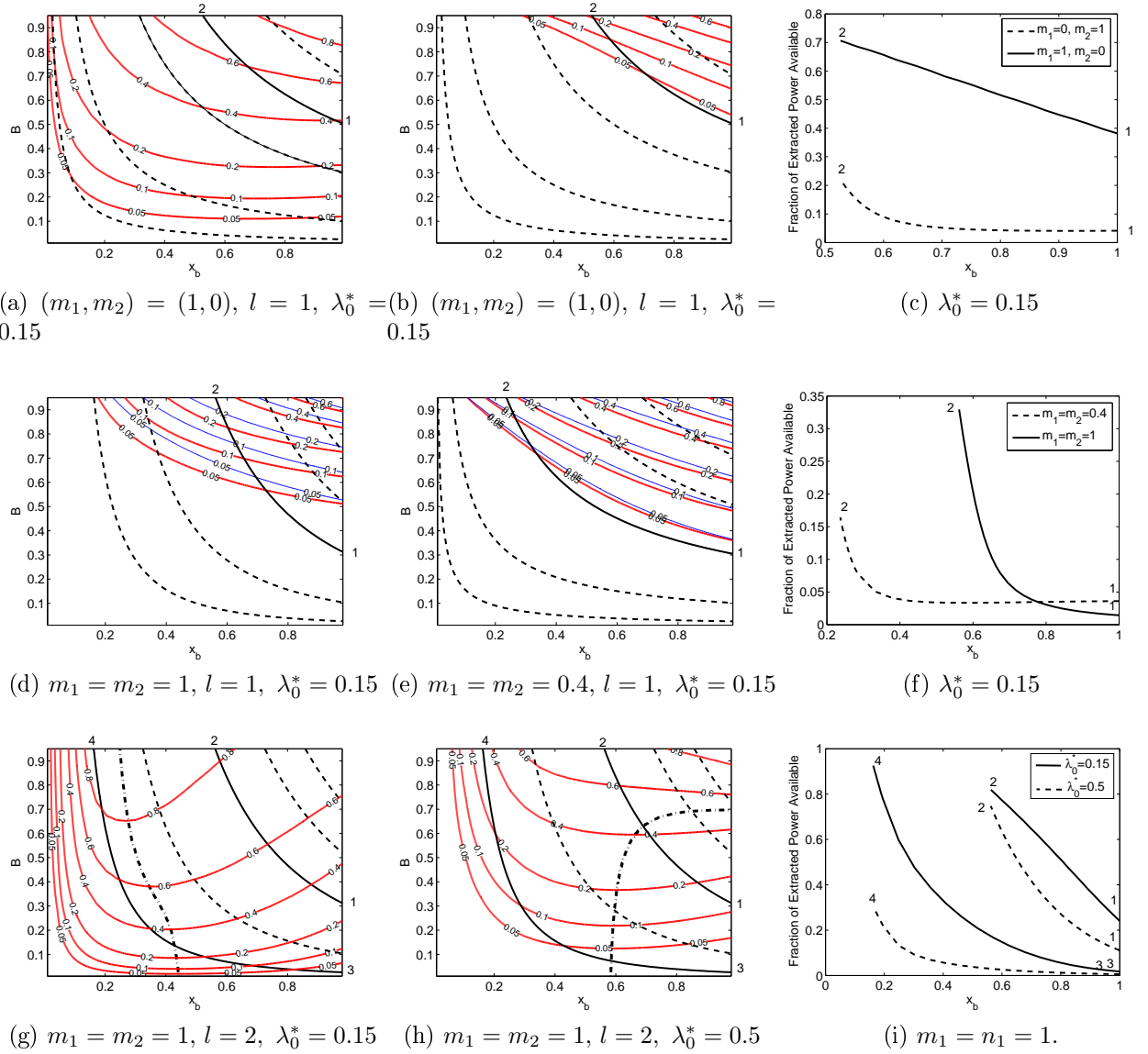


Figure 6.20: (a,b,d,e,g,h) Maximum available power, normalised by maximum extractable power from the bay, as a function of fence blockage ratio  $B$  and fence location  $x_b$ . Dotted and solid lines track tidal fences with constant area. In Figures (d,e) the additional thin contour lines represent  $\lambda_0^* = 1.0$ . In Figures (g,h) the thick chained lines locate the maximum available power as a function of blockage ratio. (c,f,i) Available power with position along the bay for a fence of fixed area: the lines correspond to the contour plots on the same row of figures.

with large blockage ratio is deployed. Furthermore, the available power is maximum along the bay if the highly blocked fence is placed at the location of maximum power extraction. For the more realistic case of a fence with a fixed number of devices, or turbine area, the optimum place to locate a fence to maximise the available power is dependent on the geometry of the bay and the number of devices installed within the fence. Importantly, this location may no longer coincide with the location of maximum power extraction.

# Chapter 7

## Coastal Headland

### 7.1 Introduction

In this chapter numerical simulations are undertaken to investigate the energy potential of a tidal fence deployed near to an idealized Gaussian-shaped headland with a sloping seabed. Simulations indicate that power extracted by the tidal fence is limited because flow will bypass the fence, predominantly on the ocean side, as the thrust applied by the devices increases. For the dynamic conditions, fence placements and headland aspect ratios considered, the maximum power extracted at the fence is not related in any obvious way to the local undisturbed kinetic flux or to the natural rate of energy dissipation due to bed friction (although both of these have been used in the past as measures of the amount of power that may be extracted). The maximum extracted power is found to be insensitive to the size and spacing of devices within the fence; however the available power (equal to the extracted power net of vertical mixing losses in the immediate wake of devices) is optimized for devices with large area and small centre-to-centre spacing within the fence. The influence of energy extraction on the natural flow field is assessed relative to changes in the M2 component of elevation and velocity, residual bed shear stress and tidal dispersion.

### 7.2 Background

A number of coastal headlands, or promontories, have been identified as promising tidal energy sites around the UK (see for example, UK 4, UK 14-16, UK 18, UK 20-21 and UK 22 in Appendix A). To date, however, studies of energy extraction from a headland, or

a two dimensional (2D) laterally unbounded flow field, have been scarce. A notable exception is that due to Blunden and Bahaj [2007b] (see also Blunden and Bahaj [2006]) who conducted numerical simulations of an array of tidal devices, represented by an added bed roughness, close to the tip of Portland Bill (UK 21). The simulations highlighted that useful power extraction may be exploited from currents close to a headland (in this case, 60-70 MW). They also indicated that, with energy extraction, the magnitude and orientation of the M2 tidal currents in the vicinity of the array could change by approximately 15 % and up to  $10^\circ$ . However, although these simulations provide useful insight into the potential and effect of energy extraction close to an actual headland by explicitly including tidal devices, they are unfortunately restricted to one specific turbine array location and a single level of added bed roughness. Consequently the results do not establish whether a limit to energy extraction exists for devices deployed near to a headland. They also do not consider the effects of extraction on tidal dynamics not encapsulated by the M2 components.

### 7.2.1 Headland Physics and UK Sites

The general physics of shallow water flow around coastal headlands have been well explored in the literature. Early work by Pingree and Maddock (Maddock and Pingree [1978], Pingree and Maddock [1979]) investigated the elevated tidal currents that form in the vicinity of a headland and outlined the importance of bottom friction and bathymetry in the generation of transient eddies observed at many real headland sites. Signell and Geyer [1991] extended the work of Pingree and Maddock [1979], developing a more general understanding of transient flow, and the phenomenon of separated flow, around shallow headlands. They outlined three dimensionless numbers to explain the basic flow features around a headland:

1. Aspect ratio of the headland, taken here to be  $\alpha = 2L_1/L_2$ , where  $L_1$  and  $L_2$  are length scales (see Figure 7.2)
2. Effective drag ratio  $C'_d = C_d(L_2/2)/h_o$ , where  $C_d$  is a constant drag coefficient and  $h_o$  is the average still water depth; and
3. Keulegan-Carpenter number  $K_c = U_o/(\omega(L_2/2))$ , where  $U_o$  is the amplitude and  $\omega$  the dominant tidal frequency.

The last two of these dimensionless numbers describe the basic dynamic conditions and define the importance of friction to advection, and advection to acceleration, in the momentum balance, respectively.

For a given tidal headland Signell and Geyer [1991] show that  $C'_d$  and  $K_c$  indicate whether separation will result at the headland tip and, if separation does occur, how the resulting eddies evolve in the local flow field. In general separation is more likely when the coastline is deep, the headland length scales are small relative to the tidal wavelength, and when the seabed is smooth (i.e.  $1/C'_d \gg 1$  or  $K_c \gg 1$ ). Separation is also more likely when the headland has a narrow aspect ratio ( $\alpha \gg 1$ ). The dependency of the headland flow field, following separation, to the dynamic conditions is given in Figure 7.1 (a) for an idealised headland of aspect ratio  $\alpha = 4$  and a Gaussian shape. For comparison the relevant dimensionless ratios  $C'_d$  and  $K_c$  of the UK headland sites listed in Appendix A, which have aspect ratios in the range  $\alpha = 2 - 6$ , are shown in Figure 7.1 (b). There is considerable spread in the dimensionless numbers for the UK sites, which would suggest a large variation in the dynamic balance and flow characteristics where energy extraction may result. For headlands located towards the upper right of Figure 7.1 (b) separation is more likely, for a given aspect ratio, leading to a transient flow regime similar to those defined in Figure 7.1 (a) (i.e. the Portland Bill (UK 21) could represent regime 3 or 4). Towards the bottom left of the Figure 7.1 (b) the headland scale is generally sufficient to suppress large scale separation and resulting large coherent eddy structures (i.e. Angelsey (UK16)).

### 7.3 Idealised Headland

To investigate energy extraction near to a coastal headland, an idealised coastline, similar to that considered by Signell and Geyer [1991], is adopted as illustrated in Figure 7.2. The headland shape approximates the function  $L_1 \exp[-(5x/L_2)^2/2]$ , where  $L_1$  is the offshore extent and  $L_2$  is the breadth at a distance  $\sim 0.96L_1$  from the tip of the headland. Following Pingree and Maddock [1979] and Signell and Geyer [1991] a sloping bathymetry is used to create the coastal boundary layer flow, instead of specifying a vertical no-slip boundary condition. The headland is located in a channel of width  $W$  to represent the coastline

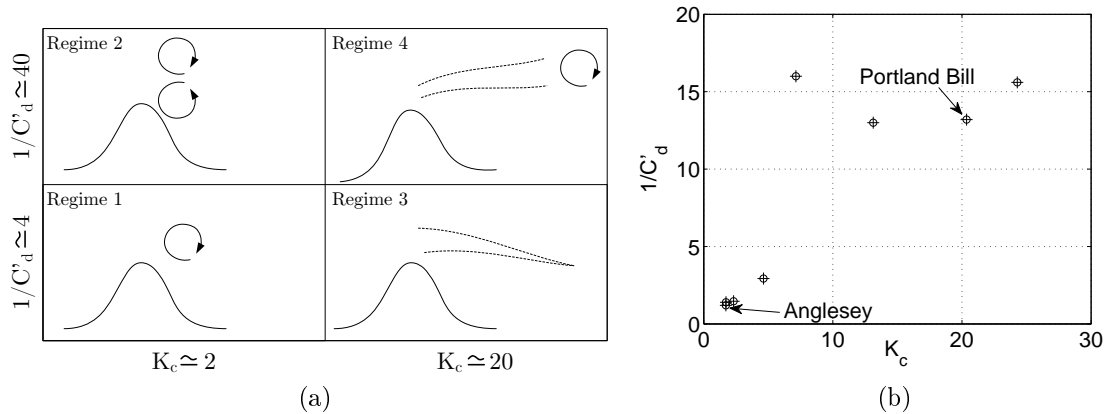


Figure 7.1: (a) Flow dependence on  $C'_d$  and  $K_c$ , adapted from Signell and Geyer [1991]. In regime 1 and 2 (left) the  $K_c$  number is small, so that eddies formed from separation at the headland tip remain close to the headland over the tidal cycle. With reducing  $C'_d$  these eddies persist over more than once cycle leading to interaction effects (regime 2). For large  $K_c$  sites (regime 3 and 4), transient eddies advect quickly from the headland tip, and decay faster in shallow water with high bed friction (regime 3). The dashed lines track the advected path of the eddy. These lines converge for regime 3 to indicate that the eddy dissipates during advection because of the increased influence of drag forces. (b) Dimensionless numbers for the headland sites listed in Appendix A.

typical of many UK sites (e.g. the Mull of Kintyre located within the Northern Passage to the Irish Sea). Boundary conditions comprise: a clamped sinusoidal current  $U_0 \sin(\omega t)$  at the west upstream boundary; a non-reflecting radiation condition at the east downstream boundary; and no-slip reflective walls along the south and north coastlines (which become slip walls when  $v_T = 0$  m<sup>2</sup>/s). Isoparametric elements are used along the headland tip to ensure that flow separation is not mesh dependent<sup>1</sup>. High-order quartic basis functions are used in the DG solution to resolve the transient features close to the headland.

Four headland cases are considered in this chapter (see Table 7.1). The dimensionless ratios span a similar range to the UK headlands in Appendix A. In all cases:  $\omega = 0.00014$  rad/s,  $U_0 = 1.5$  m/s,  $h_0 = 30$  m,  $f = 0$  rad/s and  $v_T = 0$  m<sup>2</sup>/s. (The effects of Coriolis acceleration and eddy viscosity are discussed in Section 7.9.)

### 7.3.1 Undisturbed Tidal Flow

In the natural state without energy extraction, the water elevation field around the headland in case 7-1 (a rough approximation to tidal flow around Anglesey) can be described in terms of M2 elevation co-amplitude lines as shown in Figure 7.4 (a). These lines converge towards

<sup>1</sup>Obviously a real coastline may have imperfections that induce separation naturally, but in this idealised example these are ignored.

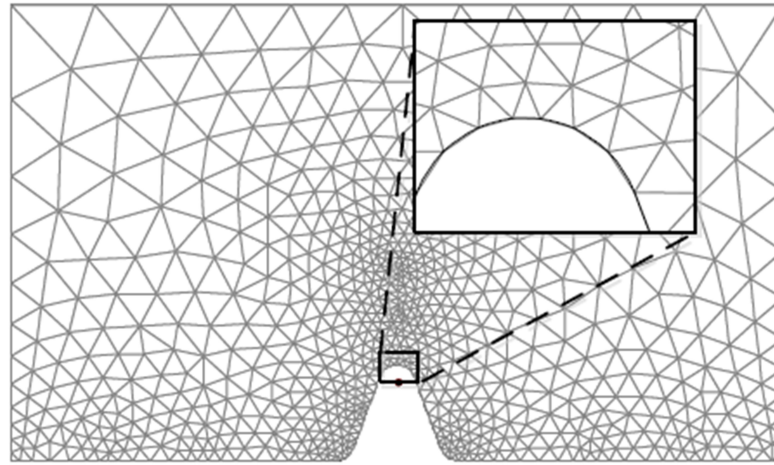
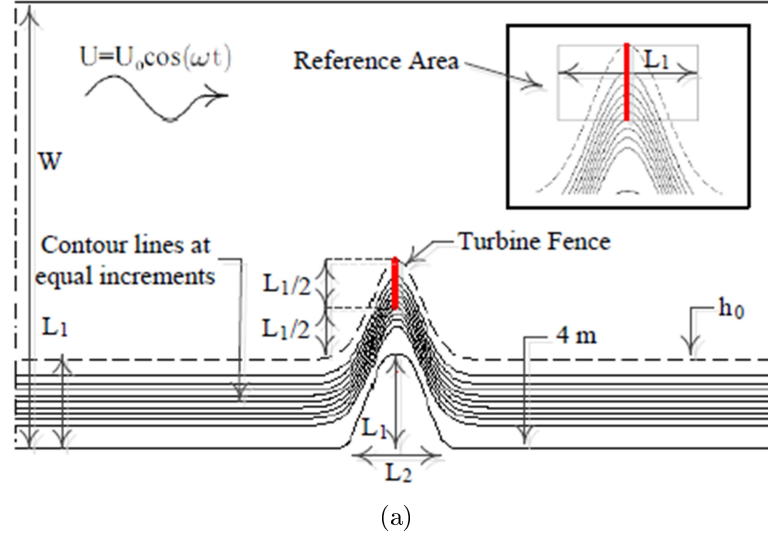


Figure 7.2: (a) Idealised headland geometry, after Signell and Geyer [1991]. Relevant dimensions are outlined in Table 7.1. The insert defines the reference area over which natural power dissipation is considered in Section 7.4. (b) Example computational mesh. The curved headland boundary is modelled with isoparametric elements. All simulations are undertaken with basis functions of order  $n = 4$ .

Case	Dimensional Parameters			Dimensionless Parameters		
	$C_d$	$L_1$ (km)	$W$ (km)	$\alpha = L_1/L_2$	$K_c$	$1/C'_d$
7-1	0.0025	10	50	2.0	2.1	2.4
7-2	0.0050	10	50	2.0	2.1	1.2
7-3	0.0025	1.5	7.5	2.0	21	24
7-4	0.0025	10	50	1.0	1.05	1.2

Table 7.1: Idealised numerical cases. In all examples the offshore depth the bed friction coefficient is constant throughout the site.

the headland tip where the acceleration of the flow around the headland is largest. The elevation co-tidal lines (Figure 7.4(b)) converge near the headland tip, as predicted in Taylor [1921]. Figures 7.4 (c-f) shows snapshots of the tidal velocity field throughout the tidal cycle. Enhanced currents are evident close to the headland tip. However, since the velocity reduces towards the coastline where the frictional force per unit depth is largest, the location of maximum velocity at  $t/T \sim 1/4$  ( $\sim 3.3$  m/s or roughly twice the background velocity) is located  $\sim 5$  km from the headland tip. To illustrate the importance of the basic dynamic conditions on the natural tidal flow Figures 7.4 (b) and (c) show the instantaneous velocity field close to maximum tidal current ( $t/T = 1/4$ ) for cases 7-2 and 7-3. The existence of transient eddies advecting far from the headland tip are most pronounced for case 7-3, which has a similar dynamic balance to Portland Bill. In contrast, the flow field for case 7-2 has no identifiable transient features, indicating that the flow has not separated and is in agreement with Signell and Geyer [1991].

### 7.3.2 Natural Energy Flux and Dissipation

As outlined in previous chapters, the natural kinetic flux has been used to assess the tidal resource in the UK (Black & Veatch Ltd [2005] and Triton Consultants Ltd. [2006]). In addition, a slightly different metric, defined as the power density,

$$P_d = \frac{1}{2} \rho \overline{|\mathbf{u}|^3}, \quad (7.1)$$

is displayed in the Atlas of UK Marine Renewable Energy resources (ABPmer et al. [2004]), where the over bar denotes averaging over a tidal cycle. The integral of this quantity over a plan area is proportional to the natural power dissipation, which has also been used to imply the size of the tidal resource (MacKay [2007b]). For reference, Figure 7.5 plots both the kinetic flux and the natural power dissipation, which is proportional to Equation 7.1 given the constant bed friction coefficient, for case 7-1. It is evident that the headland creates a region of elevated kinetic flux which, because of the sloping seabed and higher frictional force per unit depth at the coastline, moves the location of maximum kinetic flux some distance offshore. Furthermore the region of high flux does not coincide with the region where transient eddies are formed in the wake of the headland. The power density

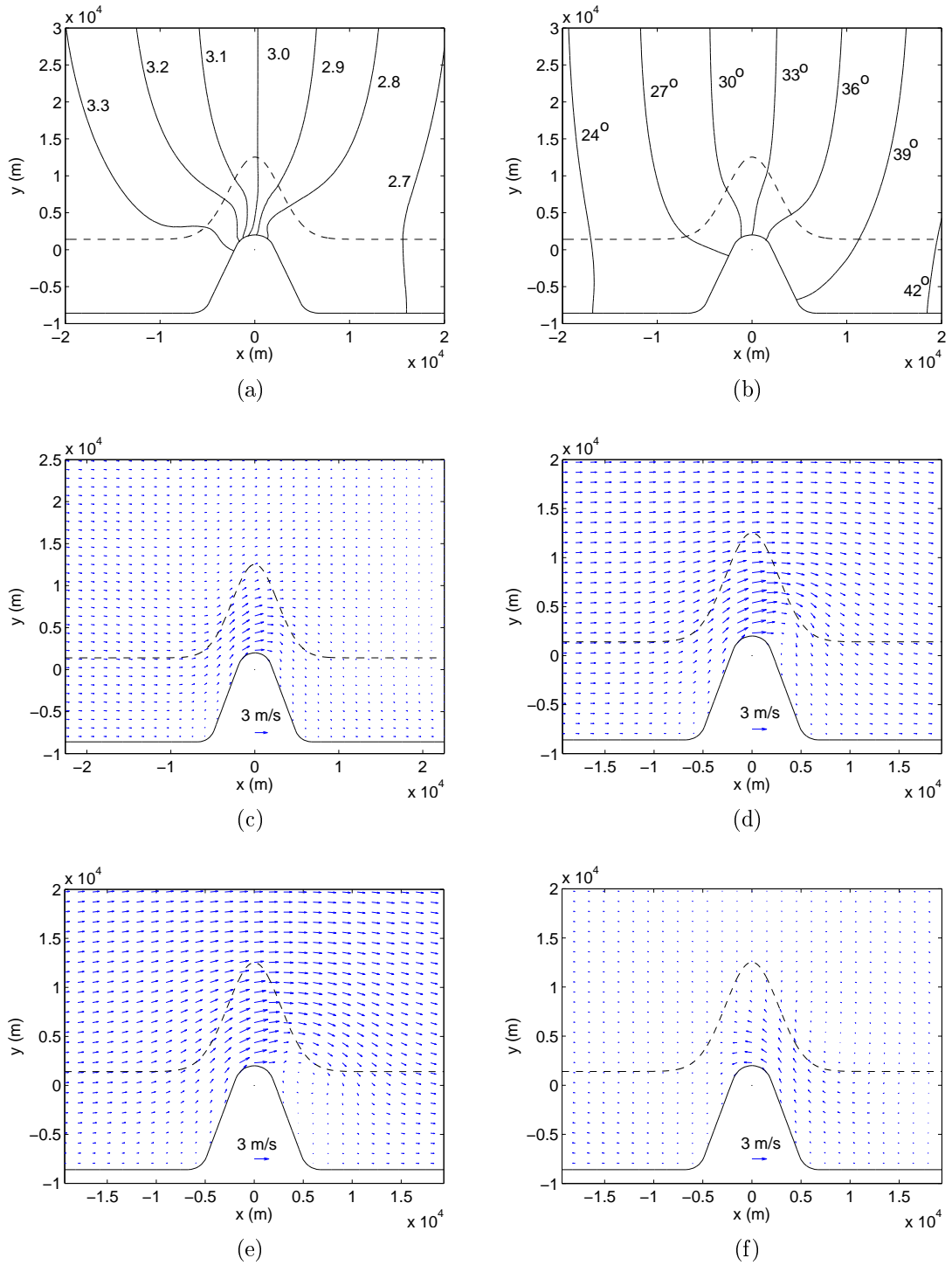


Figure 7.3: Natural flow conditions for case 7-1. (a) Co-amplitude lines for the M2 elevation constituent, (b) Co-tidal lines for the M2 elevation constituent (the phase lag behind the driving current at the western boundary is labelled), (c-f) snapshots of velocity through the tidal cycle: (c)  $t/T = 0$ , (d)  $t/T = 1/12$ , (e)  $t/T = 1/4$ , and (f)  $t/T = 1/2$ .

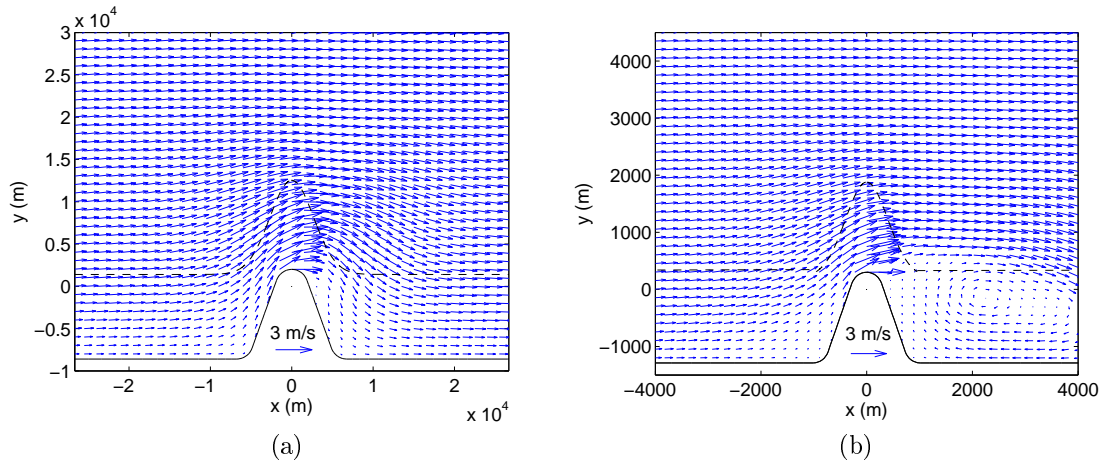


Figure 7.4: Velocity field at  $t/T = 1/4$  for (a) case 7-2 and (b) case 7-3.

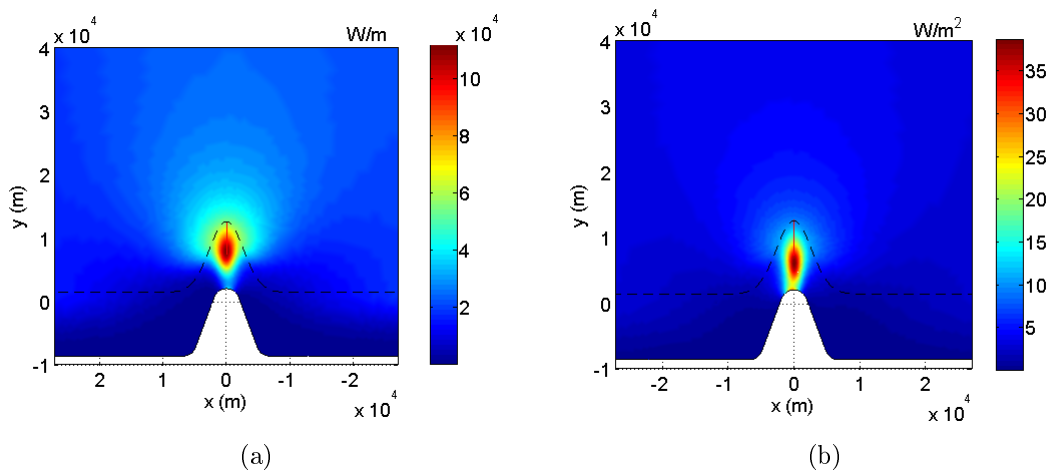


Figure 7.5: (a) Kinetic flux per meter width (defined as  $\frac{1}{2}\rho u^3 h$ ) averaged over a tidal period for case 7-1 in the natural state. This flux can be converted into a time averaged power by integrating over a line orientated in the  $y$ -direction. (b) Natural power dissipation, per square meter, for case 7-1 in the natural state. The location of the turbine fence, considered later in the chapter, is superimposed on both plots.

is more representative of the depth-averaged velocity and has a maximum slightly closer to the headland tip.

## 7.4 Limits to Power Extraction

### 7.4.1 Example case: Case 7-1

The flow field at the point of maximum tidal current ( $t/T \sim 1/4$ ) is shown in Figures 7.6 (a-d) for case 7-1 when a tidal fence is deployed in the location of highest natural flux (see Figure 7.2 for location). In each figure, the devices within the fence have  $\alpha_4 = 1/3$

and a different fixed blockage ratio<sup>2</sup>. It is evident that the instantaneous velocity through the fence reduces with increasing blockage ratio. This trade-off between blockage ratio (or effective resistance of the fence) and the local velocity through the fence is qualitatively similar to that between porosity and velocity in the classic Lanchester-Betz actuator disc analysis. For the tidal fence, no power can be extracted at either of the two extremes of zero or unit blockage ratio; power extraction is maximum at some intermediate (optimum) blockage ratio. A similar result should apply for any fence deployed in a laterally unbounded flow. The extracted power, averaged over a tidal cycle, is plotted in Figure 7.7 (a) as a function of the maximum total flow rate through the fence,  $Q_f$  for several blockage ratios. Up to 560 MW can be extracted when  $Q_f \approx 60\%$  of the maximum in the natural state and the blockage ratio is close to 0.6. Given that  $\alpha_4 = 1/3$ , the overall efficiency of the devices within the fence is approximately 41% over the tidal cycle, implying that only 230 MW is available for generation.

There is little variation in power extraction over the length of the fence (Figure 7.7 (b)). However, prior to maximum extraction slightly more power (between 1 and 15%) is removed from the southern end of the fence. Beyond maximum power extraction, an increasing proportion of the power comes from the northern end of the fence. Although not pursued here, the model could be used to optimise the distribution of devices along the fence.

To compare the extracted power with natural energy dissipation Figure 7.7 (a) displays the total power dissipated (due to bed friction and the turbine fence) in a reference area surrounding the fence (see Figure 7.2). It is evident that the total dissipation also has a maximum value, which peaks before that of the turbine fence itself. The difference between both curves, which represents the power that is dissipated naturally due to bed friction, decreases monotonically with the fence blockage ratio. The undisturbed time-averaged kinetic flux passing through the location of the turbine fence (also illustrated in Figure 7.2 (a)) overestimates the maximum power extraction.

---

<sup>2</sup>Since the bathymetry is non-uniform at the location of the devices fixed blockage ratio implies that the spacing between devices, or the device diameter, varies slightly along the fence. Furthermore, a value of  $\delta = 1/40$  is used to smooth the singularity at the edge of the fence (see Section 4.5.2, Chapter 4).

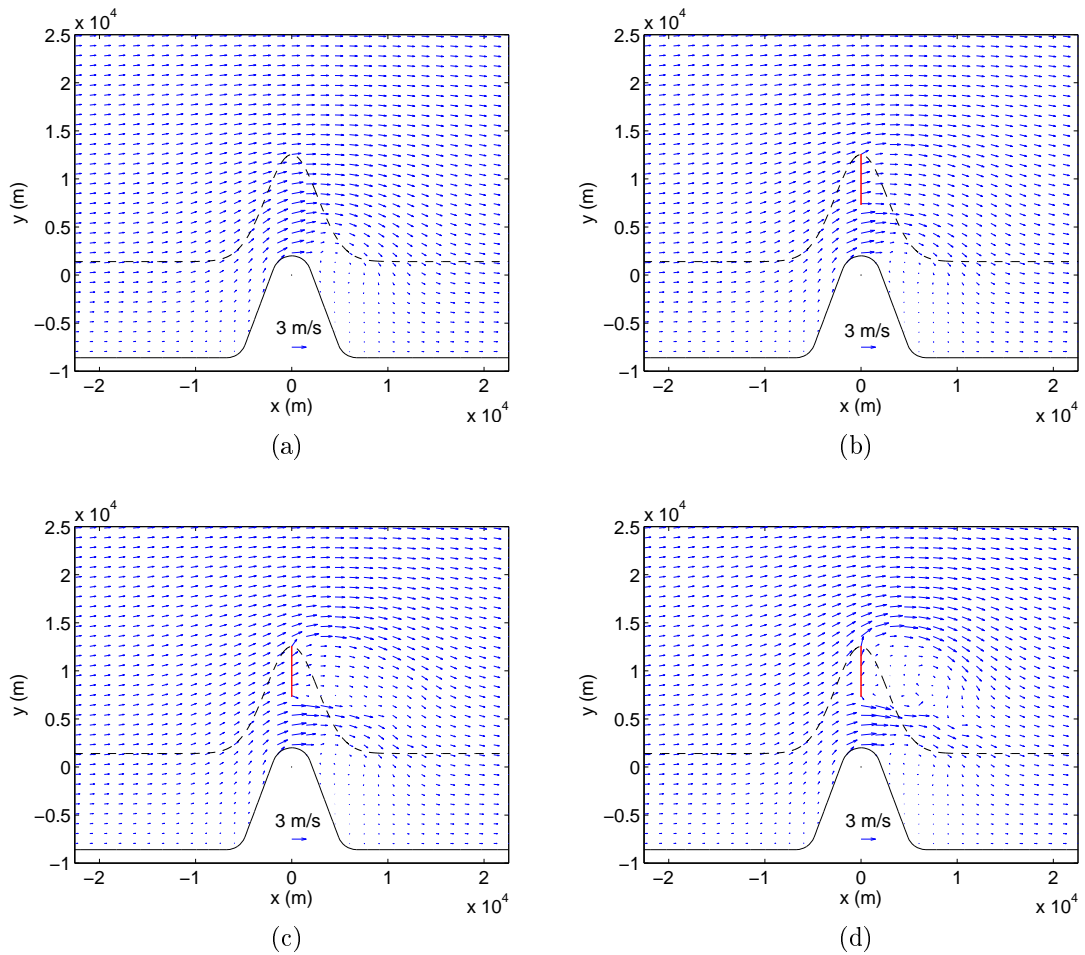


Figure 7.6: Velocity field at  $t/T = 1/4$  (close to maximum tidal current) in the natural state (a), and in the presence of a turbine fence with an effective blockage ratio of (b)  $B = 0.4$ , (c)  $B = 0.6$  and (d)  $B = 0.8$ . The maximum power extraction occurs close to  $B = 0.6$ .

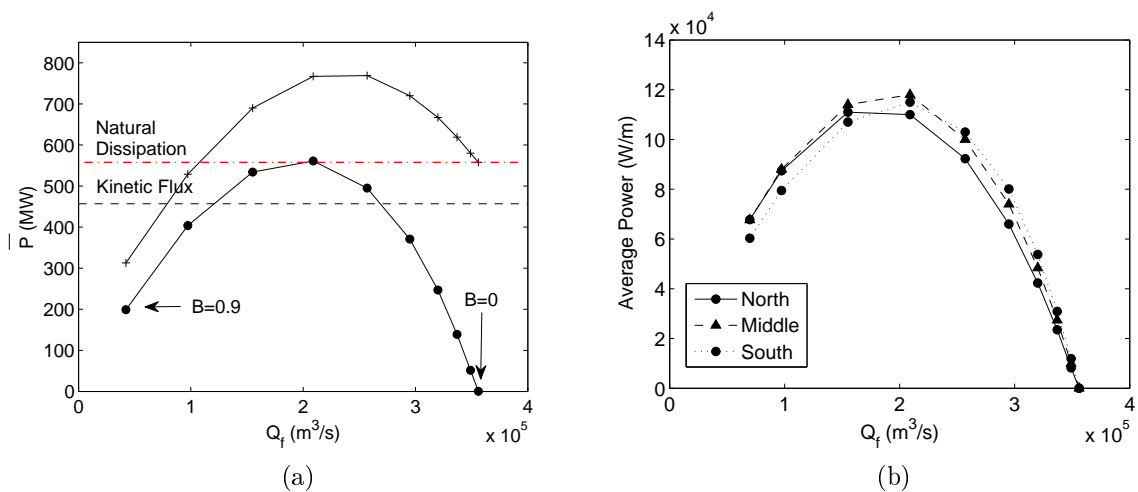


Figure 7.7: (a) Power extraction for for case 7-1. Solid-circle line: power extracted by the turbine fence. Solid-cross line: total power dissipated in the reference area. Note: The kinetic flux and natural dissipation in the reference area are labeled. (b) Extracted power along the fence at various points in the tidal cycle. North and South refer to points one fifth of the fence length from the Northern and Southern ends of the fence, respectively. Middle refers to a point located in the center of the fence.

## 7.4.2 Variation in Dynamic Balance

Figures 7.8 (b) and (c) present the extracted power curves for cases 7-2 and 7-3, together with the undisturbed kinetic flux and natural power dissipation. For case 7-2 the natural dissipation is higher than the maximum extracted power, whilst for case 7-3 the natural dissipation is significantly lower. This suggests, independent of the reference area selected, that natural dissipation does not provide a useful guide to power potential over a realistic range of tidal dynamics. The result is perhaps to be expected, given that a fence deployed near to a headland with no seabed drag could still extract energy but, of course, the natural dissipation would be zero and provide no guide to the maximum energy extraction.

A lack of correlation between the undisturbed time-averaged kinetic flux and the maximum extracted power is illustrated by the different headland cases in Figures 7.7 and 7.8, with the ratio of extracted power to undisturbed kinetic flux equal to approximately 1.2, 1.6 and 0.7 for cases 7-1, 7-2 and 7-3, respectively. The highest kinetic efficiency (defined as the optimal power potential divided by the kinetic flux) is achieved for case 7-2, where friction forces are the largest compared to advection (i.e. largest  $C'_d$ ) and local acceleration is the largest compared with advection (i.e. smallest  $K_c$ ). This suggests that it is harder for flow to bypass a fence when the seabed friction and local acceleration surrounding the fence are significant, compared with advection, in the natural state. More importantly the results in Figures 7.7 and 7.8 indicate that the undisturbed time-average kinetic flux appears to be a poor predictor of the energy potential in the vicinity of a tidal headland because the undisturbed kinetic flux provides no indication of the ability for the flow to divert around the turbine fence. (It should be noted that this is different to the discussion in Chapter 5, where the natural kinetic flux was seen to be a poor indicator of the energy potential for a tidal channel because the flow rate through the channel, and consequently the kinetic flux, reduced with energy extraction.)

Comparing the absolute maximum power extraction across all three cases most power is extracted in case 7-1, followed by case 7-2 (530 MW) and case 7-3 (50 MW). Consequently in these simulations, although case 7-2 has higher kinetic efficiency than case 7-1, case 7-2 extracts less power than case 7-1 because, for the fixed western boundary tidal current, the increased bed friction in case 7-2 reduces natural tidal currents and kinetic flux at the headland tip. The extracted power in case 7-3 is 9% of that in case 7-1 because the turbine

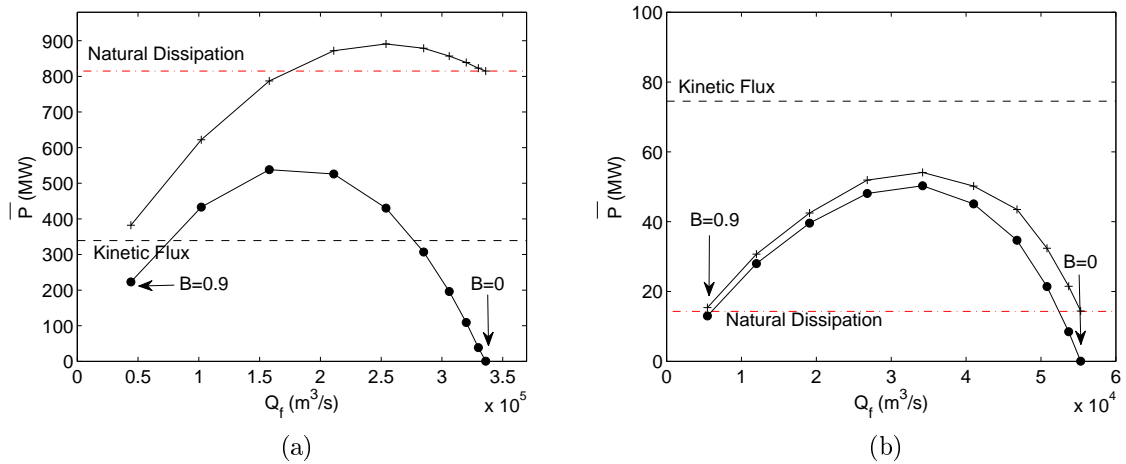


Figure 7.8: See caption of Figure 1.6 (a). (a) case 7-2; (b) case 7-3.

fence deployed in case 7-3 has reduced cross-sectional area (approx. 15% of case 7-1) and because it is relatively easier for the flow to bypass, consistent with the kinetic efficiency.

### 7.4.3 Locating the Turbine Fence

Despite the inability of natural kinetic flux to determine absolute power extraction, it is nevertheless intuitive that the location of maximum kinetic flux may indicate the best position to site tidal devices. For example Figure 7.9 (a) shows the power extracted at two alternative fence locations. In both cases, it is evident that placing the turbine fence away from the location of maximum natural kinetic flux results in significantly less power, even though placing the turbine fence further offshore results in more power than moving the fence closer to the coastline. The ratio of extracted power to undisturbed kinetic flux of the fence is 1.7 and 0.8 for Positions 1 and 2, respectively, compared with 1.2 for case 7-1. As the turbine is placed further offshore the extracted power is therefore a higher fraction of the undisturbed flux. This indicates that the flow bypasses the fence most easily when it is placed in shallow water next to the headland, and is consistent with the surrounding water on the ocean side being relatively deeper so as to offer less impedance to the bypassing flow.

### 7.4.4 Headland Geometry

To examine what effect the headland shape has on the flow field Figure 7.9 (b) plots the undisturbed kinetic flux for cases 7-1 and 7-4. The power extracted by the fence of

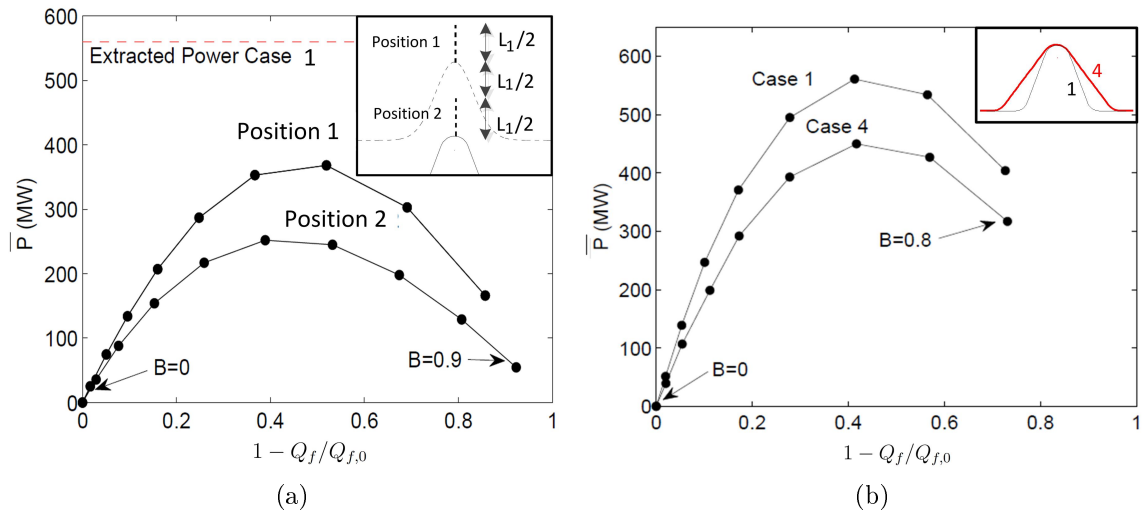


Figure 7.9: (a) Location of alternative turbine fence for case 7-1 and respective power curves for each fence location. (b) Power curve for headland cases 7-1 and 7-4.

turbines declines substantially as the aspect ratio  $\alpha$  reduces. This is despite the fact that the channel width, measured between the tip of the headland and the northern channel wall ( $W - L$ ), is identical for both aspect ratios. Consequently the shape of the headland can have a significant effect on the power potential, for a given background tidal current. This is primarily because the shape of the headland dictates the size of the tidal currents in the natural state, with a narrower headland leading to faster natural tidal streams in the natural state and at a given level of power extraction.

## 7.5 Boundary Conditions

For the idealised domain used in Section 7.4 the flow rate at the western boundary was clamped. However, in reality, the tide is driven by elevation differences across the seas and oceans so that as a consequence the total flow rate through the channel may reduce as turbines are introduced. This reduction in flow rate will be dependent on the connecting boundary conditions to the channel and (see Chapter 5 for example) the power dissipated by the turbines over and above the natural dissipation. To investigate the boundary conditions further, Figure 7.10 (a,b) presents an alternative numerical domain to that in Figure 7.2 where the tide is introduced as a driving elevation along the open ocean boundary in an identical manner to that discussed in Chapter 5. Using this geometry the analysis for case 7-1 was repeated (denoted case 7-1a), with the amplitude of the incoming tidal wave adjusted until the maximum natural flow rate through the channel was similar to that

specified in the clamped simulations (this required elevation difference across the channel of 2.8 m in the natural state).

Figure 7.10 (c) compares the power extracted by the tidal fence for case 7-1 and case 7-1a using a turbine fence of various fixed blockage ratio and  $\alpha_4 = 1/3$ . Figure 7.10 (d) displays the power dissipation due to bed friction and the total dissipation within the channel (due to bed friction and devices) together with the maximum flow rate through the channel  $Q_c$ . From these figures it is evident that the channel flow rate reduces as the tidal fence is introduced. The reduction in flow rate is however only 2% and appears to have a small effect on the power extracted by the fence. Additional simulations of case 7-3, in which the turbine bed friction is a higher fraction of the total dissipation in the channel, led to a reduction in flow rate of less than 5% at maximum power extraction. As such it would appear that a clamped upstream velocity boundary condition is a sensible approximate boundary condition for the headland geometries and turbine fence modelled.

With reference to Figures 7.10 (c) and (d) it is evident that the introduction of the turbine fence leads to an initial reduction in natural dissipation but an increase in total dissipation within the channel. This is consistent with the total dissipation in the channel being below an optimum amount for maximum power dissipation in the channel. Interestingly, as the tidal fence blockage ratio increases above 0.6, the power extracted by the fence reduces and, although the flow rate continues to reduce because the unblocked area of the channel is smaller than without tidal devices, the power dissipation due to bottom bed friction increases. This can be explained by the fact that the velocity bypassing the fence increases with the fence blockage ratio, eventually increasing the total dissipation due to bed friction.

## 7.6 Available Power

It was noted in Draper et al. [2010] that operating at a wake velocity coefficient higher than  $1/3$  can increase device efficiency by reducing mixing losses. Figure 7.11 (a) therefore plots the extracted power for case 7-1 as a function of the fence depth-averaged turbine thrust  $C_{d,eff}$  (computed when  $F_r = 0$ ) for fences of devices with various fixed  $\alpha_4$  values. Interestingly, although the near-field solution (Chapter 2) indicates that for each fence the

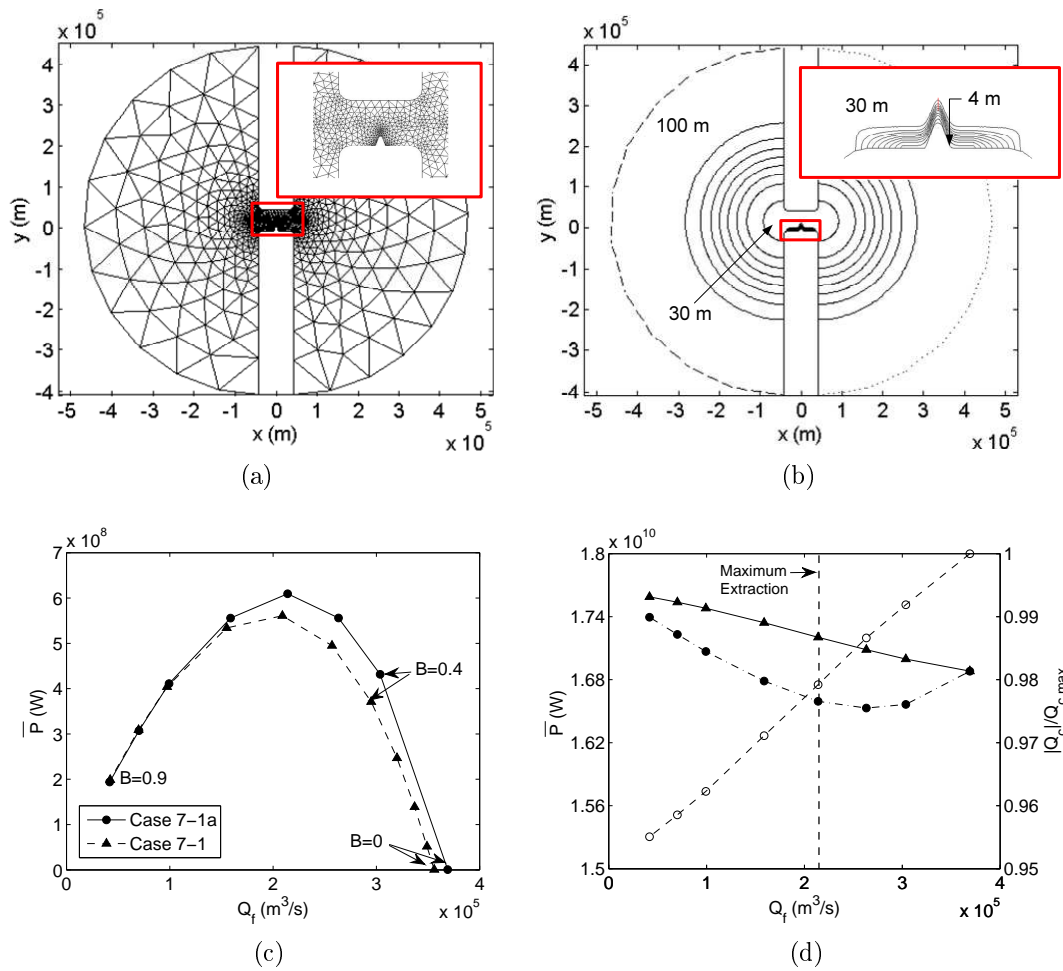


Figure 7.10: (a), (b) mesh and bathymetry for case 7-1a. (c) Extracted power extraction for cases 7-1 and 7-1a. (d) Left axis, solid line and triangles: Total power dissipated in channel due to natural bed friction and fence; Left axis, dash-dot line and circles: Power dissipated in channel due to bed friction only; Right axis, dashed line and circles: Maximum flow rate through the channel  $Q_c$  normalised by the maximum flow rate without tidal devices.

depth-averaged turbine thrust coefficient  $C_{d,eff}$  will vary over the tidal cycle with Froude number by an amount dependent on the depth change and therefore the particular fence blockage ratio and wake velocity coefficient, all points appear to lie on the same line in Figure 7.11 (a), with only minor deviation for  $\alpha_4 = 3/4$  at higher  $C_{d,eff}$  values. This result suggests that for realistic blockage ratio and wake velocity coefficient the variation in  $C_{d,eff}$  with  $F_r$  over the tidal cycle, which should be different for different fences, must have a negligible effect on power extraction. The coefficient  $C_{d,eff}$  calculated for  $F_r = 0$  therefore uniquely defines the power extraction to a good approximation. A similar result was also observed for cases 7-2, 7-3 and 7-4 (not shown).

Exploiting the weak dependence of  $C_{d,eff}$  on  $F_r$  the extracted power can be calculated for a fence of any given  $B$  and  $\alpha_4$  by first computing  $C_{d,eff}$  with  $F_r = 0$  and then interpolating the extracted power from the curve in Figure 7.11 (a). The available power can then be found to an acceptable level of accuracy by multiplying the extracted power by the efficiency assuming  $F_r = 0$ . Using this approach the extracted power and available power, normalised by the maximum extractable power, are plotted for cases 7-1 and 7-3 as a function of fence blockage ratio and wake velocity coefficient in Figures 7.11 (b) and (c). Consistent with the findings in Vennell [2010], Figure 7.11 (b) shows that maximum power extraction can be achieved for a range of combinations of  $\alpha_4$  and  $B$  (dashed lines), with each combination having the same (optimal)  $C_{d,eff}$  coefficient highlighted in Figure 7.11 (a). The fraction of maximum power available to the devices within the fence, however, is maximised when the blockage ratio and wake velocity coefficient approach unity (Figure 7.11 (c)). This is because devices with large  $B$  and  $\alpha_4$  are most efficient (Draper et al. [2010]) and provide sufficient thrust to extract the maximum power.

Interestingly, for general blockage ratio (i.e.  $B = 0.5$  in Figure 7.11) the available power is maximised when power extraction is not maximised (see the circles in Figure 7.11). This is because the gain in efficiency achieved by operating at a higher  $\alpha_4$  than required for maximum extraction more than offsets the reduction in power extraction. Consequently, for typical values of  $B$ , the maximum available power may not coincide with the maximum extracted power. Consistent with findings in Vennell [2010] for a tidal channel, there is therefore a need to “tune” the velocity coefficient of a fence of devices near a headland to maximise available power. This tuning requires knowledge of the complete power curve in

Figure 7.11 (a). For complicated coastal geometries such as headlands this curve can only be obtained using a model similar to that employed here.

Comparing the two cases in Figure 7.11 (c), it is interesting to note that a larger fraction of the maximum extractable power for a given fence blockage ratio below unity is available to the fence in case 7-3 than case 7-1 (see the circles in Figure 7.11), although more power in absolute terms is available for case 7-1. This result is consistent with the requirement for the turbine fence in case 7-1 to provide a higher effective thrust coefficient at maximum power, and at a given fraction thereof, to compete with the increased importance of bed friction and acceleration in the momentum balance (i.e. higher  $C'_d$  and lower  $K_c$ ). Since a higher thrust coefficient for a given blockage ratio can only be achieved with a lower velocity coefficient, the fence efficiency must reduce due to (3). This ultimately reduces the fraction of extractable power available to the devices for case 7-1 at a given blockage ratio. It should also be noted that this result is true for all  $B$  regardless of the fact that at suboptimal conditions of high  $B$  and very low  $\alpha_4$  (bottom right corner of Figure 7.11 (c)) the normalised extracted power, and consequently the normalised available power, is higher for case 7-1.

Lastly Figure 7.11 (d) plots the available power at two locations along the fence for case 7-1: one-fifth the distance from the northern and southern ends of the fence, respectively. For a given blockage ratio, it is evident that a higher fraction of the extracted power is available on the southern side of the fence. Since an identical blockage ratio and a very similar efficiency is realised on both sides of the fence, this result is consistent with the slightly greater extraction of power noted on the southern side of the fence.

## 7.7 Comparison to Added Bed Roughness

Figure 7.12 (b) displays the extracted power when an additional bed roughness is introduced over a rectangular region close to the tip of the idealised headland for case 7-1 (Figure 7.12 (a)). As the region of bed roughness limits to a line, the power extraction approaches the results obtained using the line sink of momentum in Section 1.4, indicating an indifference between a line sink of momentum and a thin strip of distributed roughness. For the larger region of bed roughness, however, more power can be extracted. This additional power

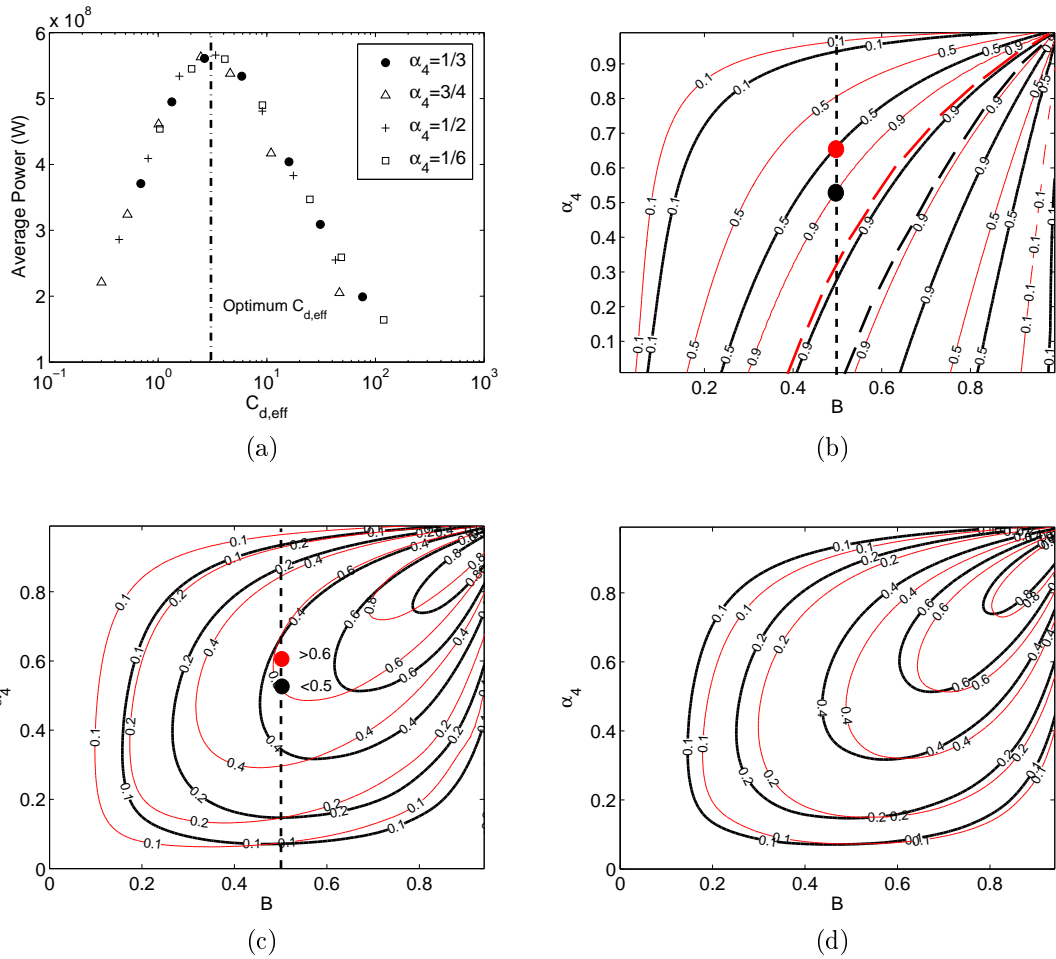


Figure 7.11: (a) extracted power for case 7-1. Markers represents blockage ratios taking the values, from left to right: (0.4,0.5,0.6,0.7,0.8,0.85,0.9). The  $C_{d,eff}$  resulting in maximum extraction is labelled, (b) extracted power, normalised by max. extracted power, for case 7-1 (thick dark lines) and case 7-3 (thin red lines), (c) as in (b) but available power, normalised by max. extractable power, (d) fraction of extracted power, per m of fence, available at two locations along the fence for case 7-1: one-fifth of fence length from southern end (thick dark lines), and from northern end (thin red lines). Circles in (b) and (c) indicate max. available power for  $B = 0.5$ .

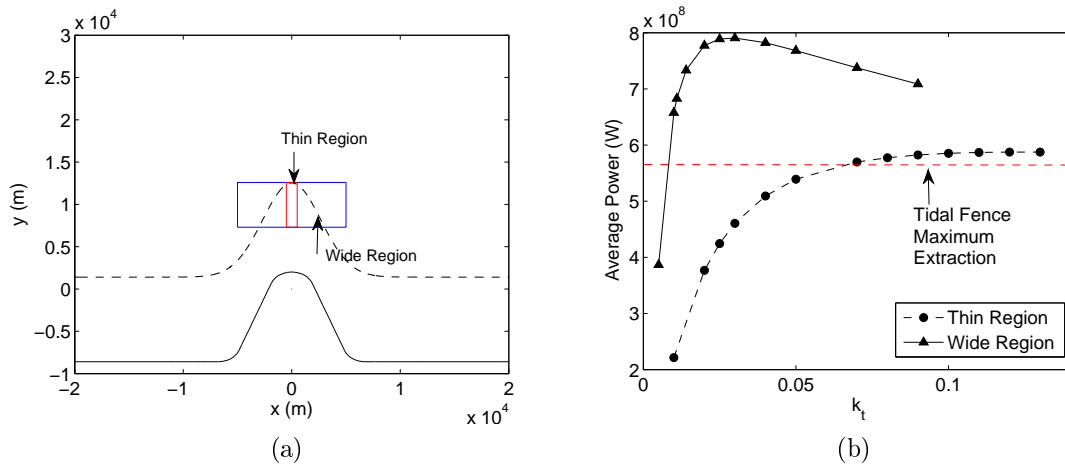


Figure 7.12: (a) Regions of added bed roughness surrounding tidal headland. (b) Extracted power as a function of added bed roughness  $k_t$ .

extraction, which occurs at a lower drag coefficient  $k_t$ , can be attributed to the flow not encountering the rectangle of bed roughness perpendicular to the western edge.

Importantly the results obtained for the two regions of bed roughness imply a tradeoff between distributing low resistance devices over a large plan area so as to extract more power and placing devices close together in a fence to efficiently extract less power. However, until a more detailed relationship between added bed roughness and an array of idealised tidal devices can be determined, so as to determine their efficiency, this trade off will be difficult to resolve.

## 7.8 Effect of Energy Extraction on the Flow Field

The analysis in this section begins with the simplest case of steady flow before considering time varying flows, and the effects of energy extraction on M2 tidal and transient currents. Finally, to better quantify the environmental impact of energy extraction mean stress and tidal dispersion are computed. For brevity all the analysis is presented hereafter for case 7-1. The results are qualitatively similar for the other cases.

### 7.8.1 Steady Tidal Flow

The general effects of a turbine fence on the flow field can be easily observed in the limit of steady flow ( $\omega \rightarrow 0$ ). Figure 7.13 plots streamlines around the headland for case 7-1 in the natural state (with  $\omega = 0$ ), together with the streamlines when a fence of turbines

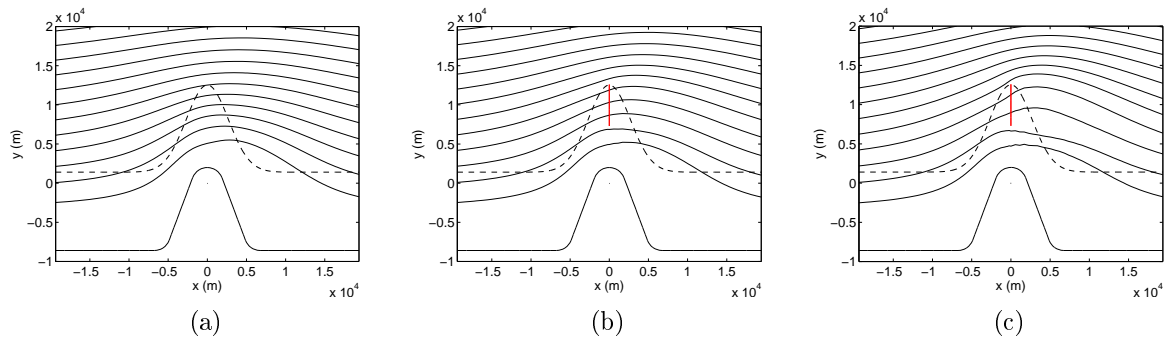


Figure 7.13: Streamlines for case 7-1, with  $\omega = 0$ : (a) Natural state. (b) Fence of tidal turbines defined by a wake velocity coefficient of  $\alpha_4 = 1/3$  and a blockage ratio of  $B = 0.4$ . (c) Same as (b), but for  $B = 0.6$ .

is extracting approximately half of the maximum power ( $B = 0.4$ ) and all of the maximum power ( $B = 0.6$ ). For all three conditions the streamline contours separate an equal amount of mass flow, becoming more widely spaced towards the coastline where the depth is shallower. Following the introduction of the turbine fence it is evident that the streamlines begin to diverge immediately upstream and downstream of the fence, indicating, as expected, a reduction in velocity through the turbines and an increase in the immediate bypass velocity. The divergence of the streamlines is however not symmetric about the center of the fence, with the increase in bypass flow rate on the coastal side accounting for only 33% and 30%, respectively, of the reduction in flow through the turbines in Figure (b) and (c). The flow will therefore tend to bypass on the ocean side where the depth is largest and the bed friction force per unit depth is lower. The average increase in velocity either side of the turbines, over a length equal to that of the fence itself, is approximately 7% on the ocean side and only 5% on the coastal side at maximum power extraction (Figure 7.13(c)).

## 7.8.2 Time Varying Tidal Flow

For time-varying tidal currents, tidal ellipses are typically used to describe the flow field (Maddock and Pingree [1978] and Blunden and Bahaj [2007b]). Figure 7.14 (a) displays the M2 tidal current ellipse minor and major axes at various points in the flow field for case 7-1 without a turbine fence. Amplification of the major axis is obvious close to the headland tip, whereas the minor axis is generally small relative to the major axis for this particular headland case. Figure 7.14 (b) presents changes to the ellipse parameters following the

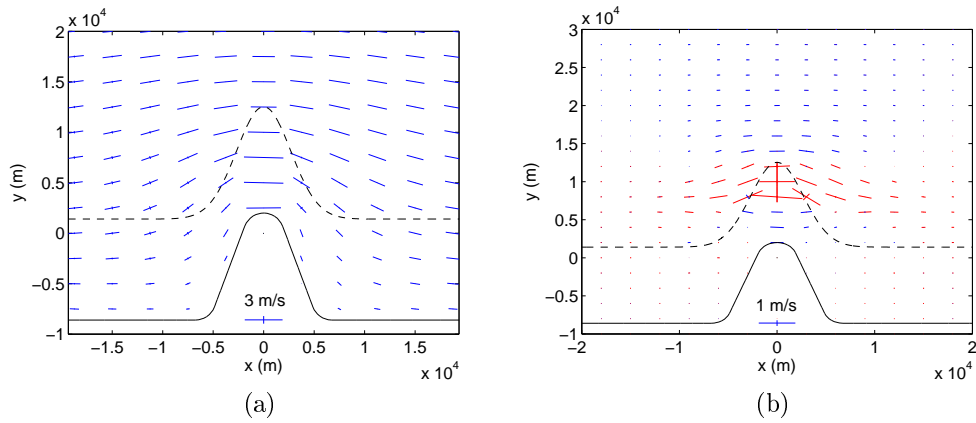


Figure 7.14: (a) Tidal ellipse parameters for case 7-1. (b) Change in tidal ellipse properties with power extraction ( $B = 0.6$ ). The ellipse axes in (b) are the absolute difference between the natural flow and flow with extraction. Red (blue) ellipse axes indicate that the natural magnitude is higher (lower) than with extraction. The change in ellipse orientation is multiplied by a factor of 3 to make the difference more visible.

introduction of a turbine fence operating close to maximum energy extraction. It is evident that there is a reduction of the major axis immediately upstream and downstream of the fence, while an inclination (declination) in orientation of the ellipse, with reference to the positive  $x$  axis, is evident further east (west) of the fence. This suggests that the flow tends to bypass on the ocean side, consistent with the findings for the steady tidal flow. Moreover the reduction in the time-averaged absolute total flow rate through the fence is  $8.2 \times 10^4 \text{ m}^3/\text{s}$  at maximum extraction, whereas the increase in time-averaged absolute total flow rate passing between the fence and coastline is just  $7.6 \times 10^3 \text{ m}^3/\text{s}$ . In the presence of energy extraction, the M2 elevation co-amplitude and co-tidal lines (Figure 7.15) concentrate towards the end of the turbine fence, consistent with the accelerating flow around the fence. An effect similar to this was noted by Blunden and Bahaj [2007b] for energy extraction close to Portland Bill.

The substantial change in the velocity field implied by 7.14 (b) indicates that the addition of a tidal device may have a significant impact on the local environment. As a compromise it is interesting to consider energy extraction at, say, one half of the maximum power extraction. In this case, simulations show the maximum flow rate through the fence decreases by 17% as opposed to 44 % incurred at maximum power. This implies that a fraction of the maximum power can be removed in the vicinity of the headland for a comparatively smaller fractional change in the natural flow conditions, and is entirely consistent with the power curves presented in Figures 7.7 and 7.8.

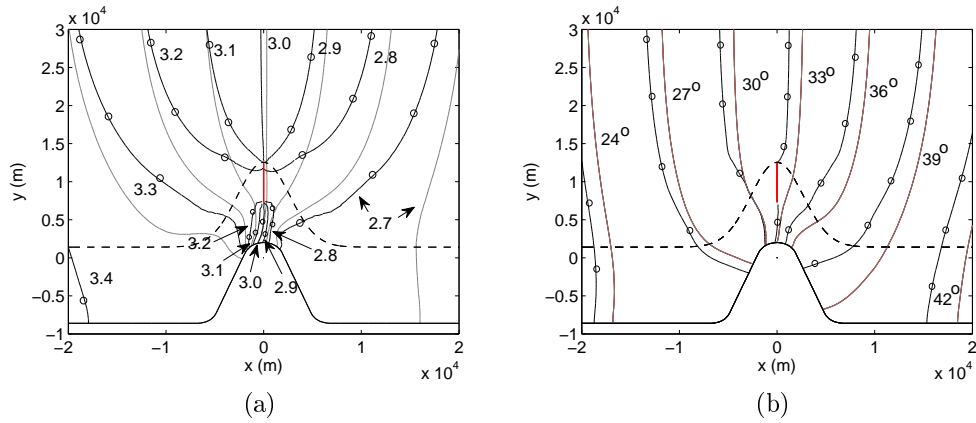


Figure 7.15: (a) M2 elevation co-amplitude lines, and (b) co-tidal lines. Lines with circles are for the scenarios with turbines operating at close to maximum power ( $B = 0.6$ ), solid lines represent the natural conditions. Phase is given as the lag behind the forcing velocity at the western boundary.

### 7.8.3 Mean Stress and Tidal Dispersion

Although the M2 constituents provide some insight into the effects of energy extraction on natural hydrodynamics, the local flow field is inherently nonlinear (Signell [1989], Pingree and Maddock [1979]). This non-linearity gives rise to compound and residual tides and contributes to residual bed shear stress and tidal dispersion. The addition of tidal devices can have an impact on these non-linear quantities.

The importance of the residual shear stress on sand transport has been demonstrated in a study of the Southern UK (Pingree and Griffiths [1979]), where the mean stress on the seabed was given by

$$(\overline{\tau_x}, \overline{\tau_y})^T = \rho C_d \overline{\mathbf{u} |\mathbf{u}|}, \quad (7.2)$$

with  $\mathbf{u}$  the depth-averaged velocity vector. Figure 7.16 (a) plots this vector quantity for the headland in case 7-1. Without energy extraction a slight asymmetry in the stress about the headland tip is evident, and is consistent with the propagation, from the west, of the damped progressive tidal wave. The general pattern of bottom stress is very similar to that calculated for actual headland sites (Pingree and Maddock [1979]) and is indicative of the continual scouring and deposition that leads to the observed grading of the seabed. To investigate the impact of energy extraction, Figure 7.16 (b) plots the vector difference in mean stress between natural conditions and those at maximum power extraction. The obvious features are the four circular regions surrounding the ends of the turbine fence. Interestingly these residual stresses mimic the stress field at the tip of the headland sug-

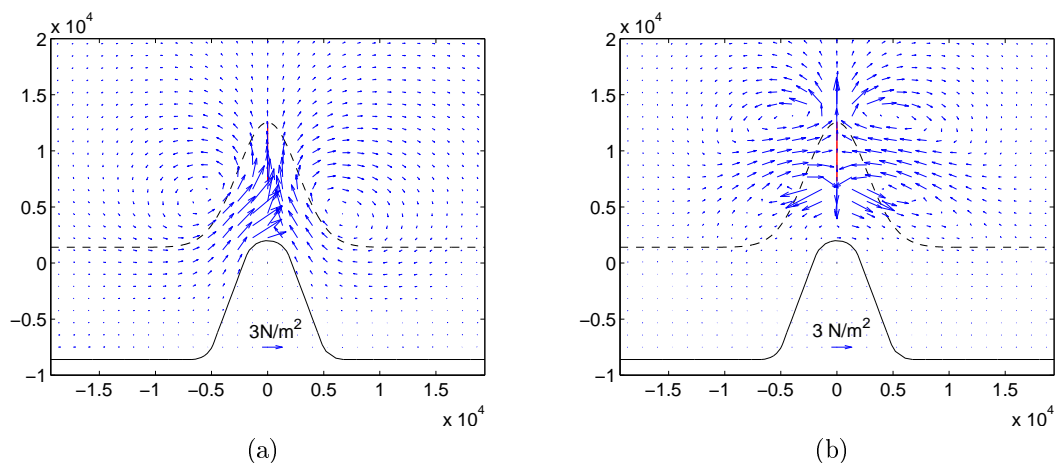


Figure 7.16: (a) Mean stress over the headland site case 7-1 in the natural state. (b) Vector difference between mean stress with a turbine fence operating at close to maximum power and the natural flow.

gesting that the tidal fence has a similar effect to that of an offshore island. The resulting changes to the bed shear stress could have a significant effect on bed load transport and grading at a sandy site, such as the Portland Bill where sand at the seabed is found offshore surrounding the headland.

In addition to the changes to mean stress, an interesting finding illustrated in Figure 7.14 is that the introduction of energy extraction in the vicinity of a headland augments natural tidal currents surrounding the turbine fence. This is in contrast to the placement of a turbine fence across a significant fraction of a narrow channel where, due to back effects on the flow rate through the channel, the velocity field close to the turbines may vary spatially but will generally be everywhere reduced. The large spatial gradient in velocity between the flow passing through and bypassing the fence is expected to alter tidal dispersion in the vicinity of the headland. To explore this further Awaji et al. [1980] suggests that a diffusion coefficient can be used to quantify the dispersion, or the degree of possible mixing, in a time-varying tidal flow. This coefficient can be related to the variance in position of a number of released particles or floats according to the expression

$$K = \frac{1}{2} \frac{d\sigma_x^2}{dt}, \quad (7.3)$$

where  $\sigma^2$  is the spatial variance in the distribution of particles, with time  $t$ , relative to the time-varying mean position  $(\bar{x}, \bar{y})$ . To obtain an estimate of this variance a box of  $N$  regularly distributed particles can be introduced at a given location and tracked over a

tidal cycle, giving a measure for  $K$ , assigned to the initial location, of (Signell [1989])

$$K = \frac{1}{2} \frac{\Delta \sigma_{\mathbf{x}}^2}{\Delta t}, \quad \text{where} \quad \frac{\Delta \sigma_{\mathbf{x}}^2}{\Delta t} = \frac{1}{2} \left( \frac{\sigma_x^2(t + \Delta t) - \sigma_x^2(t)}{\Delta t} + \frac{\sigma_y^2(t + \Delta t) - \sigma_y^2(t)}{\Delta t} \right), \quad (7.4)$$

with  $\sigma_x^2$  and  $\sigma_y^2$  the variance in  $x$  and  $y$  positions of the  $N$  particles relative to the time-varying mean position. A useful location to investigate tidal dispersion is in the gap between the tidal fence and the coastline. Figure 7.17 presents snapshots of 153 particles released in a region  $(x, y) \in [-1000, 1000] \text{ m} \times [4000, 5000] \text{ m}$  for case 7-1 both with and without energy extraction. In the second of these plots,  $t/T = 1$ , the particles released with energy extraction are already beginning to stretch over a larger distance than those released without energy extraction due to the increased bypass velocity. At  $t/T = 5$  many particles released in the presence of energy extraction have encountered the tidal fence (red particles) and there is a visible increase in dispersion compared to those particles released without energy extraction. The variation in  $K$  over several tidal cycles is plotted for both scenarios in Figure 7.18. The results confirm that tidal dispersion does increase when energy is extracted and implies that the mixing of suspended sediment and pollutant transport can be augmented (in this case by a factor of 2) close to the headland.

## 7.9 Discussion and Conclusions

In each of the simulations performed in this paper both Coriolis and viscous terms have been neglected. Setting the Coriolis parameter to  $f = 0.00012 \text{ rad/s}$  (representative of latitude  $55^\circ\text{N}$ ) and repeating the simulations for case 7-1 led to an increase in maximum power extraction of  $\sim 20\%$ . This increase is to be expected since the effect of the Coriolis forcing on the eastward propagating tidal wave is to increase the tidal range and tidal currents close to the headland, which lie to the right hand side of the progressive wave. Introduction of depth-averaged eddy viscosity coefficients of  $1 \text{ m}^2/\text{s}$  and  $5 \text{ m}^2/\text{s}$  had negligible effect on the extracted power (less than  $5\%$  change) for all of the cases.

A main conclusion from the work in this chapter is that the power that can be extracted from a tidal fence located next to a tidal headland is limited because the flow can bypass when energy is extracted. Analysis of the flow field shows that the bypass flow is not symmetric round the fence, but is greater on the ocean side where the depth is greater.

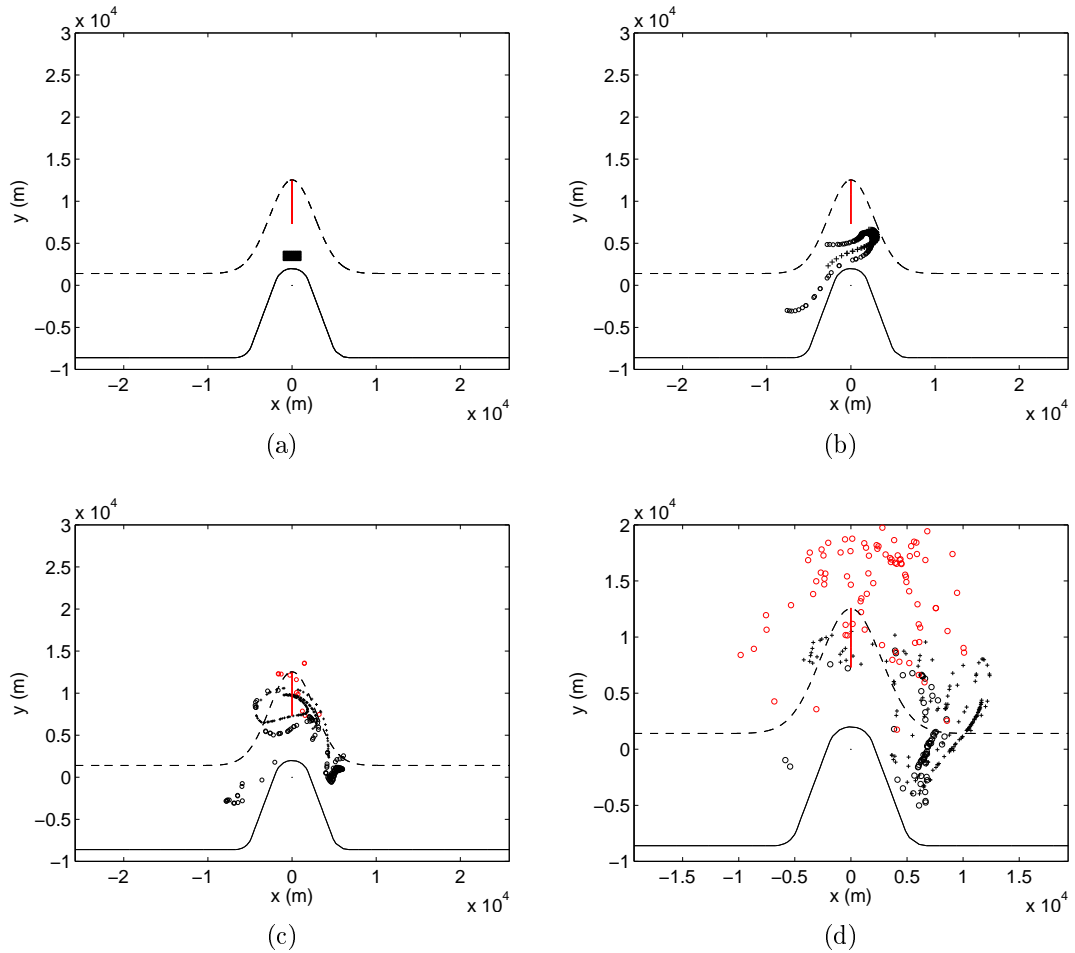


Figure 7.17: Tidal dispersion for Case A. (a) Initial location of 152 particles. (b) Particle positions at  $t/T = 1$ . (c) Particle positions at  $t/T = 5$ . The crosses represent particles released without energy extraction and the circles with energy extraction ( $B = 0.6$ ). Circles coloured red have passed through the tidal fence.

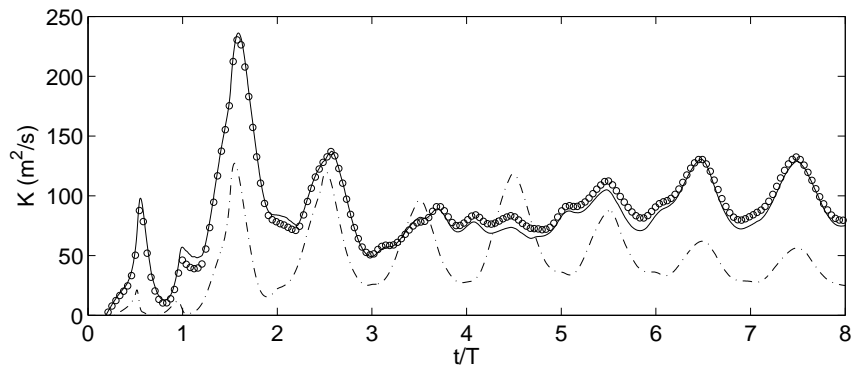


Figure 7.18: Time varying diffusion coefficient evaluated relative to the released particles. Dash-dot line is without energy extraction, solid line is with energy extraction ( $B = 0.6$ ) and the circles indicate the diffusion coefficient obtained when 561 particles are released in the presence of energy extraction.

Importantly, natural dissipation and kinetic flux are not a consistent fraction of the maximum power extraction over the range in dynamic conditions typical to the tidal headlands found around the UK. Despite this, the kinetic flux does appear to be potentially useful in identifying the best location to deploy a fence in the vicinity of a headland. It is not unreasonable to expect that this will also be the case for other laterally unbounded tidal flows.

Numerous combinations of device blockage ratio and velocity coefficient can be chosen to maximise power extraction. However, consistent with results discussed in Vennell [2010] for a tidal channel, the available power is maximised when devices with large blockage ratio are used within the fence. The results also demonstrate that the fraction of maximum extractable power available to devices within the fence is dependent on their location along the fence as well as the tidal dynamics. Moreover, a greater fraction of extractable power appears to be available, for a given blockage ratio, when acceleration and bed friction effects are small relative to advection terms in the momentum balance.

Energy extraction can augment both residual shear stress at the seabed and the potential for mixing of suspended material at a coastal headland site. Interestingly, the second of these effects may have beneficial environmental consequences, helping to dilute contaminants introduced at sewage outfalls, which are commonly located close to headlands.

# Chapter 8

## Conclusions

### 8.1 Introduction

This thesis is concerned with estimating the tidal energy potential of various coastal sites, or basins, and the effect of energy extraction on natural hydrodynamics. In each case emphasis has been placed on introducing tidal energy devices as a momentum sink that can be related directly, via momentum actuator disc theory, to a fence of actual tidal devices of known diameter, spacing and wake velocity coefficient. This has enabled models and simulations of both the extracted and available power for a tidal fence deployed at each coastal site. In this chapter, the main conclusions of the work are summarised and possible future research is suggested.

### 8.2 Conclusions

#### 8.2.1 The local Field

- Linear momentum actuator disc theory (LMADT) has been applied to a tidal device placed in a uniform tidal stream, allowing for both a deformable free surface and downstream mixing (pressure-volume constrained flow). This application of LMADT has effectively combined the previous analysis of Garrett and Cummins [2007] (for a fixed free surface) and Whelan et al. [2007] (without downstream mixing), to establish a measure of efficiency  $\eta$ , for a tidal device in a tidal stream of finite Froude number.
- The measure of efficiency  $\eta$  has allowed for a distinction to be made between the

power extracted by a tidal fence and the power available to tidal devices within the fence. The most efficient fences are comprised of devices with large area and small center to center spacing.

- Because the power that can be extracted from a tidal site is generally limited (see Section 8.2.3), the measure of efficiency becomes as important in tidal turbine design as the traditional power coefficient. In fact, if a fence is operating at maximum power extraction, an efficient device will yield the most available power, not a device operating at maximum power coefficient. Moreover, at all levels of power extraction the available power is defined by the product of efficiency and extracted power.
- In a tidal stream with negligible Froude number,  $\eta$  is consistent with the measure of efficiency derived by Garrett and Cummins [2007] for a tidal channel with a fixed free surface. However for finite Froude number, the effect of the free surface is to reduce the efficiency  $\eta$  by an amount that is approximately  $1 - \Delta h/2h$ , where  $\Delta h/h$  is the dimensionless depth change across the turbine fence.
- The application of LMADT to a tidal device in a tidal stream with a deformable free surface has provided a relationship between the depth and velocity both upstream and downstream of a tidal fence. Unlike a similar relationship that can be obtained for a device in a tidal stream with a free surface that is assumed to be fixed (Garrett and Cummins [2007]), the relationship established here conserves mass and is therefore better suited to the representation of a momentum sink in a shallow water model.
- Lastly, for the pressure-volume constrained flow it has been shown that solutions to the actuator disc model become physically inadmissible when the bypass flow is hydraulically critical. It has also been noted that the traditional power coefficient increases rapidly as the blockage ratio approaches unity. This latter result was also noted for an actuator disc in a volume constrained flow and, consequently, a revised power coefficient has been suggested to normalise for the head difference that results between the upstream and downstream flow.

## 8.2.2 Simulation of Tidal Flow

- The numerical code OxTide has been written to solve the Shallow Water Equations (SWEs) with the discontinuous Galerkin Finite Element Method. A series of validation and verification tests (Appendix B) have shown that the code achieves satisfactory results for linear, non-linear and viscous simulations. It has also been demonstrated that the code is well balanced in the sense that it can simulate quiescent initial conditions in cases when the bed topography is varying.
- A line sink of momentum has been implemented within the numerical code to simulate momentum extraction by a tidal fence of devices in a shallow water flow. It has been shown that the perturbation in depth and velocity across the tidal fence can be defined by LMADT when the devices with the fence have a known blockage ratio and wake velocity coefficient. This provides a means to relate the momentum sink within the shallow water model to a real configuration of devices. Hence estimates can be made of both the extracted and available power for a tidal fence deployed within any coastal geometry. This is distinct from previous research concerning 2D shallow water tidal models.

## 8.2.3 Analysis of Coastal Sites

### 8.2.3.1 General Results

- Based on a desktop survey of various coastal sites, which have been earmarked for tidal stream energy extraction, four classes of coastal geometry have been defined. Each of the surveyed sites listed in Appendix A can be classified into one of these four classes of geometry, or a combination thereof. Several idealised cases of these generic classes have been modelled numerically and analytically, with the following common conclusions:
  - For all coastal sites modelled, the amount of power that could be extracted by a tidal fence deployed at the site was limited (i.e. a maximum power extraction was shown to exist).
  - For all coastal sites considered the maximum power extraction was not related

in any simple way to the natural kinetic flux or the natural rate of energy dissipation due to bed friction.

- The available power from a tidal fence was maximised when tidal devices with large blockage ratio and high wake velocity coefficient were used. In contrast the extracted power was generally indifferent to the blockage ratio of devices within the fence.
- Maximum available power does not generally coincide with the point of maximum power extraction. This result is consistent with the recent work of Vennell [2010] for an idealised rectangular channel, and implies that more than just the maximum power extraction from a coastal site is required to identify the optimum available power. A numerical model which can represent tidal devices, such as the model developed in this thesis, is therefore necessary to determine the available power at a given coastal site.

#### **8.2.3.2 Tidal Channel**

- The theoretical model of Garrett and Cummins [2004], which described the power extraction in terms of the natural channel flow rate and driving tide, agrees well with numerical simulations of an idealised tidal channel. The theoretical model is less accurate for multiply connected channels when tidal devices are deployed in a subchannel. Furthermore, an alternative model has been presented to predicted the maximum extractable power for cases when the subchannel has an impedance that is much smaller than that of the total multiply connected channel.
- For a single fence of given blockage ratio, a greater fraction of the maximum extractable power can be removed from advection dominated channels (shallow and short channels) than for acceleration and drag dominated channels (long, deep and rough channels).

#### **8.2.3.3 Oscillating Bay**

- The maximum extracted power predicted by the theoretical model of Blanchfield et al. [2008] agrees well with numerical simulations of isolated enclosed bays connected

to an adjoining sea or ocean by a single inlet channel. For more complicated geometry, resembling two inlet channels to the bay, the theoretical model is not appropriate and provides an inaccurate indication of the maximum power extraction. Numerical simulations or alternative theoretical models are required to predict the power extraction for these, more complicated, geometries.

- Wetting and drying in an enclosed bay connected to the open ocean by a narrow channel has been shown to introduce time asymmetry into the time series of extracted power but have little effect on the limit to power extraction.
- The power that can be extracted from an open non-enclosed bay varies along the bay length. Taking the tidal elevation at the mouth of the bay to be fixed, the extracted power is generally largest at the mouth of the bay unless the bay is longer than some resonant length. For any bay length the optimum place to locate a fence along the bay to maximize the available power is dependent on the geometry of the bay and the number of devices installed within the fence.

#### **8.2.3.4 Coastal Headland**

- The power that can be extracted from a tidal fence deployed near to a coastal headland is limited because flow will tend to bypass, predominantly on the ocean side. The maximum power is not well predicted by the undisturbed kinetic flux or the natural dissipation of energy due to bed friction. For a given background tidal current, the extractable power increases when the device is placed at the location of maximum natural kinetic flux.
- Unlike the deployment of tidal devices in channels and inlets where the reduction in tidal flushing may be of major concern, the deployment of a tidal fence near to a headland can lead to an increase in mean bed shear stress and tidal dispersion, increasing the potential for bed load transport, and the mixing and transport of suspended sediment and pollutants, respectively.

## 8.3 Future Research

### 8.3.1 Verification of Local Field

Actuator disc theory has been used in the present thesis to approximate the local field around a tidal device. However, this theory cannot account for a rough seabed or non-uniform and unsteady upstream flow. It is therefore indifferent to the shape and position of the actuator disc in the fluid cross-section. To understand better the local field about a tidal fence 3D numerical simulations of porous plates, similar to those being conducted at Southampton University (see, for example, Harrison et al. [2010]), should be undertaken but with an emphasis on varying the disc shape, disc placement and flow conditions (i.e. non-uniform and non-steady) in a variety of rough channel cross-sections. An important metric to compare across these numerical experiments will be the thrust applied by the disc for a given quantity of power removed at the disc, which together with the device blockage ratio, will also define the disc efficiency.

Models of the local field should also be extended to incorporate supporting structure, such as foundation or moorings. Models of this kind are necessary to estimate the thrust of the tidal device and the drag due to the supporting structure, the latter of which will increase the power extracted from the flow but not generally the power available to the turbines. Consequently these models will allow for a better estimation of the installed efficiency of a tidal device.

### 8.3.2 Shallow Wake of a Tidal Fence

In the present thesis a line sink of momentum has been used to introduce a tidal fence, comprised of many tidal devices, into a 2D model based on the SWEs. When the fence is laterally unbounded, as for the case of flow around a fence near to a headland, a shallow water wake is simulated behind the fence that eventually mixes with the surrounding tidal stream. To use the 2D model to accurately assess the environmental effects of energy extraction, and the interaction between unbounded fences placed in close proximity, it is important to verify if the shallow wake simulated with the 2D model is an accurate representation of reality. This verification could be undertaken by comparing simulations to experimental results (for example those of Chen and Jirka [1995] concerning perforated

plates that extend over the full depth of a shallow water flow, or new experiments on porous strips that do not traverse the full depth of the fluid). 3D numerical models would also provide a useful comparison.

### 8.3.3 Compound Sites and Fence Interaction

Using a line sink of momentum to represent a fence of tidal devices in a shallow water model, several idealised coastal basins have been investigated in the present thesis. It has been shown in each case that there is a limit to power extraction and available power. Due to time constraints many other idealised cases of interest, including (1) various compound additions of the individual class of geometry outlined in Chapter 3 and (2) the introduction and interaction of numerous tidal fences at a given coastal site, have not been analysed in this work. The numerical code and representation of tidal fences developed in this thesis can, however, be applied to such cases.

There is also capability, with the simple numerical representation of tidal fence discussed in this thesis, to model fence comprised of turbines which have cut-in and cut-out power limits. This would be achieved by calculating the momentum sink for a fence that has a turbine porosity ( $\alpha_2$ ) which is defined by a simple function of the power removed by the turbines or the magnitude and direction of the incident tidal current. Modelling turbines in this way would allow for a more realistic representation of turbines. Furthermore, since the cut-in and cut-out limits will effect the structural requirements and thus cost of the turbines, this modelling could also be used to determine the most appropriate turbine loading range (i.e. cut-in and cut-out limits) to reduce the cost of the turbines relative to the power they remove.

### 8.3.4 Analysis of Actual Coastal Basins

It is inevitable that, prior to the installation of tidal fences or farms, site specific models will be required. These models will need to provide estimates of available tidal energy and inform environmental effects, such as localised changes in tidal range, currents and inter-tidal area. The models will also need to account for the interaction of tidal farms placed in close proximity, which appears to be inevitable given the recent leasing of 10 individual sites clustered in the Pentland Firth and Orkney waters (Crown Estate, 2010).

Research currently underway at Oxford is investigating energy extraction from three UK sites: Pentland Firth, Anglesey, and Bristol Channel. It is intended that this work will introduce tidal devices using the line sink of momentum suggested in this thesis. Another important aspect of that research will concern the treatment of open boundary conditions, particularly for a resonant site such as the Bristol Channel (Rainey [2009]). A simple characteristic boundary condition, similar to that presented in Chapter 4, would be a useful starting point to avoid the excitation of artificial resonant modes when tidal devices are introduced.

# Appendix A

## Survey of Tidal Stream Sites

The growing interest in tidal power around the globe has led to the investigation of numerous coastal sites. This appendix surveys some of these sites, focusing on North America and the United Kingdom. The aim of the survey is determine general topography, bathymetry and seabed conditions across the range of identified sites.

### A.1 United Kingdom

A study of the UK tidal stream resource has been conducted by Black and Veatch Ltd, 2005 (and Black and Veatch Ltd, 2004), in which 57 UK sites were investigated. The characteristics of a number of these sites are summarised in Table A.1, together with a classification based on the generic set of coastal basins discussed in Chapter 3. The characteristics include, where relevant, length scale  $L$ ,  $L_1$  and  $L_2$  (see Figure 3.2), average site depth  $h_d$  close to the location of peak tidal currents, width  $W$  (for a channel), basin area  $S_0$  (for an enclosed bay) and peak tidal current on spring (Sp.) tides and neap (Np.) tides. General topography, bathymetry and (predominant) seabed conditions are also noted and a sketch of each site is given in Figure A.3. The regional locations of the individual sites around the UK are outlined in Figure A.1.

### A.2 North America

The tidal stream resource on the West and East coasts of North America have also been investigated by Triton Consultants Ltd. [2006] and EPRI [2006]. Figure A.2 outlines several regional locations of perspective tidal sites highlighted in these investigations. Table A.2

records similar characteristics to Table A.1 and Figure A.4 sketches the individual sites. Current velocities are often recorded as peak velocities in the literature, and are assumed to be representative of Spring tidal velocities.

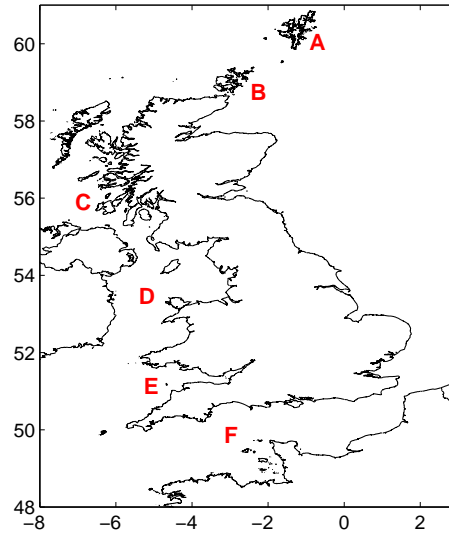


Figure A.1: Regional locations around the UK (A-F) of the sites listed in Table A.1. The axis are degrees of longitude and latitude.

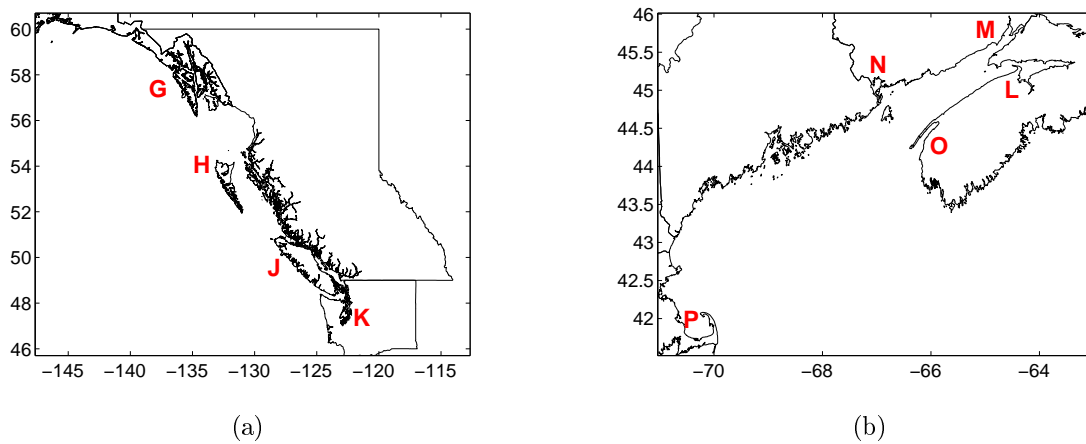


Figure A.2: Regional locations around North America (G-P) of the sites listed in Table A.2 (a) The West Coast, (b) The East Coast. The axis are degrees of longitude and latitude.

Site Name (Loc.)	Parameters <sup>(1,2)</sup>						Comments				
	$L$ km	$h_d$ m	$W$ km	$S_0$ km <sup>2</sup>	$U$ , m/s Sp. Ne.		Topography <sup>(1,2)</sup>	Bathymetry <sup>(1,3)</sup>	Seabed <sup>(4)</sup>	Class	Sketch
Yell Sound (A)	3	30	1.5	-	3.45	1.72	Two ~1.5 km wide channels separated by string of islands.	Average depth 30 m.	RSG	a	UK 1
Bluemull Sound (A)	5	25	1.5	-	3.45	1.72	1 km wide constriction near Belmont.	Average depth 25 m.	RSG	a	UK 2
Pentland Firth (A)	24	59	12	-	6.18	2.64	Three main islands interrupt the strait, (Swona, Stroma and the Muckle Skerry.)	Depth 60-80 m over majority of Strait.	Bedrock.	a/c	UK 3
Dunscansby Head (A)	4x4	65	-	-	5.15	2.2	Smooth headland. Adjacent island Stroma is ~1 x 2 km.	Bathymetry contours follow coastline. Depth drops smoothly to 70 m at 200 m from shore.	Bedrock. GS near shore.	d	UK 4
Inner Sound (A)	2	33	2	-	3.35	1.44	Located between Stroma and the Scottish Mainland.	Average depth 33 m.	RSG	a/c	UK 5
Papa Westray (A)	7	30	2.5	-	2.93	1.46	Papa Westray Is. is ~2 km wide by 7 km long.	Average depth 30 m.	RSG	a/c	UK 6
Fall of Warness <sup>(5)</sup> (A)	2	18	1.5	-	3.45	1.72	EMEC tidal testing site. Muckle Green Holm Is. provides some constriction.	Test locations depth ~20 m.	RSG	a/d	UK 7
FersNess (A)	6	25	1	-	2.59	1.29	Channel turns to the west 90 degrees.	Average depth 25 m.	RSG	a	UK 8
Gulf of Corryvreckan (B)	2	22	1	-	2.6	1.29	Site of the world's third largest whirlpool.	Significant variation in bathymetry.	RSG	a/c	UK 9
Dorus Mor (B)	.75	22	.75	-	4.1	2.04	Island diameter <1 km.	Average depth 22 m.	RSG	a/d	UK 10
Loche Linnhe - Corran (C)	1	30	0.4	-	2.59	1.29	Large currents flow through constriction North of Loche.	Average depth 30 m.	RSG	a/b	UK 11
Kyle Rhea (C)	3	22	0.4	-	4.1	2.04	Slight meander along the channel. Part of channel network.	Average depth 22 m.	RSG	a/b	UK 12

Table A.1: Summary of tidal sites around the United Kingdom - Part (1)

Sanda Sound (D)	1	22	-	-	2.6	1.29	Sanda Is. diameter 1 km.	Average depth 22 m.	SG	c/d	UK 13
Mull of Kintyre (D)	12x12	22	-	-	2.6	1.29	Rounded headland.	Average depth 22 m.	SG	d	UK 14
Mull of OA (D)	6x6	22	-	-	2.6	1.29	Rounded headland.	Average depth 22 m.	RSG	d	UK 15
Anglesey (D)	20x20	35	-	-	3.21	1.61	Rounded headland.	Depth increases to 40-60 m far from shore.	SG	d	UK 16
Rathlin Island (D)	10	80	5	-	2.6	1.4	Rathlin Island has dimensions of 1.5x5 km.	Depth increases to 100 m 2 km beyond Rathlin Is.	RSG	c	UK 17
Mull of Galloway (D)	4x6	80	-	-	2.6	1.4	Rounded headland with a thin cape.	Average depth 33 m.	SG	d	UK 18
Bristol Channel <sup>(6)</sup> (E)	100	33	40	-	2.6	1.4	Linear reduction in width East of Ilfracombe (40 km wide)	Bathymetry reduces linearly inland.	Sand & mud.	b	UK 19
Isle of Wight (F)	20x20	30	-	-	3.2	1.6	Relatively well rounded island/headland.	Depth slopes to 80 m depth 20-30 km to South.	RSG	d	UK 20
Portland Bill <sup>(7)</sup> (F)	2x5	33	-	-	3.8	1.9		Average depth 33 m. Slopes to 50 m depth over 20 km.	SG	d	UK 21
Alderney Race <sup>(8)</sup> (F)	2x5	39	10	-	4.4	2.4	Right angled headland. Forms 10 km channel with Alderney Is.	10 km north of Alderney depth 80 m.	RSG	c/d	UK 22
Casquets (F)	-	70	-	-	2.6	1.4	Flow beyond Alderney Island.	Average depth 70m.	RSG	c/d	UK 23
North West Guernsey (F)	-	57	-	-	2.1	1.1	Flow around Guernsey Is., which is 10 km long.	Average depth 57 m.	RSG	d	UK 24
North East Jersey (F)	-	22	-	-	3.1	1.7	Continuation of the Alderney Race. Jersey Is. 10 km long.	Average depth 22 m.	RSG	d	UK 25

Sources: (1) Black and Veatch [2005]; (2) Google Maps: maps.google.co.uk/; (3) Tidal Stream Atlas' UKHO; (4) British Geological Survey (BGS); (5) European Marine Energy Centre: www.emec.org.uk; (6) Rainey [2009]; (7) Bahaj and Myers [2004]; (8) Blunden and Bahaj [2007]

Notes: RSG=Rock, Sand and Gravel, SG=Sandy Gravel, for class (d) sites  $L \equiv L_1 \times L_2$ .

Table A.1: Summary of tidal sites around the United Kingdom - Part (2)

Site Name (Loc.)	Parameters					Comments				
	$L$ km	$h_d$ m	$W$ km	$S_0$ km <sup>2</sup>	$U$ , m/s	Topography	Bathymetry	Seabed	Class	Sketch
N. Inian Pass <sup>(4,5)</sup> (G)	6	230	3	-	4.1		Deep site, flat bottom at depths > 290 m.	Rock	a/b	US 1
S. Inian Pass <sup>(4,5)</sup> (G)	5	45	1.5	-	4.9		45 m averaged depth, 120 m max. depth.	Rock	a/b	US 2
N. Passage <sup>(4,5)</sup> (G)	8	110	3	-	2.9	Width increases linearly to west.	110 m average depth, 140 m max. depth.	Rock	a/b	US 3
S. Passage <sup>(4,5)</sup> (G)	8	90	4	-	3.3		90 m average depth 140 m max. depth. Slope of 20-30 m.	Rock	a/b	US 4
Haidai Gwaii <sup>(6,7)</sup> (H)	27	14	2.5	-	2.5	Long inlet to a small basin.	14 m average depth, 40-75 m max. depth.	SG	b	US 5
Johnstone Strait <sup>(8)</sup> (J)	100	5	400	-	6.7	Uniform width. Many tributaries exist.	Mid channel depth up to 400 m.	Rock, mud & silt.	a	US 6
Admiralty Inlet <sup>(9,10)</sup> (K)	20	50	5	-	2	Island forms south-west boundary.	Average depth of 35-50 m, 120 m max. depth.	SG	a/b	US 7
Tacoma Narrows <sup>(11)</sup> (K)	8	40	1.2	-	3.3	Uniform width and substantial bend.	Average depth of 40 m, 68 m max. depth.	SG	a/b	US 8
San Francisco <sup>(9,10)</sup> (-)	10	70	1.5	1000	2.5		Under bridge 70 m average depth.	Bedrock & Sand	b	US 9
Minas Channel <sup>(1)</sup> (L)	13.1	40	3.9	600	2.5	Strong separation near the cape (Split). Area of bay at HW 3x area at LW.	40 m averaged depth, 70 m max. depth.	Bedrock	b	US 10
Minas Passage <sup>(1)</sup> (L)	4.5	50	1.4	660	4	Western exit dominated by cape (Split). Area of bay at HW 3x area at LW.	50 m averaged depth, 100 m max. depth.	Bedrock	b	US 11
Cobequid Bay <sup>(1)</sup> (L)	7	10	2.1	120	2	Short bay ~20 km long. No notable constrictions	6 m averaged depth, 8-12 m max. depth. > linear slop to shore	SG	b	US 12

Table A.2: Summary of tidal sites around North America - Part (1)

Cumberland Basin <sup>(1)</sup> (M)	2.2	10	0.4	13.2	2.3	25% change in A between LW & HW.	Uniform rectangular section. At entrance 10 m averaged depth, 18-23 m max. depth.	GSB.	b	US 13
Digby Gut <sup>(1)</sup> (O)	3.5	25	0.8	75	3.5		20-25 m average depth, up to 90 m max. depth.	Sand, & Boulders.	b	US 14
Petit Passage <sup>(1)</sup> (O)	3.7	16	0.6	-	3.5	Parallel channel sides, with a step change at half way.	16 m average depth, up to 40 m max. depth.	Sand, & Boulders.	a/b	US 15
Muskaget Channel <sup>(3)</sup> (P)	7	22	2.5	-	2	Wide channel between Nantucket Is. and mainland.	16 m deep channel (width 7 km) located on northern edge.	Bedrock	a/c	US 16
Lubec Narrows <sup>(2)</sup> (N)	.1	7.5	0.025	-	1.6	Small capes at inlet and outlet.	Deep trench, 50 m max. depth.	GMB	a/b	US 17
Western Passage <sup>(2)</sup> (N)	7	30	2	-	2	Part of a channel network. Very turbulent flow conditions	108 m depth towards the Southern end of the channel.	GMB	a/b	US 18
Harbour Passage <sup>(2)</sup> (N)	7	30	2	-	2	Many islands and interconnected channels. Entry and exit poorly defined in South.	30 m average depth, 90m max. depth.	GMB	a/b	US 19
Latete Passage <sup>(2)</sup> (N)	7	20	2	-	2.5	Two islands to the North. Stream meanders to South..	10-20 m average depth, 40 m max. depth.	Bedrock	a/b	US 20

Sources: (1) EPRI-TP-003-NS; (2) EPRI-TP-003-NB; (3) EPRI-TP-003-MA; (4) EPRI-TP-003-AK; (5) NOAA Electronic Navigational Charts;(6) Blanchfield et al. [2008]; (7) Dept. Fisheries & Oceans (CHS): <http://www.dfo-mpo.gc.ca>; (8) Sutherland et al. [2005]; (9) Puget Sound Tidal Energy: <http://www.pstidalenergy.org>; (10) NOAA Tidal Current Predictions; (11) EPRI-TP-006-WA; (12) EPRI-TP-006-CA

Notes: RSG=Rock, Sand and Gravel, SG=Sandy Gravel, GMB=Gravel, Mud and Bedrock, for class (d) sites  $L \equiv L_1 \times L_2$ .

Table A.2: Summary of tidal sites around North America - Part (2)

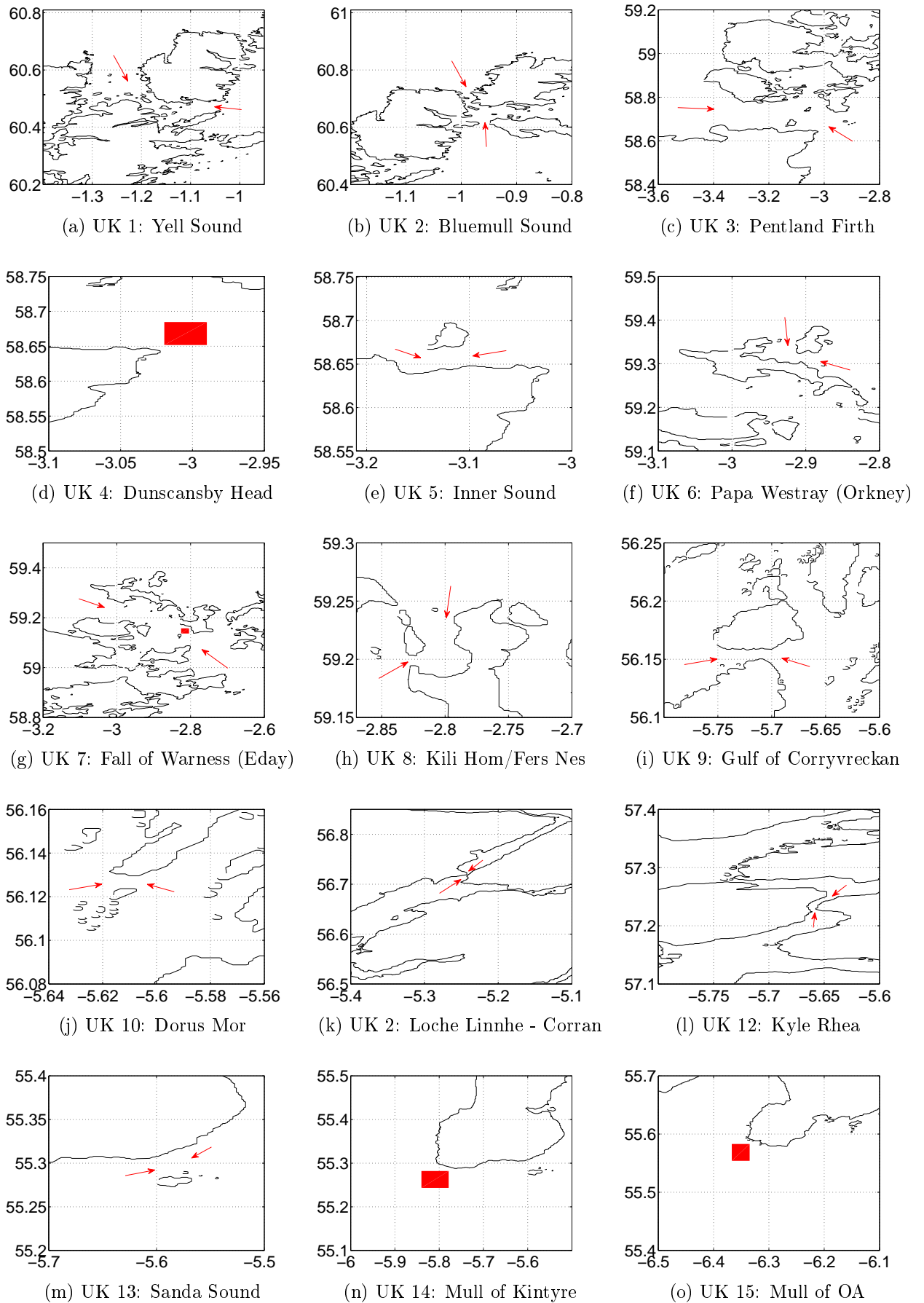


Figure A.3: Sites around the UK documented in Table A.1 (Part 1).

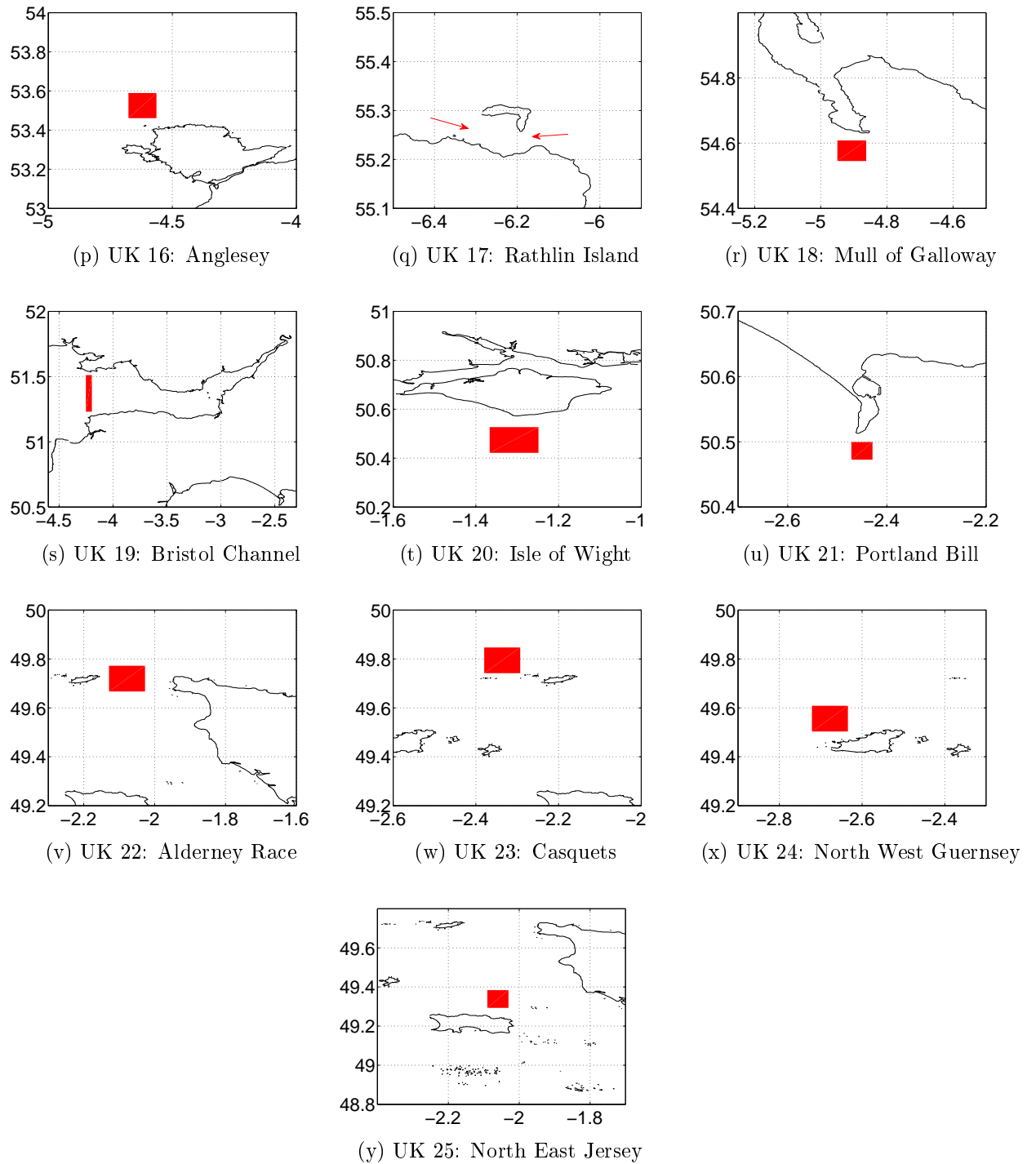


Figure A.3: Sites around the United Kingdom documented in Table A.1 (Part 2).

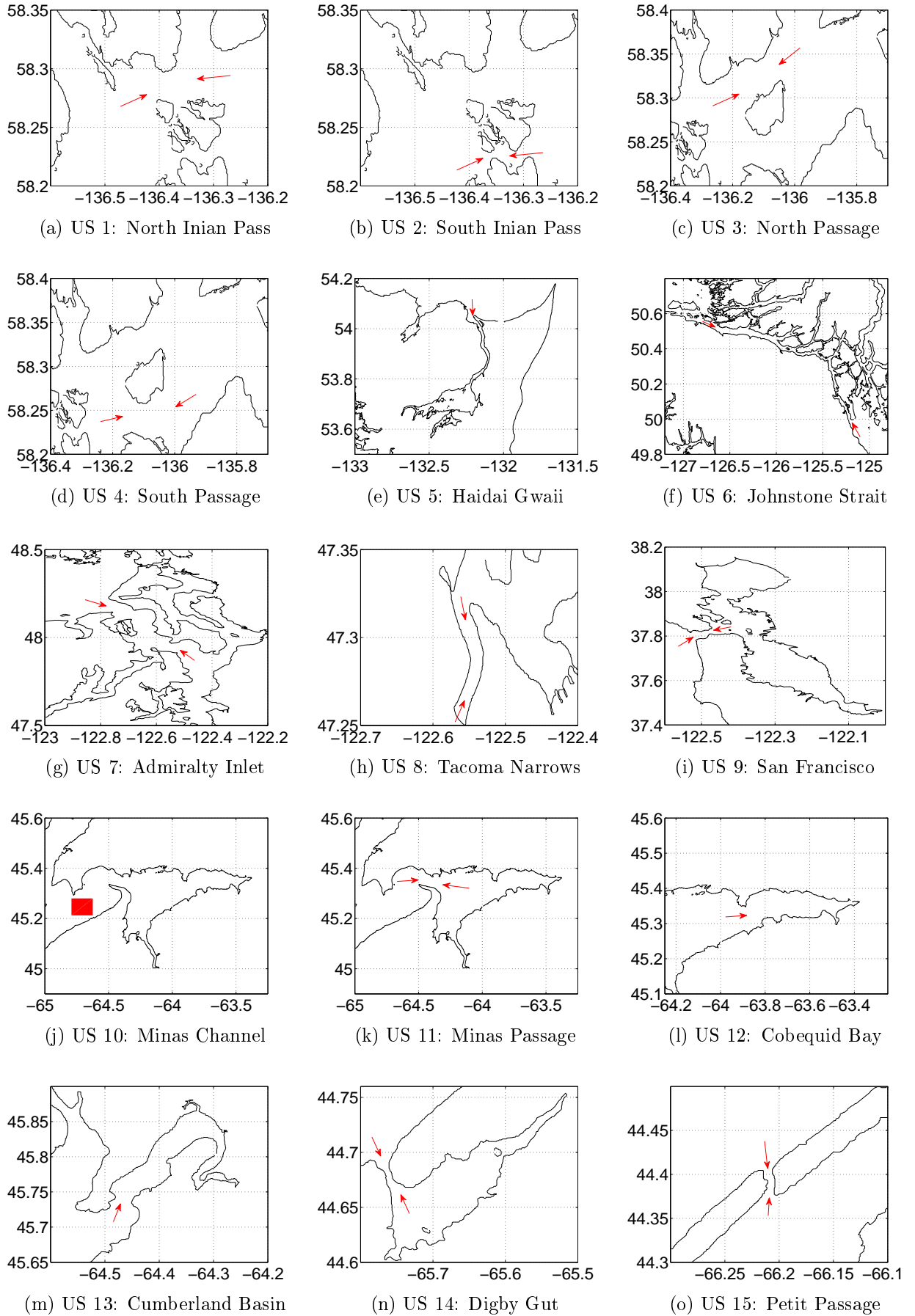


Figure A.4: Sites around North America documented in Table A.2 (Part 1).

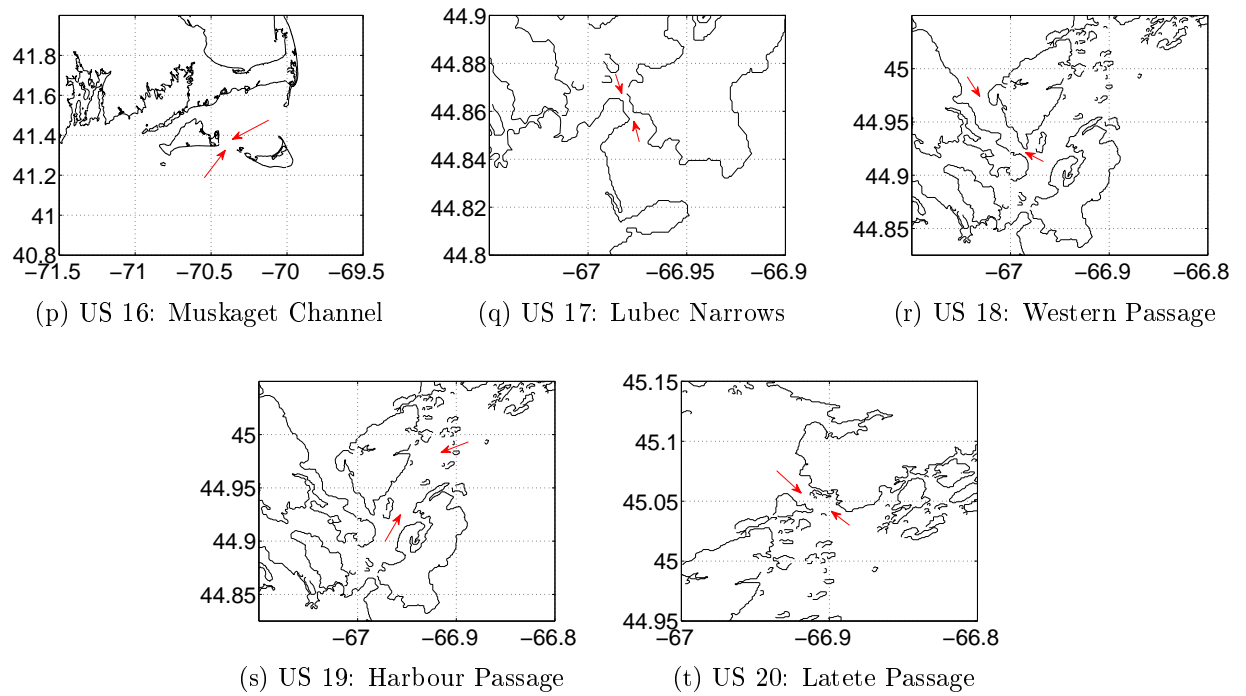


Figure A.4: Sites around North America documented in Table A.2 (Part 2).

# Appendix B

## DG Numerical Solver (OxTide)

This appendix documents (1) the detailed numerical solution of the discrete system of equations outlined in Section 4.4, which has been implemented into a numerical code called OxTide, and (2) validation tests of OxTide for a series of linear, non-linear and viscous benchmark problems and experiments.

### B.1 Numerical Solution

To implement the DG formulation of the SWEs the semi-discrete system of equations outlined in Section 4.4, Chapter 4, must be formed at each time step and for every element  $\Omega_e$ . This requires specification of the shape and basis functions and the subsequent formulation of the terms in the discrete equations.

#### B.1.1 Shape Functions

The elements usually considered in the present work are three node straight sided triangular elements. (Triangular isoparametric elements are also used in some of the simulations. Section B.1.5 discusses the implementation of these elements.) Triangular elements have been adopted, as opposed to say structured and unstructured rectangles or curvilinear rectangles, because of the availability of open source triangle mesh generators and the practical need to model complex geometry with little effort (Persson [2004]).

A linear three node triangle in *global*  $(x, y)$  coordinates is shown in the top left of Figure B.1. As in the standard finite element approach it is efficient to specify a set of basis functions  $\psi_k$  or  $\ell_k$ , in a natural coordinate system  $\vec{\xi} = (\xi_1, \xi_2)$  which will ensure that

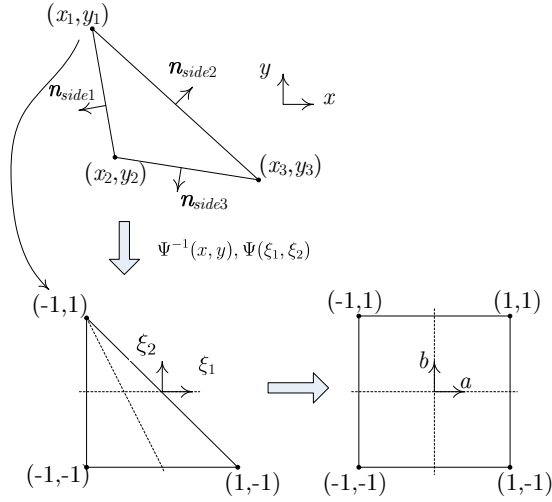


Figure B.1: Linear triangular elements mapped to the natural coordinates  $(\xi_1, \xi_2)$  via the transformation  $\Psi(\xi_1, \xi_2)$ , and subsequently mapped onto the warped square defined in integration coordinates  $(a, b)$ .

the numerical integration is identical for each element. Therefore, the global triangle is mapped to the standard natural triangle defined for  $\{0 \leq \xi_1, \xi_2; \xi_1 + \xi_2 \leq 0\}$ , as shown in the bottom left of Figure B.1. This mapping is achieved with the shape functions:

$$N_1(\xi_1, \xi_2) = \frac{1 + \xi_2}{2}, \quad N_2(\xi_1, \xi_2) = -\frac{\xi_1 + \xi_2}{2}, \quad N_3(\xi_1, \xi_2) = \frac{1 + \xi_1}{2}. \quad (\text{B.1})$$

The global coordinates are then related to the natural coordinates through the following relationships  $x(\xi_1, \xi_2) = \mathbf{N}(\xi_1, \xi_2) \cdot \mathbf{x}_i$ , and  $y(\xi_1, \xi_2) = \mathbf{N}(\xi_1, \xi_2) \cdot \mathbf{y}_i$ , where  $\mathbf{N}(\xi_1, \xi_2)$  is the vector of the shape functions defined in Equation B.1, and the vectors  $\mathbf{x}_i$  and  $\mathbf{y}_i$  describe the vertex coordinates (listed in anticlockwise order). The Jacobian associated with the transformation is

$$J_{\vec{x}, \vec{\xi}} = \frac{\partial(x, y)}{\partial(\xi_1, \xi_2)} = \frac{1}{4} ((x_1 - x_2)(y_3 - y_2) - (x_3 - x_2)(y_1 - y_2)). \quad (\text{B.2})$$

## B.1.2 Basis Functions

From the discussion in Section 4.4 it is clear that either modal or nodal basis functions can be adopted. Theoretically numerical convergence can be proved when either approximation is used, and so either form is an acceptable choice in a finite element context (Hesthaven and Warburton [2008]). In fact, when the true solution is a polynomial with degree less than  $n$ , both approaches will yield identical results. In practice however, the nodal approach

provides one subtle advantage in that physical boundary conditions, as would be required in coastal models near an open boundary, can be introduced directly through a nodal value rather than via a projection into modal space (Giraldo and Warburton [2008]). Nodal basis functions are therefore adopted herein.

### B.1.2.1 Choice of Nodal Points

The set of element nodal points that provide the best polynomial approximation minimise the Lebesgue constant (Karniadakis and Sherwin [2005]). A number of nodal point sets for natural triangles exist which give consistent results with respect to the Lebesgue constant (see, for example, Karniadakis and Sherwin [2005]). In the present thesis, warped equispaced points are used. MATLAB algorithms to compute these points for the natural triangle are available in Warburton [2006]. Example points for  $n = 2, 4$  and  $8$  are given in Figure B.2.

### B.1.2.2 Choice of Nodal Basis Functions

There are no known explicit nodal basis functions that pass through the warped equispaced nodal points. Instead the basis functions must be defined implicitly in terms of a set of auxiliary polynomials  $\{\phi_k\}$ , which can be arbitrary provided that they have the required polynomial degree, by writing

$$\sum_k^M \check{s}_k \phi_k(\vec{\xi}_i) = \sum_k^M s_k \ell_k(\vec{\xi}_i), \text{ for all } i \leq M, \quad (\text{B.3})$$

where  $\{\check{s}_k\}$  are a set of modal coefficients,  $\{s_k\}$  are nodal coefficients and  $\ell(\vec{\xi})$  are nodal basis functions, which have the typical Lagrangian property that at the  $M$  node points  $\ell_k(\vec{\xi}_i) = \delta_{ki}$ , where  $\delta$  is the Kronecker delta. Equation B.3 can be expressed in matrix form by enforcing the Lagrangian property of the functions  $\{\ell_k\}$ , as

$$s_k = \mathcal{V} \check{s}_k, \text{ with } \mathcal{V}_{(i,k)} = \phi_k(\vec{\xi}_i), \quad (\text{B.4})$$

where  $\mathcal{V}$  is termed the *Vandermonde* matrix. The nodal basis functions are therefore related to the auxiliary polynomials  $\{\phi_k\}$  by

$$\mathcal{V}^T \{\ell_k\} = \{\phi_k\}, \quad \text{or} \quad \ell_k(\vec{\xi}) = \sum_j^M (\mathcal{V}^T)_{(k,j)}^{-1} \phi_j(\vec{\xi}), \quad (\text{B.5})$$

which illustrates that the nodal basis functions are dependant on the nodal points and the choice of auxillary polynomials. An obvious choice for the auxillary polyomials is  $\xi_1^\alpha \xi_2^\beta$ , where  $\{\alpha, \beta : 0 \leq \alpha, \beta; \alpha + \beta \leq n\}$ . However, as pointed out by numerous authors (see, for example, Dubiner [1991], Kirby and Sherwin [2006]), these basis functions are only well-conditioned when  $n$  is small (meaning that for larger  $n$  ( $\gtrsim 6$ ) the Vandermonde matrix will have a large condition number). Dubiner [1991] has proposed a set of basis functions on the natural triangle that is well conditioned for large  $n$ . These functions are orthonormal and constitute a *warped* tensor product of Jacobi polynomials given by

$$\phi_k(a, b) = \theta_{m,j}(a, b) = \sqrt{\frac{2}{2m+1} \left( \frac{2^{2m+2}}{m+j+1} \right)} P_m^{0,0}(a) (1-b)^m P_j^{2m+1,0}(b), \quad (\text{B.6})$$

where the subscripts  $m$  and  $j$  are such that  $\{0 \leq m, j; m+j \leq n\}$  giving in total  $M$  functions. The coordinates  $(a, b)$  are related to the natural coordinates  $(\xi_1, \xi_2)$  by (see the bottom right of Figure B.1 for a geometrical representation of the coordinates  $(a, b)$ )

$$a = 2 \frac{(1 + \xi_1)}{1 - \xi_2}, \quad b = \xi_2, \quad \text{or} \quad \xi_1 = \frac{(1+a)(1-b)}{2} - 1, \quad \xi_2 = b, \quad (\text{B.7})$$

and  $P_n^{\alpha,\beta}$  is a Jacobi polynomial defined by

$$P_n^{\alpha,\beta}(x) = \frac{(-1)^n d^n [(1-x)^\alpha (1+x)^\beta (1-x^2)^n]}{n! 2^n dx^n} (1-x)^{-\alpha} (1+x)^{-\beta}. \quad (\text{B.8})$$

Using Equation B.6 a set of  $M$  auxiliary polynomials  $\{\phi_k\}$  can be formed that, combined with a set of  $M$  nodal points, can be used to define a set of nodal functions through Equation B.5. For example, an approximating polynomial of order  $n = 2$  ( $M = 6$ ) would require the set of auxilliary polynomials  $\{\theta_{0,1}, \theta_{0,1}, \theta_{1,0}, \theta_{0,2}, \theta_{2,0}, \theta_{1,1}\}$  from which six nodal basis functions  $\{l_1, l_2, l_3, l_4, l_5, l_6\}$  follow from Equation B.5 when six node points  $\{\xi_i\}$  are defined (see Figure B.2 for an example).

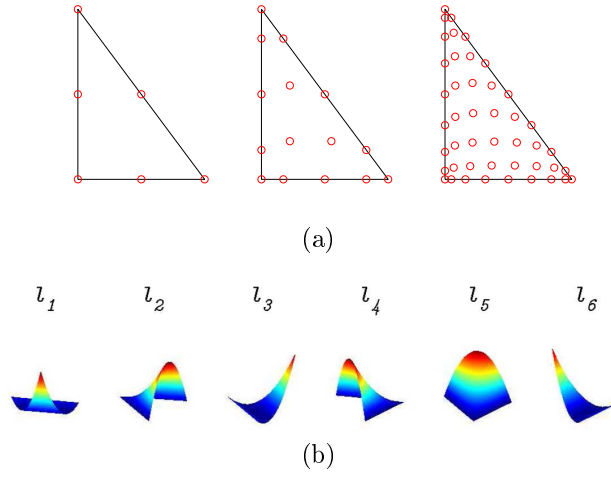


Figure B.2: (a) From left to right, example warped nodal points on the triangle for  $n = 2, 4$  and 8. (b) Plots of the computed nodal basis function  $\{l_k\}$ , for  $n = 2$ . The nodal basis functions take a value of unity at the nodal points illustrated for  $n = 2$  in sub-figure (a).

### B.1.3 Forming the Spatial Operators

#### B.1.3.1 Mass Matrix, $\mathcal{M}$

Adopting nodal basis functions  $\{l_k\}$  and introducing the relevant Jacobian (Equation B.2), the elements within the mass matrix can be written as

$$\mathcal{M}_{(i,k)} = J_{\vec{x},\vec{\xi}} \iint_{\Omega_e} l_i l_k d\xi_1 d\xi_2, \quad (\text{B.9})$$

where the variable  $\mathcal{T}$  refers to the natural triangle defined in Section 4.5.1. Based on Equation B.5, Equation B.9 can be rewritten in terms of the Vandermonde matrix to give

$$\mathcal{M}_{(i,k)} = J_{\vec{x},\vec{\xi}} \iint_{\Omega_e} \left( \sum_j^M (\mathcal{V}^T)^{-1}_{(i,j)} \phi_j \right) \left( \sum_m^M (\mathcal{V}^T)^{-1}_{(k,m)} \phi_m \right) d\xi_1 d\xi_2. \quad (\text{B.10})$$

Since the polynomials  $\{\phi_k\}$  are orthonormal over the triangle  $\mathcal{T}$ , this integral can be evaluated exactly to give  $\mathcal{M} = J_{\vec{x},\vec{\xi}} (\mathcal{V}\mathcal{V}^T)^{-1}$ , which is easily computed for a given element in the domain.

### B.1.3.2 Area Integrals, $\mathcal{B}, \mathcal{E}, \mathcal{G}$

Initially consider  $\mathcal{B}$ . Adopting nodal basis functions and natural coordinates, the  $i$ th term of the vector  $\mathcal{B}$  becomes

$$\mathcal{B}_{(i)}^x = J_{\vec{x}, \vec{\xi}} \iint_{\Omega_e} \left( \frac{\partial \ell_i}{\partial x} \mathbf{F}(\mathbf{U}_h, \mathbf{Q}_h) \right) d\xi_1 d\xi_2 + J_{\vec{x}, \vec{\xi}} \iint_{\Omega_e} \left( \frac{\partial \ell_i}{\partial y} \mathbf{G}(\mathbf{U}_h, \mathbf{Q}_h) \right) d\xi_1 d\xi_2 \quad (\text{B.11})$$

which can be expanded via the chain rule to read and split into two integrals by factoring out the constant derivatives  $\partial \xi_1 / \partial x$  and  $\partial \xi_2 / \partial x$  (the second part  $\mathcal{B}_{(i)}^y$ , is not written for brevity)

$$\mathcal{B}_{(i)}^x = J_{\vec{x}, \vec{\xi}} \frac{\partial \xi_1}{\partial x} \iint_{\Omega_e} \frac{\partial \ell_i}{\partial \xi_1} \mathbf{F}(\mathbf{U}_h, \mathbf{Q}_h) d\xi_1 d\xi_2 + J_{\vec{x}, \vec{\xi}} \frac{\partial \xi_2}{\partial x} \iint_{\Omega_e} \frac{\partial \ell_i}{\partial \xi_2} \mathbf{F}(\mathbf{U}_h, \mathbf{Q}_h) d\xi_1 d\xi_2. \quad (\text{B.12})$$

The flux terms within this expression are determined relative to Equation 4.3, as

$$\mathbf{F}(\mathbf{U}_h, \mathbf{Q}_h) = \begin{bmatrix} \mathbf{U}_h^{(2)} \\ \left( \mathbf{U}_h^{(2)} \right)^2 / \mathbf{U}_h^{(1)} + \frac{1}{2} g \left( \mathbf{U}_h^{(1)} \right)^2 + 2v_T \mathbf{U}_h^{(1)} \mathbf{Q}_h^{(1)} \\ \mathbf{U}_h^{(2)} \mathbf{U}_h^{(3)} / \mathbf{U}_h^{(1)} + v_T \mathbf{Q}_h^{(1)} \left( \mathbf{Q}_h^{(3)} + \mathbf{Q}_h^{(2)} \right) \end{bmatrix} \quad (\text{B.13})$$

where  $\mathbf{U}_h^{(i)} = \sum_k^M \mathbf{U}_k^{(i)} \ell_k$  refers to the  $i$ th element of the vector  $\mathbf{U}_h$ , for example, and  $g$  and  $v_T$  are gravity and depth-averaged eddy viscosity. The numerical computation of Equation B.12 is achieved with quadrature over the triangular domain  $\Omega_e$  for each element

$$\begin{aligned} \mathcal{B}_{(i)}^x &= J_{\vec{x}, \vec{\xi}} \frac{\partial \xi_1}{\partial x} \sum_q^Q \left[ w_q \frac{\partial \ell_i(\vec{\xi}_q)}{\partial \xi_1} \mathbf{F}(\mathbf{U}_h(\vec{\xi}_q), \mathbf{Q}_h(\vec{\xi}_q)) \right] + \\ & J_{\vec{x}, \vec{\xi}} \frac{\partial \xi_2}{\partial x} \sum_q^Q \left[ w_q \frac{\partial \ell_i(\vec{\xi}_q)}{\partial \xi_2} \mathbf{F}(\mathbf{U}_h(\vec{\xi}_q), \mathbf{Q}_h(\vec{\xi}_q)) \right], \end{aligned} \quad (\text{B.14})$$

where  $\{w_q\}$  are a set of quadrature weights corresponding to the quadrature points  $\{\vec{\xi}_q\}$ . A set of exact quadrature points on the right angled triangle are used (compiled by Hesthaven and Warburton [2008]), which can integrate polynomials up to  $n = 28$  exactly. However it should be noted that the integrand in Equation B.12 is a rational function (due to the division by  $\mathbf{U}_h^{(1)} = \sum_k^M \mathbf{U}_k^{(1)} \ell_k$ , in various terms of the flux vector) and so integration is not exact using quadrature. Despite this, the assumption is made herein that the flux vector is

at most of order  $3n$  and so quadrature is performed on Equation B.12 assuming that the integrand is at most order  $4n - 1$  (where an additional  $n - 1$  occurs due to the derivatives of the basis functions).

To compute the quadrature formulae in Equation B.14, the gradients of the nodal basis functions are evaluated, together with the fluxes, at the quadrature points. The gradients of the basis functions are computed from (only the  $\xi_1$  direction is considered for brevity)

$$\left. \frac{\partial \ell_k}{\partial \xi_1} \right|_{\vec{\xi}_q} = \sum_j^M (\mathcal{V}^T)^{-1}_{(k,j)} \left. \frac{\partial \phi_j}{\partial \xi_1} \right|_{\vec{\xi}_q}, \quad (\text{B.15})$$

where the derivatives of the polynomials  $\{\phi_k\}$  are found from

$$\left. \frac{\partial \phi_k}{\partial \xi_1} \right|_{\vec{\xi}_q} = \frac{\partial a}{\partial \xi_1} \left. \frac{\partial \phi_k}{\partial a} \right|_{\vec{\xi}_q} + \frac{\partial b}{\partial \xi_1} \left. \frac{\partial \phi_k}{\partial b} \right|_{\vec{\xi}_q}. \quad (\text{B.16})$$

For convenience a differentiation matrix  $\mathcal{D}_{\vec{\xi}}$ , containing the derivatives for each nodal basis function at each quadrature point, is defined as

$$\mathcal{D}_{\xi_1} = \mathcal{V}_{\xi_1} \mathcal{V}^{-1}, \quad \text{where} \quad \mathcal{D}_{\xi_1, (q,k)} = \left. \frac{\partial \ell_k}{\partial \xi_1} \right|_{\vec{\xi}_q} \quad \text{and} \quad \mathcal{V}_{\xi_1, (q,k)} = \left. \frac{\partial \phi_k}{\partial \xi_1} \right|_{\vec{\xi}_q}. \quad (\text{B.17})$$

Noting that the conserved and auxiliary variables can be obtained at the quadrature points via

$$\{\mathbf{U}(\vec{\xi}_q)\} = \{\mathbf{U}_q\} = \mathcal{V}_Q \mathcal{V}^{-1} \{\mathbf{U}_k\}, \quad \text{and} \quad \{\mathbf{Q}(\vec{\xi}_q)\} = \{\mathbf{Q}_q\} = \mathcal{V}_Q \mathcal{V}^{-1} \{\mathbf{Q}_k\}, \quad (\text{B.18})$$

with  $(\mathcal{V}_Q)_{(q,k)} = \phi_k(\vec{\xi}_q)$ , introducing Equation B.17 into B.14 gives

$$\mathcal{B}_{(i)}^x = J_{\vec{x}, \vec{\xi}} \frac{\partial \xi_1}{\partial x} \sum_q^Q [w_q (\mathcal{D}_{\xi_1})_{(q,i)} \mathbf{F}(\mathbf{U}_q, \mathbf{Q}_q)] + J_{\vec{x}, \vec{\xi}} \frac{\partial \xi_2}{\partial x} \sum_q^Q [w_q (\mathcal{D}_{\xi_2})_{(q,i)} \mathbf{F}(\mathbf{U}_q, \mathbf{Q}_q)],$$

so that the complete vector  $\mathcal{B}^x$  is simply  $J_{\vec{x}, \vec{\xi}} \frac{\partial \xi_1}{\partial x} \mathcal{D}_{\xi_1}^T \{w_q \mathbf{F}_q\} + J_{\vec{x}, \vec{\xi}} \frac{\partial \xi_2}{\partial x} \mathcal{D}_{\xi_2}^T \{w_q \mathbf{F}_q\}$ , where  $\{w_q \mathbf{F}_q\}$  represents the vector  $(w_1 \mathbf{F}(\mathbf{U}_1, \mathbf{Q}_1), \dots, w_Q \mathbf{F}(\mathbf{U}_Q, \mathbf{Q}_Q))^T$ .

The formation of  $\mathcal{G}$ , which contains the viscous fluxes, is similar to that of  $\mathcal{B}$ . The

resulting calculation for the first component amounts to

$$\mathcal{G}^x = J_{\vec{x}, \vec{\xi}} \frac{\partial \xi_1}{\partial x} \mathcal{D}_{\xi_1}^T (\{w_q \mathbf{R}_{x,q}\}) + J_{\vec{x}, \vec{\xi}} \frac{\partial \xi_2}{\partial x} \mathcal{D}_{\xi_2}^T \{w_q \mathbf{R}_{x,q}\}, \quad (\text{B.19})$$

where  $\{w_q \mathbf{R}_{x,q}\}$  is the vector  $(w_1 \mathbf{R}_x(\mathbf{U}_1), \dots, w_Q \mathbf{R}_x(\mathbf{U}_Q))^T$ . Again the integration of the viscous fluxes using quadrature is inexact because of the presence of rational functions. Satisfactory results have, however, been achieved using quadrature sufficient to integrate a polynomial of order  $3n - 1$ .

$\mathcal{E}$  can be computed as  $|J_{\vec{x}, \vec{\xi}}| (\mathcal{V}_Q \mathcal{V}^{-1})^T \{w_q \mathbf{S}_q\}$ , where  $\{w \mathbf{S}_q\} = (w_1 \mathbf{S}(\mathbf{U}_1), \dots, w_Q \mathbf{S}(\mathbf{U}_Q))^T$ . The quadratic friction term introduces rational functions into the source terms. However quadrature sufficient to integrate a polynomial of order  $4n$  has been found to work satisfactorily.

## B.1.4 Forming the Line Integrals

Calculation of the terms  $\mathcal{S}$  and  $\mathcal{A}$  can be split into two steps: (1) evaluation of the numerical flux, and (2) quadrature of the line integral.

### B.1.4.1 Evaluation of the Numerical Flux

The numerical flux at a point along an element boundary  $\vec{\xi}_b$ , is dependent on the interpolated field variables within the element  $(\mathbf{U}_h(\vec{\xi}_b), \mathbf{Q}_h(\vec{\xi}_b)) = (\mathbf{U}_L, \mathbf{Q}_L)$ , and values external to the element  $(\mathbf{U}_R, \mathbf{Q}_R)$ , which may be obtained from an adjacent element or from a global boundary condition. (Here the subscripts  $L$  and  $R$  describe the left and right side of a positively oriented boundary.) Two approaches are used herein to evaluate the numerical fluxes.

**1. Lax-Friedrich Method** In the presence of viscosity ( $v_T \neq 0$ ) the numerical flux is computed with the Lax-Friedrich method (see, for example, LeVeque [2002]) such that

$$\begin{aligned} \hat{\mathbf{F}}(\mathbf{U}_h, \mathbf{Q}_h) n_x + \hat{\mathbf{G}}(\mathbf{U}_h, \mathbf{Q}_h) n_y &= \hat{\mathbf{H}}_I(\mathbf{U}_L, \mathbf{Q}_L, \mathbf{U}_R, \mathbf{Q}_R) \\ &= \frac{1}{2} \left( \mathbf{F}(\mathbf{U}_L, \mathbf{Q}_L) n_x + \mathbf{F}(\mathbf{U}_R, \mathbf{Q}_R) n_x + \mathbf{G}(\mathbf{U}_L, \mathbf{Q}_L) n_y + \right. \\ &\quad \left. \mathbf{G}(\mathbf{U}_R, \mathbf{Q}_R) n_y \right) - C(\mathbf{U}_L - \mathbf{U}_R) \end{aligned} \quad (\text{B.20})$$

where  $C$  is the maximum eigenvalue at the element edge, taken to be

$$C = \max \left( \sqrt{u_L^2 + v_L^2} + \sqrt{gh_L}, \sqrt{u_R^2 + v_R^2} + \sqrt{gh_R} \right). \quad (\text{B.21})$$

The viscous fluxes are calculated by taking a simple average (Schwanenberg and Harms [2004])

$$\begin{aligned} \widehat{\mathbf{R}}_x(\mathbf{U}_h)n_x + \widehat{\mathbf{R}}_y(\mathbf{U}_h)n_y &= \widehat{\mathbf{H}}_V(\mathbf{U}_L, \mathbf{U}_R) \\ &= \frac{1}{2} \left( \mathbf{R}_x(\mathbf{U}_L)n_x + \mathbf{R}_x(\mathbf{U}_R)n_x + \mathbf{R}_y(\mathbf{U}_L)n_y + \mathbf{R}_y(\mathbf{U}_R)n_y \right). \end{aligned} \quad (\text{B.22})$$

**2. HLLC Riemann Solver** In absence of viscosity ( $v_T = 0$ ) the numerical flux is computed by constructing a one dimensional Riemann problem at the interface of an element. The solution is approximated using the Harten, Lax and van Leer Contact (HLLC) method (Toro et al. [1994]). The advantages of pursuing this more involved numerical flux for inviscid problems are: (1) the HLLC method can be used when the depth of fluid on one side of the interface is zero, allowing for implementation of a wetting and drying scheme (Toro [2001]); and (2) the HLLC method is less dissipative than the Lax-Friedrich method allowing for better resolution of hydraulic jumps and tidal bores (LeVeque [2002], Toro [2001]), which occur in locations such as the Severn Estuary, for example (Pugh [1987]).

The Riemann problem at a point along the boundary of an element is formed by projecting the dependant variables onto a local coordinate system, with axis  $x'$  normal to the element boundary, using the transformation matrix

$$\mathbf{T} = \begin{bmatrix} 1 & 0 & 0 \\ 0 & n_x & n_y \\ 0 & -n_y & n_x \end{bmatrix} \quad \text{or} \quad \mathbf{T}^{-1} = \begin{bmatrix} 1 & 0 & 0 \\ 0 & n_x & -n_y \\ 0 & n_y & n_x \end{bmatrix}, \quad (\text{B.23})$$

so that  $\widehat{\mathbf{F}}(\mathbf{U})n_x + \widehat{\mathbf{G}}(\mathbf{U})n_y = \widehat{\mathbf{H}}_I(\mathbf{U}_L, \mathbf{U}_R) = \mathbf{T}^{-1}\widehat{\mathbf{E}}(\mathbf{T}\mathbf{U}) = \mathbf{T}^{-1}\widehat{\mathbf{E}}(\mathbf{Y})$ , where  $\widehat{\mathbf{E}}(\mathbf{Y})$  represents the one dimensional flux in the direction normal to the boundary and  $\mathbf{T}\mathbf{U} = \mathbf{Y} = [h \quad h\bar{u} \quad h\bar{v}]^T$  are the conserved variables in the rotated coordinate system - i.e. the normal velocity to the boundary is  $\bar{u}$  and the tangential velocity to the boundary is  $\bar{v}$  (see

Figure B.3). The one dimensional flux is then obtained from the approximate solution of the Riemann problem

$$\frac{\partial \mathbf{Y}}{\partial t} + \frac{\partial \mathbf{E}(\mathbf{Y})}{\partial x} = \mathbf{0}, \quad (\text{B.24})$$

with initial conditions  $\mathbf{Y}(x, 0) = \mathbf{Y}_L$ ,  $x < 0$ , and  $\mathbf{Y}(x, 0) = \mathbf{Y}_R$ ,  $x > 0$ , obtained from the nodal points on either side of the boundary where the flux is to be calculated. The approximate solution using the HLLC method assumes a linear wave structure in the vicinity of the element edge, as shown in Figure B.4, and estimates the wave speeds to be

$$S_L = \bar{u}_L - \sqrt{gh_L} s_L, \quad S_R = \bar{u}_R + \sqrt{gh_R} s_R \quad (\text{B.25})$$

$$S_* = \frac{S_L h_R (\bar{u}_R - S_R) - S_R h_L (\bar{u}_L - S_L)}{h_R (\bar{u}_R - S_R) - h_L (\bar{u}_L - S_L)} \quad (\text{B.26})$$

where the final speed  $S_*$  is formed by considering continuity over the wave region and the Rankine-Hugoniot condition (Toro et al. [1994]). A correction in the presence of shock waves is introduced via the variables  $s_L$  and  $s_R$ , which are defined as

$$s_{(L,R)} = \begin{cases} \sqrt{(h_*^2 + h_* h_{(L,R)})/2h_{(L,R)}^2} & \text{if } h_* > h_{(L,R)}, \\ 1 & \text{if } h_* \leq h_{(L,R)}. \end{cases} \quad (\text{B.27})$$

where the height  $h_* = \frac{1}{g} \left( \frac{1}{2} (\sqrt{gh_L} + \sqrt{gh_R}) + \frac{1}{4} (\bar{u}_L - \bar{u}_R) \right)^2$ . The flux over the computational timestep is then given as:

$$\hat{\mathbf{E}}(\mathbf{Y}) = \begin{cases} \mathbf{E}(\mathbf{Y}_L) & \text{if } S_L \geq 0, \\ \mathbf{E}(\mathbf{Y}_{*L}) & \text{if } S_L \leq 0 \leq S_*, \\ \mathbf{E}(\mathbf{Y}_{*R}) & \text{if } S_* < 0 \leq S_R, \\ \mathbf{E}(\mathbf{Y}_R) & \text{if } S_R \leq 0. \end{cases} \quad (\text{B.28})$$

where the  $*$  fluxes in the interior region are  $\mathbf{E}(\mathbf{Y}_{*L}) = (\mathbf{F}_*^{(1)}, \mathbf{F}_*^{(2)}, \bar{u}_L \mathbf{F}_*^{(1)})^T$  and  $\mathbf{E}(\mathbf{Y}_{*R}) = (\mathbf{F}_*^{(1)}, \mathbf{F}_*^{(2)}, \bar{u}_R \mathbf{F}_*^{(1)})^T$ , with  $\mathbf{F}_*^{(i)}$  the  $i$ th term of the vector

$$\mathbf{F}_* = \frac{S_R \mathbf{F}(\mathbf{Y}_L) - S_L \mathbf{F}(\mathbf{Y}_R) + S_L S_R (\mathbf{Y}_R - \mathbf{Y}_L)}{S_R - S_L}, \quad (\text{B.29})$$

with  $\mathbf{F}$  as defined in Section 4.3 for  $v_T = 0$ .

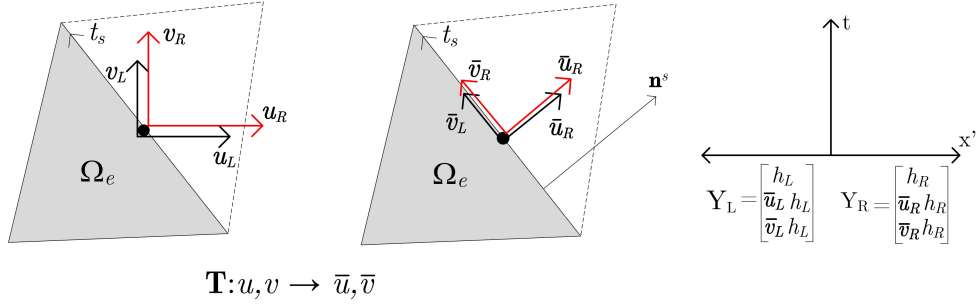


Figure B.3: Coordinate transformation at a given point along an element boundary to yield a local one dimensional Riemann problem. Variables with subscript  $L$  are internal to the element at the boundary. Variables with subscript  $R$  are obtained from an adjacent element or global boundary conditions.

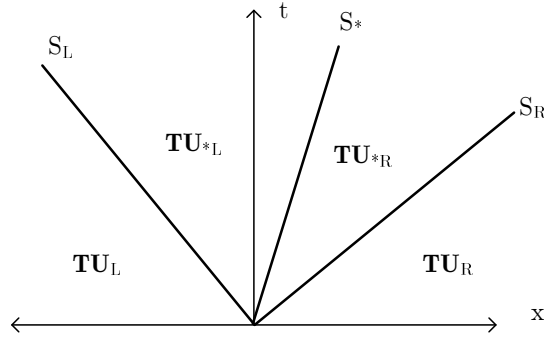


Figure B.4: The assumed wave structure of the HLLC Riemann solver.

#### B.1.4.2 Quadrature of the Line Integrals $\mathcal{S}, \mathcal{A}$

Following the solution of the numerical fluxes, the line integrals for triangular elements can be restated as

$$\mathcal{S}_{(i)} = \sum_s^3 \left( \int_{\Gamma_s} \ell_i \hat{\mathbf{H}}_I(\mathbf{U}_L, \mathbf{Q}_L, \mathbf{U}_R, \mathbf{Q}_R) d\Gamma_s \right) \text{ and } \mathcal{A}_{(i)} = \sum_s^3 \left( \int_{\Gamma_s} \ell_i \hat{\mathbf{H}}_V(\mathbf{U}_L, \mathbf{U}_R) d\Gamma_s \right), \quad (\text{B.30})$$

where the summation considers the line integral over all three edges of the triangle. Parameterising each edge with a positively orientated coordinate  $t_s(\xi_1, \xi_2)$ , such that

$$t_s := \begin{cases} \xi_1 = -1, \xi_2 = -t, & |t| \leq 1, \text{ along side 1,} \\ \xi_1 = t, \xi_2 = -1, & |t| \leq 1, \text{ along side 2,} \\ \xi_1 = -t, \xi_2 = t, & |t| \leq 1, \text{ along side 3,} \end{cases}$$

where the side numbers are referenced in Figure B.1, leads to the integral ( $\mathcal{A}_{(i)}$  is similar)

$$\mathcal{S}_{(i)} = \sum_s^3 \left( \int_{-1}^1 \ell_i \hat{\mathbf{H}}_I(\mathbf{U}_L, \mathbf{Q}_L, \mathbf{U}_R, \mathbf{Q}_R) \left| \frac{\partial \mathbf{x}}{\partial t_s} \right| dt_s \right), \quad (\text{B.31})$$

with the Jacobian resulting from the parametrization of the edges. Conveniently for a straight edge this Jacobian will be

$$\left| \frac{\partial \mathbf{x}}{\partial t_s} \right| = \sqrt{\left( \frac{\partial x}{\partial \xi_1} \frac{\partial \xi_1}{\partial t} + \frac{\partial x}{\partial \xi_2} \frac{\partial \xi_2}{\partial t} \right)^2 + \left( \frac{\partial y}{\partial \xi_1} \frac{\partial \xi_1}{\partial t} + \frac{\partial y}{\partial \xi_2} \frac{\partial \xi_2}{\partial t} \right)^2} = J_{\vec{x}, \vec{\xi}}^s = \frac{L_{x,y}^s}{2},$$

where  $L_{x,y}^s$  is the length of the triangular edge  $s$  in global coordinates.

Evaluating the integrals in Equation B.32 with quadrature leads to

$$\mathcal{S}_{(i)} = \sum_s^3 J_{\vec{x}, \vec{\xi}}^s \sum_{q_s}^{Q_s} \left( w_{q_s} \ell_i(\vec{\xi}_{q_s}) \hat{\mathbf{H}}_I \left( \mathbf{U}_L(\vec{\xi}_{q_s}), \mathbf{Q}_L(\vec{\xi}_{q_s}), \mathbf{U}_R(\vec{\xi}_{q_s}), \mathbf{Q}_R(\vec{\xi}_{q_s}) \right) \right), \quad (\text{B.32})$$

where  $\{w_{q_s}\}$  are the quadrature weights and  $\{\vec{\xi}_{q_s}\} = \{(\xi_1(t_q), \xi_2(t_q))\}$  are Gauss quadrature points along the interval  $(-1, 1)$ . Lastly, introducing the implicit definition of the nodal basis functions (Equation B.5), both vectors can be computed with the matrix operations

$$\mathcal{S} = \sum_s^3 J_{\vec{x}, \vec{\xi}}^s (\mathcal{V}_{Q_s} \mathcal{V}^{-1})^T \{w_{q_s} \hat{\mathbf{H}}_{I,q_s}\}, \text{ and } \mathcal{A} = \sum_s^3 J_{\vec{x}, \vec{\xi}}^s (\mathcal{V}_{Q_s} \mathcal{V}^{-1})^T \{w_{q_s} \hat{\mathbf{H}}_{V,q_s}\}, \quad (\text{B.33})$$

with  $\hat{\mathbf{H}}_{I,q_s} = \hat{\mathbf{H}}_I \left( \mathbf{U}_L(\vec{\xi}_{q_s}), \mathbf{Q}_L(\vec{\xi}_{q_s}), \mathbf{U}_R(\vec{\xi}_{q_s}), \mathbf{Q}_R(\vec{\xi}_{q_s}) \right)$ , and  $\hat{\mathbf{H}}_{V,q_s} = \hat{\mathbf{H}}_V \left( \mathbf{U}_L(\vec{\xi}_{q_s}), \mathbf{U}_R(\vec{\xi}_{q_s}) \right)$ , where  $\{w_{q_s} \hat{\mathbf{H}}_{(I,V),q_s}\} = (w_1 \hat{\mathbf{H}}_{(I,V),1}, \dots, w_{Q_s} \hat{\mathbf{H}}_{(I,V),Q_s})^T$ , while  $\mathcal{V}_{Q_s}$  has elements  $(\mathcal{V}_{Q_s})_{(q_s,k)} = \phi_k(\vec{\xi}(t_{q_s}))$ .

### B.1.5 Boundary Conditions

The treatment of boundary conditions in the DG formulation is straightforward in principle and amounts to the specification of the depth and velocity components along the exterior of the numerical boundary,  $\mathbf{U}_b$ . These values are then used to construct the numerical flux for an element on the domain boundary, as explained in Section B.1.4 (for example  $\mathbf{U}_b = \mathbf{U}_R$ ). Several boundary conditions are implemented, including: (1) simple reflective boundaries; (2) constant flow rate boundaries; (3) radiation, or open, boundaries; and (4) a line sink of momentum to represent a fence of tidal devices. The last two of these conditions have been discussed in depth in Chapter 4. A reflective boundary condition is simulated

by specifying the boundary values (LeVeque [2002])

$$h_b = h_{in}, \quad \bar{u}_b = -\bar{u}_{in}, \quad \bar{v}_b = \begin{cases} \bar{v}_{in}, & \text{slip} \\ 0, & \text{no slip} \end{cases}, \quad (\text{B.34})$$

where the subscript  $b$  refers to the solution external to the boundary, the subscript  $in$  refers to the solution just within the computational domain (for example  $\mathbf{Y}_{in} = (h_{in}, \bar{u}_{in}h_{in}, \bar{v}_{in}h_{in})^T = \mathbf{TU}_L$ ) and,  $\bar{u}$  and  $\bar{v}$  denote the normal and tangential velocities to the boundary. As expected, Equation B.34 can be interpreted as the solution of a Riemann problem normal to the boundary shown in Figure 4.7. For example, setting  $\bar{u}_*(t) = 0$  will ensure zero mass flux at the wall, and the appropriate  $h_*$  can be calculated so as to conserve the Riemann invariant  $I^+$ , along the right going characteristic line. Using a zero order extrapolation to obtain the invariant gives

$$2\sqrt{gh_*} = I^+ = \bar{u}_{in} + 2\sqrt{gh_{in}}. \quad (\text{B.35})$$

Conservation of the Riemann invariant along the left going characteristic line ( $I^- = \bar{u}_* - 2\sqrt{gh_*} = \bar{u}_b - 2\sqrt{gh_b}$ ) is therefore automatically satisfied if  $\bar{u}_b = -\bar{u}_{in}$  and  $h_b = h_{in}$  in agreement with Equation B.34. A constant flow rate boundary condition is introduced by considering the same one dimensional problem outlined in Figure 4.7. For a predefined flow rate  $Q$ , the boundary values are obtained by solving the system of equations

$$\bar{u}_*h_* = Q \quad \text{and} \quad \bar{u}_{in} + 2\sqrt{gh_{in}} = \bar{u}_* + 2\sqrt{gh_*}, \quad (\text{B.36})$$

which amounts to the solution of the cubic

$$2c_*^3 - \left(\bar{u}_{in} + 2\sqrt{gh_{in}}\right) c_*^2 + gQ = 0, \quad \text{where} \quad c_* = \sqrt{gh_*}. \quad (\text{B.37})$$

Setting  $\bar{u}_b = \bar{u}_*$  and  $h_b = h_*$  automatically satisfies the left going characteristic. The tangential component  $\bar{v}_b$  is specified directly.

## B.1.6 Isoparametric Elements

When simulating shallow coastal flows it is often necessary to use mesh that can conform to a smooth coastline. This is because, although real coastal geometry will not be perfectly

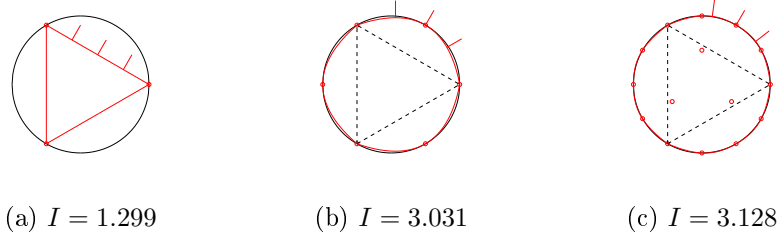


Figure B.5: Example of high order mapping for a triangular element (shown in red). (a)  $n = 1$ , (b)  $n = 2$ , (c)  $n = 4$ . Location of global coordinates given by red circles. The three small lines indicate the normal direction to the element boundary. The area of the element  $I = \int \int_{\mathcal{T}} J_{\vec{x}, \vec{\xi}} d\xi_1 d\xi_2$  is given below each sub-figure.

smooth, it is important to use a mesh that will not trigger artificial separation at mesh dependent locations. Bernard et al. [2009] present a good example of this artificial separation when analysing shallow non-steady wakes behind Rattray Island, Australia. For this reason high-order curved triangular elements have also been used in addition to the straight edged linear triangles discussed in Section B.1.1. The geometry of the high order elements is described by

$$x(\xi_1, \xi_2) = \sum_k^R N_k(\xi_1, \xi_2)x_k, \quad \text{and} \quad y(\xi_1, \xi_2) = \sum_k^R N_k(\xi_1, \xi_2)y_k, \quad (\text{B.38})$$

where  $\{N_k\}$  is a set of nodal shape functions and  $\{x_k\}$  and  $\{y_k\}$  are the global coordinates of the nodal points in the natural triangle. In practice there are several choices available for the shape functions  $\{N_k\}$ . Here the order of the shape functions is kept the same as the order of the numerical approximation  $n$  (i.e. elements are isoparametric). Furthermore, following Hesthaven and Warburton [2008], the nodal basis functions defined in Section 4.5.2.2 are used for the shape functions (i.e  $l_k = N_k$  and  $R = M$ ). Although this choice of shape function is convenient computationally, serendipity shape functions, or other alternatives, may be more useful in some circumstances (Bernard et al. [2009]). Figure B.5 illustrates the accuracy achieved by using higher order shape functions to represent a unit circle with a single element. The computation of the area of the element approaches  $\pi$  rapidly.

Introducing curved elements defined by Equation B.38, the formation of the spatial operators described above require modification to account for the variation the spatial Jacobian, line Jacobian and outward pointing normal around the element boundary, with  $\xi_1$  and  $\xi_2$ . To illustrate how this is achieved the formulation of the mass matrix  $\mathcal{M}$  and the

two vectors  $\mathcal{B}$  and  $\mathcal{S}$  will be outlined briefly (the remaining terms follow similarly). The discussion follows that of Hesthaven and Warburton [2008].

To begin, the mass matrix is now given generally by

$$\mathcal{M}_{(i,k)} = \int_{\mathcal{T}} \int_{\mathcal{T}} l_i l_k J_{\vec{x},\vec{\xi}} d\xi_1 d\xi_2, \quad (\text{B.39})$$

where

$$J_{\vec{x},\vec{\xi}} = \frac{\partial x}{\partial \xi_1} \frac{\partial y}{\partial \xi_2} - \frac{\partial x}{\partial \xi_2} \frac{\partial y}{\partial \xi_1}. \quad (\text{B.40})$$

Solving Equation B.39 using cubature now leads to  $\mathcal{M} = (\mathcal{V}_Q)^T \mathcal{W} \mathcal{V}_Q$ , where  $\mathcal{V}_{Q,(q,k)} = \phi_k(\vec{\xi}_q)$ ,  $\mathcal{W} = \text{diag}(w_1 J_{\vec{x},\vec{\xi}}(\vec{\xi}_1), \dots, w_Q J_{\vec{x},\vec{\xi}}(\vec{\xi}_Q))$ ,  $\{w_q\}$  are the cubature weights and  $\{J_{\vec{x},\vec{\xi}}(\vec{\xi}_q)\}$  represents the Jacobian calculated at the quadrature points  $\{\vec{\xi}_q\}$ . The Jacobian can be calculated at each of the quadrature points via

$$\{J_{\vec{x},\vec{\xi}}(\vec{\xi}_q)\} = \mathcal{D}_{\xi_1} \{x_k\} \cdot \mathcal{D}_{\xi_2} \{y_k\} - \mathcal{D}_{\xi_2} \{x_k\} \cdot \mathcal{D}_{\xi_1} \{y_k\}, \quad (\text{B.41})$$

where  $\mathcal{D}_{\xi_{1,2}(q,k)} = \left. \frac{\partial l_k}{\partial \xi_{1,2}} \right|_{\vec{\xi}_q}$ . Likewise, the operator  $\mathcal{B}$  now becomes

$$\mathcal{B}^x = \mathcal{D}_{\xi_1}^T \{w_q \mathbf{F}_q J_{\vec{x},\vec{\xi}}(\vec{\xi}_q) \left. \frac{\partial \xi_1}{\partial x} \right|_{\vec{\xi}_q}\} + \mathcal{D}_{\xi_2}^T \{w_q \mathbf{F}_q J_{\vec{x},\vec{\xi}}(\vec{\xi}_q) \left. \frac{\partial \xi_2}{\partial x} \right|_{\vec{\xi}_q}\}, \quad (\text{B.42})$$

where  $J_{\vec{x},\vec{\xi}}(\vec{\xi}_q)$  is calculated as above and the partial derivatives can be taken from the vectors  $\mathcal{D}_{\xi_1} \{x_k\}$  and  $\mathcal{D}_{\xi_2} \{x_k\}$ , respectively. Lastly, the line integral  $\mathcal{S}$  requires two modifications. First the numerical flux is evaluated using either approach in B.1.4, but with the normal directions computed at the quadrature points along the element edge. Secondly the line Jacobian at the quadrature points must be evaluated at each point according to

$$J_{\vec{x},\vec{\xi}}^s(\vec{\xi}_{q_s}) = \left| \frac{\partial \mathbf{x}(\vec{\xi}_{q_s})}{\partial t_s} \right| = \sqrt{\left( \left. \frac{\partial x}{\partial \xi_1} \right|_{\vec{\xi}_{q_s}} \frac{\partial \xi_1}{\partial t} + \left. \frac{\partial x}{\partial \xi_2} \right|_{\vec{\xi}_{q_s}} \frac{\partial \xi_2}{\partial t} \right)^2 + \left( \left. \frac{\partial y}{\partial \xi_1} \right|_{\vec{\xi}_{q_s}} \frac{\partial \xi_1}{\partial t} + \left. \frac{\partial y}{\partial \xi_2} \right|_{\vec{\xi}_{q_s}} \frac{\partial \xi_2}{\partial t} \right)^2},$$

which can be given in terms of the normal directions as  $J_{\vec{x},\vec{\xi}}^s(\vec{\xi}_{q_s}) = \sqrt{(n_x(\boldsymbol{\xi}_{q_s}))^2 + (n_y(\boldsymbol{\xi}_{q_s}))^2}$ .

## B.2 Validation Tests

A series of benchmark tests have been undertaken to validate the DG numerical solver. In many cases the error is investigated by computing the  $L_1$  and  $L_2$  norms, defined as

$$L_1 = \int_{\Omega} |g(x, y)| d\Omega \quad L_2 = \sqrt{\int_{\Omega} (g(x, y))^2 d\Omega}, \quad (\text{B.43})$$

where  $g(x, y)$  is the variable to be measured or the error between the computed solution and a reference solution.

Firstly, two linear problems are considered, with the flux terms in the numerical solution replaced with the linearised versions given in Section 4.3, Chapter 4. The aim of the initial linear tests were to verify the coding of the quadrature and connectivity routines, etc. by comparison to exact solutions. In the subsequent test problems (i.e. non-linear, viscous and non-trivial boundary conditions) non-linear terms in the flux and source terms are computed.

### B.2.1 Linear Problems

#### B.2.1.1 L1 Seiching in a Rectangular Basin

This first problem considers seiching in a constant depth domain  $(x, y) \in [0, L] \times [0, L]$ . The analytical solution for the amplitude of the free surface is available in many texts (see, for example Mei [1989])

$$\xi(x, y) = \sum_{n,m}^{\infty} A_{n,m} \cos\left(\frac{n\pi x}{L}\right) \cos\left(\frac{m\pi y}{L}\right) \cos(\omega_{n,m} t), \quad (\text{B.44})$$

where  $A_{n,m}$  represent the various modal amplitudes determined from the initial conditions and distinguished by the integers  $n$  and  $m$ . The associated modal angular frequencies are  $\omega_{n,m} = \pi\sqrt{(n/L)^2 + (m/L)^2}$ . Convergence of the numerical solution towards the analytical solution is investigated for four uniform meshes having a different element size, indicated by  $h_m$ . The coarsest mesh coincides with  $h_m = L/2$  (see Figure B.6). Both the first mode ( $n = 1, m = 0$ ) and the third mode ( $n = 1, m = 1$ ) of seiching in the basin are simulated. In both cases, the water depth is 10 m, the maximum free surface amplitude is 0.01 m and the basin length is  $L=1000$  m. The initial conditions are obtained from the analytical

$n$		$h$	Order	$h/2$	Order	$h/4$	Order	$h/8$	Order
First Mode ( $n = 1, m = 0$ )									
1	$L_2$	2.903E+01	-	6.640E+00	2.13	1.368E+00	2.28	2.966E-01	2.21
	CPU	1.00		2.24		7.15		32.2	
2	$L_2$	1.190E+00	-	9.689E-02	3.62	1.086E-02	3.16	1.331E-03	3.03
	CPU	2.27		5.53		18.5		96.6	
5	$L_2$	3.917E-04	-	6.411E-06	5.93	1.020E-07	5.97	1.621E-09	5.98
	CPU	10.2		31.2		132		852	
8	$L_2$	4.407E-08	-	1.065E-10	8.69	1.702E-10	-0.68		
	CPU	25.9		94.4		464			
Third Mode ( $n = 1, m = 1$ )									
1	$L_2$	4.211E+01	-	1.060E+01	1.99	2.221E+00	2.25	4.618E-01	2.27
	CPU	1.00		2.27		7.35		31.7	
2	$L_2$	2.167E+00	-	3.054E-01	2.83	2.951E-02	3.37	3.521E-03	3.07
	CPU	2.28		5.61		19.5		97.1	
5	$L_2$	7.949E-03	-	8.794E-05	6.41	1.374E-06	6.00	2.186E-08	5.97
	CPU	10.0		32.8		12.3		891	
8	$L_2$	8.127E-07	-	8.585E-09	6.56	4.158E-10	4.37		
	CPU	25.9		98.3		492			

Table B.1: A selection of convergence results for the L1 test case of seiching in a rectangular basin. The CPU time is normalised by the the time required to compute the lowest polynomial order at the largest mesh size.

solution, and the numerical solution is compared against the analytical solution after four periods of oscillation, where the period is  $T = \omega_{n,m}/2\pi$ . Table B.1 and Figure B.7 show the convergence test results and the normalized computational time<sup>1</sup> required to perform the calculations. The convergence achieved is order  $n + 1$  for both mode shapes in almost all test cases. The one exception is the case  $n = 8$  for the finer mesh. Since refinement of the time step (one tenth of that in Equation 4.28) provided no change to the results for this high order case it was concluded that computational precision had been reached. Lastly it is interesting to note that less computational time is required to achieve high order accuracy if a polynomial refinement is used as opposed to mesh size refinement.

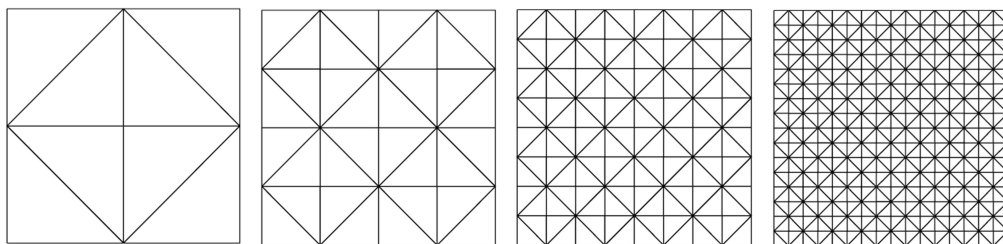


Figure B.6: Computational mesh used in the convergence study for L1. The element size reduces by one half between successive mesh.

<sup>1</sup>Computations were performed on a standard 2.0 GHz Intel Core 2 Duo processor.

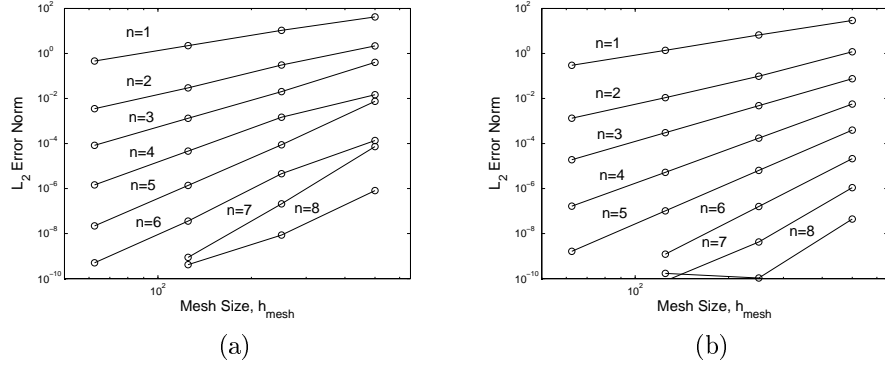


Figure B.7: Error convergence plots for seiching in a rectangular basin: (a)  $n = 1, m = 0$ , (b)  $n = m = 1$ .

### B.2.1.2 L3 Linear Kelvin Wave

This test validates the Coriolis source term in the linearized numerical model. The test problem, referenced by Eskilsson and Sherwin [2004], Giraldo and Warburton [2008], considers the westward propagation of an initial mound due to Coriolis forcing. The problem works on a dimensionless form of the SWEs, by introducing the following non-dimensional variables

$$\mathbf{x} = \frac{r}{E^{1/4}} \mathbf{x}', \quad t = \frac{E^{1/4}}{2\Omega} t', \quad \xi = h_o \xi' \quad \mathbf{u} = \sqrt{gh_o} \mathbf{u}', \quad f = \frac{2\Omega}{E^{1/4}} y' \quad (\text{B.45})$$

where  $E = 4\Omega^2 r^2 (gh_o)^{-1}$  is the Lamb parameter,  $r$  is the radius of the Earth ( $6.38 \times 10^6$  m),  $\Omega = 2\pi \text{ day}^{-1}$  is the angular frequency of the Earth's rotation and  $h_o$  is the standard mean depth (Note, the non-dimensional velocity is defined incorrectly by Giraldo and Warburton [2008]). Ignoring bed friction, the linearized SWEs now become

$$\frac{\partial \xi'}{\partial t'} + \nabla \cdot \mathbf{u}' = 0, \quad \text{and} \quad \frac{\partial \mathbf{u}'}{\partial t'} + \nabla \mathbf{x}' = (-\mathbf{k} \times \mathbf{u}') y'. \quad (\text{B.46})$$

For initial conditions  $\xi'(\mathbf{x}', 0) = \exp(-y'^2/2) \exp(-(x' + 5)^2/2)$ ,  $u'(\mathbf{x}', 0) = \xi'$  and  $v'(\mathbf{x}', 0) = 0$ , Boyd [1980] gives the analytical solution:

$$\xi'(\mathbf{x}', t') = \exp\left(\frac{-y'^2}{2}\right) \exp\left(\frac{-(x' + 5 - t')^2}{2}\right), \quad u'(\mathbf{x}', t') = \xi', \quad v'(\mathbf{x}', t') = 0. \quad (\text{B.47})$$

A spatial domain  $(x', y') \in [-10, 10] \times [-5, 5]$  was used ( $h_o$  was set to 1.0 m, with Coriolis force specified as  $f = (2\Omega/r)y$  and  $(x, y) \in (E^{1/4}/r)[-10, 10] \times [-5, 5]$ ). Convergence

$n$		$h$	Order	$h/2$	Order	$h/4$	Order	$h/8$	Order
1	$L_2$	1.164E+00	-	5.314E-01	1.13	1.352E-01	1.97	3.001E-02	2.17
	CPU	1.00		4.04		24.2		191	
2	$L_2$	5.756E-01	-	6.401E-02	3.17	4.306E-03	3.89	4.386E-04	3.30
	CPU	3.24		11.0		66.8		546	
3	$L_2$	1.087E-01	-	6.138E-03	4.14	3.396E-04	4.18	2.116E-05	4.00
	CPU	7.81		25.0		148		1270	
4	$L_2$	2.293E-02	-	8.559E-04	4.74	2.544E-05	5.07	8.059E-07	4.98
	CPU	9.77		52.3		303		2750	
8	$L_2$	7.638E-05	-	2.798E-07	8.09	1.045E-08	4.74		
	CPU	51.6		361		3350			

Table B.2: Convergence for the linear equatorial (L3) Kelvin wave test case. The CPU time is normalised by the the time required to compute the lowest polynomial order at the largest mesh size.

was analysed for four meshes at a non-dimensional time  $t' = 5$  (the meshes were similar to those in Figure B.6, with the largest having  $h_{mesh} = 2.5$  non dimensional units, and the remainder reducing in element size by one half). Boundary conditions were set to simple reflective boundaries. Satisfactory spatial convergence is recorded in Table B.2 together with computational time. Again an increased accuracy is achieved, for a given computational time, when polynomial refinement is used instead of mesh size refinement.

## B.2.2 Non-Linear Problems

### B.2.2.1 NL1 Convergence to Linearized Analytical Solutions

The first test problem undertaken with the non-linear terms (but with  $v_T = 0$ ) was used to test the consistency of the code in the linear limit  $\xi/h_o \rightarrow 0$ . A test setup identical to that considered in the L1 linear test was used. Table B.3 presents the convergence of the non-linear solution to the linear solution for the seiching mode  $n = 1, m = 0$ . Notably the requirement on linearity becomes more stringent as  $n$  increases. The agreement is satisfactory for sufficiently small  $\xi/h_o$  in each case.

### B.2.2.2 NL2 Comparison against the Method of Characteristics

The previous test case proved the consistency of the non-linear model under linearized conditions, however it did not validate the ability of the model to simulate non-linear flow. This test considers the convergence of a non-linear numerical solution to an alternative numerical solution obtained using the Method of Characteristics (MoC). The MoC theory

$n$	$\xi/h_o$		$h$	$h/2$	Order	$h/4$	Order	$h/8$	Order
1	1E+00	$L_2$	3.331E+02	1.178E+02	1.50	1.474E+02	-0.32	1.708E+02	-0.21
	1E-01	$L_2$	3.290E+01	5.886E+00	2.48	1.305E+00	2.17	4.182E-01	1.64
	1E-02	$L_2$	3.289E+00	5.815E-01	2.33	1.215E-01	2.26	2.783E-02	2.13
2	1E-01	$L_2$	1.455E+00	2.900E-01	2.33	2.476E-01	0.23	2.472E-01	0.00
	1E-02	$L_2$	1.388E-01	1.347E-02	3.36	1.443E-03	3.22	2.981E-04	2.28
	1E-03	$L_2$	1.387E-02	1.342E-03	3.37	1.403E-04	3.26	1.574E-05	3.16
5	1E-04	$L_2$	4.520E-07	7.110E-09	5.99	4.947E-10	3.85		
	1E-05	$L_2$	4.519E-08	7.362E-10	5.94	4.108E-10	0.84		
	1E-06	$L_2$	4.523E-09	2.399E-10	4.24	4.066E-10	-0.76		

Table B.3: Convergence of the non-linear numerical solution to a linearized analytical solution under the limit  $\xi/h_o \rightarrow 0$ .

and numerical approach is explained in more detail by Abbott [1979] and Draper [2008].

The reference MoC solution is formed in the one dimensional domain  $x \in [0, L]$ ,  $L = 100$  m, for the splitting of a Gaussian mound defined by

$$h(x) = h_o + \xi e^{-0.01(x-L/2)^2}. \quad (\text{B.48})$$

where  $h_o = 10$  m and three separate amplitudes  $\xi = 1, 5$  and  $10$  m are considered each having a different height to depth ratio  $\xi/h_o$  describing the degree of non-linearity. Figures B.8(a)-(c) present the characteristic hodograph for the three values of  $\xi/h_o$  and  $t \in (0, 6)$  s. Typically between 5000 and 10000 characteristic lines have been used to generate the reference solutions, with every 100 lines shown in Figure B.8. The DG numerical solution is calculated in a basin  $(x, y) \in [0, 100] \text{ m} \times [0, 50] \text{ m}$ , with an initial surface profile constant in the  $y$  coordinate and equivalent to Equation B.48 in the  $x$  coordinate. The numerical mesh is uniform with  $h_m = 10$  m, which amounts to 100 triangular elements.

Figure B.8 shows that the most non-linear case ( $\xi/h_o = 1.0$ ) develops a discontinuity at around  $t = 3$  s. The comparison between the DG solution and the MoC is therefore conducted at  $t = 2$  s. Figure B.9 illustrates the effect of the non-linearity on the numerical solution at this time. Figure B.10 displays the exponential convergence of the DG method to the MoC for the three non-linear cases. Agreement is satisfactory.

The same methodology adopted above in the frictionless case was also used to test the non-linear solver for problems involving quadratic bottom friction. The effect of the additional bottom friction when  $c_d = 4$ , compared to the frictionless non-linear simulation (for  $\xi/h_o = 0.1$ ), is seen clearly in Figure B.9(d). Figure B.10(d) presents the convergence

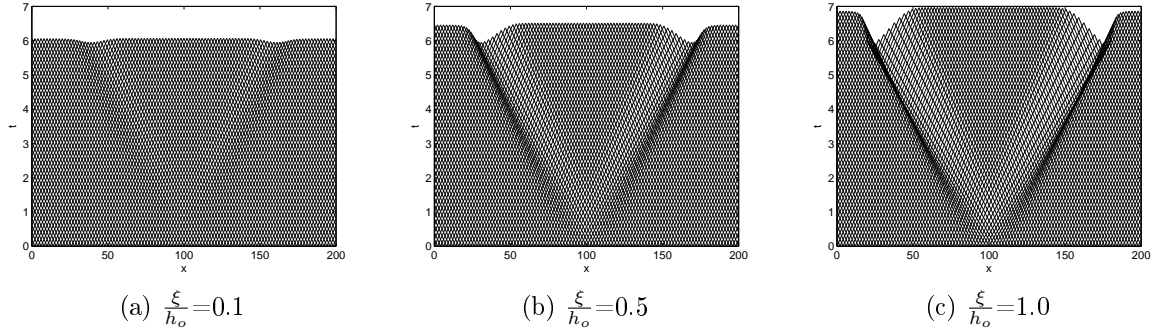


Figure B.8: Characteristic hodographs for three (NL2) non-linear benchmark test cases. The cases involve the splitting of an initial Gaussian mound of amplitude  $\xi$ , in a still water channel of depth  $h_o$ . (a)  $\xi/h_o = 0.1$ , (b)  $\xi/h_o = 0.5$ , (c)  $\xi/h_o = 1.0$

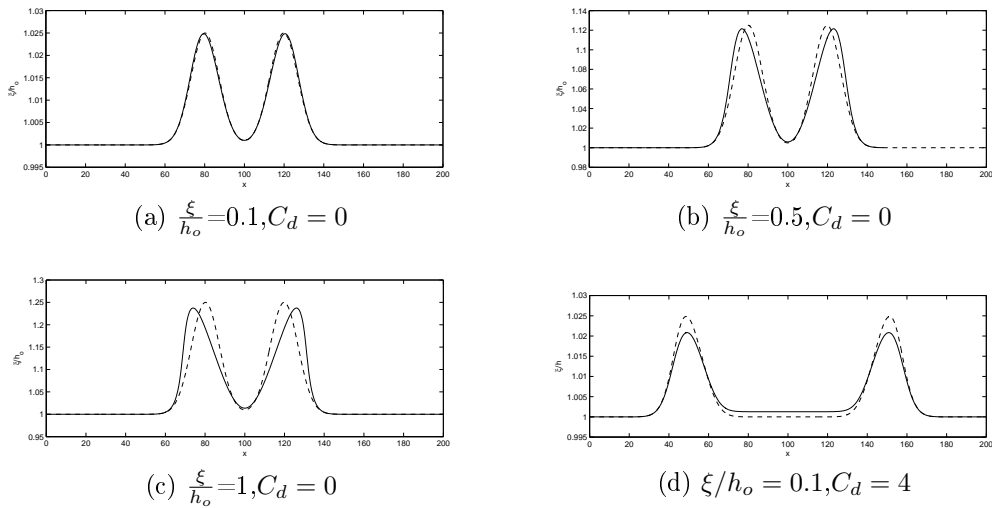


Figure B.9: Comparison between linear and non-linear solutions for the splitting of an initial Gaussian mound of amplitude  $\xi$ , in a still water channel of depth  $h_o$ . (a)  $\xi/h_o = 0.1$ , (b)  $\xi/h_o = 0.5$ , (c)  $\xi/h_o = 1.0$ , (d) same as (a) but with quadratic friction factor  $C_d = 4$ . Solid lines represent the non-linear solution, dashed lines represent the linear solution.

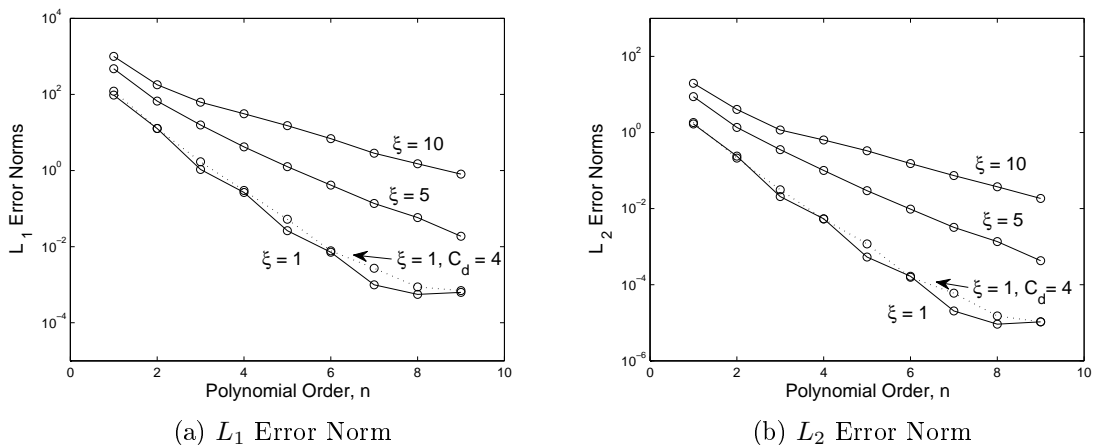


Figure B.10: Error norms between the DG method and the MoC for the non-linear test cases shown in Figure B.9. A numerical mesh of 100 elements is used.

of the DG solution to the MoC for this particular case. The agreement is again satisfactory.

### B.2.2.3 NL3 Steady Uniform Flow in a Channel

This test examines the bed slope term introduced in the SWEs to account for variable bathymetry. The test is very simple and considers a sloping channel with dimensions  $(x, y) \in [0, 1000] \times [0, 500]$  m. The initial water depth  $h$  is set to 10 m and the surface slope is  $S_o = 1/1000$ . The upstream and downstream depths are set to 10 m using a clamped boundary condition and a quadratic bed friction of  $C_d = 0.005$  is adopted. Equating forces along the slope of the channel gives the analytical expression for the depth-averaged velocity (see, for example, Young et al. [2001])  $u = \sqrt{ghS_o/C_d} = 4.429446918070$  m/s. Using a uniform triangular mesh with  $h_m = 50$  m, gives  $u = 4.429446918070$  m/s, correct to 13 significant figures.

### B.2.2.4 NL4 Non-Linear Rossby Wave

Lastly, a westward propagating solitary Rossby wave is simulated to test the accuracy of the non-linear terms in the presence of Coriolis forcing. This test case has been considered by Eskilsson and Sherwin [2004] and Giraldo and Warburton [2008] among others, for qualitative validation. An approximate analytical solution for a westward traveling Rossby wave is given by Boyd [1984]:

$$\xi'(\mathbf{x}', t') = A(\eta, x) \left( \frac{9c^1(-5 + 2y'^2)}{16} + \frac{3 + 6y'^2}{4} + A(\eta, x)\bar{\xi}^{(1)} \right) \exp\left(-\frac{y'^2}{2}\right), \quad (\text{B.49})$$

$$u'(\mathbf{x}', t') = A(\eta, x) \left( \frac{9c^1(3 + 2y'^2)}{16} + \frac{-9 + 6y'^2}{4} + A(\eta, x)\bar{u}^{(1)} \right) \exp\left(-\frac{y'^2}{2}\right), \quad (\text{B.50})$$

$$v'(\mathbf{x}', t') = \frac{\partial}{\partial x} (A(\eta, x)) \left( 2y' \exp\left(-\frac{y'^2}{2}\right) + A(\eta, x)\bar{v}^{(1)} \right), \quad (\text{B.51})$$

where primes indicate non-dimensional variables defined relative to Equation B.45, the terms  $\bar{\xi}^{(1)}$ ,  $\bar{u}^{(1)}$  and  $\bar{v}^{(1)}$  are infinite Hermite series with coefficients given in Boyd [1984], and

$$A(\eta, t) = 0.771a^2 \text{sech}^2(a\eta), \quad \text{where } \eta = x' - ct', \quad (\text{B.52})$$

in which  $c = -1/3 - c^1 = -1/3 - 0.395a^2$ . Figure B.11(b) presents a plot of the numerical solution obtained using the present DG method, taking  $a = 0.394$ , together with the

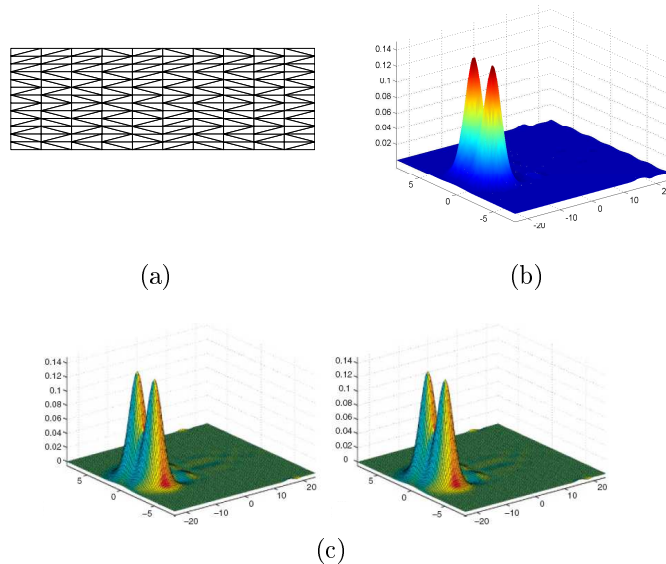


Figure B.11: (a) Numerical mesh and (b) simulated non-Linear Rossby wave at  $t = 40$ s. (c) Numerical solution obtained by Giraldo and Warburton [2008] using the DG method (left) and a spectral element method (right).

solution of Giraldo and Warburton [2008] obtained using a DG method and a continuous Spectral FE method. The numerical mesh used consisted of 260 elements, each with  $n = 8$  (see Figure B.11(a)) and was similar to that employed by Giraldo and Warburton [2008]. The domain spanned  $(x', y') \in [-24, 24] \times [-8, 8]$ , and reflecting boundary conditions were applied along the boundaries. Equations B.49-B.51 were used for initial conditions. Figure B.11 shows that the agreement between the numerical solutions at  $t' = 40$  is very good. Furthermore, the computed phase velocity was approximately  $-0.77$  m/s, in agreement with  $-0.77$  m/s simulated by Eskilsson and Sherwin [2004] and the approximate analytical solution of  $-0.78$  m/s given by Boyd [1984].

## B.2.3 Viscous Problems

### B.2.3.1 V1 Sidewall Expansion

The problem of laminar flow past a sidewall expansion provides a useful test of the viscous and non-linear advection terms. In particular, as the flow passes the expansion, shown in Figure B.12(a), separation occurs followed by downstream reattachment. For laminar flow the reattachment length has been shown experimentally to vary with the inlet Reynolds number (Denham and Patrick, O'Leary and Mueller [1969])  $Re_I = U_B b / \nu$ , where  $U_B$  defines the mean stream-wise flow velocity at the upstream inlet,  $b$  is width of the sidewall

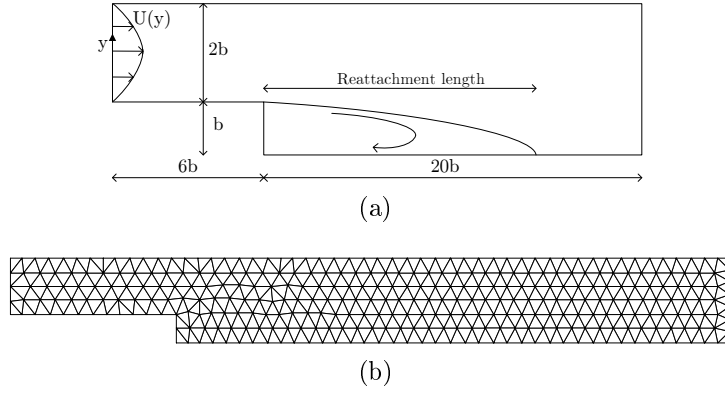


Figure B.12: (a) Sidewall expansion problem geometry and schematic flow. (b) Computational mesh.

expansion and  $\nu$  is kinematic eddy viscosity, taken here to be the turbulent depth-averaged eddy viscosity  $\nu_T$ . Various numerical and experimental studies of this problem have been considered in the literature. Denham and Patrick conducted experiments in an enclosed flume and O’Leary and Mueller [1969] measured reattachment lengths for a range of inlet Reynolds numbers using a towing tank facility. Numerical simulations have been presented by Anastasiou and Chan [1997] for the viscous SWEs. Provided that the variation in surface elevation is negligible, the numerical simulations based on the SWEs should be essentially identical to the results obtained by O’Leary and Mueller [1969] and Denham and Patrick. Here the simulated reattachment length is used to assess the ability of the numerical code to approximate the physical flow.

The verification test adopts the geometry in Figure B.12, with  $b$  set to 1.0 m. At the inlet a parabolic velocity profile of the form:

$$U(y) = \frac{3}{2}U_B \left(1 - \left(\frac{y}{b} - 1\right)^2\right), \quad (\text{B.53})$$

is specified. This parabolic profile, which is a sensible approximation for the open channel flow (when the change in depth across the channel section is small), was chosen to reduce the simulation time to achieve a steady solution. For all tests  $U_B$  was set to 0.5 m/s and the downstream depth to 1.0 m. The computational mesh consisted of 553 unstructured elements (Figure B.12(b)), with average edge length of 0.5 m. Polynomial approximations up to order  $n = 4$  were adopted to simulate flows having inlet Reynolds numbers of 7.9, 50, 73, 98, 150 and 229.

A plot of the streamlines  $\Psi$ , defined by the relations  $u = (1/h)\partial\Psi/\partial y$  and  $v =$

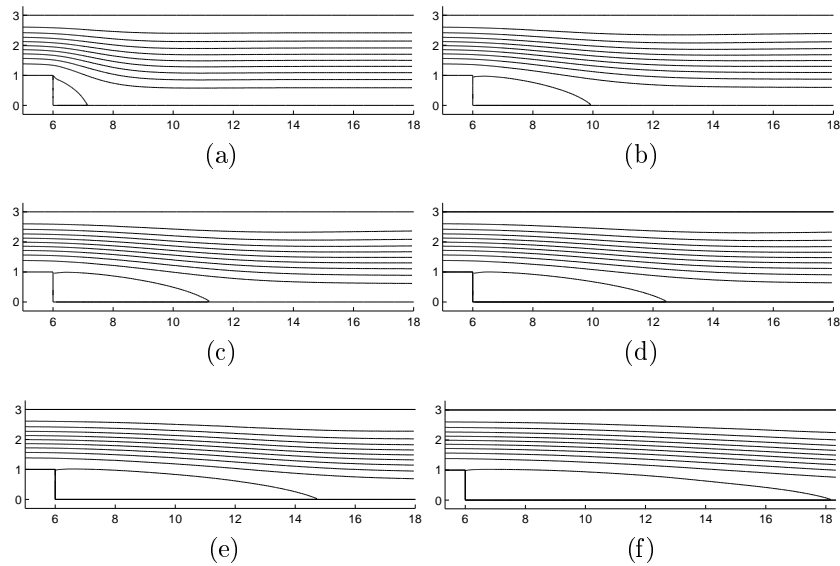


Figure B.13: Streamline plots at steady state for the sidewall expansion problem. (a)  $Re_I = 7.9$ , (b)  $Re_I = 50$ , (c)  $Re_I = 73$ , (d)  $Re_I = 98$ , (e)  $Re_I = 150$ , (f)  $Re_I = 229$ .

$(-1/h)\partial\Psi/\partial x$ , is presented for each of Reynolds number in Figure B.13. The reattachment length clearly increases with the inlet Reynolds number. Figure B.14 plots the simulated reattachment length against Reynolds number and compares the results with the experimental data of Denham and Patrick and O'Leary and Mueller [1969]. At lower Reynolds number ( $Re < 150$ ) the agreement is satisfactory. For higher Reynolds number the numerical reattachment length increases above experimental data as the polynomial order of approximation  $n$  increases. Therefore, to further compare the simulated and experimental results Figure B.15 superimposes the simulated along channel velocity profiles, obtained when  $n = 3$ , with the profiles presented by Denham and Patrick at an inlet Reynolds number of 73 and 229. Agreement at the lower of these two Reynolds numbers is very good throughout. Discrepancy at the higher Reynolds number is visible, however it is also clear that the inlet profile for the experiment is not fully developed, which Denham and Patrick report may be a result of *skewness* introduced by the asymmetry of their upstream inlet.

### B.2.3.2 V2 Jet-Forced Flow in a Circular Reservoir

A second well known validation test for the viscous SWEs concerns the simulation of laminar jet forced flow in a flat bottomed circular reservoir. The geometry of this problem is given in Figure B.16(a). Previous numerical simulations of the SWEs have been conducted by Anastasiou and Chan [1997] among others. The validation test employs the mesh depicted in Figure B.16(b). The inlet width of the stem is  $b = 0.156$  m, the inlet and outlet

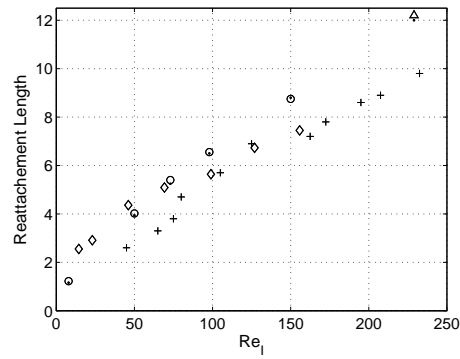
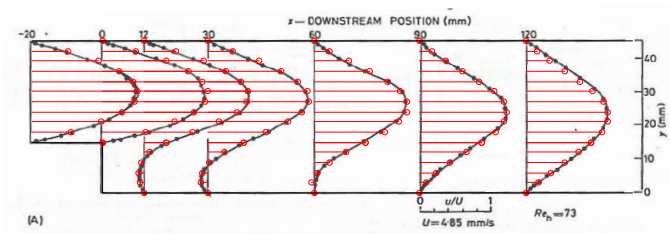
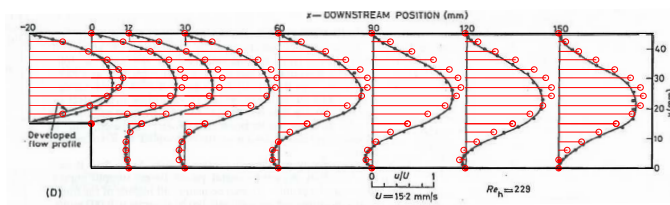


Figure B.14: Reattachment length as a function of inlet Reynolds number  $Re_I$ . Simulation results  $n = 2$  (o),  $n = 3$  (.),  $n = 4$  ( $\Delta$ ); Experimental results due to Denham and Patrick (+); Experimental results due to O'Leary and Mueller [1969] ( $\diamond$ ).



(a)



(b)

Figure B.15: Comparison of simulated horizontal flow profiles with those recorded experimentally by Denham and Patrick. (a)  $Re_I = 73$ . (b)  $Re_I = 229$ .

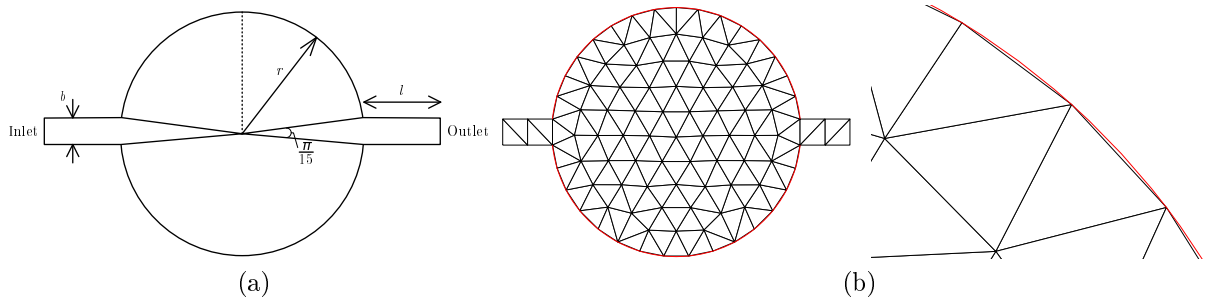


Figure B.16: (a) Jet flow geometry. (b) Computational mesh (the red line indicates the curved boundary of the isoparametric elements formed for  $n = 4$ ).

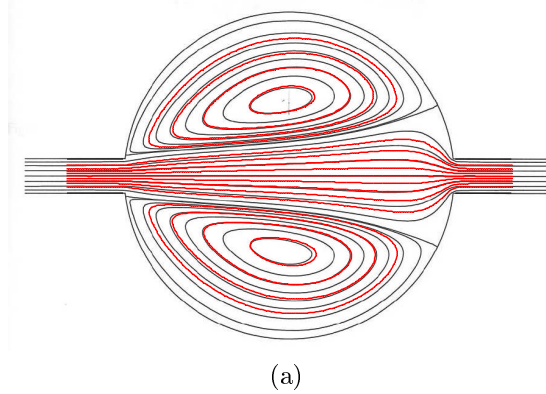


Figure B.17: Jet forced flow at  $Re_I = 10$ . Overlay of streamlines for  $n = 5$  and the most refined numerical result computed by Rogers [2001].

lengths are  $l = 0.5$  m and the radius of the reservoir is  $r = 0.75$  m. The computational elements bordering the perimeter of the reservoir are isoparametric to conform to the circular boundary (red line in Figure B.16(b)). The mean inlet velocity was  $U_b = 0.1$  m/s and a parabolic profile was assumed (see Equation B.53). The initial water depth was 0.1 m and fixed at the outlet boundary. All remaining boundaries were no slip and bed friction and Coriolis forces were ignored. The depth-averaged eddy viscosity was set to  $\nu_T = 0.000784$  m<sup>2</sup>/s, so that the inlet Reynolds number  $Re_I$  is 10, where  $Re_I = U_b b / (2\nu_T)$ .

Figure B.17 compares the result obtained with  $n = 5$  to that obtained by Rogers [2001] using over 16 000 finite volume elements at  $t = 300$  s. The agreement is good and indicates that a high order polynomial approximation on a coarse grid can produce similar results to low order methods on very fine numerical grids. Figure B.17 is also in qualitative agreement with those produced by Anastasiou and Chan [1997].

## B.2.4 Quiescent Initial Conditions

A useful and necessary property of a numerical code concerns the ability to simulate quiescent still water conditions. For a basin with depth  $h(x, y)$  and variable bathymetry  $z(x, y)$ , quiescent conditions exist when:

$$h + z = C \quad \text{and} \quad h\mathbf{u} = 0, \quad (\text{B.54})$$

for some constant  $C$ . The DG method developed here preserves quiescent conditions of this form provided bathymetry and depth are continuous spatial functions. This is because symmetric nodal basis functions are adopted and the numerical flux is calculated at the edge of each individual element. As a result the polynomial representation of the initial still water depth will be identical either side of element boundaries. This ensures that the numerical flux normal to the element boundaries reduces to  $\hat{\mathbf{F}}(\mathbf{U}_h) = (0, g(\mathbf{U}_h^{(1)})^2/2, 0)^T$ . For a given element the  $x$  momentum equation, for example, then reduces to

$$-\int_{\Omega} g \frac{(\mathbf{U}_h^{(1)})^2}{2} \frac{\partial l_k}{\partial x} d\Omega + \int_{\Gamma} g \frac{(\mathbf{U}_h^{(1)})^2}{2} l_k n_x d\Gamma = -\int_{\Omega} g h_h \frac{\partial z_h}{\partial x} l_k, \quad \text{for } k \leq M, \quad (\text{B.55})$$

where  $l_k$  are the respective test functions. Equation B.55 is satisfied exactly if the bed slope is formed from the polynomial representation of depth (i.e.  $\partial z_h / \partial x = -\partial(\mathbf{U}_h^{(1)}) / \partial x$ ), and quadrature is performed exactly. Both these conditions are satisfied in the present numerical code. To illustrate the well balanced nature of the numerical model, a test identical to that employed by Ern et al. [2008] has been undertaken. In this case  $h + z = 1$  m, and the bathymetry is defined as

$$z(x, y) = \left( 10e^{-x^2} + 15e^{-(x-2.5)^2} + 10e^{-(x-5)^2/2} + 6e^{-2(x-7.5)^2} + 16e^{-(x-10)^2} \right) / 20,$$

over the domain  $(x, y) \in [0, 10]^2$ . Figure B.18 plots the free surface elevation after  $t = 1$  s (the time considered by Ern et al. [2008]) when 100 triangular elements of order  $n = 2$  are used. It is clear that still water conditions are simulated accurately. The error in the velocity field after  $t = 100$  s (Figure B.18 (b)) is at numerical precision.

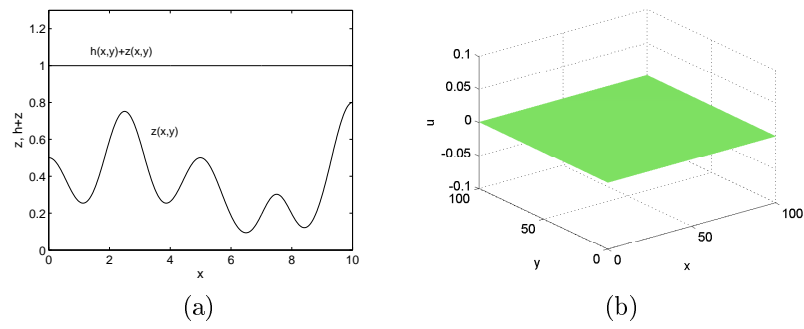


Figure B.18: Numerical simulation of quiescent conditions for variable bathymetry. Polynomial order  $n = 2$ . (a) is the free surface level  $h + z$ , at  $t = 1$  s, (b) the velocity magnitude at  $t = 100$  s.

# Bibliography

- M B Abbott. *Computational Hydraulics: Elements of the theory of free surface flows*. Pitman Publishing Limited, London, 1979.
- ABPmer, MET, Garrad Hassan, and Proudman Oceanographic Laboratory. Atlas of UK Marine Renewable Energy Resources. Technical report, 2004.
- V. Aizinger and C. Dawson. A Discontinuous Galerkin Method for Two-Dimensional Flow and Transport in Shallow Water. *Advances in Water Resources*, 25(1):67–84, 2002.
- K. Anastasiou and C.T. Chan. Solution of the 2D Shallow Water Equations using the Finite Volume Method on Unstructured Meshes. *International Journal for Numerical Methods in Fluids*, 24(11):1255–1245, 1997.
- B K Arbic and C Garrett. A Coupled Oscillator Model of Shelf and Ocean Tides. *Continental Shelf Research*, In Press, 2009.
- A.L. Atkins. Continued Development of the Discontinuous Galerkin Method for Computational Aeroacoustic Applications. *AIAA Journal*, pages Paper 97–1581, 1997.
- H.L. Atkins and C.W. Shu. Quadrature-Free Implementation of Discontinuous Galerkin Method for Hyperbolic Equations. *AIAA Journal*, 36(5):775–782, 1998.
- T. Awaji, N. Imasato, and H. Kunishi. Tidal exchange through a strait: A Numerical Experiment using a simple model basin. *Journal of Physical Oceanography*, 10:1499–1508, 1980.
- P.E. Bernard, J.F. Remacle, and V. Legat. Boundary Discretization for High-Order Discontinuous Galerkin Computations of Tidal Flows Around Shallow Islands. *International Journal for Numerical Methods in Fluids*, 59:535–557, 2009.
- A. Betz. Das maximum der theoretisch möglichen ausnützung des windes durch windmotoren. *Z. Gesamte Turbinenwesen*, 26, 1920.
- J. Blanchfield, C Garrett, A. Rowe, and P. Wild. Tidal Stream Power Resource Assessment for Masset Sound, Haida Gwaii. *IMechE Part A: J. Power and Energy*, 222(5):485–492, 2008a.
- J. Blanchfield, C. Garrett, P. Wild, and A. Rowe. The Extractable Power from a Channel Linking a Bay to the Open Ocean. *IMechE Part A: J. Power and Energy*, 222:289–297, 2008b.
- E. Blayo and L. Debreu. Revisiting Open Boundary Conditions from the Point of View of Characteristic Variables. *Ocean Modelling*, 9:231–252, 2005.
- L.S. Blunden and A.S. Bahaj. Initial Evaluation of Tidal Stream Energy Resources at Portland Bill, UK. *Renewable Energy*, 31:121–132, 2006.
- L.S. Blunden and A.S. Bahaj. Tidal Energy Resource Assessment for Tidal Stream Generators. *IMechE Part A: J. Power and Energy*, 221:137–146, 2007a.
- L.S. Blunden and A.S. Bahaj. Effects of tidal energy extraction at portland bill, southern uk predicted from a numerical model, 2007b.
- H. Bondi. The Simplified Mathematics of Tidal Power. *Teaching Mathematics and its Applications*, 1(3):106–111, 1982.
- J. D. Boon and R. J. Byrne. On Basin Hypsometry and the Morphodynamic Response of Coastal Inlet Systems. *Marine Geology*, 40:27–48, 1981.

- Boussinesq. Théorie de l'écoulement tourbillant. *Mem. Presentes par Divers Savants Acad. Sci. Inst. Fr.*, 23:46–50, 1877.
- J.P. Boyd. The Nonlinear Equatorial Kelvin Wave. *Journal of Physical Oceanography*, 10:1–11, 1980.
- I. G. Bryden and S.J. Couch. ME1-Marine Energy Extraction: Tidal Resource Analysis. *Renewable Energy*, 31:133–139, 2006.
- I. G. Bryden, S. J. Couch, A. Owen, and G. Melville. Tidal Current Resource Assessment. *Proc. IMech Vol. 221 Part A: J.Power and Energy*, 221:125–135, 2007.
- I.G. Bryden and S.J. Couch. How Much Energy can be Extracted from Moving water with a Free Surface: A Question of Importance in the Field of Tidal Current Energy? *Renewable Energy*, 32:1961–1966, 2007.
- I.G. Bryden, T. Grinsted, and G.T. Melville. Assessing the Potential of a Simple Tidal Channel to Deliver Useful Energy. *Applied Ocean Research*, 26:198–204, 2005.
- S. Bunya, E.J. Kubatko, J.J. Westerlink, and C. Dawson. A Wetting and Drying Treatment for the Runge-Kutta Discontinuous Galerkin Solution to the Shallow Water Equations. *Computational Methods in Applied Mechanical Engineering*, 198:1548–1562, 2009.
- T. Burton, D. Sharpe, N. Jenkins, and E. Bossanyi. *Wind Energy Handbook*. John Wiley & Sons, Ltd, West Sussex, 2001.
- D.C. Chapman. Numerical Treatment of Cross-Shelf Open Boundaries in a Barotropic Coastal Ocean Model. *Journal of Physical Oceanography*, 15:1060–1075, 1985.
- D. Chen and G.H. Jirka. Experimental Study of Plane Turbulent Wakes in a Shallow Water Layer. *Fluid Dynamics Research*, 16:11–41, 1995.
- B. Cockburn and C.W. Shu. Local Discontinuous Galerkin Method for Time-Dependant Convection-Diffusion Systems. *SIAM J. Numerical Analysis*, 35(6):2440–2463, 1998.
- B. Cockburn, S.Y. Lin, and C.W. Shu. TVB Runge-Kutta local projection discontinuous Galerkin finite element method for scalar conservation laws. Part III. One-dimensional systems. *J. Comput. Phys.*, 84: 90–113, 1989.
- European Commission. The exploitation of tidal and marine energy currents. Wave energy. Project results. Technical report, 1996.
- C.N. Dawson and J. Proft. Coupled Discontinuous and Continuous Galerkin Finite Element Methods for the Depth-Integrated Shallow Water Equations. *Computational Methods in Applied Mechanical Engineering*, 193(3-5):289–318, 2004.
- R. G. Dean and R. A. Dalrymple. *Water Wave Mechanics For Engineers and Scientists*, volume 2 of *Advanced Series on Ocean Engineering*. World Scientific, Singapore, 1984.
- A. Defant. *Physical Oceanography*, volume 2. Pergamon, 1961.
- M.K. Denham and M.A. Patrick. Laminar Flow Over a Downstream-Facing Step in a Two-Dimensional Flow Channel, journal = Chemical Engineering Research and Design, volume = 52a, pages = 361-367, year = 1974.
- S. Draper. Tidal Stream Energy Extraction in Coastal Basins Transfer Report. Technical report, University of Oxford, 2008.
- S. Draper, G.T. Houlsby, M.L.G. Oldfield, and A.G.L. Borthwick. Modelling Tidal Energy Extraction in a Depth-Averaged Coastal Domain. *IET Renew. Power Gener.*, (4):545–554, 2010.
- M. Dubiner. Spectral Methods on Triangles and Other Domains. *Journal of Scientific Computing*, (6): 345–390, 1991.
- G D Egbert and R D Ray. Estimates of M2 Tidal Energy Dissipation from TOPEX/Poseidon Altimeter Data. *Journal of Geophysical Research*, 106(C10):22475–22502, 2001.

- EIA. Energy Information Administration: International Energy Outlook 2009, 2009.
- J.W. Elder. The Dispersion of Marked Fluid in Turbulent Shear Flow. *Journal Fluid Mechanics*, 5(4): 544–560, 1959.
- EPRI. California Electric Power Research Institute reports on Tidal Stream Power, 2006.
- A. Ern, S. Piperno, and K. Djadel. A Well-Balanced Runge-Kutta Discontinuous Galerkin Method for the Shallow-Water Equations with Flooding and Drying. *International Journal for Numerical Methods in Fluids*, 58:1–25, 2008.
- C. Eskilsson and S.J. Sherwin. A Triangular Spectral/hp Discontinuous Galerkin Method for Modelling 2D Shallow Water Equations. *International Journal for Numerical Methods in Fluids*, 45:605–623, 2004.
- R.A. Falconer. An Introduction to Nearly-Horizontal Flows. *Coastal, Estuarial and Harbour Engineer's reference book.*, Chapman & Hall, 1993.
- B.A. Flather. A Tidal Model of the Northwest European Continental Shelf, journal = Mem.Sco. R. Sci., volume = 6, pages = 141-164, year = 1976.
- P.L. Fraenkel. Power from Marine Currents. *Proc. IMech Vol. 216 Part A: J.Power and Energy*, 216 (Special):1–14, 2002.
- C.T. Friedrichs and D.G. Aubrey. Non-Linear Tidal Distortion in Shallow Well-Mixed Estuaries: A Synthesis. *Estuarine, Coastal and Shelf Science*, 27(5):521–545, 1988.
- R.E. Froude. Transactions, Institute of Naval Architects. 30:390, 1889.
- C. Garrett. Tidal Resonance in the Bay of Fundy and Gulf of Maine. *Nature*, 238:441–443, 1973.
- C Garrett. Tides in Gulfs. *Deep-Sea Research*, 22:23–35, 1975.
- C. Garrett and P. Cummins. Generating Power from Tidal Currents. *J. Wtrwy., Port, Coast., and Oc. Engrg.*, 130:114–118, 2004.
- C. Garrett and P. Cummins. The Power Potential of Tidal Currents in Channels. *Proc. R. Soc. Lond. A*, 461:2563–2572, 2005.
- C. Garrett and P. Cummins. The Efficiency of a Turbine in a Tidal Channel. *Journal of Fluid Mechanics*, 588:243–251, 2007.
- C. Garrett and P. Cummins. Limits to Tidal Current Power. *Renewable Energy*, In Press, 2008.
- C Garrett and D Greenberg. Predicting Changes in Tidal Regime: The Open Boundary Problem. *Journal of Physical Oceanography*, 7:171–181, 1977.
- F.X. Giraldo and T. Warburton. A high-order Triangular Discontinuous Galerkin Shallow Water Model. *International Journal for Numerical Methods in Fluids*, 56:899–925, 2008.
- H. Glauert. *The Elements of Aerofoil and Airscrew Theory*. Cambridge University Press, Cambridge, second edition, 1947.
- D. Gregory, B. Petrie, F. Jordan, and P. Langille. Oceanographic, Geographic, and Hydrological Parameters of Scotia-Fundy and Southern Gulf of St Lawrence Inlets. Technical report, Physical and Chemical Sciences Branch. Dept. of Fisheries and Oceans, Canada, 1993.
- M.E. Harrison, W.M.J. Batten, L.E. Myers, and A.S. Bahaj. Comparison between CFD simulations and experiments for predicting the far wake of horizontal axis tidal turbines. *IET Renewable Power Generation*, 4:613–627, 2010.
- R.A. Heath. Resonant Period and Q of the Celtic Sea and Bristol Channel. *Estuarine, Coastal and Shelf Science*, 12(3):291–301, 1981.
- J.S. Hesthaven and T. Warburton. *Nodal Discontinuous Galerkin Methods*. Texts in Applied Mathematics. Springer, New York, 2008.

- G.T. Houlsby, S. Draper, and M.L.G. Oldefield. Application of Linear Momentum Actuator Disc Theory to Open Channel Flow. Technical Report OUEL 2296/08, January 2008 2008.
- W.F. Hughes and J.A. Brighton. *Schaum's Outline of Theory and Problems of Fluid Mechanics*. McGraw-Hill, New York, 1967.
- J.N. Hunt. Tidal Oscillations in Estuaries. *Geophys. J. R. astr. Soc.*, 8:440–455, 1964.
- M. Iskandarani, D.B. Haidvogel, and J.P. Boyd. A Staggered Spectral Element Model with Application to the Oceanic Shallow Water Equations. *International Journal for Numerical Methods in Fluids*, 20: 393–414, 2005.
- G.H. Jirka. Large scale Flow Structures and Mixing Processes in Shallow Flows. *Journal of Hydraulic Research*, 39(6):567–573, 2002.
- G.E. Karniadakis and S. Sherwin. *Spectral/hp Element Methods for Computational Fluid Dynamics*. Oxford Science Publications. Oxford University Press, Oxford, 2nd edition, 2005.
- R. H. Karsten, J. M. McMillan, M. J. Lickley, and R. D. Haynes. Assesment of Tidal Current Energy in the Minas Passage, Bay of Fundy. *IMEchE Part A: J. Power and Energy*, 222:493–507, 2008.
- G. Kesserwani, R. Ghostine, J. Vazquez, A. Ghenaim, and R. Mose. Application of a Second Order Runge-Kutta Discontinuos Galerkin Scheme for the Shallow Water Equations with Source Terms. *International journal for numerica methods in fluids*, 56:805–821, 2008.
- R.M. Kirby and S.J. Sherwin. Aliasing Errors due to Quadratic Nonlinearities on Triangular Spectral/hp Element Discretisations. *Journal of Engineering Mathematics*, 56:273–288, 2006.
- E.J. Kubatco, J.J. Westerlink, and C. Dawson. hp Discontinuous Galerkin Methods for Advection Dominated Problems in Shallow Water Flow. *Computational Methods in Applied Mechanical Engineering*, 196:437–451, 2006a.
- E.J. Kubatco, J.J. Westerlink, and C. Dawson. An Unstructured Grid Morphodynamic Model with Discontinuous Galerkin Method for Bed Evolution. *Ocean Modelling*, 15(1-2):71–89, 2006b.
- E.J. Kubatco, S. Bunya, C. Dawson, J.J. Westerlink, and C. Mirabito. A Performance Comparison of Continuous and Discontinuous Finite Element Shallow Water Models. *Journal of Scientific Computing*, 40:315–339, 2009.
- H. Lamb. *Hydrodynamics*. Cambridge University Press, 6th edition, 1932.
- F.W. Lanchester. A Contribution to the Theory of Propulsion and the Screw Propeller. *Trans. Inst. Naval Archit.*, LVII:98–116, 1915.
- J.W. Lavelle and W.C. Thacker. A pretty good sponge: Dealing with open boundaries in limited-area ocean models. *Ocean Modelling*, 20:270–292, 2008.
- J.H. Lee and M.D. Greenberg. Line Momentum Source in Shallow Inviscid Fluid. *Journal of Fluid Mechanics*, 145:287–304, 1984.
- J.H. Lee and G.H. Jirka. Multiport Diffuser as a Line Source of Momentum in Shallow Water. *Water Resources Research*, 16:695–708, 1980.
- R.J. LeVeque. *Finite Volume Methods for Hyperbolic Problems*. Cambridge texts in applied mathematics. Cambridge university press, NY, USA, 2002.
- H. Li and R.X. Liu. The Discontinuous Galerkin Finite Element Method for the 2D Shallow Water Equations. *Mathematics and Computers in Simulation*, 56:171–184, 2001.
- Q. Liang and A. G. L. Borthwick. Adaptive Quadtree Simulation of Shallow Flows with Wet-Dry Fronts over Complex Topography. *Computers & Fluids*, 38:221–234, 2009.
- J. Lighthill. *Waves in Fluids*. Cambridge University Press, 1978.
- Black & Veatch Ltd. Phase I: UK Tidal Stream Energy Resource Assessment. Technical report, 2004.

- Black & Veatch Ltd. Phase II: UK Tidal Stream Energy Resource Assessment. Technical report, 2005.
- Triton Consultants Ltd. Canada Ocean Energy Atlas (Phase 1) potential tidal current energy resource analysis background. Prepared for the Canadian Hydraulics Centre, Natural Resources Canada. Technical report, 2006.
- D.R. Lynch and W.G. Gray. A Wave Equation Model for Finite Element Tidal Computations. *Computers & Fluids*, 7(207):207–228, 1979.
- H. Ma. A Spectral Element Basin Model for the Shallow Water Equations. *Journal of Computational Physics*, 109:133–149, 1993.
- L. R. M. Maas. On the Nonlinear Helmholtz Response of Almost-Enclosed Tidal Basins with Sloping Bottoms. *J. Fluid Mech.*, 349:361–380, 1997.
- D.J.C. MacKay. Enhancing Electrical Supply by Pumped Storage in Tidal Lagoons. Available at <http://www.inference.phy.cam.ac.uk/mackay/Environment.html>, 2007a.
- D.J.C. MacKay. Under-Estimation of the UK Tidal Resource. Available at <http://www.inference.phy.cam.ac.uk/mackay/Environment.html>, 2007b.
- L. Maddock and R.D. Pingree. Numerical Simulation of the Portland Tidal Eddies. *Estuarine and Coastal Marine Science*, 6:353–363, 1978.
- E.A. Martinsen and H. Engedahl. Implementation of a Lateral Boundary Scheme as an Open Boundary Condition in a Barotropic Ocean Model. *Coastal Engineering*, 11:603–627, 1987.
- B. Massey. *Mechanics of Fluids*. Stanley Thornes, Cheltenham, U.K., 7 edition, 1998.
- R. McAdam, G. T. Houlsby, M.L.G Oldfield, and M.D. McCulloch. Experimental Testing of the Transverse Horizontal Axis Water Turbine, 2009.
- Chiang C. Mei. *The Applied Dynamics of Ocean Surface Waves*. advanced series on ocean engineering. World Scientific Publishing, London, UK, 1989.
- J. W. Miles. Resonant Response of Harbours: An Equivalent-Circuit Analysis. *J. Fluid Mech.*, 46:241–265, 1971.
- L.M. Milne-Thomson. *Theoretical Aerodynamics*. St Martin’s Press, New York, 4th edition, 1966.
- A. Modave, E. Deleersnijder, and E. J. M. Delhez. On the Parameters of Absorbing Layers for Shallow Water Models. *Ocean Dynamics*, 60(1):65–79, 2009.
- L. E. Myers and A. S. Bahaj. Experimental Analysis of the Flow Field around Horizontal Axis Tidal Turbines by use of Scale Mesh Disk Rotor Simulators. *Ocean Engineering*, 37:218–227, 2010.
- NOAA. National Oceanic and Atmospheric Administration (US): Tides and Currents, 2010.
- J. Nycander and K. Doos. Open Boundary Conditions for Barotropic Waves. *Journal Geophysical Research*, 108(C5):doi:10.1029/2002JC001529, 2003.
- R.A. O’Leary and T.J. Mueller. Correlation of Physical and Numerical Experiments for Incompressible Laminar Separated Flows. Technical report, Notre Dame Univ. Ind. Coll. of Engineering, 1969.
- F. O’Rourke, Boyle F, and A. Reynolds. Tidal Energy Update 2009. *Applied Energy*, 87:398–409, 2010.
- I Paraschivoiu. *Wind Turbine Design: With Emphasis on Darrieus Concept*. Polytechnic International Press, Canada, 2002.
- Per-Olof Persson. *Mesh Generation for Implicit Geometries*. PhD thesis, MIT, 2004.
- R.D. Pingree and D.K. Griffiths. Sand Transport Paths around the British Isles Resulting from M2 and M4 Tidal Interactions. *Journal Marine Biology Ass.*, 59:497–513, 1979.
- R.D. Pingree and L. Maddock. The Tidal Physics of Headland Flows and Offshore Tidal Bank Formation. *Marine Geology*, 32:269–289, 1979.

- G.W. Platzman. Tidal Evidence for Ocean Normal Modes. *In: Parker, B.B. (Ed.), Tidal Hydrodynamics. Wiley New York, pp. 13-26, 1991.*
- B Polagye, P Malte, M Kawase, and D Durran. Effect of Large-Scale Kinetic Power Extraction on Time-Dependant Estuaries. *Proc. IMechE Part A: J.Power and Energy*, 222:471–484, 2008.
- B. L. Polagye and P. C. Malte. Far-field dynamics of Tidal Energy Extraction in Channel Networks. *Renewable Energy*, 36:222–234, 2011.
- D. Prandle. Simple Theory for Designing Tidal Power Schemes. *Advances in Water Resources*, 7:21–27, 1984.
- D. Prandle. Classification of Tidal Response in Estuaries from Channel Geometry. *Geophys. J. R. astr. Soc.*, 80:209–221, 1985.
- D. Prandle and M. Rahman. Tidal Response in Estuaries. *J. Phys. Oceanogr.*, 10:1552–1573, 1980.
- D.T. Pugh. *Tides, Surges and Mean Sea-Level*. John Wiley and Sons, 1987.
- R.C.T. Rainey. The Optimum Position for a Tidal Power Barrage in the Severn Estuary. *Journal of Fluid Mechanics*, 636:497–507, 2009.
- W.J. Rankine. Transactions, Institute of Naval Architects. 6:13, 1865.
- W.H. Reed and T.R. Hill. Triangular Mesh Methods for the Neutron Transformation Equation. Technical report, Los Alamos Scientific Laboratory Report, 1973.
- O. Reynolds. On the Dynamical Theory of Incompressible Viscous Fluids and the Determination of the Criterion. *Phil. Trans. Royal Socceity*, 174:935–982, 1895.
- I.S. Robinson. Tides in the Bristol Channel - An Analytical Wedge Model with Friction. *Geophys. J. R. astr. Soc.*, 62:77–95, 1980.
- I.S. Robinson and J.M. Perry. Tidal Power from Rectangular Estuaries: Tidal Dynamics Constraints. *J. Hydraul. Div.*, 106:1915–1934, 1980.
- B.D. Rogers. *Refined Localised Modelling of Coastal Flow Features using Adaptive Quadtree Grids*. PhD thesis, University of Oxford, 2001.
- D. Schwanenberg and M. Harms. Discontinuous Galerkin Finite-Element Method for Transcritical Two-Dimensional Shallow Water Flows. *Journal of Hydraulic Engineering*, 130:412–421, 2004.
- R.P. Signell. *Tidal Dynamics and Dispersion Around Coastal Headlands*. PhD thesis, Massachusetts Institute of Technology, 1989.
- R.P. Signell and W.R. Geyer. Transient Eddy Formation Around Headlands. *Journal of Geophysical Research*, 96:2561–2575, 1991.
- R.J. Sobey. Wetting and Drying in Coastal Flows. *Coastal Engineering*, 56(5-6):565–576, 2008.
- J.N. Sorensen, W.Z. Shen, and X. Munduate. Analysis of Wake States by a Full-field Actuator Disc Model. *Wind Energy*, 1:73–88, 1998.
- R. Soulsby. *Dynamics of Marine Sands*. Thomas Telford Services Limited, 1997.
- P.E. Speer and D.G. Aubrey. A Study of Non-Linear Tidal Propagation in Shallow Inlet/Estuarine Systems Part 2:Theory. *Estuarines, Coastal and Shelf Science*, 21(2):207–224, 1985.
- P.K. Stansby. A Mixing-Length Model for Shallow Turbulent Wakes. *Journal Fluid Mechanics*, 495: 369–384, 2003.
- P.K. Stansby. Limitations of Depth-Averaged Modelling for Shallow Wakes. *ASCE J. Hydraulic Engineering*, 132(7):737–740, 2006.
- J.J. Stoker. *Nonlinear Vibrations in Mechanical and Electrical Systems*, volume 2. Interscience publishers, New York, 1950.

- G. Sutherland, M. Foreman, and C. Garrett. Tidal Current Energy Assessment for Johnstone Strait, Vancouver Island. *Proc. IMechE Part A: J. Power and Energy*, 221:147–157, 2007.
- G. I. Taylor. Tidal Friction in the Irish Sea. *Phil. Trans. Royal Society of London, Series A*, 220:1–33, 1920.
- G. I. Taylor. Tides in the Bristol Channel. *Proc. Camb. Phil. Soc.*, 20:320–325, 1921.
- G.M. Terra, A. Doelman, and L.R.M. Maas. Weakly Nonlinear Cubic Interactions in Coastal Resonance. *J. Fluid Mech.*, 520:93–134, 2004.
- Pulse Tidal. Pulse Tidal, 2010.
- E.F. Toro. Shock-Capturing Methods for Free-Surface Shallow Flows, 2001. Book covering Riemann problems and programming practically. Interesting derivation of shallow water equations, talk on primitive variables. And derivation of 2nd order Riemann approx.
- E.F. Toro, M. Spruce, and W. Speares. Restoration of the Contact Surface in the HLL-Riemann Solver. *Shock Waves*, 4:25–34, 1994.
- I. Townend. An Examination of Empirical Stability Relationships for UK Estuaries. *Journal of Coastal Research*, 21(5):1042–1053, 2005.
- Marine Current Turbines. Marine Current Turbines, 2010.
- Edinburgh University. Tidal Current Energy: Device Performance Protocol - Response to feedback from 19th July workshop and consultation. Technical Report 07/839, 2007.
- G.A.M. van Kuik. The Edge Singularity of an Actuator Disc with a Constant Normal Load. *AIAA Journal*, 0365:62–72, 2003.
- G.A.M. van Kuik. The Lanchester-Betz-Joukowski Limit. *Wind Energy*, 10:289–291, 2007.
- R. Vennell. Tuning Turbines in a Tidal Channel. *Journal Fluid Mechanics*, 663:253–267, 2010.
- T. Warburton. An Explicit Construction of Interpolation Nodes on the Simplex. *Journal of Engineering Mathematics*, 56:247–262, 2006.
- J.I. Whelan, M. Thomson, J.M.R. Graham, and J. Peiro. Modelling of Free Surface Proximity and Wave Induced Velocities Around a Horizontal Axis Tidal Stream Turbine, 2007.
- J.I. Whelan, J.M.R. Graham, and J. Peiro. A Free-Surface and Blockage Correction for Tidal Turbines. *Journal Fluid Mechanics*, 624:281–291, 2009.
- F.M. White. *Fluid Mechanics*. McGraw-Hill, London, third edition, 1994.
- R.E. Wilson. Wind-Turbine Aerodynamics. *J. of Industrial Aerodynamics*, 5:357–372, 1980.
- R.E. Wilson and P.B.S. Lissaman. Applied Aerodynamics of Wind Power Machines. Technical report, 1974.
- Donald. F. Young, Bruce. R. Munson, and Theodore. H. Ikiishi. *A Brief Introduction to Fluid Mechanics*. John Wiley & Sons, Inc., USA, 2nd edition, 2001.